Large eddy simulation of liquid-fuel film : sooting-flame interaction in wall bounded turbulent flows

Mohamed Amine Chemak

Normandie Université

THÈSE

Pour obtenir le diplôme de doctorat

Spécialité Energétique

Préparée à l'IFP Energies Nouvelles

Large Eddy Simulation of Liquid-Fuel Film/Sooting-Flame Interaction in Wall Bounded Turbulent Flows

présentée et soutenue par

Mohamed Amine Chemak

Thèse soutenue publiquement le 19 Mai 2022 devant le jury composé de		
F. Chedevergne	Ingénieur de Recherche, ONERA	Rapporteur
R. Vicquelin	Professeur à l'école CentraleSupélec, EM2C - CNRS	Rapporteur
F. Nicoud	Professeur Université de Montpelier, IMAG - CNRS	Examinateur
B. Franzelli	Chargé de Recherche, EM2C - CNRS	Examinatrice
L. Vervisch	Professeur à l'INSA de Rouen, CORIA - CNRS	Directeur de thèse
O. Colin	Ingénieur de Recherche, IFPEN	Co-directeur de thèse

□ **Thèse dirigée et encadrée par :**

- **Directeur de thèse : Prof. Luc Vervisch**
- **Co-directeur de thèse : Dr. Olivier Colin**
- **Encadrant : Dr. Damien Aubagnac-Karkar**

INSA INSTITUT NATIONAL DES SCIENCES APPLIQUÉES ROUEN NORMANDIE — ED PSIME — CORIA UMR 6614 — IFP Energies nouvelles

Abstract

The interaction of premixed flame with a liquid fuel film is the main source of soot generation in Gasoline Direct Injection engines. The objective of this thesis is the detailed modeling with Large Eddy Simulation of the involved physical phenomena, which includes: near wall turbulent flow, liquid film evaporation, flame-wall interaction, and soot formation. The canonical turbulent channel flow is chosen for this study. The liquid film evaporation models available in the literature is first evaluated and a new wall model is proposed to improve the results. The behavior of the Thickened Flame Model during the flame wall interaction is studied in detail. Then, the soot formation is studied during the interaction of a turbulent flame with a liquid film. The reference computation allows to understand the phenomenology of soot formation under these conditions. Finally, the influence of the different wall and combustion models is evaluated.

Remerciements

Je remercie tout d'abord mes encadrants, Prof. Luc Vervisch de l'INSA Rouen, Dr. Olivier Colin et Dr. Damien Aubagnac-Karkar de l'IFP Energies Nouvelles. Leurs conseils ont été fondamentaux pour façonner ma recherche et leur encouragement constant a été une source constante de motivation. Je suis très honoré d'avoir pu bénéficier de leur encadrement. Merci pour tout.

J'adresse mes remerciements les plus distingués aux membres de mon jury de thèse pour avoir accepté d'évaluer mon travail. Je remercie Dr. François Chaudevergne et Prof. Ronan Vicquelin pour leurs lectures minutieuses de mon manuscrit et avoir rédigé leurs rapports. Je remercie Prof. Franck Nicoud et Dr. Benedetta Franzelli pour leurs évaluations et remarques pertinentes.

Je remercie Dr. Stéphane Jay et Dr. Guido Lodato, membres de mon comité de suivi individuel de l'école doctorale pour leurs disponibilités et leurs conseils.

Je remercie les chercheurs du département "Modélisation Numérique des Système Energétiques" de l'IFP Energies Nouvelles pour leurs avis et aides à différentes occasions durant mes travaux. Un très grand merci à Dr. Gilles Bruno, le chef de département, pour son suivie engagée et pour son soutien inoubliable. Je souhaite exprimer ma gratitude à Dr. Karine Trufin pour son aide précieuse. Je remercie Dr. Chaouki Habchi pour ses conseils et discussions intéressantes sur les problèmes diphasiques. Je remercie également Dr. Cedric Mehl pour son accompagnement sur les modèles de Combustion.

Je remercie évidemment les nombreux doctorants et les postdocs de l'IFP Energies Nouvelles qui m'ont accompagné pendant la thèse. Les nombreuses heures passées ensemble à discuter d'idées, les rires et la camaraderie ont rendu l'expérience encore plus enrichissante. Je remercie aussi les doctorants à l'INSA Rouen pour leur accueil chaleureux lors de mon déplacement.

Je remercie aussi tous mes amis en dehors de l'IFP Energies Nouvelles. Je remercie ma bien-aimée Aicha pour sa bienveillance et pour son soutien continu. Enfin, je tiens à exprimer ma profonde reconnaissance à ma famille, mon frère et mes chers parents, pour leurs soutiens et leurs sacrifices durant toutes ces années, sans eux je ne serais pas arrivé à ce point, merci infiniment.

Contents

List of symbols

Roman characters

Symbol	Description	Unit
$\boldsymbol{A}$	Area	m^2
$\boldsymbol{V}$	volume	m^3
B_q	Heat flux parameter	[-]
B_M	Spalding mass transfer number	[-]
D	Mass diffusion coefficient	$m^2.s^{-1}$
E	Efficiency factor	[-]
F	Thickening factor	[-]
J	Mass diffusion flux	$kg.m^{-2}.s^{-1}$
L	Latent heat of evaporation	$J.kg^{-1}$
N	Total number of species on the mixture	[-]
P	Pressure	Pa
R	Universal gas constant	$J.mol^{-1}.K^{-1}$
T	Temperature	K
U	Velocity vector	$m.s^{-1}$
$U_{//}$	Wall parallel velocity component	$m.s^{-1}$
V	Mass diffusion velocity	$m.s^{-1}$
W	Molecular weight	$g.mol^{-1}$
X	Species molar fraction	[-]
Y	Species mass fraction	[-]
x	Characteristic length	m
c	Progress variable	[-]
c_p	Specific heat capacity at constant pressure	$J.kg^{-1}.K^{-1}$
c_v	Specific heat capacity at constant volume	$J.kg^{-1}.K^{-1}$
e_s	Sensible internal energy	$J.kg^{-1}$
g	Mass transfer conductance	$kg.m^{-2}.s^{-1}$
h_s	Sensible enthalpy	$J.kg^{-1}$
h_c	Convective heat transfer coefficient	$W.K^{-1}.m^{-2}$
l_m	Mixing-length scaled	m
$\dot{m}$	Mass evaporation rate per unit surface	$kg.m^{-2}.s^{-1}$
q	Heat flux	$W.m^{-2}$
t	Time	s
u, v, w	Velocity vector components (streamwise, normalwise, spanwise)	$m.s^{-1}$
y	Distance from the wall	m
x	Coordinate system vector	m
y	Distance from the wall	m

Greek characters

Symbol	Description	Unit
Δy	Mesh cell size	m
Θ	Reduced Temperature	[-]
β	Temperature exponent in Arrhenius law	[-]
δ	Channel half height	m
δ_L	Laminar flame thickness	m
δ_M	Mass boundary layer thickness	m
δ_U	Dynamic boundary layer thickness	m
δ_T	Thermal boundary layer thickness	m
δ_{ij}	Kronecker symbol	[-]
δ_l	Wall-film thickness	m
δ_{wf}	Wall-film thickness	m
δ_ν	Wall viscous length scale	m
κ	The Von Karman constant	[-]
λ	Thermal conductivity	$W.m^{-1}.K^{-1}$
μ	Dynamic viscosity	$kg.m^{-1}.s^{-1}$
ν	Kinematic viscosity	$m^2.s^{-1}$
ρ	Density	$kg.m^{-3}$
τ (τ_{ij})	Shear stress (shear stress tensor)	$kg.m^{-1}.s^{-2}$
τ_t	Turbulent time scale	s
$\dot{\omega}_T$	Chemical heat release	$W.m^{-3}$
$\dot{\omega}_k$	Mass species reaction rate	$kg.m^{-3}.s^{-1}$

Dimensionless numbers

Symbol	Description
Re	Reynolds number
Sc	Schmidt number
Nu	Nusselt number
Sh	Sherhood number
Le	Lewis number
Pr	Prandtl number
P	Peclet number
$\mathcal{F}$	Heat flux scaled by reference flame power
Da	Damköhler number
Ka	Karlovitz number

Subscripts

Symbol	Description
1	Quantity at the center of the wall adjacent cell
F	Fuel or evaporated species
i, j	indices used for spatial directions
k	index used for chemical species
g	gas
l	liquid
s	gas/liquid interface
w	wall
t	Turbulent quantity
$tran$	Laminar/turbulent transition
b	Burned quantity
u	Unburned quantity

Acronyms

Acronym	Definition
AMR	Adaptive Mesh Refinement
CFD	Computational Fluid Dynamics
CFL	Courant-Friedrichs-Lewy
DI	Direct Injection
DNS	Direct Numerical Simulation
DRGEP	Directed Relation Graph with Error Propagation
FFI	Flame-Film Interaction
FWI	Flame-Wall Interaction
GDI	Gasoline Direct Injection
GER	Global Evaporation Rate
HAB	Height Above Burner
HOQ	Head-On Quenching
ICE	Internal Combustion Engine
LES	Large Eddy Simulation
LLM	Log-Layer Mismatch
NEDC	New European Driving Cycle
ODEs	Ordinary Differential Equations
ORCh	Optimized Reduced Chemistry
PAH	Polycyclic Aromatic Hydrocarbons
PFI	Port Fuel Injection
PISO	Pressure Implicit with Splitting of Operator
PM	Particulate Matter
PN	Particulate Number
PSDF	Particle Soot Distribution Function
QSS	Quasi-Steady State
RANS	Reynolds-Avereged Numerical Simulation
SGS	Sub-Grid Scale
SSM	Sectional Soot Model
TFM	Thickened Flame Model
UHC	Unburnt Hydro-Carbons
WMLES	Wall-Modeled LES

List of Figures

List of Tables

Chapter 1

Introduction

Contents

1.1 Context

1.1.1 Cars engines: Source of global and local pollution

The global warming is generally associated to the global increase of energy consumption in the last decades. With about 20% of the global energy consumption, the transport sector is considered as one of the main greenhouse emitter [2]. About 22 million barrels of oil per day were consumed only by cars in 2017 [3]. Despite the continuous rise of activity, and according to the New Policies Scenario developed by the international energy agency, it is expected that cars will have the same oil demand as in 2017 by 2040. The increase of activity will be compensated by the use of more electric engines, biofuels, natural gas, and mainly by improving fuel efficiency.

In addition to greenhouse emissions, cars are also one of the main responsible of the local pollution, due to NOx and Particulate Matter (PM) emissions. These emissions have hazardous health effect and they causes many diseases as shown in Figure 1.1. PM with mean diameter of $2.5\mu m$ or less ($PM_{2.5}$) is one of the most relevant pollutants linked to health problems and premature mortality. It is estimated that, in 2018, there were about 379 000 premature deaths in the 28 members states of the European Union attributable to $PM_{2.5}$ [4]. During the Covid-19 pandemic, some works suggested that the rapid spread and mortality in cities may be related to PM emissions [5, 6].

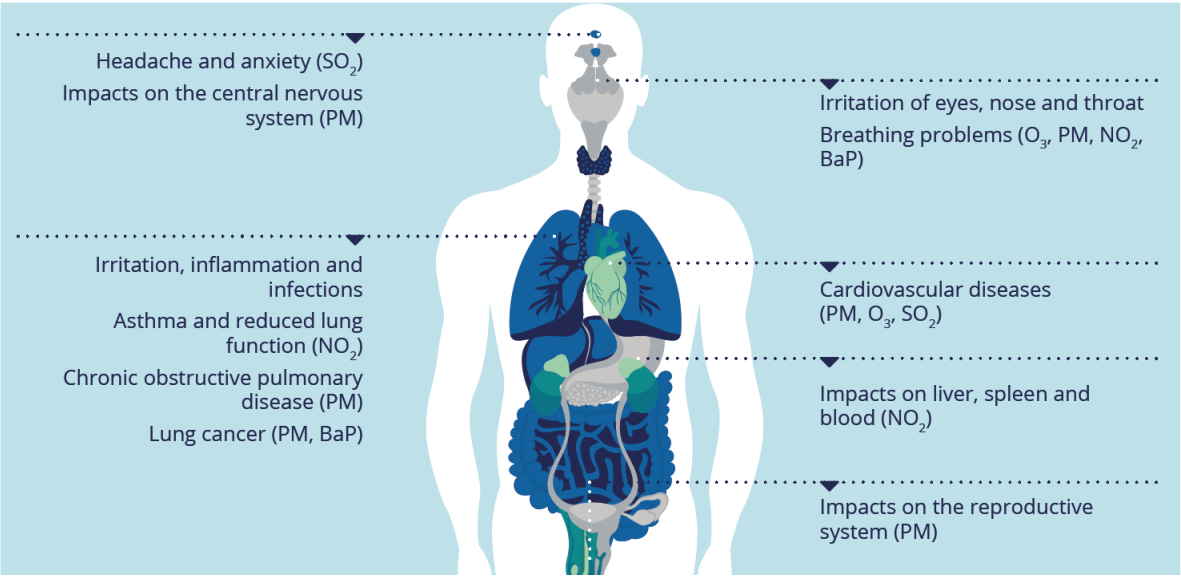

Figure 1.1: Major sources of ambient air pollution and potential human health impacts [4]

Due to adverse environmental and health effects, particle emitted from gasoline engines are regulated with more and more strict standards. The European Commission introduced a limit on particle (5.10^{-3} g/km) mass as part of the Euro 5 standard. In addition, particle number emissions were limited to 6.10^{12} particles/km by legislation at the Euro 6 stage in 2014, and this limit is further reduced to 6.10^{11} particles/km in 2017. Currently, only particles larger than 23nm are counted for the regulations.

1.1.2 Gasoline Direct Injection engine technology

Internal Combustion Engines (ICEs) are generally classified according to fuels: Diesel or gasoline engines. Diesel engines are compression ignition engines where the fuel is injected at the end of the compression stroke and is auto-ignited. Gasoline engines are generally spark-ignition engines where the ignition is controlled by an external source of energy. Despite their high power efficiency, Diesel engines are less and less used in the car market due to the high PM and NOx emissions. Gasoline engines are classified according to the injection technology. In Port Fuel Injection (PFI) gasoline engines fuel is injected in front of the intake valve. This allows an almost complete evaporation of the fuel and leads to a good fuel air mixture. In order to improve engine efficiency, reduce fuel consumption and therefore reduce CO2 emissions, the fuel is directly injected into the cylinder in Gasoline Direct Injection (GDI) engines. Injecting the fuel in the cylinder has the effect of reducing the charge temperature which allows to reach high compression ratio, and hence increasing power efficiency, with limited risk of knock. GDI engines have been improved through the years and many injection technologies were developed. In the wall-guided Direct Injection engine, the fuel is injected into the combustion chamber by a side-mounted injector as shown in figure 1.2a. The mixture is then guided towards the spark-plug region by the charge motion and a spoon-shaped piston crown. Because of the piston crown geometry, wall-guided combustion chambers features a high surface area to volume ratios, which decreases the thermodynamic performance by heat loss through the combustion chamber surfaces. In the spray-guided Direct Injection engine, the injector and spark plug are mounted close together in the top of a pent roof combustion chamber as shown in figure 1.2b. With the later injection technology, the thermodynamic performance should also be improved as a conventional flat top piston crown geometry is used. Engines operating with wall-guided injection are considered as first generation GDI engines, while engines operating with spray-guided injection are considered as second generation GDI engines. The GDI engine can operate in two modes: stratified or homogeneous charge, though in practice, there is not a sharp dividing line between them. Injecting fuel late, during the latter half of the compression stroke, leads to a stratified charge. In contrast, early injection leads to a homogeneous charge combustion resembling that of

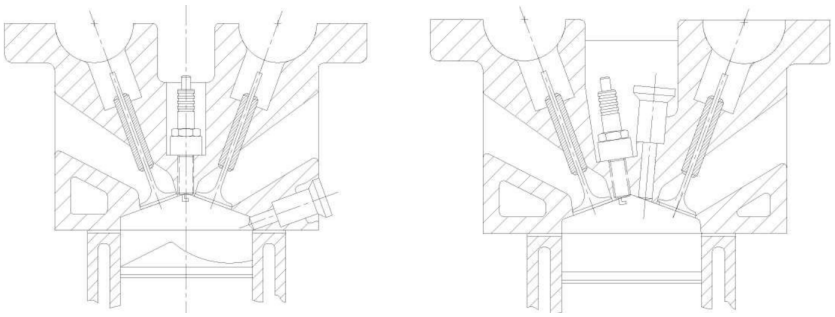

(a) Wall-guided DI **(b)** Spray-guided DI

Figure 1.2: Diagram of Direct Injection combustion systems [7]

a PFI engine.

1.1.3 PM emissions by GDI engines

Experimental investigation gives an insight into the influencing parameters of soot formation in GDI engines. Some experiments are performed on commercial engines, where the exhaust soot mass and number can be related to the engine and driving conditions (cold start vs warm engine, fuel characteristics, engine speed and load, etc). Some other experiments are carried out on research optical engines, where the influence of engine combustion characteristics (charge mixture, injection strategy, wall wetting, etc) on soot formation is easier to figure out.

GDI engines compared to other ICEs

According to the experimental measurements of Whitaker et al. [8] in 2011, shown in Figure 1.3, PFI engines emits at least one order of magnitude of particle mass less than GDI engines. First generation GDI engines, operating with a wall-guided injection, exceed both PM and Particulate Number (PN) standards by a considerable factor, whereas second generation GDI engines, operating with spray-guided injection, meet the Euro 5 PM standard but exceed the Euro 6 PN Standard. For both first and second generation GDI engines, the highest particulate number levels are produced during the cold start and during transient operation while the engine is cold as shown in Figure 1.4. Chen et al. [9] reported similar results with cold start emissions accounted for more than 50% of the total particle number for GDI vehicles and approximately 70% for PFI vehicles over the New European Driving Cycle (NEDC). Once the PFI engine is warmed-up the particulate number is significantly reduced, however the GDI engine continues to produce high PN levels during accelerations.

Causes of GDI engine emissions

The formation of soot particles is known to be very dependent on the local equivalence ratio [10]. The higher soot emissions from GDI engines than from PFI engines is due to a higher occurrence of locally rich zones, which is due to two main reasons: shorter fuel-air mixing time and the presence of wall fuel film. As the fuel is injected directly in the cylinder, the mixing process of fuel and air is limited. As soot are formed in rich zones, increasing the overall or local equivalence ratio will increase soot formation. Maricq et al. [11] showed that the stratified charge mode increases further particulate emissions compared to homogeneous charge operation. In spray-guided GDI engines, increasing fuel injection pressure reduces droplets size and distributes them more widely in the combustion chamber, thus enhancing evaporation, improving mixture quality and finally lowering the occurrence of high equivalence ratio regions [12].

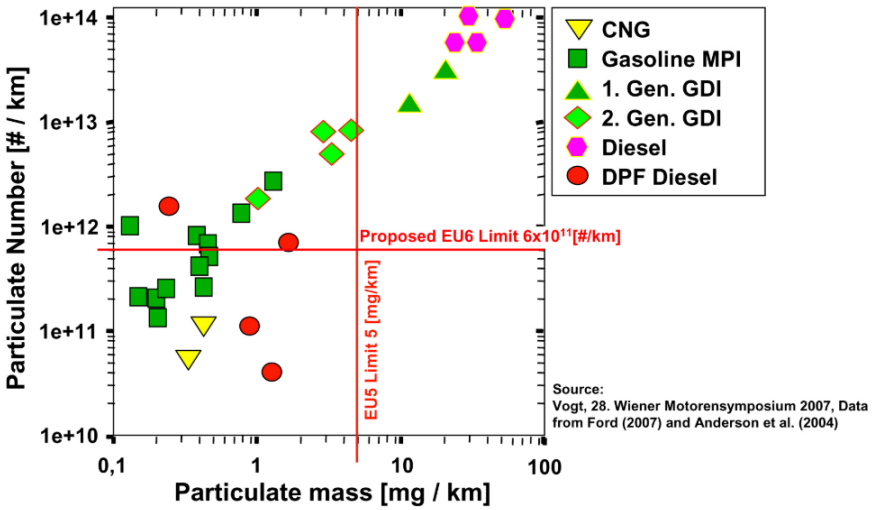

Figure 1.3: Comparison pf particulate number and mass emissions for GDI [8].

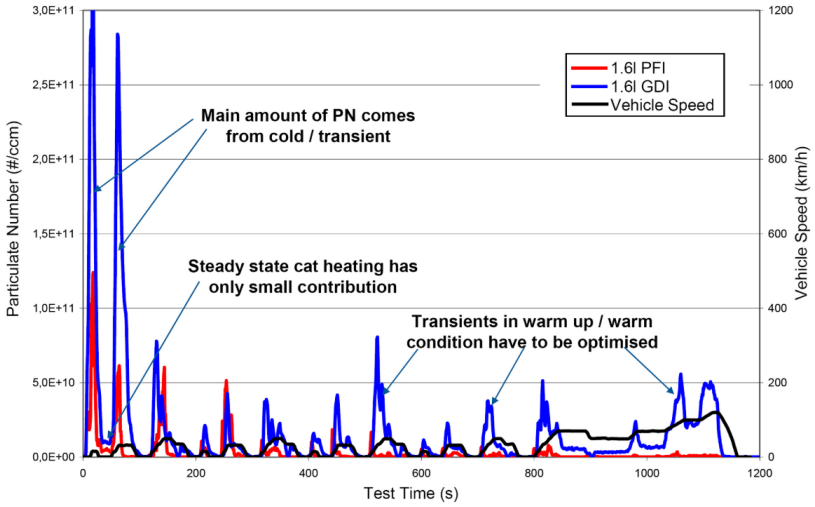

Figure 1.4: Comparison of Euro 5 PFI and GDI particulate number over NEDC cycle [8].

The interaction of the flame with the liquid wall-film is also one of the characteristic modes of soot formation in GDI engines. Due to direct injection, the fuel spray impinges on the piston head and the cylinder wall to form a liquid wall film. Experimental observations showed a clear correlation between the remaining wall-film quantity at the spark ignition and the particulate emissions [7, 13, 14]. This mode of soot generation explains the high particulate emissions at cold start and during accelerations as shown in figure 1.4. The lower particulate emissions in the second generation, operated with spray-guided injection, compared to the first generation GDI engines, operating with wall-guided injection, is generally explained also by less wall wetting [7]. The interaction of the flame with the liquid wall-film may lead to a pool fire above the piston head. The experiment of Bardi et al. [14] indicates that when pool fires were detected, the global particulate number is increased drastically. Stevens and Steeper [15] observed a pool fire attached to the fuel wall-film on the piston top and following the piston movement during the expansion stroke for late injection timings on an optical GDI engine. They also observed that pool fire does not always occur even when the fuel film persist at spark ignition.
Fuel composition may influence any phenomenon involved in soot formation. Correlations which characterize this dependence where proposed by analyzing the engine-out smoke [7, 16]. Fuels with higher aromatic hydrocarbons share lead to higher particulate matter emissions. Drake et al. [17] reported that using a single component fuel (iso-octane), with same average boiling point as a multi-component gasoline surrogate fuel, leads to low wall wetting, which leads in turn to a different engine-out smoke. The differential volatility of fuel components has therefore a non-negligible influence on soot formation process. Stevens and Steeper [15] hypothesized the lack of pool fire for the early injection timing by the evaporation of the light, more volatile fuel components, leaving a reduced film of heavier components which do not ignite.

Strategies to control/limit GDI engines emissions

Farron et al. [10] identified injection timing as one of the most important engine parameters that impact particulate emissions. Early and late injections lead to higher wall wetting, leading to higher soot emissions. In the experiments of Stevens and Steeper [15], the wall-film was observed for all injection timings, but it does not always remain until the combustion occurs. Only early and late injections produce wall-films that persist through the compression stroke. They reported also that quantity of fuel film is higher for late than for early injection, what they attributed to the film mass decreasing in time due to evaporation. Piston wetting and soot generation are also related to the injection pressure. Although increasing fuel injection pressure improves mixture quality, it also increases the likelihood of piston impingement and particulates emissions. A trade-off between atomization and wall wetting can be found by splitting the required duration of injection into multiple injections. At high speed the opportunity for multiple injections may be limited due to the short time available for injection and the high amount of fuel to inject. During cold start and low speed operation, there is ample time available and fuel quantities are much lower. Whitaker et al. [8] demonstrated the benefit of multiple injections in reducing particulate emissions during cold start and transient high load warmed-up engine conditions.

1.2 Different CFD approaches to model combustion and flame/wall interaction in GDI engines.

Soot modeling in ICE was subject of recent research given the increasing regulations on soot emissions. To meet recent and future standards, numerical tools should be able to well predict not only soot mass, but also their size distribution. As described previously, the interaction between the premixed flame front and the liquid wall-film is considered as the primary source of soot in GDI engine. Consequently, modeling soot formation in this configuration requires the simulation of all the involved chemical and physical phenomena, which include: near-wall turbulent flow, turbulent combustion, Flame-Wall Interaction (FWI), wall-film formation and evaporation, soot precursor formation, soot inception, growth and oxidation. Simulating all these phenomena and finding a trade-off between result accuracy and reasonable computational cost is still a challenging task. Some CFD simulations of GDI engine including soot modeling can be found in the literature. The simulations of Seo and coworkers [18, 19] succeeded to reveal a correlation between wall

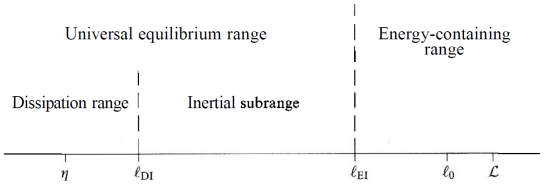

Figure 1.5: Eddy sizes l (on a logarithmic scale) at very high Reynolds number, showing the various lengthscales and rages [20].

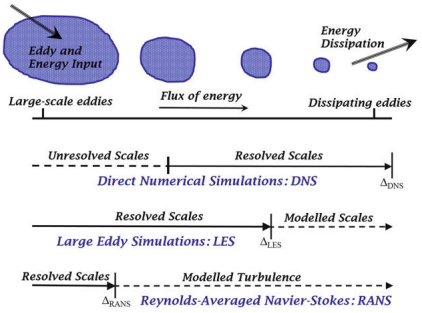

Figure 1.6: Illustration of the turbulent flow energy cascade and the different modeling approaches.

wetting and soot emissions, but without the detailed description of soot formation dynamic neither the influence of combustion parameters on the particles size distribution. In the following, we present a brief state of the art of the available strategies and challenges to model each of these phenomena.

1.2.1 Turbulence modeling and near-wall turbulent flow

The transition from laminar flow to turbulent flow is characterized by the Reynolds number comparing the inertia forces with viscous forces. For large Reynolds number, inertia forces are dominant and the turbulent flow is characterized by a wide variety of scales. As illustrated in Figures 1.6 and 1.5, the kinetic energy of the large eddies is transferred to smaller scales, down to the Kolmogrov scales, where it is converted to heat by molecular viscosity. In CFD, three different approaches exist to simulate turbulent flows:

- **Direct Numerical Simulation (DNS)**: All the turbulent scales are represented by solving directly the Navier-Stokes equations, which requires a very refined mesh. This approach is the most accurate but also computationally the most expensive, and too expansive to be used in engine simulations.
- **Large Eddy Simulation (LES)**: The Navier-Stokes equations are filtered in space to only solve the largest turbulent eddies and the small scales are modeled. The characteristic mesh cell size is used as filter cut-off length scale. The large scales behavior differ from an application to another, while small scales have a more universal behavior, and are therefore easier to model. This approach provides high fidelity results and requires less computational resources than DNS.
- **Reynolds Averaged Navier-Stockes Simulation (RANS)**: Only mean quantities are solved by the averaged Navier-Stokes equations and all turbulent scales are modeled. The computational cost is strongly reduced compared to LES and DNS and the modeling effort increases. This approach is the most used for industrial cases.

By decreasing the LES mesh cell size, more scales can be solved. If the mesh is sufficiently refined, and in non reactive flow, the LES results will be similar to DNS results. Thanks to the recent advances in the computational resources, LES is more and more affordable for practical cases. In the case of ICE simulation, LES allows to better predict the turbulent flow during the intake stroke (tumble motion) and its evolution during the compression stroke (eddies break-up). Coupled with two-phase flow modeling approach, LES can also better predict spray break-up and atomization as these phenomena mainly depend on the large turbulent eddies.
For wall-bounded turbulent flows, the turbulent structures get smaller and smaller as the distance to the wall decreases until the flow becomes driven by viscous diffusion. Thus, a wall-refined LES will tend toward a DNS near the wall. In order to keep a reasonable computational cost in an industrial case, the inner region

of the turbulent boundary layer need to be modeled. In the case of reactive flow with wall heat and mass transfer, wall modeling may have a great impact on the results. This is especially true in spark-ignition engines where a large fraction of the fuel/air mixture burns close to the chamber walls.

1.2.2 Wall-film formation and evaporation

When the spray impinges on the wall, the spray/wall interaction is modeled and part of the liquid phase will stick to the wall to form the wall-film. The existence of the wall-film and its initial characteristics (wetted area, thickness, temperature, ...) depend on this crucial step. Once the wall film is formed, models describing the main physical phenomena (heat transfer, evaporation, etc) are activated. Wall-film evaporation is one of the main physical phenomena involved in Flame-Film Interaction. The evaporation promotes the local rich regions where soot is formed. Accurate modeling of this phenomenon is a key step to setup a numerical tool for detailed soot modeling in GDI engines. Different wall-film evaporation models exist in the literature. These models are generally not specifically developed for LES and their accuracy and dependence to wall stress and heat modeling is not well investigated.

1.2.3 Combustion modeling

In a typical premixed flame in ICE relevant conditions, the flame thickness is generally in the order of $20\mu m$, which is smaller than typical characteristic LES mesh cell sizes. In cases involving combustion, most of the heat is released in thin reaction zones in the size of the smallest turbulent scales. Small-scale turbulence is modeled in LES, and thus, combustion is mainly a sub-grid scale phenomena. The major challenge of turbulent combustion modeling consists in averaging rates that depend on the local temperature in high non-linear manner, while the temperature exhibits strong fluctuations in a turbulent flame. Three main approaches were developed to model flame-turbulence interaction:

- **Turbulent mixing:** The reaction rate is assumed limited by turbulent mixing, described in terms of scalar dissipation rates.
- **Statistical analysis:** Statistical properties of scalar fields may be collected and analyzed for any location within the flow.
- **Geometrical analysis:** Flame is described as a geometrical surface.

The full description of chemical reactions in flames may involve hundreds of species and thousands of reactions, which increases significantly the computational cost. Various approaches have been proposed to reduce chemical schemes: global schemes, tabulated chemistry, in situ adaptive tabulation, or automatically reduced schemes based on graphs analysis and optimization. In cases where soot emissions need to be modeled, the combustion modeling and reduced chemistry approaches should be able to predict soot precursor species. As we are interested here to soot formation due to the interaction of a turbulent flame with a fuel wall-film, it is also necessary to check that the selected combustion and wall models allow to well predict the FWI phenomena.

1.2.4 Soot formation

Soot are commonly defined as solid agglomerates, containing thousands of carbon atoms, and formed from gaseous hydrocarbon molecules. The global path leading to soot formation is known but the detailed description of the formation phases is still an open topic. As shown in Figure 1.7, soot formation begins with the formation of Polycyclic Aromatic Hydrocarbons (PAH) during fuel combustion. These soot precursors undergo an inception process to form the initial soot particles, called also primary particles. The initial particles grow to larger particles through collisional phenomena and surface chemistry, to finally form agglomerates of non-spherical shapes with sizes in the order of hundreds of nanometers.

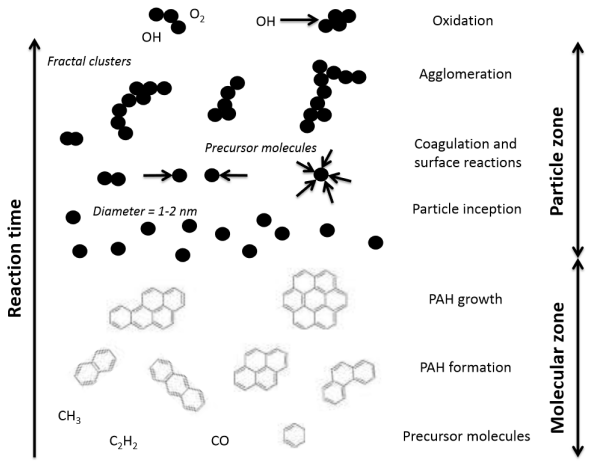

Figure 1.7: Illustration of soot formation [21].

1.2.5 Selected numerical tools and models

The CONVERGE CFD software is used during this thesis. It is currently the reference CFD software in French, US, and Japanese car industry. IFPEN is one of the research labs which support model development in this software. Different modeling approaches are selected to investigate the involved phenomena.

- The Flame-Wall Interaction is a transient phenomena and RANS simulation is not adapted for such configuration. **Large Eddy Simulation** is used in this current work to benefit from solve the flow field to have instantaneous and accurate results of transient phenomena. Wall-refined LES will be considered as reference results to assess the wall models used for wall-modeled LES.

- The liquid phase will be represented by the **Lagrangian approach**. Spray/wall interaction and film formation modeling are out of the scope in this work and the wall-film will be always initialized at the beginning of the simulation. The focus will be only given to the wall-film stationary and transient evaporation.

- Accurate prediction of chemical species is essential for soot modeling. Combustion models based on tabulated approaches are not adapted because: (i) it is not straightforward to consider the feedback of soot model on the gas phase, (ii) the tabulated condition may not be representative of near wall conditions encountered during flame quenching. Thus, the **Thickened Flame Model (TFM)** with resolved chemistry is selected for combustion modeling. However, the use of this model for near wall combustion is not well investigated in the literature and motivates part of this thesis.

- In order to get soot precursors, detailed chemical mechanisms need to be used. An efficient reduction methodology is needed to have a reasonable computational cost while maintaining accurate prediction of soot precursors. The **Optimized Reduced Chemistry (ORCh)** tool of CORIA [22] is used for this task.

- The **Sectional Soot Model (SSM)** developed by Aubagnac-Karkar [23] is used for soot modeling. This model describes particles as distinct dispersed phase interacting with the gaseous phase. It relies on the discretization of the particles mass range, and thus, allows to have the particle sizes distribution. Sub-models are used for detailed description of soot inception, growth and oxidation.

1.3 Objectives and outline

1.3.1 Objectives

The main objective of this thesis is to improve soot modeling for GDI engine simulations. Soot formation mechanisms during the interaction of a turbulent premixed flame with a liquid fuel film are not yet well understood. The detailed description of soot formation dynamic requires a high fidelity numerical tool. Each of the involved physical phenomena in this configuration need to be investigated in order to assess the accuracy of the selected model modeling approach, and eventually to improve it. Performing such detailed investigations in an engine case is not straightforward and a specific academic case need to be setup for this purpose. The turbulent channel flow case was selected as base configuration during all this work. This configuration will allow to focus on near wall phenomena with controlled turbulence and thermodynamic conditions, and it was already considered for similar multi-physical investigations in the literature. Bruneaux et al. [1] performed DNS of FWI in turbulent channel flow. Desoutter [24] considered also this configuration to perform DNS of turbulent boundary layer over a stationary evaporating wall-film.
The work carried out during this thesis is articulated around the following points:

- The assessment of classical algebraic stress and heat wall models in isothermal and anisothermal turbulent channel flows.
- The assessment and the improvement of wall-film evaporation modeling through stationary and transient evaporation in turbulent channel flow.
- The investigation of the use of TFM for FWI:
  - In 1D configuration of flame Head-On Quenching in engine relevant conditions.
  - FWI in half turbulent channel flow.
- Simulation of Flame-Film Interaction (FFI) with soot formation in half turbulent channel flow.

The various configurations and objectives are summarized in Figure 1.8.

1.3.2 Outline

Chapter 2: Flow governing equations

This chapter introduces the governing equations and the physical modeling of the gaseous phase. Details will be provided about the modeling of heat and mass diffusion fluxes. The filtered LES equations will be also presented.

Chapter 3: Turbulent boundary layer modeling

Chapter 3 presents the fundamental characteristics of isothermal and anisothermal turbulent boundary layers. A literature review is also conducted for wall-stress and wall heat transfer modeling in order to understand the model developments and highlights the main assumptions. A focus will be given to algebraic wall models. The minimal channel flow case setup is also presented in this chapter. Wall-refined and wall-modeled cases of isothermal and anisothermal turbulent channel flow are performed in order to provide a first evaluation before moving toward cases with wall-film evaporation.

Chapter 4: Wall-film governing equations and literature review

This chapter is dedicated to the wall-film governing equations and the different evaporation modeling approaches existing in the literature. The wall-film numerical description used during this work is also presented.

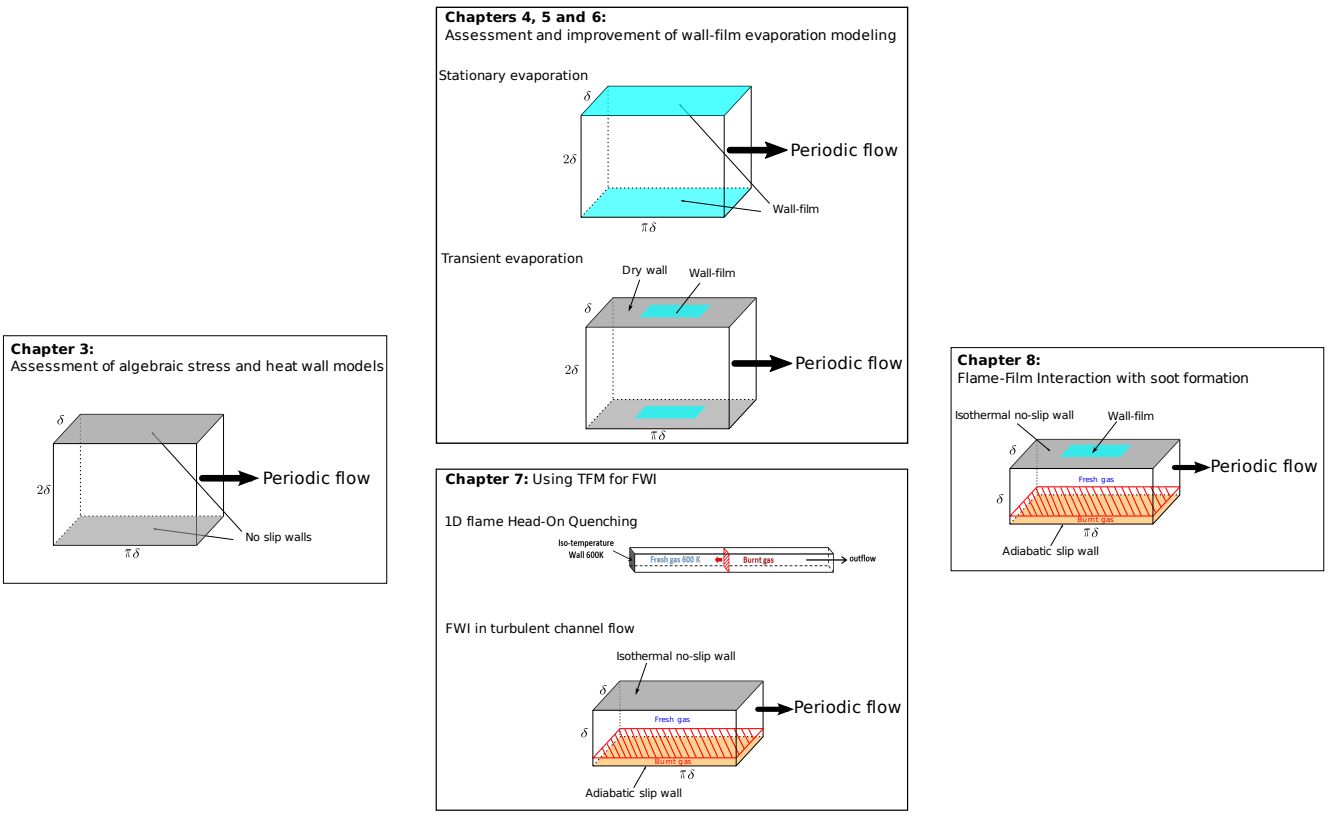

Figure 1.8: The considered canonical configurations in this thesis.

Chapter 5: Assessment of algebraic wall-film evaporation models

Based on the literature review proposed in chapter 4, the retained wall-film evaporation model is assessed in two configurations:

- The steady wall-film evaporation in turbulent channel flow. It is a first step to assess the wall-film modeling in simplified problem where heat and mass transfer are decoupled at the liquid/gas interface.
- The transient wall-film evaporation in turbulent channel flow, which allows the assessment in a configuration of real practical wall-film evaporation.

Chapter 6: Ordinary Differential Equations based Wall-Modeled LES of wall-film evaporation

In this chapter, the Ordinary Differential Equations (ODEs) based wall modeling approach is extended for wall-film evaporation. The considered equations for the wall-film evaporation and their numerical implementation will be detailed. The proposed wall-model will be assessed on the stationary and transient wall-film evaporation cases introduced in Chapter 5.

Chapter 7: Flame-Wall Interaction simulation

Chapter 7 presents the TFM formulation. A brief review about FWI phenomenology is presented. The issues related to the use of TFM for FWI were pointed out. These issues are investigated, first through a 1D configuration of flame Head-On Quenching in engine relevant conditions, then through the FWI in turbulent channel flow. The used chemical mechanism is specifically reduced for this case.

Chapter 8: Flame-Film Interaction with soot formation

In this chapter, all the different physical phenomena are assembled in the same case to simulate flame-film interaction with soot formation. The complex physics leading to soot formation mechanism in this configuration is described thanks to the wall-refined simulation. The different involved models are assessed in the Wall-Modeled LES cases.

Part I

LES of Turbulent Boundary Layer

Chapter 2

Flow Governing Equations

Contents

In this chapter, the governing equations and the physical modeling of the gaseous phase are presented. The fundamental concept of LES is introduced along with the resulting filtered equations. Numerical details about the resolution of these equations are briefly presented in appendix A.

2.1 Governing equations for the gaseous phase

2.1.1 Conservation of momentum

The compressible form of the momentum equation is given by:

$$\frac{\partial \rho U_i}{\partial t} + \frac{\partial \rho U_i U_j}{\partial x_j} = -\frac{\partial P}{\partial x_i} + \frac{\partial \tau_{ij}}{\partial x_j} \qquad \text{for } i = 1, 2, 3 \tag{2.1}$$

where U is the velocity vector, ρ is density, P is pressure, and τ is the viscous stress tensor which reads:

$$\tau_{ij} = \mu \left(\frac{\partial U_i}{\partial x_j} + \frac{\partial U_j}{\partial x_i} \right) - \frac{2}{3} \mu \left(\frac{\partial U_m}{\partial x_m} \delta_{ij} \right) \tag{2.2}$$

where μ is the dynamic molecular viscosity, and δ_{ij} the Kronecker symbol. During all the work carried during this thesis, it is assumed that the dynamic molecular viscosity μ is equal to the one of air mixture and it depends only on temperature. The momentum equation 2.1 does not account for any volume forces (gravity, ...) as they are completely neglected in this work.

2.1.2 Conservation of mass and species

The total mass balance equation is given by:

$$\frac{\partial \rho}{\partial t} + \frac{\partial \rho U_j}{\partial x_j} = 0 \tag{2.3}$$

The conservation equation of the species k in a compressible reacting flow is given by:

$$\frac{\partial \rho_k}{\partial t} + \frac{\partial \rho_k U_j}{\partial x_j} = -\frac{\partial}{\partial x_j}\left(J_{k,j}\right) + \dot{\omega}_k \qquad \text{for } k = 1..N \tag{2.4}$$

where ρ_k, J_k and $\dot{\omega}_k$ are respectively the partial density, the mass diffusion flux and the mass reaction rate of species k in a mixture of N species. The mass concentration of species k can be expressed using its mass fraction in the mixture $\rho_k = \rho Y_k$. The total mass and species balance equations are related, the sum of the species mass gives the total mass, which can be written per unit volume as:

$$\rho = \sum_{k=1}^{N} \rho_k = \sum_{k=1}^{N} \rho Y_k \quad \Longleftrightarrow \quad \sum_{k=1}^{N} Y_k = 1 \tag{2.5}$$

It should be noted here that the N species equations are solved, Eq. 2.3 is also solved to ensure the global mass conservation, which leads to an over determined system with N unknowns and $N+1$ equations. In this section we focus only on the physical modeling of the different terms, the solution procedure and the numerical details are presented in Appendix A. In the following, the considered expressions for the diffusive flux and reaction rate are detailed.

2.1.2.1 Reaction rate

The mass reaction rate $\dot{\omega}_k$ of species k is the sum of rates produced by all M reactions provided in the reaction mechanism:

$$\dot{\omega}_k = \sum_{r=1}^{M} \dot{\omega}_{k,r} \tag{2.6}$$

The chemical reaction r involving N species can be written as:

$$\sum_{k=1}^{N} \nu'_{k,r} \mathcal{M}_k \rightleftharpoons \sum_{k=1}^{N} \nu''_{k,r} \mathcal{M}_k \tag{2.7}$$

where $\mathcal{M}_k$ is a symbol for species with index k, $\nu'_{k,r}$ and $\nu''_{k,r}$ are the molar stochiometric coefficients of species k in reaction r. With this notation, the reaction rate $\dot{\omega}_{k,r}$ is expressed as:

$$\dot{\omega}_{k,r} = \mathcal{Q}_r W_k \left(\nu''_{k,r} - \nu'_{k,r}\right) \tag{2.8}$$

where W_k is the molecular weight of species k and $\mathcal{Q}_r$ is the rate of progress of reaction r, which can be written as:

$$\mathcal{Q}_r = \mathbf{k}_{F,r} \prod_{k=1}^{N} \left[C_k\right]^{\nu'_{k,r}} - \mathbf{k}_{R,r} \prod_{k=1}^{N} \left[C_k\right]^{\nu''_{k,r}} \tag{2.9}$$

where C_k is the concentration of species k, and $\mathbf{k}_{F,r}$ and $\mathbf{k}_{R,r}$ are the forward and reverse rates of reaction r, which is usually modeled using the empirical Arrhenius law:

$$\mathbf{k} = aT^{\beta} exp\left(-\frac{E_a}{RT}\right) \tag{2.10}$$

where T the temperature, R the universal gas constant, a a pre-exponential constant, β a temperature exponent and E_a an activation energy.

2.1.2.2 Species mass diffusion flux

The species mass diffusion flux can be expressed using the diffusion velocity:

$$J_{k,i} = \rho V_{k,i} Y_k \tag{2.11}$$

The exact solution of the diffusion velocities V_k can be obtained by solving a linear system of size N^2 in each direction at each point and at each instant, which is difficult and costly [25]. Approximations are commonly used to express the diffusion velocity.

Hirschfelder and Curtiss approximation

The Hirschfelder and Curtiss approximation is the best first order approximation to the exact solution of the diffusion velocity [25]. Even if this approximation has not been used for the 3D simulations carried during this work, its understanding remains useful for the following. The Hirschfelder and Curtiss approximation states that:

$$V_{k,i}^{HC} X_k = -D_k^{HC} \frac{\partial X_k}{\partial x_i} \tag{2.12}$$

with

$$D_k^{HC} = \frac{1 - Y_k}{\sum_{j \neq k} X_j / \mathcal{D}_{jk}} \tag{2.13}$$

where X_k is the molar fraction of species k, $\mathcal{D}_{jk}$ the binary diffusion coefficient, and D_k^{HC} is an equivalent diffusion coefficient of species k in the mixture. The HC superscript on the diffusion velocity and coefficient denotes the definition according to the Hirschfelder and Curtiss approximation. The ratio of momentum diffusivity and mass diffusivity defines the Schmidt number. Using the diffusion coefficient as defined by the Hirschfelder and Curtiss approximation, and for a given mixture composition, temperature and pressure, the Schmidt number of a species k is given by:

$$Sc_k = \frac{\mu}{\rho D_k^{HC}} \tag{2.14}$$

The binary diffusion coefficients $\mathcal{D}_{jk}$ are computed using the molecular transport properties of the species and depend also on temperature and pressure. Thus, D_k^{HC} depends on the mixture composition, temperature and pressure. So, in the context of 3D CFD simulations, the diffusion coefficients needs to be computed for each species, at each point and at every time step. Tabulation techniques can be used during the simulation setup to accelerate the computation of $\mathcal{D}_{jk}$, but the additional cost to compute D_k^{HC} remains significant, especially when reactive flows with large numbers of species are involved.

Fick's law

The Fick's law was used during this thesis to approximate the species mass diffusion flux in the 3D CFD simulations:

$$J_{k,i} = \rho V_{k,i} Y_k = -\rho D_k \frac{\partial Y_k}{\partial x_i} \tag{2.15}$$

The species diffusion coefficient was modeled in this work as follows:

$$\rho D_k = \frac{\mu}{Sc_k} \tag{2.16}$$

The Schmidt number Sc_k is set constant for each species k and it is computed before the simulation using Cantera [26]. Eq. (2.14) is used for this purpose. The species mass diffusion coefficient correspond to the one found in the burnt gas of 1D stationary premixed flames and it is modeled using the Hirschfelder and Curtiss approximation, i.e. D_k^{HC} as defined in Eq. (2.13). The relation between the Hirschfelder and Curtiss

approximation and the Fick's law is detailed in the following. In order to be coherent with the momentum diffusivity of the 3D simulation (see section 2.1.1), the viscosity used to compute Sc_k correspond to air viscosity at the same pressure and temperature as used to compute D_k^{HC}.

Correction velocity

Summing all species equations (2.4) must lead to the total mass conservation (2.3). Using Eq. (2.11) leads to the following necessary condition:

$$\sum_{k=1}^{N} Y_k V_{k,i} = 0 \qquad \text{for } i = 1, 2, 3 \tag{2.17}$$

The use of Fick's law (or any other approximation) to model the diffusion velocities of the species doesn't necessarily satisfy this condition. In order to maintain the global mass conservation, a correction velocity V_c is introduced in the species conservation equations in such a way as to get the total mass conservation when the N species equations are summed up:

$$J_{k,i} = -\frac{\mu}{Sc_k}\frac{\partial Y_k}{\partial x_j} + \rho V_c Y_k \tag{2.18}$$

where

$$\rho V_c = \sum_{k=1}^{N} \frac{\mu}{Sc_k}\frac{\partial Y_k}{\partial x_j} \tag{2.19}$$

Comments on the species mass diffusion flux modeling

Modeling the species mass diffusion fluxes using the Fick's law with constant set of Sc_k (for $k = 1..N$) deserves to be discussed, especially in the scope of the work carried during this thesis.

- **Comment 1**: As pointed out previously, the diffusion coefficients according to the Hirschfelder and Curtiss approximation (Eq. (2.13)) depend on the mixture composition, temperature and pressure. So it should also be the case for the Schmidt numbers Sc_k used in Eq. (2.16). The fact of using a constant set of Sc_k will not be representative of all the local conditions of the 3D simulation. Using constant Schmidt numbers is classically considered for application cases, and also in some academic studies involving near wall turbulent flows with heat and mass transfer [24, 27].

- **Comment 2**: The diffusion velocity according to Fick's law is proportional to the species mass fraction gradient, while it is proportional to the species molar fraction gradient according to the Hirschfelder and Curtiss approximation. Starting from Eq. (2.12), and using $Y_k = W_k X_k / W$, one can write:

$$\begin{aligned} -Y_k V_{k,i}^{HC} &= D_k^{HC}\frac{Y_k}{X_k}\frac{\partial X_k}{\partial x_i} \\ &= D_k^{HC}\frac{W_k}{W}\frac{\partial}{\partial x_i}\left(Y_k\frac{W}{W_k}\right) \\ \Rightarrow\ -Y_k V_{k,i}^{HC} &= \underbrace{D_k^{HC}\frac{\partial Y_k}{\partial x_i}}_{\text{Fick's law}} + D_k^{HC}\frac{Y_k}{W}\frac{\partial W}{\partial x_i} \end{aligned} \tag{2.20}$$

  So Fick's law neglects the mass diffusion due to the mixture molecular weight gradient $\partial W/\partial x_i$ compared to the Hirschfelder and Curtiss approximation. This assumption is acceptable when the local equivalence ratio variation in the flow is low, which is generally the case through a premixed flame front. However, this is not the case considering a mixture stratification, typically above an evaporating wall-film, where the mass fraction of the fuel and $\partial W/\partial x_i$ get relatively high values. The error induced by such an assumption on the wall-film evaporation will be discussed in Section 5.1.2.

- **Comment 3**: Fick's law, and Hirschfelder and Curtiss approximation as well, account only for mass diffusion due to the mixture composition variation. **The Soret effect**, i.e. the diffusion of mass due to temperature gradient, also known as thermophoresis, is then neglected. This assumption is widely considered for turbulent multi-species reactive flow simulations. Rodrigues [28] considered the Soret effect for soot diffusion with an adapted model for aerosol particles [29] for the simulation of turbulent sooting flame with wall heat transfer. Faghih et al. [30] included the diffusion due to a temperature gradient along with the Hirschfelder and Curtiss approximation to model the species diffusion velocities in the case of premixed iso-octane flame propagation under engine-relevant conditions. They showed that the effect of Soret diffusion on the burning rate is negligible. However, the Soret effect is not that insignificant in the case of near wall reactive flows. Hasse et al. [31] highlighted more than 20 years ago that it has a significant impact on the oxidation process in the case of the quenching of laminar iso-octane flames at cold walls. Nevertheless, the Soret effect is still neglected in some numerical studies of FWI. Chauvy et al. [32] used only Fick's law to model species mass diffusion to study Unburned Hydrocarbons formation due to flames Head-On Quenching (HOQ) on complex geometries. Narukawa et al. [33] also neglected the Soret effect for the investigation of the influence of surface reactions on the near-wall flame propagation behavior. The Soret effect was neglected during the work carried out during this thesis.

The used species mass diffusion model will allow to investigate the studied physics. Using more elaborated models like Hirschfelder and Curtiss approximation along with Soret effect should not change the modeling strategies of the wall-film and artificially thickened flame proposed in this thesis.

2.1.3 Conservation of energy

The sensible internal energy e_s is defined by:

$$e_s = \int_{T_0}^{T} c_v dT - \frac{RT_0}{W} \tag{2.21}$$

where c_v is the specific heat capacity at constant volume and T_0 is a reference temperature. Its conservation equation is given by:

$$\frac{\partial \rho e_s}{\partial t} + \frac{\partial \rho e_s U_j}{\partial x_j} = -P\frac{\partial U_j}{\partial x_j} + \tau_{ij}\frac{\partial U_i}{\partial x_j} + \frac{\partial q_j}{\partial x_j} + \dot{\omega}_T \tag{2.22}$$

where the $\dot{\omega}_T$ is the chemical heat release, related to species mass reaction rate by:

$$\dot{\omega}_T = -\sum_{k=1}^{N} \Delta h^o_{f,k} \dot{\omega}_k \tag{2.23}$$

where Δh^0_f is the mass formation enthalpy at reference temperature. The heat flux q is given by:

$$q_j = \lambda \frac{\partial T}{\partial x_j} + \sum_{k=1}^{N} h_{s,k} J_{k,j} \tag{2.24}$$

It includes the heat diffusion term expressed by Fourier's law and a second term due to the diffusion of species with different sensible enthalpies h_s with:

$$h_{s,k} = \int_{T_0}^{T} c_{p,k} dT \tag{2.25}$$

where c_p is the specific heat capacity at constant pressure. The specific heat capacities and the mass formation enthalpy are computed using the classical NASA polynomials. The Dufour effect, the reciprocal effect of Soret diffusion, was neglected in Eq. (2.24). Unlike the Soret effect, Hasse et al. [31] found it does not influence significantly the results of FWI for wall temperatures up to 600 K. Cabrit and Nicoud [27] confirmed also

that the Dufour effect can be neglected for multicomponent compressible reacting compressible turbulent flows. After solving the energy equation, the sensible internal energy is converted into temperature. The ideal gas state equation is used to couple density, pressure, and temperature.

$$P = \rho \frac{R}{W} T \tag{2.26}$$

More details about the coupling procedure are given in appendix A.

2.1.4 Additional source terms

Additional source terms can be added in the right hand side of the previous flow governing equations to account for the different physical sub-models (spray coupling, evaporation, ...). They are denoted respectively S_{mom}, S_{mass}, S_k and S_e for the momentum, total mass, species mass and energy conservation equations:

$$\frac{\partial \rho U_i}{\partial t} + \frac{\partial \rho U_i U_j}{\partial x_j} = -\frac{\partial P}{\partial x_i} + \frac{\partial \tau_{ij}}{\partial x_j} + S_{mom,i} \qquad \text{for } i = 1,2,3 \tag{2.27}$$

$$\frac{\partial \rho}{\partial t} + \frac{\partial \rho U_j}{\partial x_j} = S_{mass} \tag{2.28}$$

$$\frac{\partial \rho Y_k}{\partial t} + \frac{\partial}{\partial x_j}\left(\rho U_j Y_k\right) = \frac{\partial}{\partial x_j}\left(J_{k,j}\right) + \dot{\omega}_k + S_k \qquad \text{for } k = 1..N \tag{2.29}$$

$$\frac{\partial \rho e_s}{\partial t} + \frac{\partial \rho e_s U_j}{\partial x_j} = -P\frac{\partial U_j}{\partial x_j} + \tau_{ij}\frac{\partial U_i}{\partial x_j} + \frac{\partial q_j}{\partial x_j} + \dot{\omega}_T + S_e \tag{2.30}$$

2.2 Large Eddy Simulation equations

All the previous governing equations are expressed using instantaneous variables. A flow variable $\phi(x,t)$ can be separated according to the Reynolds average into a mean component (time-averaged) $\overline{\phi}(x)$ and a fluctuating component $\phi'(x,t)$:

$$\phi(x,t) = \overline{\phi}(x) + \phi'(x,t) \tag{2.31}$$

In the LES approach however, the flow field is separated according to a low-pass filtering operation. Here no explicit filter is applied and the flow field is simply separated on the mesh grid into resolved field $\hat{\phi}$ and a sub-grid scale (SGS) field ϕ^{sgs} as follows:

$$\phi(x,t) = \widehat{\phi(x,t)} + \phi^{sgs}(x,t) \tag{2.32}$$

The Favre average is generally considered for compressible flows:

$$\tilde{\phi} = \frac{\widehat{\rho\phi}}{\widehat{\rho}} \tag{2.33}$$

Thus, the set of the filtered governing equations are given by:

$$\frac{\partial \bar{\rho}}{\partial t} + \frac{\partial \bar{\rho}\tilde{U}_i}{\partial x_i} = S \tag{2.34}$$

$$\frac{\partial \bar{\rho}\tilde{U}_i}{\partial t} + \frac{\partial \bar{\rho}\tilde{U}_i\tilde{U}_j}{\partial x_j} = -\frac{\partial \bar{P}}{\partial x_i} + \frac{\partial}{\partial x_j}\left(\bar{\tau}_{ij} + \bar{\tau}_{ij}^{sgs}\right) + S_i \tag{2.35}$$

$$\frac{\partial \bar{\rho}\tilde{e}}{\partial t} + \frac{\partial \bar{\rho}\tilde{U}_j\tilde{e}}{\partial x_j} = -\bar{P}\frac{\partial \tilde{u_j}}{\partial x_j} + \left(\bar{\tau}_{ij} + \bar{\tau}_{ij}^{sgs}\right)\frac{\partial \tilde{u_i}}{\partial x_j} + \frac{\partial}{\partial x_j}\left(\bar{Q}_j + \bar{Q}_j^{sgs}\right) + \bar{\dot{\omega}}_T + S_e \tag{2.36}$$

$$\frac{\partial \bar{\rho}\tilde{Y_k}}{\partial t} + \frac{\partial \bar{\rho}\tilde{Y_k}\tilde{u_j}}{\partial x_j} = -\frac{\partial}{\partial x_j}\left(\bar{J}_{j,k} + \bar{J}_{j,k}^{sgs}\right) + \bar{\dot{\omega}}_k + S_k \tag{2.37}$$

The sub-grid terms, denoted by superscript ^{sgs}, are modeled. The eddy viscosity assumption is used for the SGS stress tensor:

$$\bar{\tau}_{ij}^{sgs} = \bar{\rho}\nu_t \left(\frac{\partial \tilde{U}_i}{\partial x_j} + \frac{\partial \tilde{U}_j}{\partial x_i} - \frac{2}{3}\frac{\partial \tilde{U}_m}{\partial x_m}\delta_{ij} \right) \tag{2.38}$$

The σ-model is used during this work to model the turbulent kinetic viscosity and it is written as[34]:

$$\nu_t = (C_\sigma \Delta_x)^2 \frac{\sigma_3 (\sigma_1 - \sigma_2)(\sigma_2 - \sigma_3)}{\sigma_1^2} \tag{2.39}$$

where C_σ is a model constant (typically $C_\sigma = 1.3$), Δ_x is the sub-grid characteristic length scale and $\sigma_1 \geqslant \sigma_2 \geqslant \sigma_3 \geqslant 0$ are the singular values of the velocity gradient tensor of the resolved scales. The σ-model is a wall adapting model, it was designed to meet the following properties:

- A positive quantity which involves only locally defined velocity gradients.
- Cubic behavior near solid boundaries.
- Zero for any two-component or two-dimensional flows.
- Zero for axisymmetric or isotropic expansion/contraction.

It was successfully used in the literature for various academic and industrial cases. In particular, it was used by Mercier et al. [35] and Koren et al. [36] for the investigation of thermal boundary conditions of swirling flame combustor. The sub-grid species and energy fluxes are expressed with turbulent diffusion coefficients as:

$$\bar{J}_{j,k}^{sgs} = -\bar{\rho} D_t \frac{\partial \tilde{Y_k}}{\partial x_j} \tag{2.40}$$

$$\bar{Q}_j^{sgs} = \lambda_t \frac{\partial \tilde{T}}{\partial x_j} + \bar{\rho} \sum_k D_t h_k \frac{\partial \tilde{Y_k}}{\partial x_j} \tag{2.41}$$

The turbulent diffusion coefficients are modeled by introducing the turbulent Prandtl and Schmidt numbers:

$$D_t = \frac{\nu_t}{Sc_t} \tag{2.42}$$

$$\lambda_t = c_p \frac{\bar{\rho}\nu_t}{Pr_t} \tag{2.43}$$

Chapter 3

Turbulent Boundary Layer Modeling

Contents

In this chapter, the fundamental characteristics of the turbulent boundary layer will be presented. A literature review is also conducted for wall-stress and wall heat transfer modeling in order to understand the model developments and highlights the main assumptions. A focus will be given to algebraic wall models. The channel flow case is a canonical case widely used for the description and model development of near wall turbulent flows. The minimal channel flow case setup will be presented in Section 3.2. Wall-refined and wall-modeled cases of isothermal and anisothermal turbulent channel flow are performed in order to provide a first evaluation before moving toward cases with wall-film evaporation.

3.1 Literature review

Figure 3.1 shows the flat channel flow configuration. The mean flow evolves along an infinite streamwise direction and the spanwise channel width is much larger than the channel height. During all this work,

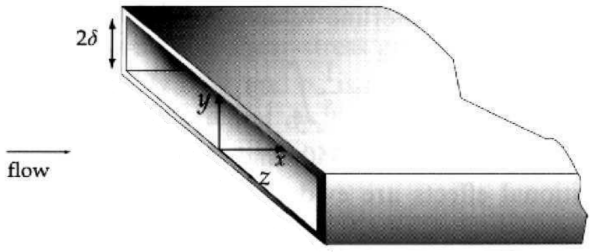

Figure 3.1: Flat channel flow configuration[20]

the streamwise direction is along the x-axis, the spanwise direction is along the z-axis and the normalwise direction is along the y-axis. The velocity components along the x, y and z axes are respectively u, v and w. In the fully turbulent regime, two boundary layers with thickness equal to the half channel height δ will develop on the upper and bottom walls of the channel.

3.1.1 Isothermal turbulent boundary layer

The turbulent boundary layer is well described in numerous textbooks [20, 37, 38]. The following simplifying assumptions are generally considered.

- Stationary flow
- Two-dimentional flow
- Couette flow assumption: Stream-wise gradient negligible with respect to the normal-wise gradient ($\partial/\partial x \ll \partial/\partial y$)
- Zero mean pressure gradient
- The wall is perfectly smooth

In this first part we consider an incompressible and isothermal flow (constant temperature, density and viscosity). According to these assumptions, the stream-wise momentum equation can be simply written as:

$$\rho v \frac{du}{dy} = \frac{d\tau}{dy} \tag{3.1}$$

with

$$\tau = \mu \frac{du}{dy} \tag{3.2}$$

The application of the Reynolds average operator (Eq. (2.31)) gives:

$$\rho \bar{v} \frac{d\bar{u}}{dy} = \frac{d\overline{\tau}_{tot}}{dy} \tag{3.3}$$

where the total shear stress accounts for molecular dissipation and the Reynolds stress $\overline{u'v'}$:

$$\overline{\tau}_{tot} = \mu \frac{d\bar{u}}{dy} - \rho\overline{u'v'} \tag{3.4}$$

Using the eddy diffusivity assumption, the total shear stress can be written as:

$$\overline{\tau}_{tot} = (\mu + \mu_t) \frac{d\bar{u}}{dy} \tag{3.5}$$

with

$$\mu_t = \frac{-\rho\overline{u'v'}}{d\bar{u}/dy} \tag{3.6}$$

In the case where there is no blowing or suction at the wall, and according to the incompressible mass conservation equation, $\bar{v} = v_w = 0$. So, the total shear stress is constant in the wall normal direction and $\overline{\tau}_{tot} = \overline{\tau}_w$. This equality is valid only in the region where the Couette flow assumption is valid, relatively near the surface, the total shear stress must go to zero at the outer edge of the boundary layer. A friction velocity, or a shear speed, u_τ can be defined from the wall shear stress τ_w as:

$$\overline{\tau}_w = \mu \left.\frac{d\bar{u}}{dy}\right|_w = \rho u_\tau^2 \tag{3.7}$$

Based on this velocity, a near wall viscous length-scale δ_ν can be defined as:

$$\delta_\nu = \frac{\nu}{u_\tau} \tag{3.8}$$

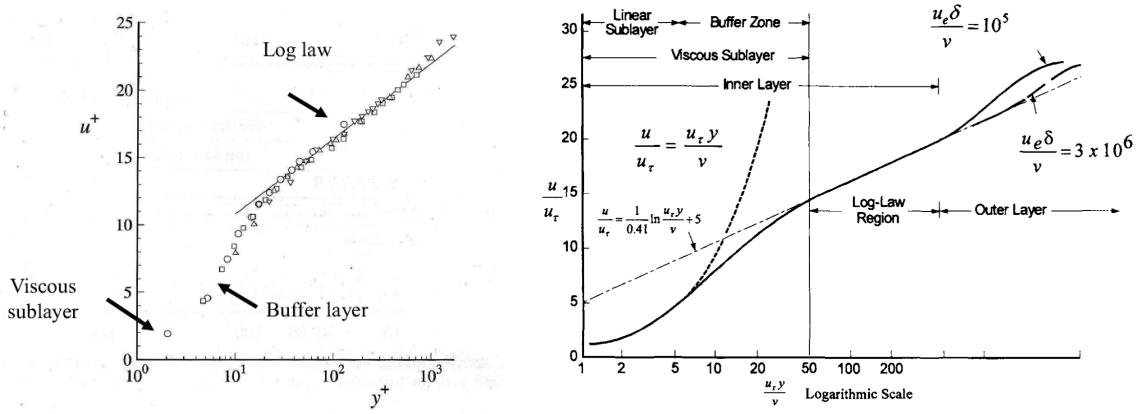

(a) Experimental measurements [20]. **(b)** Regions of the turbulent boundary layer [37].

Figure 3.2: Mean streamwise velocity profile in fully developed turbulent channel flow.

Based on u_τ and δ_ν, a dimensionless wall distance and velocity can be defined as:

$$y^+ = \frac{y}{\delta_\nu} = \frac{yu_\tau}{\nu} \tag{3.9}$$

$$u^+ = \frac{\bar{u}}{u_\tau} \tag{3.10}$$

Using these dimensionless variables, Eq. (3.5) can be written as:

$$1 = \left(1 + \frac{\mu_t}{\mu}\right)\frac{du^+}{dy^+} \tag{3.11}$$

The dimentionless distance at the center of the channel defines a characteristic Reynolds number Re_τ:

$$Re_\tau = \frac{\delta u_\tau}{\nu} \tag{3.12}$$

Structure of incompressible turbulent boundary layer

Figure 3.2 shows the mean streamwise velocity profile in fully turbulent channel flow. The turbulent boundary layers is generally treated as a composite layer constituted of inner and outer layers.
The inner layer: In the inner 10-20% of the entire boundary layer thickness, the mean velocity is independent of δ. Three regions can be identified within the inner layer:

- **Linear sub-layer**: For small y^+ ($y^+ < 5$), the flow is driven by viscous diffusion and $\mu \gg \mu_t$. The velocity profile is linear in this region:
$$u^+ = y^+ \tag{3.13}$$

- **Log-law region**: For large y^+ ($y^+ > 30$), the molecular viscosity has a little effect and the shear stress is dominated by the Reynolds stress. According to the Prandtl mixing-length theory, the turbulent shear stress can be expressed by:
$$-\overline{u'v'} = l_m^2\left(\frac{d\bar{u}}{dy}\right)^2 \tag{3.14}$$
where l_m is a mixing-length scaled on the distance from the wall with a proportionality factor $\kappa = 0.41$, known as von Karman constant:
$$l_m = \kappa y \tag{3.15}$$

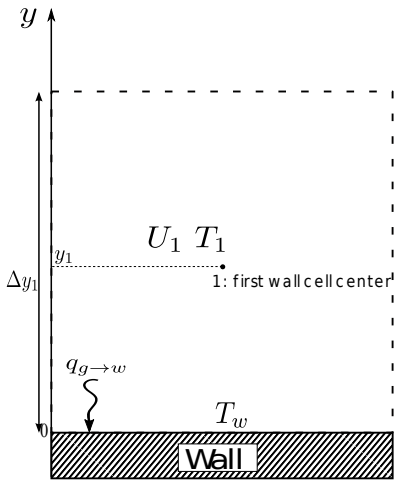

Figure 3.3: Wall cell schematic.

Neglecting the molecular shear stress in Eq. (3.4) and using $\overline{\tau}_{tot} = \overline{\tau}_w$, the mixing length formula can written also as:

$$\frac{\partial \bar{u}}{\partial y} = \frac{u_\tau}{\kappa y} \tag{3.16}$$

which leads to:

$$\frac{\mu_t}{\mu} = \kappa y^+ \tag{3.17}$$

Integrating Eq. (3.11) using Eq. (3.17) and assuming $\mu_t/\mu \gg 1$, leads to a logarithmic law in the form:

$$u^+ = \frac{1}{\kappa} ln\left(y^+\right) + B \tag{3.18}$$

with $B = 5$ according to the experimental results fitting.

- **Buffer layer**: The transition region between the linear sub-layer and the log-law region.

The outer layer: In the outer region, the flow is intermittently turbulent and the mean streamwise velocity depend on δ and on the mean velocity in the edge of the boundary layer (u_e in Figure 3.2).
Several DNS of incompressible turbulent channel flows are available in the literature and provide second and high order statistics.

3.1.1.1 Wall-refined wall-stress

In a turbulent boundary layer, the turbulent structures gets smaller and smaller as the distance to the wall decreases. In wall-refined LES, most of these turbulent structures are solved and the simulation will tend toward DNS near the wall. The use of wall-adapting sub-grid scale turbulent viscosity ensures the correct damping of the turbulent shear stress. In the context of 3D simulations, the wall shear stress has a streamwise and a spanwise component and its magnitude is computed from the wall parallel velocity component ($U_{//} = \sqrt{u^2 + w^2}$) gradient. Using the notations defined in Figure 3.3, the wall-refined formulation is given by:

$$\tau_w^{refined} = \mu \frac{U_{//,1}}{y_1} \tag{3.19}$$

According to Zang et al. [39], the mesh resolution requirements for wall-refined LES able to achieve correct mean flows and root-mean-square velocity fluctuations in turbulent boundary layer are the following: $\Delta x^+ \approx 80$, $\Delta z^+ \approx 30$, $y_1^+ \approx 2$ and approximately three points between the wall and $y^+ = 10$.

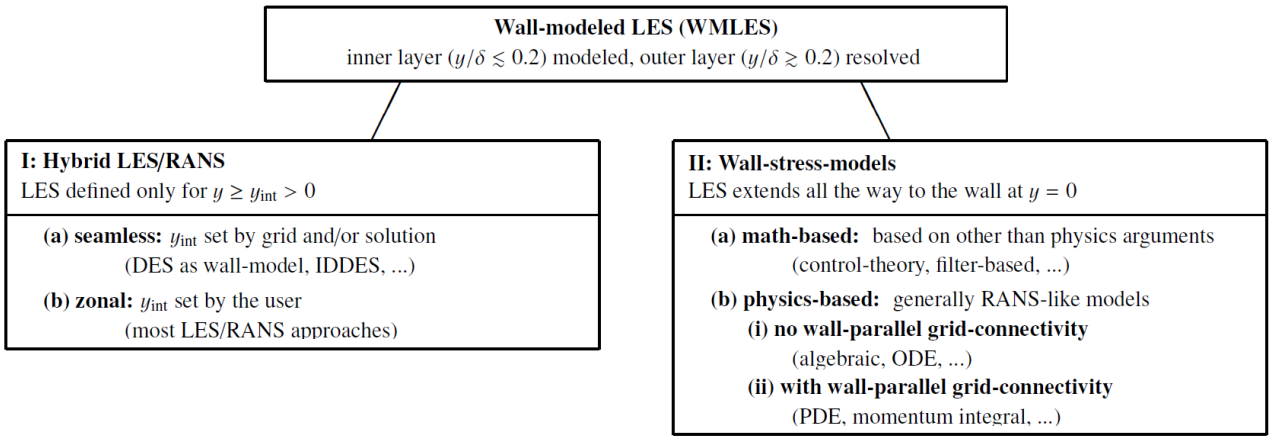

Figure 3.4: Classification of Wall-Modeled LES approaches according to Larsson et al. [40].

3.1.1.2 Wall-stress modeling

Solving the near wall turbulent structures in practical turbulent cases requires fine mesh. In practice simulations are performed with relatively coarse meshes, known as Wall-Modeled LES (WMLES), the inner layer (or at least part of it) is modeled and the outer layer is resolved. The velocity gradient estimation at the wall similar to the wall-refined LES is no longer possible and an alternative formulation for the wall shear stress is needed. Different WMLES approach exists in the literature. Larsson et al. [40] and Bose and Park [41] provided an overview of the WMLES approaches which exist in the literature. Figure 3.4 shows a classification of the different approaches as proposed by Larsson et al. [40]. Very recently, De Vanna et al. [42] proposed a promising general strategy to unify the wall-resolved and wall-modeled approaches for LES of compressible turbulent wall-bounded flows. In this work we consider only physics-based wall-stress models with no wall-parallel grid-connectivity. We focus only on algebraic wall models in this section, while ODEs based WMLES will be discussed later in Chapter 6. Using the wall-adjacent LES data as an input for the wall-stress models is known to lead to an erroneous shift of the mean velocity profile below or above the logarithmic layer, known in the literature as Log-Layer Mismatch (LLM) [40, 43]. A common remedy for this problem is to consider LES data at higher distance from the wall, 2-3 cells away from the wall. Larsson et al. [40] provided detailed guidelines for a robust methodology to avoid the LLM problem. Yang et al. [43] proposed a simpler remedy by time-filtering the instantaneous LES data at the first wall mesh cell over a characteristic time window. One should keep in mind that CONVERGE software is used for industrial configurations (complex geometry, moving wall, ...) and it includes many features for easy domain meshing: Cartesian mesh with octree Adaptive Mesh Refinement (AMR), cut-cell method,.... For this reason, no remedy was considered for the present work and the wall-stress models are always operated with the LES instantaneous velocity at the center of the wall mesh cell.

Standard law-of-the-wall model

The most intuitive way to formulate a wall-stress model is by assuming an artificial two-layer model: a linear velocity profile as given by Eq. (3.13) up to a transition distance $y^+_{tran,U}$, and then a logarithmic velocity profile as given by Eq. (3.18). It is important to highlight a compulsory assumption to consider in this algebraic WMLES: the law-of-the-wall describes the behavior of mean streamwise velocity, while in the context of LES, the instantaneous filtered wall parallel velocity component is used to express the modeled wall shear stress. Then the modeled wall shear stress is expressed by:

$$\tau_w^{lin-log} = \begin{cases} \frac{\mu U_{//,1}}{y_1} & \text{for } y_1^+ \leqslant y^+_{tran,U} \\ \rho \left(\frac{U_{//,1}}{\frac{1}{\kappa} ln\left(y_1^+\right) + B} \right)^2 & \text{for } y_1^+ > y^+_{tran,U} \end{cases} \tag{3.20}$$

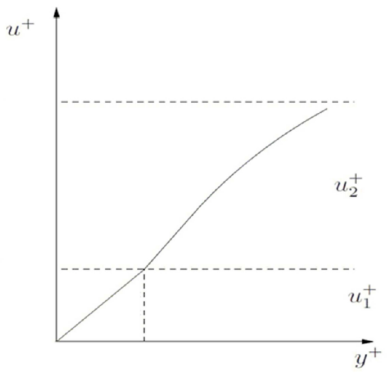

Figure 3.5: Mean dimentionless velocity profil considered for Werner-Wengle model [44].

$y^+_{tran,U} = 10.8$ ensures the continuity of the velocity profile between the linear sub-layer and the log-law layer. This model will be referred here after as *lin-log* model. In the previous expression (3.20), y_1^+ depends on u_τ and thus on the shear stress. So, the model is computed iteratively until convergence of the results.

Werner and Wengle wall model

Werner and Wengle [45] proposed an algebraic wall-stress model specifically for LES. They assumed also an artificial two-layer model as shown in Figure 3.5: a linear then a power law velocity profile of the form:

$$u^+ = A\left(y^+\right)^B \tag{3.21}$$

with $A = 8.3$ and $B = 1/7$. This model assumes that instantaneous tangential velocity components at the first near-wall nodes are in phase with the wall shear stress. By integrating the velocity profile over the height of wall cells, the wall shear stress formulations is obtained explicitly without iteration method, unlike the standard law-of-the-wall model:

$$\tau_w^{WW} = \begin{cases} \frac{\mu U_{//,1}}{y_1} & \text{if } U_{//,1} \leqslant U_{tran} \\ \rho\left[\frac{1-B}{2} A^{\frac{1+B}{1-B}} \left(\frac{\mu}{\rho\Delta y_1}\right)^{1+B} + \frac{1+B}{A}\left(\frac{\mu}{\rho\Delta y_1}\right)^B U_{//,1}\right]^{\frac{2}{1+B}} & \text{if } U_{//,1} > U_{tran} \end{cases} \tag{3.22}$$

with

$$U_{tran} = \frac{\mu}{2\rho\Delta y_1} A^{\frac{2}{1-B}} \tag{3.23}$$

Plengsaard and Rutland [44] provided the detailed derivation of the model. In order to account for the effect of near-wall sub-grid scale motions for LES, they suggested also to use the total viscosity ($\mu_t = \mu + \mu^{sgs}$) instead of the molecular one in the formulation of τ_w^{WW} if $U_{//,1} > U_{tran}$. We used here the original formulation of the model.

3.1.2 Anisothermal turbulent boundary layer

In the case of anisothermal flow, the temperature form of the energy equation (Eq. (2.22)) is given by:

$$c_p\frac{\partial \rho T}{\partial t} + c_p\frac{\partial \rho U_i T}{\partial x_i} = \frac{\partial P}{\partial t} + U_i\frac{\partial P}{\partial x_i} + \tau_{ij}\frac{\partial U_i}{\partial x_j} + \frac{\partial}{\partial x_i}\left(\lambda\frac{\partial T}{\partial x_i}\right) - \left(\rho\sum_{k=1}^{N} c_{p,k}J_{k,j}\right)\frac{\partial T}{\partial x_i} - \sum_{k=1}^{N} h_k\dot{\omega}_k \tag{3.24}$$

with the species mass diffusion flux J_k is given in Eq. (2.18). In addition to the assumptions made for isothermal turbulent boundary layers modeling, the following simplifying assumptions are introduced for the analysis of anisothermal turbulent boundary layer:

- Stationary flow: here the pressure is assumed independent of time too. Analysis and modeling of anisothermal turbulent boundary layer which includes the effect of time dependent pressure are also available in the literature [46, 47].
- Low flow velocity: the heating due to shear stress is neglected.
- Non reacting flow.
- Mass fractions of mixture components are constant near the walls.
- Wall constant temperature.

Considering these assumptions, the streamwise momentum and the energy equations read:

$$\frac{d\left(\rho v u\right)}{dy} = \frac{d\tau}{dy} \tag{3.25}$$

$$c_p \frac{d\left(\rho v T\right)}{dy} = \frac{dq}{dy} \tag{3.26}$$

with

$$\tau = \mu \frac{du}{dy} \qquad\qquad q = \lambda \frac{dT}{dy} \tag{3.27}$$

Here we continue to use the Reynolds averaging to get the mean governing equations instead of Favre averaging, as usually done for variable density flows, in order to highlight the effect of density fluctuation. Considering $\overline{v} = 0$ in the case of near wall flows without suction and blowing, the dynamic and energy governing equation become:

$$0 = \frac{d\overline{\tau}_{tot}}{dy} \tag{3.28}$$

$$0 = \frac{d\overline{q}_{tot}}{dy} \tag{3.29}$$

Similarly to the mean total shear stress, the mean total heat flux is constant in the wall normal direction and equal to the mean wall heat flux: $\overline{q}_{tot} = \bar{q}_w$. This equality is valid only in the region where the Couette flow assumption is valid, relatively near the surface, the total heat flux must go to zero at the outer edge of the boundary layer. The wall shear stress and heat flux are given by:

$$\overline{\tau}_w = \mu_w \left.\frac{d\bar{u}}{dy}\right|_w \qquad\qquad \bar{q}_w = \lambda_w \left.\frac{d\bar{T}}{dy}\right|_w \tag{3.30}$$

As density and viscosity are no longer constant near the wall, the classical dimensionless distance should be redefined using the wall values:

$$y^+ = \frac{y u_\tau}{\nu_w} \tag{3.31}$$

$$u_\tau = \sqrt{\frac{\tau_w}{\rho_w}} \tag{3.32}$$

A shear temperature can also be introduced as:

$$T_\tau = \frac{|\bar{q}_w|}{\rho_w c_{p,w} u_\tau} \tag{3.33}$$

A heat flux parameter B_q and a dimentionless temperature T^+ can be defined as the following:

$$B_q = \frac{T_\tau}{T_w} \tag{3.34}$$

$$T^+ = \frac{\left|\overline{T} - T_w\right|}{T_\tau} \tag{3.35}$$

Angelberger [48] provided a detailed discussion about the physical interpretation of the heat flux parameter.

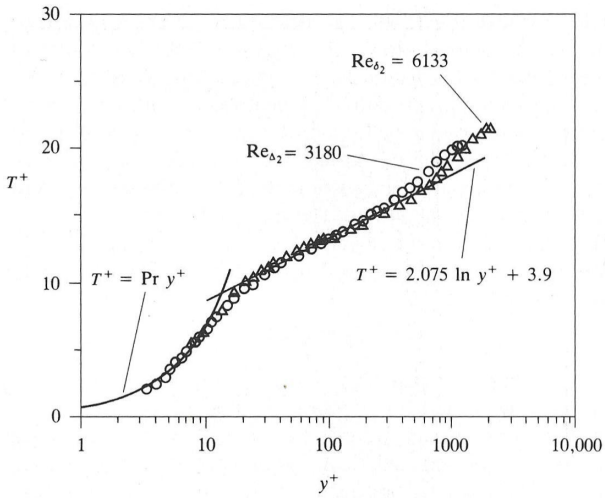

Figure 3.6: A thermal law of the wall for air [38].

Structure of the thermal turbulent boundary layer in the quasi-isothermal case

In the quasi-isothermal case, i.e. $B_q \to 0$, and assuming constant properties, the temperature equation can be written as :

$$1 = \left(\frac{1}{Pr} + \frac{1}{Pr_t} \frac{\mu_t}{\overline{\mu}} \right) \frac{dT^+}{dy^+} \tag{3.36}$$

Figure 3.6 shows experimental values of the mean dimensionless temperature profile in anisothermal turbulent air boundary layer. Similarly to the dynamic turbulent boundary layer, for small y^+, the turbulent heat flux is negligible with respect to the molecular heat diffusion and the mean temperature profile is linear:

$$T^+ = Pry^+ \tag{3.37}$$

For large y^+, the molecular heat diffusion will be negligible compared to the turbulent heat diffusion. Using Eq. (3.17) to integrate Eq. (3.36) and assuming constant Pr_t, one can get a log-law temperature profile:

$$T^+ = \frac{Pr_t}{\kappa} lny^+ + C \tag{3.38}$$

Both profiles expressed Eq. (3.37) and Eq. (3.38) meet at a certain transition location $y^+_{tran,T}$. So the temperature profile in the log-law region have the following general expression:

$$T^+ = \frac{Pr_t}{\kappa} lny^+ + y^+_{tran,T} Pr - \frac{Pr_t}{\kappa} lny^+_{tran,T} \tag{3.39}$$

For air, the experimental results gives $Pr = 0.7$, $Pr_t = 0.85$, and $y^+_{tran,T} = 13.2$ [38], thus:

$$T^+ = 2.075 lny^+ + 3.9 \tag{3.40}$$

Effect of variable density and viscosity on the turbulent boundary layer

Temperature variations in the flow lead naturally to flow properties variations too. The fluctuations of the molecular viscosity, thermal conductivity and specific heat capacity at constant pressure are commonly neglected [48]: $\overline{\mu} = \mu\left(\overline{T}\right)$, $\overline{\lambda} = \lambda\left(\overline{T}\right)$ and $\overline{c_p} = c_p\left(\overline{T}\right)$. Cabrit and Nicoud [27] checked that turbulent stress due to viscosity fluctuations can be neglected through DNS of multicomponent reacting compressible turbulent flows. Compared to the isothermal incompressible turbulent boundary layer, additional terms will arise in the total shear stress due to density fluctuations:

$$\overline{\tau}_{tot} = \bar{\mu} \frac{d\bar{u}}{dy} - \left[\bar{\rho}\overline{u'v'} + \bar{u}\overline{\rho'v'} + \bar{v}\overline{\rho'u'} \right] \tag{3.41}$$

For most practical cases, the density fluctuations are only a small fraction of the mean density [49]. Thus it is generally assumed that the effect of density fluctuations on the fluctuating velocity field ($\bar{u}\overline{\rho' v'}$ and $\bar{v}\overline{\rho' u'}$) is quite small and neglected in the analysis and model development of compressible turbulent boundary layers [49]. The total heat flux reads:

$$\overline{q}_{tot} = \bar{\lambda}\frac{d\bar{T}}{dy} - \left[\bar{\rho}\overline{T'v'} + \bar{T}\overline{\rho' v'} + \bar{v}\overline{\rho' T'}\right] \tag{3.42}$$

Assuming that the effect of density fluctuations on the fluctuating temperature field is negligible, and using the eddy diffusivity assumption for heat flux, the total heat flux can be expressed as:

$$\overline{q}_{tot} = \left(\bar{\lambda} + \lambda_t\right)\frac{d\bar{T}}{dy} \tag{3.43}$$

with

$$\lambda_t = c_p\frac{\mu_t}{Pr_t} \tag{3.44}$$

With heat transfer and variable density and viscosity, the mean velocity profile is no longer universal in the inner layer using the classical scaling as it was the case for the incompressible isothermal turbulent boundary layer. Many transformations exist in the literature which attempt to map the mean velocity profiles of compressible wall-bounded turbulent flows to the incompressible law of the wall. The van Driest transformation [50] allows to collapse velocity profiles of highly compressible flows (and thus a variable density flow) over adiabatic walls with velocity profiles from constant-properties flows. It is defined as:

$$u^+_{VD} = \int_0^{u^+}\sqrt{\frac{\overline{\rho}}{\rho_w}}du^+ \tag{3.45}$$

However, this transformation shows deviations when applied to diabatic flows and for flows with strong near-wall gradients in density and viscosity [51–56] (cf Figure 3.7a). Nicoud and Bradshaw [57] provided an analytical approximation of the van Driest transformation which includes the effect of the wall heat flux using the the Prandlt length formula (Eq. (3.16)) and assuming constant turbulent Prandtl number:

$$u^+_{VD} \approx \frac{2}{Pr_t B_q}\left[\sqrt{1 + Pr_t B_q u^+} - 1\right] \tag{3.46}$$

They pointed out that this approximation is mathematically analogous to the velocity transformation due to wall mass transfer as it will be presented later in section 4.3.2.1. Always based on the van Driest transformation, Cabrit and Nicoud [27] extended the analysis to develop dynamic and thermal wall models for multicomponent reacting compressible turbulent flows. In order to develop wall models for ICE simulations, Han and Reitz [58] proposed a set of transformation in order to take into account the effect of variable properties on the velocity and temperature profile. The dimensionless dynamic and thermal governing equations considering variable density and viscosity can be written as:

$$\left(1 + \frac{\nu_t}{\overline{\nu}}\right)\frac{du^+}{dy^+} = \frac{\rho_w}{\overline{\rho}}\frac{\nu_w}{\overline{\nu}} \tag{3.47}$$

$$\left(\frac{1}{Pr} + \frac{1}{Pr_t}\frac{\nu_t}{\overline{\nu}}\right)\frac{dT^+}{dy^+} = \frac{\rho_w}{\overline{\rho}}\frac{\nu_w}{\overline{\nu}} \tag{3.48}$$

c_p here is still assumed constant, which is quite acceptable for flows without mixture variation. By introducing the following transformations:

$$d\eta^+ = \frac{\nu_w}{\nu}dy^+ \qquad d\psi^+ = \frac{\overline{\rho}}{\rho_w}du^+ \qquad d\theta^+ = \frac{\overline{\rho}}{\rho_w}dT^+ \tag{3.49}$$

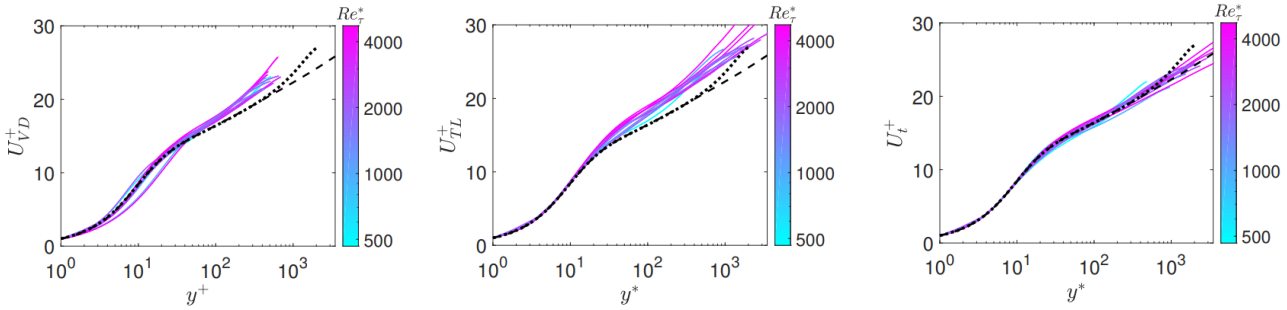

(a) van Driest transformation **(b)** Trettel-Larson transformation **(c)** Total-stress-based transformation

Figure 3.7: Compressible velocity transformations applied to data from diabatic turbulent boundary layers for different conditions as presented in Griffin et al. [56]. Incompressible channel data of Lee and Moser [61] with $Re_\tau \approx 5200$ (black dashed lines) and the zero-pressure-gradient boundary layer data of Sillero et al. [62] with $Re_\tau \approx 2000$ (blackdotted lines) are shown for reference.

equations (3.47) and (3.48) become:

$$\left(1 + \frac{\nu_t}{\overline{\nu}}\right) \frac{d\psi^+}{d\eta^+} = 1 \tag{3.50}$$

$$\left(\frac{1}{Pr} + \frac{1}{Pr_t}\frac{\nu_t}{\overline{\nu}}\right) \frac{d\theta^+}{d\eta^+} = 1 \tag{3.51}$$

which is a similar form to the quasi-isothermal formulation in equations (3.11) and (3.36). η^+, ψ^+ and θ^+ are known in the literature as LnKc variables. Huang et al. [59] suggested the semi-local wall coordinates, defined as:

$$y^* = \frac{y u_\tau^*}{\nu} \tag{3.52}$$

$$u_\tau^* = \sqrt{\frac{\tau_w}{\rho}} \tag{3.53}$$

to better match the van Driest velocity and second order turbulent statistics of compressible turbulent channel flow with incompressible results. Nicoud [60] confirmed the advantage of using the semi-local wall coordinates for low-speed flow with strong heat transfer. More recently, Patel et al. [53] investigated in detail the effect of variable density and viscosity on near-wall turbulence modification and scaling of turbulent statistics in channel flows. They concluded that, although the van Driest velocity and second order turbulent statistics are strong functions of the semi-local wall coordinates, flow quantities like mixing length, turbulence anisotropy and turbulent vorticity fluctuations do not show a universal scaling very close to the wall. Patel et al. [54] and Trettel and Larsson [52] both proposed a similar modification of the van Driest transformation which includes explicitly the effect of local viscosity and improves the normalization of the velocity profiles (cf Figure 3.7b). Patel et al. [55] applied also such an approach to normalize the mean temperature profiles. Very recently, Griffin et al. [56] proposed a total-stress-based transformation which successfully map the modified mean velocity profile to the incompressible law of the wall across the entire inner layer of the boundary layer (including the viscous sub-layer, buffer layer, and logarithmic layer) regardless of the wall thermal condition (cf Figure 3.7c).

3.1.2.1 Wall-refined formulation

In the case of anisothermal flow, the wall-refined formulation of the wall shear stress (Eq. (3.19)) should be redefined using the molecular viscosity at the wall temperature:

$$\tau_w^{refined} = \mu_w \frac{U_{//,1}}{y_1} \tag{3.54}$$

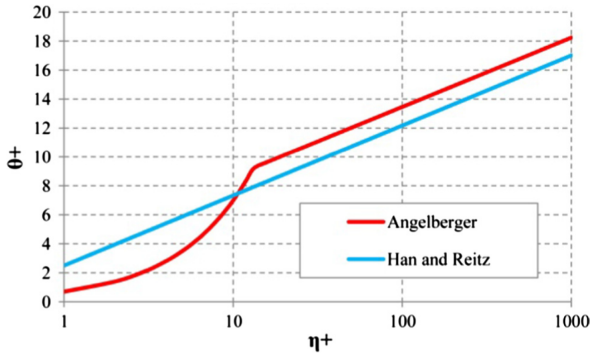

Figure 3.8: Temperature wall-law plotted in LnKc variables: *Angelberger* formulation (Eq. (3.64)) Vs *Han&Reitz* formulation (Eq. (3.58)) [64].

The wall-refined formulation of the wall heat flux is expressed as following:

$$q_w^{refined} = \lambda_w \frac{T_1 - T_w}{y_1} \tag{3.55}$$

The mesh grid should be sufficiently refined to capture the velocity and temperature wall gradients. Cabrit and Nicoud [27] used $\Delta y_1^+ = 1.4$ for wall-refined LES of multicomponent reacting compressible turbulent channel flow.

3.1.2.2 Algebraic wall heat models

As pointed previously for the dynamic wall models, the following wall heat models are based on time averaged equations and they are originally developed for RANS simulations. In the context of LES, instantaneous filtered quantities are used instead.

O'Rourke&Amsden model

O'Rourke&Amsden model [63] is based on the quasi-isothermal assumption detailed previously. The properties are considered constant in the context of this assumption. In the linear sub-layer, the dimensionless temperature is given in Eq. (3.37). For the log-law region, *O'Rourke&Amsden* model considers the general temperature expression (3.39) and assumes only $y^+_{tran,T} = y^+_{tran,U} = 11.05$. Using the velocity log-law (3.18), the dimensionless mean temperature is given by:

$$T^+ = Pr_t \left[\frac{1}{\kappa} ln\left(y^+\right) + B + 11.05 \left(\frac{Pr}{Pr_t} - 1 \right) \right] \tag{3.56}$$

The implantation in the current work consider the properties values at the center on the wall mesh cell. Thus, the modeled wall heat flux is given by:

$$q_w = \begin{cases} \frac{\mu_1 c_{p,1}(T_1 - T_w)}{Pr y_1} & y_1^+ \leqslant 11.05 \\ \frac{\rho_1 c_{p,1} u_\tau (T_1 - T_w)}{Pr_t \left[\frac{1}{\kappa} ln(y^+) + B + 11.05 \left(\frac{Pr}{Pr_t} - 1 \right) \right]} & y_1^+ > 11.05 \end{cases} \tag{3.57}$$

Han&Reitz model

Han&Reitz model [58] is based on the LnKc transformations as explained previously. In the original formulation of the model, Han and Reitz [58] considered a unique expression of the mean transformed temperature in the whole inner layer expressed by:

$$\theta^+ = 2.1 ln\left(\eta^+\right) + 2.5 \tag{3.58}$$

This thermal wall function is based on fitting function to express the turbulent heat diffusion of and assumes that the values of y_1^+ is higher than 40 [44, 47]. At this point, an expression need to be derived in order to relate the transformed temperature with the wall heat flux. Assuming a flow without mixture variation, the ideal gas equation of state leads to $\rho T = \rho_w T_w$. Including this property in the definition of the LnKc temperature transformation, one can get:

$$d\theta^+ = \frac{T_w}{\overline{T}} d\left(\frac{\overline{T} - T_w}{T_\tau}\right) \tag{3.59}$$

After integration, the wall heat flux reads:

$$\overline{q}_w = \frac{c_{p,w}\rho_w u_\tau T_w ln\left(\frac{\overline{T}}{T_w}\right)}{\theta^+} \tag{3.60}$$

Again based on the assumption of a flow without mixture variation and on the ideal gas equation of state, the term $c_p \rho T$ evaluated at the wall in the previous expression can also be evaluated at the center of the wall mesh cell. So the modeled heat flux can be implemented as:

$$q_w = \frac{c_{p,1}\rho_1 u_\tau T_1 ln\left(\frac{T_1}{T_w}\right)}{\theta_1^+} \tag{3.61}$$

where θ_1^+ evaluated at η_1^+ simply approximated as:

$$\eta_1^+ = \frac{\nu_w}{\nu_1} y_1^+ \tag{3.62}$$

As the original model formulation of Han and Reitz [58] is only suitable for high y_1^+ values, a modified version of the model is considered during this work using the *O'Rourke&Amsden* model formulation for the linear sub-layer:

$$q_w = \begin{cases} \frac{\mu_1 c_{p,1}(T_1 - T_w)}{Pr y_1} & \eta_1^+ \leqslant 11.05 \\ \frac{c_{p,1}\rho_1 T_1 ln\left(\frac{T_1}{T_w}\right)}{2.1 ln\left(\eta_1^+\right) + 2.5} & \eta_1^+ > 11.05 \end{cases} \tag{3.63}$$

Other versions exist also in the literature [44, 65] to improve the original formulation of Han and Reitz [58] model.

Angelberger model

Angelberger model [48] is also based on the LnKc transformations. By analogy with the quasi-isothermal expression, the thermal wall laws can be rewritten using LnKc variables as:

$$\theta^+ = \begin{cases} Pr\eta^+ & \eta^+ \leqslant 13.2 \\ 2.075 ln\left(\eta^+\right) + 3.9 & \eta^+ > 13.2 \end{cases} \tag{3.64}$$

which assumes implicitly to model the viscosity ratio in Eq. (3.51) as:

$$\nu_t = l_m^2 \frac{\overline{\rho}}{\rho_w} \frac{d\overline{u}}{dy} \tag{3.65}$$

Figure 3.8 shows the comparison between the thermal wall-laws considered by Han and Reitz [58] and Angelberger [48]. Desoutter et al. [66] performed a DNS of anisothermal turbulent boundary layer of lean air/iso-octane mixture with a heat flux parameter $B_q = 0.0354$. Figure 3.9 shows the mean temperature profile plotted in classical wall units and LnKc variables with the following fitted law of the wall:

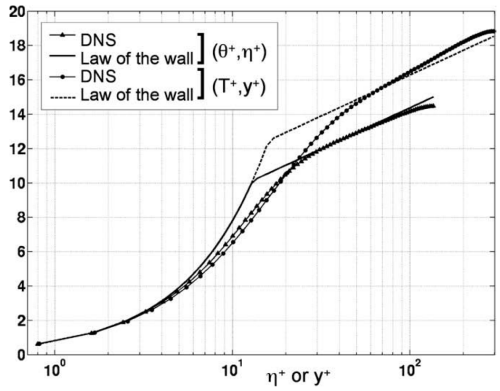

Figure 3.9: Mean temperature profile in anisothermal turbulent channel flow plotted using classical wall units (T^+, y^+) and LnKc variables (θ^+, η^+) [66].

$$\theta^+ = \begin{cases} Pr\eta^+ & \eta^+ \leqslant 13.0 \\ 2.075ln\left(\eta^+\right) + 4.82 & \eta^+ > 13.0 \end{cases} \tag{3.66}$$

The slope in the log-law region meets perfectly those of the quasi-isothermal case when they are plotted in LnKc variables. However, the laminar/turbulent transition locations and the additional constant in the log-law region are different. As for *Han&Reitz* model, the modeled wall heat flux is expressed using Eq. (3.61), with θ_1^+ evaluated this time using (3.64).

GruMo-UniMORE model

The model proposed by Berni et al. [64], called here *GruMo-UniMORE* model, is based on the quasi-isothermal formulation but uses the semi-local variables (Eq. (3.52) and (3.53)) instead of the classical wall units. The thermal wall-law in the log-law region is again based on the quasi-isothermal expression (3.39), with only $Pr_t = 0.85$ and $y^*_{tran,T} = 13.2$ are assumed a priori. So the modeled wall heat flux is given by:

$$q_w = \frac{\rho_1 c_{p,1} u^*_\tau \left(T_1 - T_w\right)}{T^*_1} \tag{3.67}$$

$$T^*_1 = \begin{cases} Pry^*_1 & y^*_1 \leqslant 13.2 \\ 2.075ln\left(y^*_1\right) + 13.2Pr - 5.34 & y^*_1 > 13.2 \end{cases} \tag{3.68}$$

Berni et al. [64] showed that this model better predict the wall heat flux than *Angelberger* and *Han&Reitz* models in the case of small values of B_q, typically smaller than 0.05.

Summary

The previous algebraic wall heat models shares common modeling assumptions. It is interesting to highlight that all of them assumes an ideal gas without mixture variation, and thus they consider constant ρT and constant c_p. Modeling choices differentiate mainly on two points:

- Effect of density variation: *O'Rourke&Amsden* model do not consider the effect of variable density in the log-law region. *Han&Reitz* and *Angelberger* consider the effect of variable density using the LnKc variables. *GruMo-UniMORE* considers the effect of variable density using the semi-local variables.
- Flow Pr number: *O'Rourke&Amsden* and *GruMo-UniMORE* allow for flows with Pr other than air, while *Han&Reitz* and *Angelberger* imposes air properties in the log-low region.

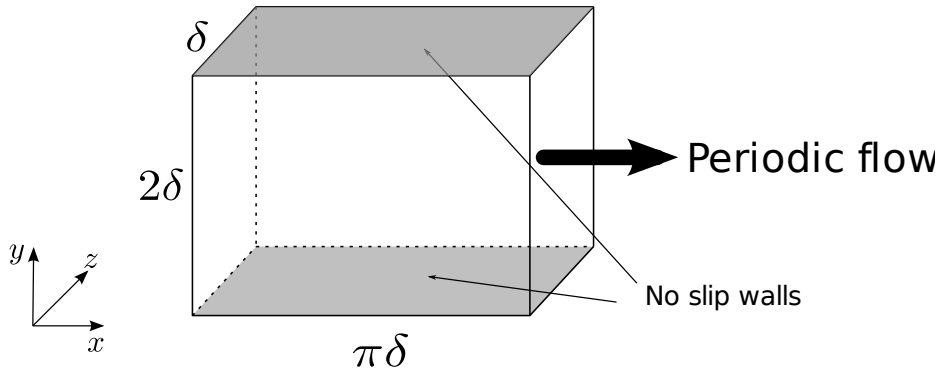

Figure 3.10: Minimal channel flow case configuration.

3.2 Minimal channel flow case

3.2.1 Case setup

Configuration

As illustrated in Figure 3.10, the standard sizing of the minimal channel flow configuration is applied. The channel width in the spanwise and streamwise directions are equal respectively to δ and $\pi\delta$. The top and bottom boundaries of the computational box are isothermal no-slip walls, while the streamwise and spanwise boundaries are periodic.

Meshing strategy

Generally in LES, the computational grid and the relevant spacing should be chosen fulfilling three main requirements:

- Maintain the low-pass filter cutoff length within the inertial sub-range in order to perform correctly resolved LES.
- Ensure proper resolution of the wall boundary layer.
- Retain a reasonable computational cost.

All along this work, two categories of meshing strategies were applied depending on the case:

- **Wall-refined case:** In this case, the meshing strategy aims mainly to satisfy the proper resolution of the boundary layer requirement. The wall mesh cell size satisfies the requirements of Zang et al. [39] as mentioned in section 3.1.1.1. In particular, the first wall mesh cell size is set such that $\Delta y_1^+ < 4$. Octree mesh grid structure is used by CONVERGE. In order to reduce the computational cost, coarser mesh grid is used in the computation domain and it is refined near the wall by dividing the base cell in each direction by 2 or 4. Each refined level contains 22 cells in the wall normal direction as shown in Figure 3.11. In non-reactive cases, grid anisotropy is allowed by $\Delta x = \Delta z > \Delta y$ while respecting the following conditions: $\Delta x < 5\Delta y$ and $\Delta x \leqslant \delta/36$, where δ denotes the half channel height (see Figure Figure 3.10).
- **Wall-modeled case:** In this case, wall models are used and the proper resolution of the wall boundary layer is no longer required. The grid is sized then to properly solve the energy containing length scales in the domain. According to Pope [20], the energy containing length scales are larger than $l_{EI} \approx \delta/6$ (see Figure 1.5). The mesh grid is isotropic ($\Delta x = \Delta y = \Delta z$) and uniform (without refinement) in all the computational domain. The mesh cell size is set such that $\Delta x = l_{EI}/6$, which leads to a cell size $\Delta x = \delta/36$. The wall cell size expressed in wall units will depend on Re_τ.

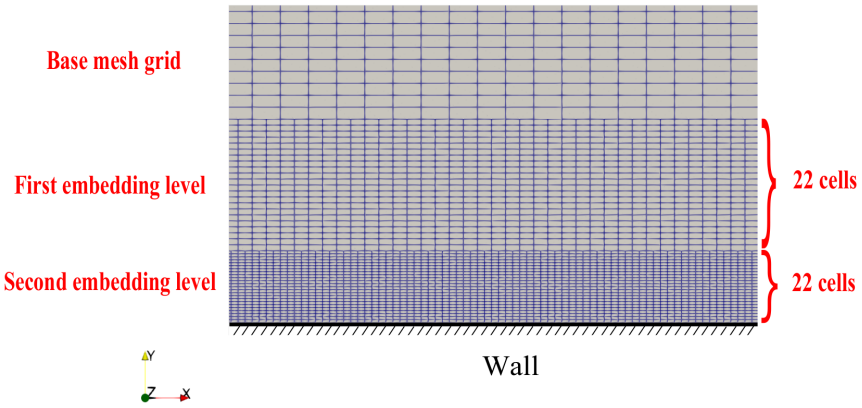

Figure 3.11: Wall-refined mesh grid with level embeddings.

Source terms for stationary flow

In order to compute a statistically steady configuration in a periodic channel, source terms need to be added in the governing equations. The streamwise momentum equation source is set as constant and it is adjusted to meet the target Re_τ or a target mean mass flow rate. In the case of anisothermal flow, the source term is added to the total energy equation is similar to the one used by Desoutter [24] for a similar case and it is expressed by:

$$S_e = \langle \rho c_v \rangle_{x,y=\delta,z} \frac{\left(T_{target} - \langle T \rangle_{x,y=\delta,z} \right)}{dt_t} \tag{3.69}$$

with T_{target} is the target temperature, $\langle . \rangle_{x,y=\delta,z}$ denote the spatial average operator over a plane in the center of the channel and $dt_t \approx \delta / 2u_\tau$ is a characteristic time of turbulent diffusion.

Post-processing

For the stationary turbulent channel flows, each case is first run until the stationary flow is reached, then the case is run at least during $100\delta/u_c$, where u_c is the mean streamwise velocity in the center of the channel. About 100 instantaneous samples sampled each δ/u_c are used to compute the mean and the root-mean square (rms) values. The temporal averaged values showed here after (denoted with $\bar{.}$) are also spatially averaged: flow quantities (as velocity, temperature, ...) are averaged along the streamwise and spanwise directions ($\langle \bar{.} \rangle_{x,z}$), and wall quantities are averaged over the wall ($\langle \bar{.} \rangle_{x,y=0,z}$).

3.2.2 Isothermal cases

Objectives and cases characteristics

The isothermal minimal channel flow configuration is performed in order to:

1. Validate the present wall-refined LES case against the reference DNS by Lee and Moser [61].
2. Assess the dynamic wall models (*lin-log* and *Werner&Wengle*) in wall-modeled LES cases.

The gas phase is a mixture of air/iso-octane at equivalence ratio 0.8, atmospheric pressure and temperature 373K. The wall temperature is also fixed at 373K. In all the cases, Re_τ is targeted and the mean and fluctuating velocity profiles are assessed. Two turbulent conditions were targeted: $Re_\tau = 550$ and $Re_\tau = 1000$. The corresponding Reynolds number, defined using the channel half height and the mean stramwise velocity in the center of the channel ($Re = \delta \overline{u}_c / \nu$), are respectively: $Re \approx 12000$ and $Re \approx 23000$. Table 3.1

Target Re_τ		550			1000		
		Δy_1^+	Δy_c^+	Re_τ	Δy_1^+	Δy_c^+	Re_τ
DNS of Lee and Moser [61]		0.019	4.5	544	0.019	6.2	1000
Wall-refined LES		3.5	14.0	587	3.3	13.2	1015
Wall-modeled LES	*lin-log*	15.4	15.4	556	28.6	28.6	1030
	Werner&Wengle	15.4	15.4	555	28.6	28.6	1036

Table 3.1: Cases characteristics for the isothermal turbulent channel flow simulations. Δy_1^+: Dimensionless wall cell size in the wall normal direction; Δy_c^+: Dimensionless cell size in the center of the channel in the wall normal direction; Re_τ: Reynolds number based on wall shear velocity.

summarizes the mesh characteristics and the actual Re_τ of each case. Performing the wall-modeled LES at two different Re_τ give us ensight on the wall models performance when the center of the wall cell is located at two different positions. For $Re_\tau = 550$, $y_1^+ \approx 7.7$, i.e. the center of the wall cell close to the linear sub-layer. While $y_1^+ \approx 14.3$ at $Re_\tau = 1000$, meaning the center of the wall cell located in the buffer sub-layer. Two levels of grid refinement were used near the wall for the wall-refined cases, leading to a total numbers of cells in the domain of about 1.2M and 4M for the wall-refined cases at $Re_\tau = 550$ and $Re_\tau = 1000$ respectively. The total numbers of cells in the domain for the wall-modeled cases is about 0.3M.

Results and discussion

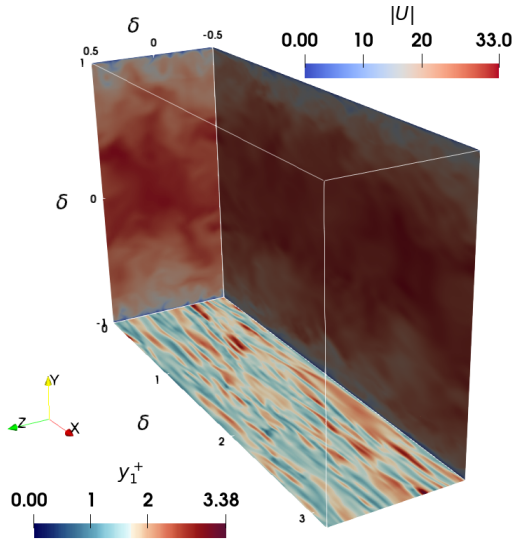

Figure 3.12: Snapshot of isothermal turbulent channel flow at $Re_\tau = 1000$: Magnitude of the velocity field on the side boundaries and y_1^+ values at the bottom wall.

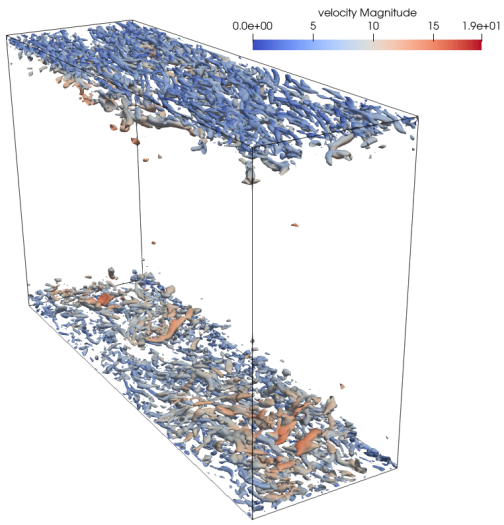

Figure 3.13: Iso-surface of Q-criterion colored with the velocity magnitude in the isothermal turbulent channel flow at $Re_\tau = 1000$.

The instantaneous filtered flow field of the wall-refined case at $Re_\tau = 1000$ is illustrated in Figures 3.12 and 3.13. Figure 3.12 shows the magnitude of the velocity field on the side boundaries and the distribution of the

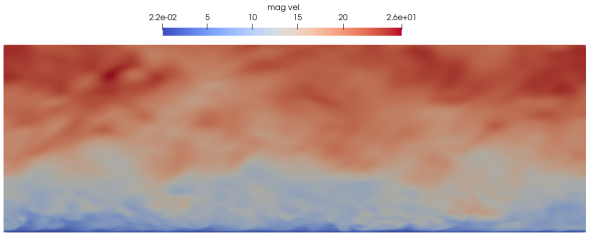

Figure 3.14: Instantaneous filtered velocity field magnitude in the $x-y$ plane at $Re_\tau = 1000$: wall-refined case.

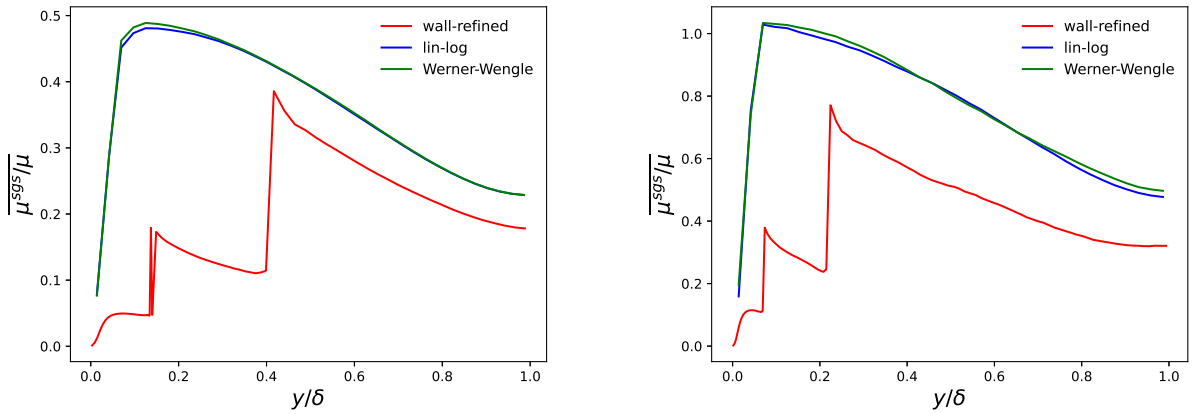

(a) At $Re_\tau = 550$ **(b)** At $Re_\tau = 1000$

Figure 3.15: Mean sub-grid scale to the molecular viscosity ratio in isothermal conditions.

y^+ values at the bottom wall. Figure 3.13 shows the near vortical structures streaks through the iso-surfaces of Q-criterion colored by the velocity magnitude. Figure 3.14 shows also the filtered velocity field magnitude of the wall-refined case in the $x-y$ computations at $Re_\tau = 1000$.

Quantitatively, Figure 3.15 shows the mean ratio of the sub-grid scale viscosity (modeled using σ-model) to the molecular one. For the wall refined cases, this viscosity ratio tends toward zero at the wall, meaning that all the turbulent structures are solved near the wall and the filtered flow in the wall mesh cell is mainly driven by the molecular viscosity, as wanted in a wall-refined LES simulation. The jumps of the viscosity ratio at higher distance from the wall corresponds to the transition to a different mesh refinement level. Figure 3.16 shows the normalized mean streamwise velocity, while the normalized streamwise and normalwise velocity fluctuations are shown in Figure 3.17. The wall-refined results are in a good agreement with the results of Lee and Moser [61] in both cases. The shape of the normalized fluctuations are well reproduced although they are under-estimated compared to the reference results at $Re_\tau = 1000$. This under-estimation can be accepted considering the difference in accuracy between the numerical methods (Lee&Moser DNS code is based on spectral method [61]).

Using the two wall-models, the mean streamwise velocity profiles are relatively well predicted at $Re_\tau = 550$. Both models overestimate the velocity in the center of the channel with an error of about 8% with respect to the reference DNS. At $Re_\tau = 1000$ however, *Werner-Wengle* gives much closer result to the DNS. The use of the *lin-log* model leads to an overestimation of the velocity in the center of the channel with an error of 25%, while this error is only 11% when *Werner&Wengle* model is used. Although the differences on the

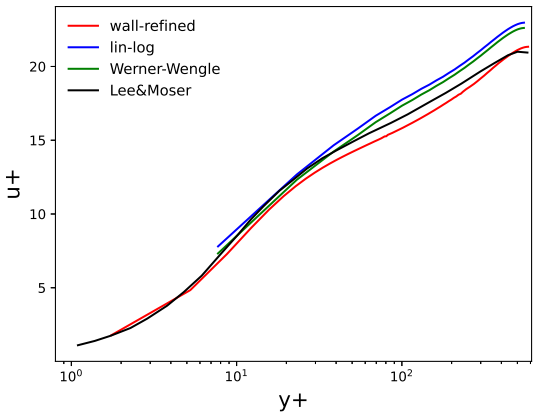

(a) At $Re_\tau = 550$

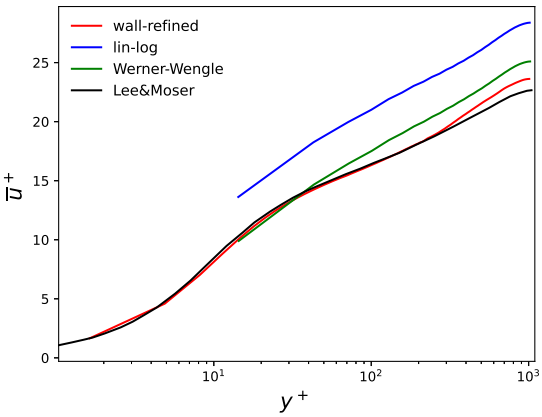

(b) At $Re_\tau = 1000$

Figure 3.16: Normalized mean streamwise velocity in isothermal conditions.

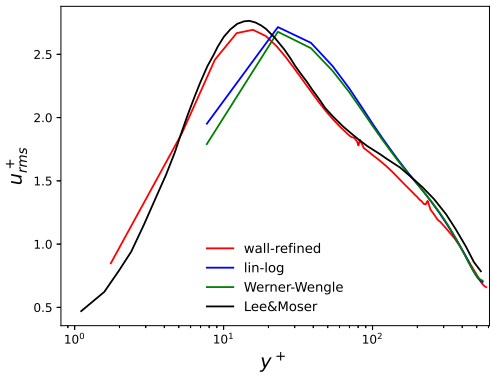

(a) Streamwise fluctuations at $Re_\tau = 550$

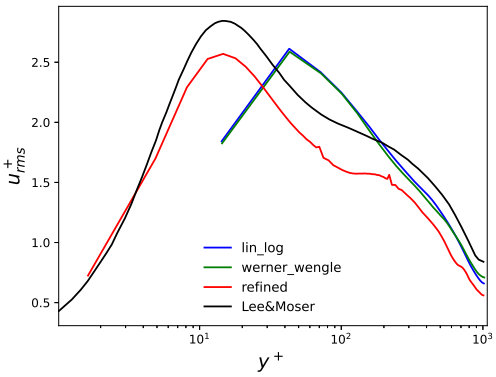

(b) Streamwise fluctuations at $Re_\tau = 1000$

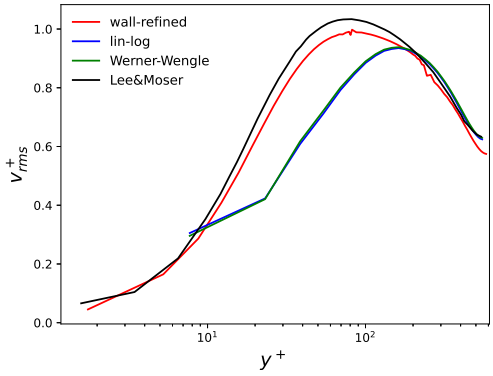

(c) Normalwise fluctuations at $Re_\tau = 550$

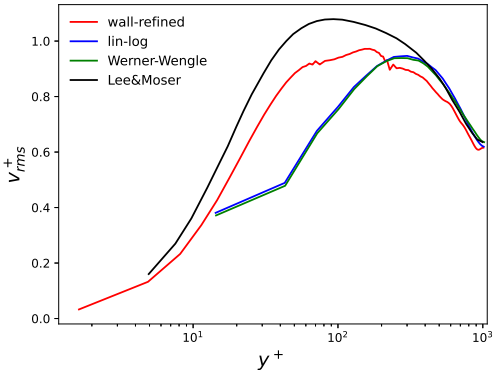

(d) Normalwise fluctuations at $Re_\tau = 1000$

Figure 3.17: Normalized streamwise and normalwise fluctuations in isothermal conditions.

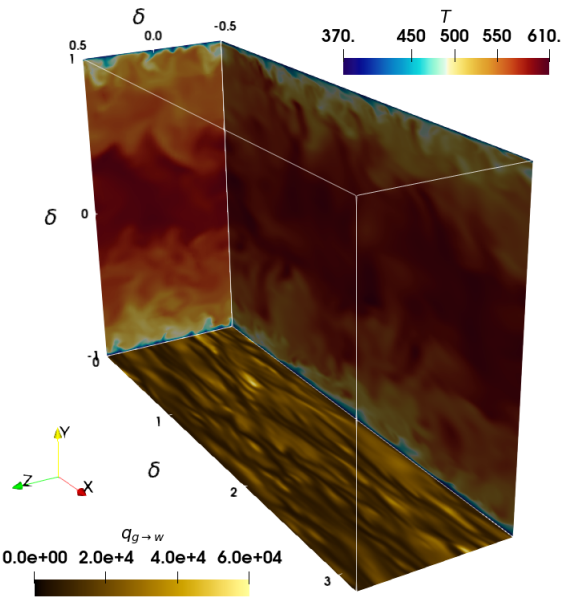

Figure 3.18: Snapshot of anisothermal turbulent channel flow at $Re_\tau = 1100$: temperature field on the side boundaries and heat flux at the bottom wall.

mean velocity profiles, the normalized resolved fluctuations obtained by the wall modeled cases are almost identical. The resolved fluctuations agree well with the reference results only for $y^+ > 200$, as the mesh is not refined enough at the wall. It is interesting to mention that these results were obtained using σ-model with the model constant $C_\sigma = 1.3$ (see Eq. (2.39)). Using different model constant C_σ may lead to different results, especially at the center of the channel. Efros [67] assessed also both dynamic wall models in WMLES of turbulent channel flow at $Re_\tau = 4000$ using Smagorinsky sub-grid scale model. His results are in agreement with the present assessment as the relative errors on the velocity in the center of the channel with respect to the DNS are 18% and 36% for the *Werner&Wengle* and *lin-log* model respectively.

3.2.3 Anisothermal cases

Objective and cases characteristics

The anisothermal turbulent channel flow case is performed in order to assess the wall heat models in wall-modeled LES compared to the wall-refined case. Four wall heat models are considered: *O'Rourke&Amsden, Han&Reitz, Angelberger* and *GruMo-UnoMORE*. The dynamic wall model for all the wall-modeled cases is *Werner&Wengle*. As for the isothermal case, the mixture is air/iso-octane at an equivalence ratio of 0.8 and atmospheric pressure. However, the flow in this case has a thermal stratification. The imposed wall temperature is 373K and source terms are set to keep a mean temperature of 600K at the center of the channel. In all the cases Re_τ is targeted, the mean and fluctuating streamwise velocity and temperature profiles, as well as the wall heat flux, are assessed. As for the isothermal cases, two turbulent conditions were targeted: $Re_\tau = 550$ ($Re \approx 6000$) and $Re_\tau = 1100$ ($Re \approx 14000$). The heat flux parameter of both conditions is about $B_q \approx 0.03$. Table 3.2 summarizes the mesh characteristics and the actual Re_τ and $\overline{T}_c$ for each case.

		Mesh	Target conditions		Results		
		Δy_1^+	Re_τ	$\overline{T}_c$ (K)	$\overline{u}_c$ $(m.s^{-1})$	$\overline{q}_{g\to w}$ $(kW.m^{-2})$	ϵ_q (%)
550	wall-refined	3.3	552	590.6	20.6	13.90	
	O'Rourke-Amsden	15.3	552	590.4	19.4	13.97	0.49
	Han-Reitz	15.4	554	590.6	19.6	14.00	0.72
	Angelberger	15.3	551	590.2	19.3	14.06	1.16
	GruMo-UnoMORE	15.4	553	596.7	19.2	13.48	-3.05
1100	wall-refined	3.36	1100	591.6	30.4	16.95	
	O'Rourke-Amsden	30.5	1096	591.3	28.0	15.85	-6.46
	Han-Reitz	30.3	1092	591.7	27.9	15.15	-10.57
	Angelberger	30.5	1098	591.7	28.1	15.02	-13.92
	GruMo-UnoMORE	30.6	1102	591.9	27.8	14.59	11.36

Table 3.2: Cases characteristics and results for the assessment of algebraic wall heat flux models. Δy_1^+: Dimensionless wall cell size in the wall normal direction; Re_τ: Reynolds number based on wall shear velocity; $\overline{T}_c$: Mean temperature in the center of the channel; $\overline{u}_c$: Mean streamwise velocity in the center of the channel; $\overline{q}_{g\to w}$: Mean wall heat flux; ϵ_q: Relative wall heat flux error with respect to wall-refined results.

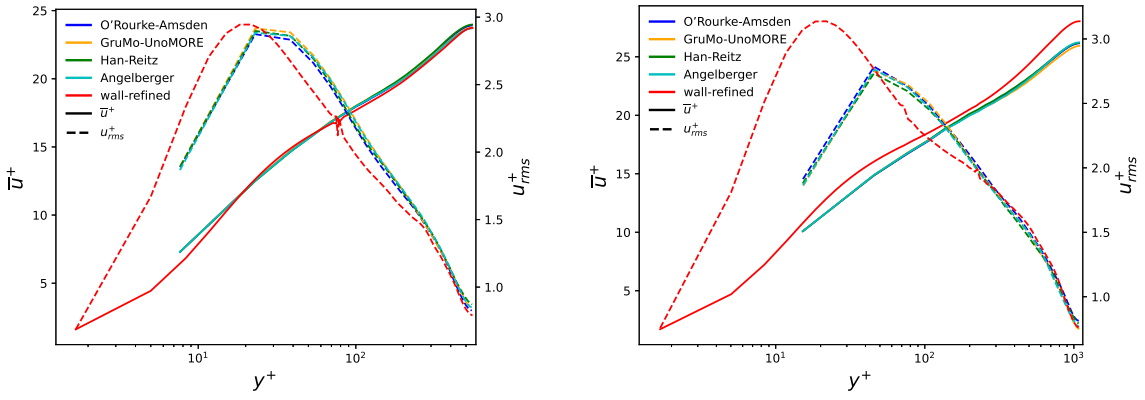

(a) At $Re_\tau = 550$ **(b)** At $Re_\tau = 1100$

Figure 3.19: Normalized mean streamwise velocity and fluctuations in the case of anisothermal flow.

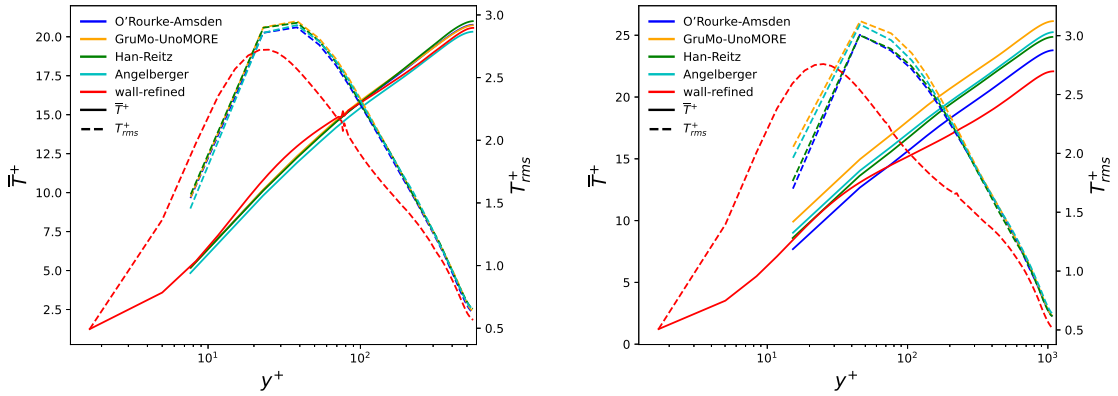

(a) At $Re_\tau = 550$ **(b)** At $Re_\tau = 1100$

Figure 3.20: Normalized mean temperature and fluctuations in the case of anisothermal flow.

Results and discussion

Figure 3.18 shows the instantaneous filtered temperature field of the wall-refined case at $Re_\tau = 1100$ in the side boundaries and the wall heat flux distribution on the bottom wall. The normalized mean streamwise velocity and its fluctuations are shown in Figure 3.19. The differences between the wall-refined and wall-modeled results are similar to the differences found in the isothermal case. There is no noticeable difference between wall-modeled cases having different wall heat models. So, for these conditions, the mean and fluctuating velocity profiles depends only on the used dynamic wall model and not on the wall heat model choice. Figure 3.20 shows the normalized profiles of the temperature mean value and fluctuations. At $Re_\tau = 550$, the wall-modeled profiles are almost identical and agree very well with the wall-refined profiles. At $Re_\tau = 1100$, the wall-modeled normalized mean temperature profiles differ slightly with globally the same slope an magnitude as the wall-refined case. At the first node corresponding to $y_1^+ \approx 15$, all the wall-modeled cases recover the wall-refined temperature within $10K$ range, i.e. with an error smaller than 3%. Table 3.2 presents also the obtained heat flux at the wall for each case along with the relative error using the wall-refined case as reference. At $Re_\tau = 550$, all the heat models predict well the wall heat flux. At $Re_\tau = 1100$, the errors are more important. *O'Rourke&Amsden, Han&Reitz* and *Angelberger* under-predict the wall heat flux with errors ranging from 6% to 14%, while *GruMo-UnoMORE* over-predict the wall heat flux by about 11%. The assessment of these models in academic anisothermal turbulent boundary layer configurations are very limited in the literature. To the best of our knowledge, there is no such assessment of the use of these models in the context of WMLES.

Part II

Wall-Film Evaporation

Chapter 4

Wall-film governing equations and literature review

Contents

Wall-film evaporation is one of the main physical phenomena involved in Flame-Film Interaction. The evaporation promotes the local rich regions where soot is formed. Accurate modeling of this phenomenon is a key step to setup a numerical tool for detailed soot modeling in GDI engines. This chapter is dedicated to the wall-film governing equations and the different evaporation modeling approaches existing in the literature. The wall-film numerical description used during this work is also presented.

Considered assumptions

During this work, some simplifying assumptions were considered in order to establish the wall-film governing equations and the different models.

- It is assumed that the liquid film is formed on a perfectly **smooth wall**. The effect of wall rugosities and coke coating, as might be found in practical ICE, are not considered.
- As engine cold start conditions are targeted during this work, the wall temperature is assumed to be below the saturation temperature of the fuel. Thus, **the film evaporates in the complete wetting regime**, i.e. without boiling.
- In engine cases, it is important to consider the multi-component nature of practical fuels as highlighted by numerous authors [68–70]. Below, only a **single-component wall-film** is considered to understand the evaporation physics and the modeling concepts. The extension of the following modeling approaches to a discrete multi-component models is possible.

Additional classical assumptions are also considered as in chapter 3: two-dimentional stationary flow, with negligible stream-wise gradient with respect to the normal-wise gradient, and without pressure gradient.

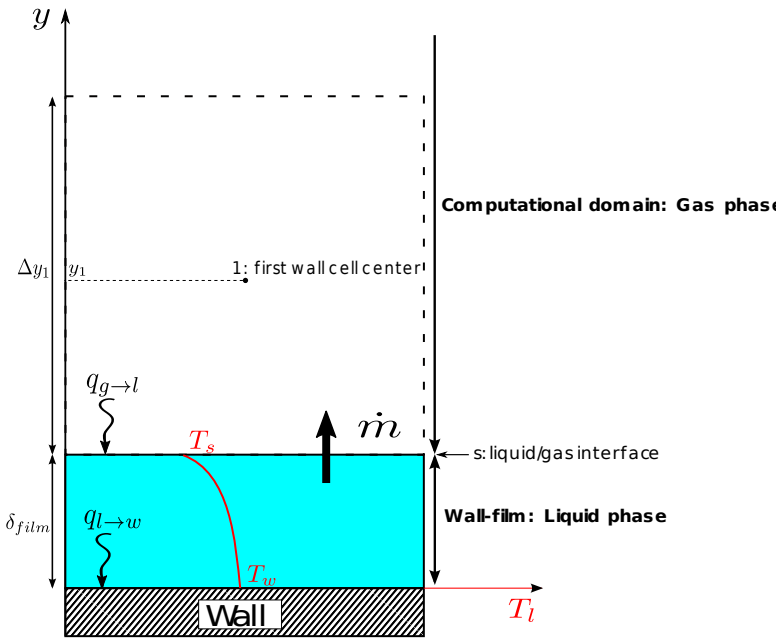

Figure 4.1: Wall mesh cell representation.

Notations

Figure 4.1 shows a wall mesh cell above a wall-film. Here, the terminology of "wall mesh cell" will always be used to refer to the boundary mesh cell, even if the wall is wetted. As all along this manuscript, the wall mesh cell face coincides with the computational domain boundary, which is in this case the liquid/gas interface. So, as long as the wall-film exists, the liquid/gas interface position is fixed in the computational domain reference frame. The subscripts g and l denote respectively the gas phase and liquid phase related quantities and the evaporated species will be denoted with the subscript F. The film normal direction will be considered along the y axis. The subscripts w, s and 1 will denote respectively the wall, the liquid/gas interface and the first wall cell center.
Figure 4.1 illustrates also the involved physical phenomena to be modeled. In the following, The momentum transfer at the liquid/gas interface will be briefly discussed. The energy governing equation and its boundary conditions will be detailed as it will be used to compute the liquid temperature across the wall-film thickness. Then, different approaches to model the evaporation rate will be presented.

4.1 Momentum transfer at the liquid/gas interface

At the liquid/gas interface, the wall tangential velocity component is zero ($U_{//,s} = 0\,m.s^{-1}$), and the evaporated species is blown with a momentum $\rho_{g,s} v_s = \dot{m}$ in the wall normal direction, where v_s is the Stefan velocity. Hence, the effect of the wall-film evaporation on the boundary layer is similar to the effect of a transpired wall [24]. The right hand side in Eq. (3.3), can no longer be simplified, meaning that the total shear stress is no longer constant in the wall normal direction. Assuming a constant Stefan velocity and an incompressible flow, the mean total shear stress can be expressed as $\overline{\tau}_{tot} = \overline{\tau}_s \left(1 + v_s^+ u^+\right)$, where $\overline{\tau}_s$ is the shear stress at the liquid/gas interface and $v_s^+ = v_s / u_\tau$. It is known in the literature that the transpiration alters the structure of the turbulent boundary layer rather considerably, affecting the shear-stress distribution, and also affecting the linear sub-layer thickness [24, 38]. In the context of LES, the shear stress at the liquid/gas interface can be computed using either wall-refined or wall-modeled formulation depending on the wall mesh cell size:

- **Wall-refined formulation:** As on a dry wall, the shear stress at the liquid/gas interface is computed as:

$$\tau_s^{refined} = \mu_s \frac{U_{//,1}}{y_1} \tag{4.1}$$

- **Wall-modeled formulation:** Chedevergne and Marchenay [71] formulated a general strategy for the modeling of transpired turbulent boundary layers in the context of RANS simulations. In the context of LES, the classical algebraic dynamic wall models presented in section 3.1.1.2, which does not consider the transpiration effect, are still generally used for wall-film evaporation simulations. Furthermore, algebraic dynamic wall models based on Prandtl mixing-length for the modeling of the turbulent shear stress ($\overline{\rho u' v'}$) classically neglect the turbulent shear stresses due to density fluctuations ($\bar{u}\overline{\rho' v'}$ and $\bar{v}\overline{\rho' u'}$ in Eq. (3.41)). Desoutter [24] shows however that $\bar{u}\overline{\rho' v'}$ have a significant contribution in the total shear stress in the case of an evaporating wall-film. Desoutter [24] also developed a dynamic wall model specific to an evaporating wall-film and it will be presented later in this chapter.

4.2 Energy governing equation in the liquid phase

The temperature in the liquid phase is continuously changing from the wall temperature T_w to the liquid/gas interface temperature T_s. For evaporating wall film, heat is also lost by latent heat due to phase change. The wall film thickness is generally negligible compared to the wetted area, therefore the assumption of 1D modeling of the liquid temperature in the wall normal direction can be applied. The advection inside the liquid phase is smaller than the diffusion and can be neglected. Assuming also constant liquid thermal conductivity λ_l, density ρ_l and specific heat capacity c_{pl}, the governing equation for the liquid temperature $T_l = T_l(y,t)$ can be expressed as:

$$\frac{\partial T_l}{\partial t} = \frac{\lambda_l}{\rho_l c_{p,l}} \frac{\partial^2 T_l}{\partial y^2} \tag{4.2}$$

This governing equation has two boundary conditions: at the gas/liquid interface and at the wall.

Heat transfer at the liquid/gas interface

The energy balance at the liquid/gas interface reads:

$$q_{g\to l} = L\dot{m} + \lambda_{l,s} \left.\frac{\partial T_l}{\partial y}\right|_s \tag{4.3}$$

where $q_{g\to l}$ is the heat flux transferred from the gas to the liquid, L is specific latent heat of evaporation and $\dot{m}$ is the mass evaporation rate per unit surface. $q_{g\to l}$ depends on the thermal mixing above the film and it is transferred locally at the liquid/gas interface by conduction. It can be computed by two different approaches depending on the near wall mesh refinement:

- **Wall-refined formulation:** The near wall mesh is sufficiently refined to capture the temperature gradient at the gas/liquid interface. The first order approximation of the temperature gradient gives:

$$q_{g\to l}^{refined} = \lambda_{g,s} \frac{(T_1 - T_s)}{y_1} \tag{4.4}$$

- **Wall-modeled formulation:** A model is used to compute $q_{g\to l}^{model}$ such as the wall heat models described in section 3.1.2.2. Whatever model is used, $q_{g\to l}^{modeled}$ can be rewritten using a heat transfer coefficient h_c as:

$$q_{g\to l}^{modeled} = h_c (T_1 - T_s) \tag{4.5}$$

  In addition to the fact that classical algebraic wall heat models do not account for the effect of transpiration, some of the main considered assumptions highlighted in section 3.1.2.2 are also no longer valid in the case of evaporating wall-film. The mixture above an evaporating wall-film is highly

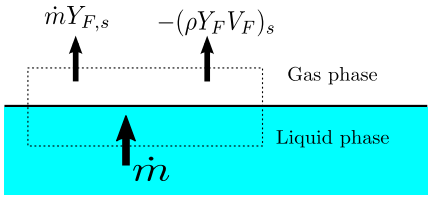

Figure 4.2: Control volume around a stationary liquid/gas interface

stratified. In this case the ideal gas state equation leads to constant $\rho T/W$ (W being the mixture molecular weight) in the boundary layer instead of constant ρT. The mixture variation induces high variation of the specific heat capacity c_p as it varies linearly with species mass fractions. Desoutter [24] proposed a thermal wall model accounting for the effect of transpiration. This model will be presented later in this chapter.

Heat transfer at the liquid/solid interface

In the wetting regime, i.e. without boiling, the heat flux transferred from the liquid phase to the wall is proportional to the liquid temperature gradient at the wall surface:

$$q_{l\to w} = \lambda_{l,w} \left.\frac{\partial T_l}{\partial y}\right|_w \tag{4.6}$$

Wall surface temperature T_w is the most influencing parameter on film evaporation [24, 70, 72]. Through 1D DNS simulation of flame/film interaction, Desoutter [24] concluded that T_w may even have a higher influence than the flame temperature on the film evaporation dynamic.

4.3 Evaporation rate modeling

In the case of a non reacting multi-species flow, the evaporated species conservation in the gas phase reads:

$$\frac{\partial \rho Y_F}{\partial t} + \frac{\partial \left(\rho Y_F U_i\right)}{\partial x_i} + \frac{\partial \left(\rho V_{F,i} Y_F\right)}{\partial x_i} = 0 \tag{4.7}$$

Considering a two-dimentional stationary flow with stream-wise gradient negligible with respect to the normal-wise gradient, the later equation can be simplified into:

$$\frac{d\left(\rho Y_F v\right)}{dy} + \frac{d\left(\rho V_F Y_F\right)}{dy} = 0 \tag{4.8}$$

Figure 4.2 shows a control volume around a stationary liquid/gas interface. In the gas phase side, the evaporated species F is advected with a momentum $\rho_s v_s = \dot{m}$, and diffused with a diffusion velocity $V_{F,s}$. In the liquid phase side, the liquid mass is removed with a rate equal to $\dot{m}$. So the mass conservation equation of the species F at the liquid/gas interface reads:

$$\dot{m} Y_{F,s} + \left(\rho Y_F V_F\right)_s = \dot{m} \tag{4.9}$$

Species mass fraction at the liquid/gas interface

The evaporated species mass fraction at the liquid/gas interface $Y_{F,s}$ can be computed using Raoult's law:

$$Y_{F,s} = \left[1 + \left(\frac{P}{P_{v,F}} - 1\right)\frac{W_{a,s}}{W_{F,s}}\right]^{-1} \tag{4.10}$$

where $W_{a,s}$ is the molar weight of the mixture without fuel and $P_{v,F}$ is the partial vapor pressure. The mass conservation of the other species at the liquid/gas interface reads:

$$\dot{m} Y_{k,s} + \left(\rho Y_k V_k\right)_s = 0 \quad \forall k \neq F \tag{4.11}$$

This later equation can be used to get $Y_{k,s}$ for all the other mixture species in order to compute $W_{a,s}$. It is assumed in all the following work that $W_{a,s} = W_{a,1}$. In other words, the differential diffusion of non-evaporating species is not considered. The partial vapor pressure $P_{v,F}$ is generally computed using the Clausius-Clapeyron relation [24]. The evaluation methods of the partial vapor pressure based on the Clausius-Clapeyron are only valid when:

- The thermodynamic conditions are far from the critical conditions
- The gas phase behave as an ideal gas, i.e. for an equilibrium at low pressures.

These assumptions are not always verified in the case of wall-film evaporation in ICEs. The pressure and temperature peaks in GDI engine can be close to the critical conditions of the hydrocarbons. In such a case, it would be better to use thermodynamic computations based on more realistic state equation for the liquid and the gas phase [73]. During this work, $P_{v,F}$ is computed and tabulated before the simulation with respect to temperature based on the Clausius-Clapeyron relation.

Mass diffusion flux modeling

The expression of $\left(Y_F V_F\right)_s$ is based on Fick's law similarly to the one used for the governing mass equations in the gas phase (Eq. (2.15)):

$$\left(\rho Y_F V_F\right)_s = -\left(\rho D_F\right)_s \left.\frac{dY_F}{dy}\right|_s \tag{4.12}$$

with $\rho D_F = \mu / Sc_F$, μ is the dynamic molecular viscosity and Sc_F is a constant Schmidt number of the evaporated species. More details about the diffusion flux modeling are given in section 2.1.2.2. The main highlighted issues are the following:

- The fact of using a constant set of Sc_k will not be representative of all the local conditions of the 3D simulation.
- Fick's law neglects the mass diffusion due to the mixture molecular weight gradient, while the mixture above an evaporating wall-film is highly stratified.

Summing the mass conservation equations of all the N gas species at the liquid/gas interface (equations (4.9) and (4.11)) should lead to $\sum_{k=1}^{N} \left(Y_k V_k\right)_s = 0$. To ensure this condition, a correction velocity should normally be introduced as done in Eq. (2.18). However, as mentioned previously, Eq. (4.11) is not used to get the non-evaporated species mass fraction at the gas/liquid interface and the differential diffusion between the gas species is simply neglected. Thus, the diffusion correction velocity will not be considered for the species mass conservation equations related to evaporation modeling.

4.3.1 Wall-refined evaporation model

Using Eq. (4.12), and using Fick's law to model the species diffusion, the evaporated species mass balance at the liquid/gas interface (Eq. (4.9)) can be written as:

$$\dot{m} Y_{F,s} - \left.\frac{\mu_s}{Sc_F} \frac{dY_F}{dy}\right|_s = \dot{m} \tag{4.13}$$

If the near wall mesh is sufficiently refined to capture the species gradient, the later equation can be used to express a wall-refined formulation of the evaporation rate:

$$\dot{m}^{refined} = \left.\frac{\mu_s}{Sc_F \left(Y_{F,s} - 1\right)} \frac{dY_F}{dy}\right|_s \tag{4.14}$$

Using a first order approximation of the gradient leads to:

$$\dot{m}^{refined} = \frac{\mu_s \left(Y_{F,1} - Y_{F,s}\right)}{Sc_F y_1 \left(Y_{F,s} - 1\right)} \tag{4.15}$$

Desoutter [24] used this modeling approach (with different mass diffusion flux modeling) to numerically study the interaction between a premixed flame front and a mono-component wall film in 1D configuration. He also used this approach in three dimensional DNS simulation of turbulent boundary layer above an evaporating mono-component wall-film.

4.3.2 Wall-modeled evaporation model

The wall-refined modeling approach is suitable only for DNS or wall-refined LES simulations. Models not based on the local gradient at the liquid/gas interface are needed for wall-modeled LES or RANS simulations. The mass conservation equation in the gas flow, with the same assumptions used to establish Eq. (4.8), leads to $\rho v = \rho_s v_s = \dot{m}$. Thus, the instantaneous evaporated species mass conservation equation reads:

$$\dot{m}\frac{dY_F}{dy} - \frac{d}{dy}\left(\rho D_F \frac{dY_F}{dy}\right) = 0 \tag{4.16}$$

When the wall-film evaporates, a fuel mass boundary layer of thickness δ_M is formed. At the edge of this mass boundary layer, the evaporated species mass fraction is equal to the far-field value $Y_{F,\infty}$. Even in this simplified configuration, integrating Eq. (4.8) over a distance above liquid/gas interface still presents some challenges compared to the dynamic and heat transfer wall modeling, mainly because of:

- Turbulence modeling: The blowing Stephan velocity due to evaporation changes significantly the near wall turbulence behavior [24]. Hence, the use of the classical assumptions to model the near wall turbulent mixing, such as Prandtl mixing length theory, is questionable.
- Properties modification: As in the case of anisothermal flow, density and diffusion properties vary first with temperature. In the case of heat and mass transfer, properties vary also with the mixture composition.

In the following, the two main algebraic modeling approaches available in the literature to model the wall-film evaporation rate in CFD simulations will be presented:

- The first approach is a **wall-law based modeling** [24, 68, 74–79]. This modeling approach is similar to the classical algebraic dynamic and wall heat models presented in section 3.1. The turbulent diffusion is neglected close to the wall, then it is modeled using the Prandtl mixing length theory starting from a laminar/turbulent transition distance. Desoutter [24] tried also to include the transpiration effect on the turbulent boundary layer and established a set of dynamic, thermal and fuel mass wall-laws based on the results of DNS simulations of a evaporating wall-film in turbulent channel flow.
- The second one is a **semi-analytical solution** based on a heat-mass transfer analogy. Models based on this approach are widely used in the literature, especially for ICE simulation cases [72, 73, 80]. Kays and Crawford [38] derived in details this approach and section 4.3.2.2 is mainly based on this reference.

Other empirical evaporation models exist also in literature [70, 81] but they will not be considered in this review.

4.3.2.1 Wall-law based models.

O'Rourke and Amsden [74] are among the first to propose a modeling approach based on wall-laws to express the wall-film evaporation rate for ICE CFD simulations. Considering Fick's law to model the mass diffusion flux, the evaporated species conservation in the gas phase (Eq. (4.8)) reads:

$$\frac{d\left(\rho v Y_F\right)}{dy} - \frac{d}{dy}\left(\frac{\mu}{Sc_F}\frac{dY_F}{dy}\right) = 0 \tag{4.17}$$

Integrating this conservation equation and using the the evaporated species mass balance at the liquid/gas interface (Eq. (4.13)), leads to:

$$\rho v Y_F - \frac{\mu}{Sc_F}\frac{dY_F}{dy} = \dot{m} \tag{4.18}$$

In order to express wall-laws in a turbulent boundary layer, the later equation need to be averaged. The advection term can be averaged as the following: $\overline{\rho v Y_F} = \overline{\rho v}\,\overline{Y}_F + \overline{(\rho v)' Y_F'}$. According to the averaged mass conservation equation: $\overline{\rho v} = \overline{\dot{m}}$. The term $\overline{(\rho v)' Y_F'}$ can be considered as the turbulent transport of the evaporated species which can be modeled using the eddy diffusivity assumption. As in the anisothermal turbulent boundary layer (section 3.1.2), the fluctuations of the molecular viscosity can be neglected. Thus, the averaged evaporated species governing equation reads:

$$\overline{\dot{m}}\,\overline{Y}_F - \left(\frac{\overline{\mu}}{Sc_F} + \frac{\mu_t}{Sc_t}\right)\frac{d\overline{Y}_F}{dy} = \overline{\dot{m}} \tag{4.19}$$

Assuming constant mean density and viscosity, wall-units can be used to express the wall-normal distance, which leads to:

$$\overline{\dot{m}}\left(\overline{Y}_F - 1\right) = \overline{\rho} u_\tau \left(\frac{1}{Sc_F} + \frac{\mu_t}{\overline{\mu}}\frac{1}{Sc_t}\right)\frac{d\overline{Y}_F}{dy^+} \tag{4.20}$$

The classical two-layers assumption is used: for small y^+,the molecular diffusion dominates over the turbulent one; starting form a certain transition distance $y^+_{tran,Y}$, only the turbulent diffusion is considered and the viscosity ratio is modeled using Eq. (3.17). So, after integration over the distance between the liquid/gas interface and the wall mesh cell center, the evaporation rate is expressed as:

$$\dot{m} = H_Y ln\left(\frac{1 - Y_{F,1}}{1 - Y_{F,s}}\right) \tag{4.21}$$

$$H_Y = \begin{cases} \frac{\rho_1 u_\tau}{y_1^+ Sc_F} & y_1^+ \leqslant y^+_{tran,Y} \\ \frac{\rho_1 u_\tau}{y^+_{tran,Y} Sc_F + \frac{Sc_t}{\kappa} ln\left(\frac{y_1^+}{y^+_{tran,Y}}\right)} & y_1^+ > y^+_{tran,Y} \end{cases} \tag{4.22}$$

O'Rourke and Amsden [74] proposed this model for RANS simulations and they assumed $y^+_{tran,Y} = 11.05$. This model was later used in the literature for RANS simulations [75–78] and recently for LES [79], always for ICE engine cases. However, this model shows a high dependency to the near wall grid size and to the transition distance $y^+_{tran,Y}$. In order to overcome this issue, Jiao and Reitz [77] suggested an *ad-hoc* solution by replacing the dimensionless wall distance by the wall-film thickness for the simulation of soot emissions from wall-films in GDI engine. In the sake of establishing a more universal wall-law, Desoutter [24] performed a DNS of a stationary evaporating wall-film in turbulent channel flow at five turbulence levels and mean evaporation rates and always with air/n-heptane mixture. Based on these results, he developed a set of dynamic, thermal and evaporated species mass wall-laws, as it will be presented in the following. Considering at first an incompressible boundary layer, the mean mass balance leads to $\overline{v} = \overline{v}_s$. A model constant C_U is introduced in the Prandtl mixing length formula (Eq. (3.16)) and the turbulent kinematic viscosity is expressed using:

$$\nu_t = \left(\frac{\kappa y}{C_U}\right)^2 \frac{\partial \overline{u}}{\partial y} \tag{4.23}$$

Thus, the momentum conservation equation expressed in wall units can be written as:

$$\frac{\partial u^+}{\partial y^+} + \left(\frac{\kappa y^+}{C_U}\frac{\partial u^+}{\partial y^+}\right)^2 = u^+ v_s^+ + 1 \tag{4.24}$$

In the linear sub-layer, the turbulent transport is neglected and the integration of the momentum equation leads to: $u^+ v_s^+ = exp\left(v_s^+ y^+\right) - 1$ which can be simplified for small values of y^+ to: $u^+ = y^+$. Starting

from a certain distance $y^+_{tran,Y}$, the turbulent transport dominates over the molecular one, and Eq. (4.24) is simplified into:

$$\left(\frac{\kappa y^+}{C_U}\frac{\partial u^+}{\partial y^+}\right)^2 = u^+ v_s^+ + 1 \tag{4.25}$$

which leads to the classical logarithmic wall function for the mean streamwise velocity:

$$u^+_{eff} = \frac{C_U}{\kappa} ln\left(\frac{y^+}{y^+_{tran,Y}}\right) + y^+_{tran,Y} \tag{4.26}$$

where the effective velocity u^+_{eff} is defined as:

$$u^+_{eff} = \frac{2}{v_s^+}\left[\sqrt{1+u^+v_s^+}-1\right] \tag{4.27}$$

In the laminar sub-layer, the approximation $u^+_{eff} = y^+$ still holds. As pointed out in section 3.1.2, this velocity transformation is analogous to the simplified van Driest velocity transformation in anisothermal flow (Eq. (3.46)) established by Nicoud and Bradshaw [57]. This analogy suggest that an incompressible wall flow subject to injection or suction has the same mean velocity profile as a low-Mach-number flow (with variable density) subjected to cooling or heating. Similarly to the momentum transfer, model constants C_T and C_Y are introduced to establish wall functions for the heat and mass transfer respectively. Effective temperature and evaporated species mass fraction are also defined as:

$$T^+_{eff} = \frac{2C_T Pr_t}{v_s^+}\left[\left(1+T^+v_s^+\right)^{1/2C_T Pr_t}-1\right] \tag{4.28}$$

$$Y^+_{F,eff} = \frac{2C_Y Sc_t}{v_s^+}\left[\left(\frac{\overline{Y}_F-1}{\overline{Y}_{F,s}-1}\right)^{1/2C_Y Sc_t}-1\right] \tag{4.29}$$

The effect of variable density and viscosity was taken into account by considering the LnKc transformations as the following:

$$\eta^+ = \frac{\nu_s}{\overline{\nu}}y^+, \qquad \overline{\phi}^+_{eff} = \frac{\overline{\rho}}{\overline{\rho}_s}\overline{u}^+_{eff}, \qquad \overline{\theta}^+_{eff} = \frac{\overline{\rho}}{\overline{\rho}_s}\overline{T}^+_{eff}, \qquad \overline{\zeta}^+_{eff} = \frac{\overline{\rho}}{\overline{\rho}_s}\overline{Y}^+_{F,eff} \tag{4.30}$$

Finally, the wall functions proposed by Desoutter [24] are expressed as:

$$\text{Dynamic:} \begin{cases} \overline{\psi}^+_{eff} = \eta^+ & \eta^+ \leqslant \eta^+_{tran,U} \\ \overline{\psi}^+_{eff} = \eta^+_{tran,u} + \frac{C_U}{\kappa} ln\frac{\eta^+}{\eta^+_{tran,u}} & \eta^+ > \eta^+_{tran,U} \end{cases} \tag{4.31}$$

$$\text{Thermal:} \begin{cases} \overline{\theta}^+_{eff} = Pr\,\eta^+ & \eta^+ \leqslant \eta^+_{tran,T} \\ \overline{\theta}^+_{eff} = Pr\,\eta^+_{tran,T} + \frac{C_U}{\kappa}\left[\frac{2C_T Pr_t + Pr\overline{v}_s^+\eta^+_{tran,T}}{2+\overline{v}_s^+\eta^+_{tran,T}}\right] ln\frac{\eta^+}{\eta^+_{tran,T}} & \eta^+ > \eta^+_{tran,T} \end{cases} \tag{4.32}$$

$$\text{Mass:} \begin{cases} \overline{\zeta}^+_{eff} = Sc\,\eta^+ & \eta^+ \leqslant \eta^+_{tran,Y} \\ \overline{\zeta}^+_{eff} = Sc\,\eta^+_{tran,Y} + \frac{C_U}{\kappa}\left[\frac{2C_Y Sc_t + Sc\overline{v}_s^+\eta^+_{tran,Y}}{2+\overline{v}_s^+\eta^+_{tran,Y}}\right] ln\frac{\eta^+}{\eta^+_{tran,Y}} & \eta^+ > \eta^+_{tran,Y} \end{cases} \tag{4.33}$$

The model parameters C_U,C_T, C_Y, $\eta^+_{tran,U}$, $\eta^+_{tran,T}$ and $\eta^+_{tran,Y}$ were fitted for each of the five DNS cases. Desoutter [24] concluded that the variation of C_U,C_T and C_Y never exceed 30% and proposed value ranges for each of theses model constants. However, the transition locations $\eta^+_{tran,U}$, $\eta^+_{tran,T}$ and $\eta^+_{tran,Y}$ varies considerably from one case to another. They increases with both density gradient and evaporation rate and ranges approximately between 7 and 15. As wall-laws in the case of mass transfer lack universality, evaporation models based on wall-laws will not be considered for the current work.

4.3.2.2 Semi-analytical solution

Semi-analytical solutions of mass transfer problems are based on the early works of Spalding [82]. They were developed at first to approximate the evaporation rate of droplets or wall-films using far-field quantities, and they were introduced later in the context of CFD. This modeling approach is derived in the following for wall-film evaporation in order to understand the main considered assumptions. For very small mass-flow rates from the interface, the velocity component v_s can be neglected, as also the advection terms in the transport equation (4.16), which leads to the following diffusion problem:

$$\frac{d}{dy}\left(\rho D_F \frac{dY_F}{dy}\right) = 0 \tag{4.34}$$

In this case, a complete analogy between heat and mass diffusion can be achieved in the boundary layer. This case is characterized by the fact that the mass-transfer rate $\dot{m} \to 0$ referred hereafter as "low mass transfer problem". If constant properties (constant density and diffusion) are also assumed, Eq. (4.34) will be linear for this special case and a mass transfer conductance g can be defined as:

$$\rho D_F \left.\frac{dY_F}{dy}\right|_s = g\left(Y_{F,\infty} - Y_{F,s}\right) \tag{4.35}$$

Combining Eq. (4.13) and Eq. (4.35) leads to:

$$\dot{m} = g\frac{Y_{F,s} - Y_{F,\infty}}{1 - Y_{F,s}} \tag{4.36}$$

A mass transfer driving force number B_M can be defined as it is classically used in droplets evaporation models:

$$B_M = \frac{Y_{F,s} - Y_{F,\infty}}{1 - Y_{F,s}} \tag{4.37}$$

and thus:

$$\dot{m} = gB_M \tag{4.38}$$

B_M is also commonly known as Spalding mass transfer number. It can be positive (evaporation) or negative (condensation), g is always positive and finite. So the case of $\dot{m} \to 0$ requires that $B_M \to 0$. When $B_M \to 0$, the mass transfer conductance will be denoted g^*:

$$g^* = \lim_{B_M \to 0} \frac{\dot{m}}{B_M} \tag{4.39}$$

The ratio g/g^* is strongly dependent on B_M, but only weakly dependent on other parameters. Kays and Crawford [38] used the heat/mass transfer analogy to evaluate the mass-transfer conductance. In mass transfer problem, the mixture composition may have a substantial influence on the transport properties, this is very much different from heat transfer problems without mass transfer, where the change in fluid properties is mostly small. Nevertheless, the constant-property solutions will be the starting point of the semi-analytical solution development.

Constant-property boundary layer for "low mass transfer problem"

The Nusselt number, which translates the ratio of convective to conductive heat transfer at the liquid/gas interface, is defined as:

$$Nu^* = \frac{h_c \mathrm{x}}{\lambda} = \frac{\mathrm{x}\left.\frac{\partial T}{\partial y}\right|_s}{T_\infty - T_s} \tag{4.40}$$

where x is a characteristic length scale. For a laminar boundary layer over a heated plate, the Nusselt number can be evaluated using the following correlation [38]:

$$Nu^* = 0.332 Pr^{1/3} Re_{\mathrm{x}}^{0.5} \tag{4.41}$$

The Sherwood number is the equivalent of the Nusselt in the mass transfer problem, and it is defined as:

$$Sh^* = \frac{g^* \mathrm{x}}{D_F} = \frac{\mathrm{x} \left. \frac{\partial Y_F}{\partial y} \right|_s}{Y_{F,\infty} - Y_{F,s}} \tag{4.42}$$

The * in the above equations denotes again that $B_M \to 0$ and $v_s \to 0$. All the governing equations and the boundary conditions have the identical structure for the temperature and the mass fractions. As a result, the dependence of the Sherwood on Re and Sc will be the same as the dependence of the Nusselt on Re and Pr:

$$Sh^* = 0.332\, Sc^{1/3} Re_x^{0.5} \tag{4.43}$$

hence,

$$\frac{Nu^*}{Sh^*} = \left(\frac{Pr}{Sc} \right)^{1/3} = Le^{-1/3} \tag{4.44}$$

In the turbulent constant-property boundary layer, and for $0.5 < Pr < 1.0$ and $5 \times 10^5 < Re_x < 5 \times 10^6$, the Nusselt number correlation becomes [38]:

$$Nu^* = 0.0287 Pr^{0.6} Re_x^{0.8} \tag{4.45}$$

So, generally:

$$\frac{Nu^*}{Sh^*} = \left(\frac{Pr}{Sc} \right)^{n} = Le^{-n} \tag{4.46}$$

with $n = 1/3$ for the laminar case and $n = 0.6$ for the turbulent case. Using the definitions of the Sherwood and Nusselt numbers (equations (4.40) and (4.42)), the mass transfer conductance in the "low mass transfer problem" can be deduced:

$$g^* = \frac{Sh^*}{Nu^*} \frac{\rho D_F h_c}{\lambda} = \frac{Sh^*}{Nu^*} Le^{-1} \frac{h}{c_p} \tag{4.47}$$

or also:

$$g^* = \frac{h_c}{c_p} Le^{-1+n} \tag{4.48}$$

If $Le = 1$, a complete analogy between heat and mass transfer exists within the boundary layer. This is because Le compares directly the thickness of the concentration to the thermal boundary layer.

"High mass transfer problem" in a laminar Couette flow

At this point, an expression for the ratio g/g^* need to be derived in order to use the "low mass transfer problem". The integration of the species mass conservation equation (Eq. (4.16)) considering the evaporated species mass balance at the liquid/gas interface (Eq. (4.13)), leads to:

$$\dot{m} Y_F + \rho D_F \frac{dY_F}{dy} = \dot{m} \tag{4.49}$$

Integrating again over the fuel mass boundary layer assuming constant properties leads to an expression of the mass evaporation rate in the form of:

$$\dot{m} = \frac{\rho D_F}{\delta_M} ln\left(1 + B_M\right) \tag{4.50}$$

with B_M the mass transfer driving force as defined in equation (4.37). Although the later equation gives an expression of the evaporation rate, the mass boundary layer thickness is not known *a priori*. To overcome this issue, it is possible to use the results obtained previously from the heat/mass transfer analogy in the case of "low mass transfer problem". From (4.50) and (4.38), one can get:

$$g = \frac{\rho D_F}{\delta_M} \frac{ln\left(1 + B_M\right)}{B_M} \tag{4.51}$$

The mass-transfer conductance g^* for the case of "low mass transfer problem" is derived from (4.39) and using L'Hospital's rule:

$$g^* = \lim_{B_M \to 0} \left(\frac{\rho D_F}{\delta_M} \frac{ln\left(1 + B_M\right)}{B_M} \right) = \frac{\rho D_F}{\delta_M} \tag{4.52}$$

Thus:

$$\frac{g}{g^*} = \frac{ln\left(1 + B_M\right)}{B_M} \tag{4.53}$$

Variable-property boundary layer for "High mass transfer problem"

The constant-property solution can be applied to variable-property application by making an empirical correction [38]. A molecular weight ratio is added to the expression (4.53):

$$\frac{g}{g^*} \left(\frac{W_\infty}{W_s} \right)^m = \frac{ln\left(1 + B_M\right)}{B_M} \tag{4.54}$$

with $m = 2/3$ for a laminar boundary layer and $m = 0.4$ for a turbulent boundary layer. All properties are otherwise evaluated at the far-field conditions.

Final expression

Finally, combining the equations (4.38) (4.48) and (4.54), the evaporation rate can be written as:

$$\dot{m} = \frac{h_c}{c_p} Le^{-1+n} \left(\frac{W_s}{W_\infty} \right)^m ln\left(1 + B_M\right) \tag{4.55}$$

It should be mentioned that this modeling approach was derived using instantaneous quantities, while, in the context of RANS simulation and LES, Reynolds-averaged and filtered quantities are used instead. Furthermore, the model is used with properties (Le, c_p) evaluated at the center of the wall cell instead of the far-field conditions. $Y_{F,1}$ is also used instead of $Y_{F,\infty}$ for the Spalding mass transfer number B_M. Dynamic and heat wall models which do not consider mass transfer are classically used with this modeling approach. The heat transfer coefficient, is evaluated using expression (4.5), with $q_{g \to l}^{model}$ evaluated using a wall heat transfer model. Thus, in the semi-analytical based evaporation model, the effect of turbulent transport is included implicitly through the modeled heat flux. Zhang et al. [73] assessed this modeling approach for RANS simulation of spray impingement and wall-film evaporation against experimental results. They showed that using Han and Reitz [58] wall heat transfer model leads to better results compared to the O'Rourke and Amsden [74] wall heat transfer model. The values $n = 1/3$ and $m = 0$ are the most used values in the literature [72, 73], meaning that laminar flow with constant properties are assumed.
An algebraic evaporation model based on semi-analytical solution is considered in this work for wall-modeled LES and the implemented formulation is the following:

$$\dot{m} = \frac{q_{g \to l}^{model}}{c_{p,1}\left(T_1 - T_s\right)} \left(\frac{Sc_F \lambda_1}{\mu_1 c_{p,1}} \right)^{-2/3} ln\left(\frac{Y_{F,1} - 1}{Y_{F,s} - 1} \right) \tag{4.56}$$

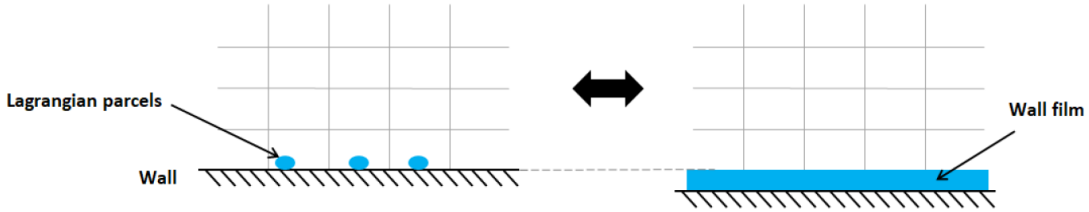

Figure 4.3: Lagrangian wall-film modeling

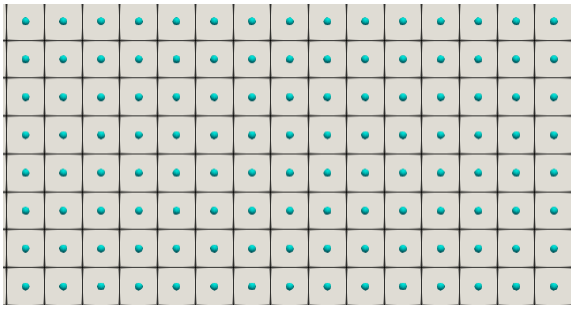

Figure 4.4: Wall-film parcels initialization

4.4 Wall-film numerical description

4.4.1 The Lagrangian approach

In ICE cases, the modeling of the liquid phase of the wall-film is closely related to spray modeling. The Lagrangian approach is generally selected for engine cases considering its cpu efficiency. This approach is also used during this work for the description of the wall-film. The liquid phase is divided into parcels where each parcel is tracked as a material point in the Lagrangian reference frame and interacts with other parcels and with the surrounding flow. When a parcel is located in a wall mesh cell, it will be accounted for as part of the wall-film and the liquid/gas interface will coincide with the computational domain boundary, as shown in Figure 4.3. It is assumed that the wall-film attached to each wall mesh cell is uniformly distributed over its boundary face. The film thickness δ_{film} is computed as:

$$\delta_{film} = \frac{\sum_{p \in f} \boldsymbol{V}_p}{\boldsymbol{A}_f} \tag{4.57}$$

where $\boldsymbol{V}_p$ is the volume of parcel p computed from its mass and the liquid density, $\boldsymbol{A}_f$ is the area of the boundary face, and the summation is overall all particles located on the boundary face f. The wall-film thickness may vary discretely from one wall cell to another depending on the wall-film formation and evaporation. In engine cases, the formation of the wall-film and its initial characteristics (wetted area, shape, thickness, temperature, ...) depend on the spray/wall modeling step. Film formation and spreading have a high influence on the evaporation dynamic. Maligne and Bruneaux [83] noticed experimentally that wall-films with discrete pocket structure have higher evaporation rate than wall films with continuous structure. The spray/wall modeling is out of the scope of this thesis and the wall-film will be always initialized with uniform parcels distribution on the walls. Figure 4.4 shows the film initialization on a wall boundary with a single Lagrangian parcels (in blue) in each wall mesh cell. This initialization procedure was specifically developed for the purpose of this work.

4.4.2 Numerical coupling between the liquid and gas phases

As the numerical coupling between the liquid and the gas phases has been already implemented in the software, the momentum, heat and mass transfer with the wall-film have been introduced as additional source terms for the gas governing equations of the wall mesh cell rather than boundary conditions:

- Momentum source term in the wall normal direction: $S_{mom} = \frac{\dot{m}}{dt}$
- Energy source term: $S_e = (h_{s,F}\dot{m} - q_{g\rightarrow l})\,\frac{\boldsymbol{A}_f}{\boldsymbol{V}_f}$
- Evaporated species mass source term: $S_{mass} = S_F = \dot{m}\frac{\boldsymbol{A}_f}{\boldsymbol{V}_f}$

where $\dot{m}$ and $q_{g\rightarrow l}$ are computed using either the wall-refined or wall-modeled formulations.

4.4.3 Resolution of the temperature profile in the liquid phase

As mentioned in section 4.2, the liquid temperature is solved only along the wall normal direction and Eq. (4.2) is its governing equation. Several methods can be considered to solve this equation. The easiest method is to assume a bi-linear temperature profile as it was done by O'Rourke and Amsden [74]. Although, this method does not require high computational cost, Zeng and Lee [84] have shown by scale analysis that the characteristic heat conduction time is as long as film lifetime, which requires a more detailed method than a bi-linear temperature profile. Second-order [81] and third-order [68, 73, 84] polynomials were also used. They succeeded to well capture the temperature profile with a relatively low additional computational cost. The numerical discretization of the energy diffusion equation allow to solve in details the temperature inside the film, but with higher computational cost [70, 75]. Desoutter [24] compared two methods in 1D simulation of flame-film interaction: an integral approach based on a third-order polynomial and a finite difference numerical discretization. He noted that the integral approach does not allow to capture all the heating phases, nevertheless it yields similar results as the ones given by the numerical discretization for a 1D flame-film interaction simulation. Recently, an analytical method was proposed in the literature [72, 80, 85, 86]. This method allows to accurately capture film heating dynamic with a low computational cost.

The selected method

The selected method is a finite volume discretization method provided by CONVERGE. This method is adapted from the temperature profile resolution for Lagrangian droplets as described by Sazhin et al. [87]. The liquid density ρ_l and the liquid heat capacity $c_{p,l}$ are considered uniform along the wall-film thickness and computed at the mass averaged liquid temperature. The film thickness is always discretized into a fixed number of nodes, 10 nodes during all the work presented in this manuscript. At initialization, the liquid temperature is set at the wall temperature along all the wall-film thickness. This initialization procedure may lead to a temperature discontinuity at the liquid/gas interface, which is non-physical. During the first iterations, the wall-film temperature will quickly evolve to ensure the continuity.

Chapter 5

Assessment of algebraic wall-film evaporation models

Contents

As detailed in the previous chapter, only evaporation models based on the semi-analytical solution are retained for wall-modeled cases. Although this approach is widely used for wall-film evaporation in practical ICE cases[72, 73, 80], its validation and its dependence on the wall heat models and wall mesh cell size remains limited, especially for LES. To our best knowledge, the dependence on the wall heat model was only investigated in the work of Zhang et al. [73]. They showed that using Han and Reitz [58] wall heat model leads to better results compared to the O'Rourke and Amsden [74] wall heat model in RANS simulation of spray impingement and wall-film evaporation. This chapter is dedicated to the assessment of this algebraic modeling approach in steady and transient wall-film evaporation in turbulent channel flow. The steady evaporation allows in a first step to assess the wall-film modeling in simplified problem where heat and mass transfer are decoupled at the liquid/gas interface. The transient evaporation allows the assessment in a configuration of real practical wall-film evaporation.

5.1 Evaporating wall-film in a stationary turbulent channel flow

The algebraic evaporation model based on the semi-analytical solution is first assessed in stationary turbulent channel flow. In the following, the case setup is presented. Wall-refined formulation of the evaporation rate was not originally available in CONVERGE and it is implemented for the purpose of this work. Its accuracy and its validity as a reference for comparison against wall-modeled results are assessed by comparison against the DNS results of Desoutter [24]. Then, wall modeled cases specific to this study are performed in order to evaluate the evaporation rate modeled using Eq. (4.56) with different wall heat closures against wall-refined results.

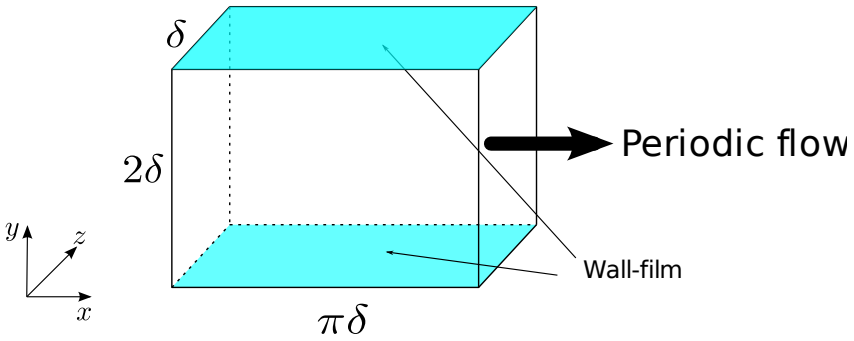

Figure 5.1: Case configuration for the stationary wall-film evaporation.

5.1.1 Case setup

Configuration

The configuration is similar to the one considered by Desoutter [24] to conduct the DNS of turbulent boundary layer over an evaporating wall-film. As illustrated in Figure 5.1, the wall-film covers all the upper and bottom wall surfaces in a minimal channel flow configuration. The wall-film is considered sufficiently thick so that its thickness and surface temperature could be set as constant during the simulation, allowing a statistically steady evaporation configuration.

Mass source term

In addition to the added momentum and energy source terms as for stationary anisothermal channel flow, and in order to compensate for the effect of evaporation, a mass source term is also added to the evaporated species mass fraction equation and it is expressed as [24]:

$$S_M = \langle \rho \rangle_{x,y=\delta,z} \frac{\left(Y_{Ftarget} - \left\langle \frac{\rho Y_F}{\rho} \right\rangle_{x,y=\delta,z} \right)}{dt_t} \tag{5.1}$$

where $Y_{F,target}$ is the target evaporated species mass fraction in the center of the channel, $\langle\rangle_{x,y=\delta,z}$ denotes the spatial average operator over a plane in the center of the channel, and $dt_t \approx \delta/2u_\tau$ is a characteristic time of turbulent diffusion.

5.1.2 Validation of wall-refined evaporation model

In order to validate our implementation of the wall-refined formulation of the evaporation rate in CONVERGE, a case from Desoutter [24], for which DNS results are available, is first performed.

Conditions

In this case, the mixture is air/n-heptane (C7H16) at atmospheric pressure. The film surface temperature is set to 309.4K, the target temperature and fuel mass fraction at the center of the channel are $T_{target} = 400K$ and $Y_{F,target} = 0.1$ respectively. The momentum source term was set in order to target a mean streamwise velocity of $50m.s^{-1}$, corresponding to $Re \approx 2500$. The mesh characteristics and the actual targeted conditions are given in Table 5.1. For a given case condition, the fuel mass fraction at the wall-film surface $Y_{F,s}$ (expression (4.10)) is constant in time and space and it is highly dependent on the case pressure and on the used $P_{v,F}$. As mentioned in Section 4.3, $P_{v,F}$ is tabulated in this work with respect to temperature based on Clausius-Clapeyron relation, which does not necessary lead to same numerical values as in the work of Desoutter [24]. In order to avoid any differences related to $Y_{F,s}$ evaluation, $Y_{F,s} = 0.3$ was imposed in the present study as obtained in the reference computation. However, the numerical methods and the species

	Mesh	Target conditions			Results		
	Δy_1^+	$\overline{u}_c$ $(m.s^{-1})$	$\overline{T}_c$ (K)	$\overline{Y}_{F,c}$	Re_τ	$\overline{q}_{g\to l}$ $(kW.m^{-2})$	$\overline{\dot{m}}$ $(g.m^{-2}.s^{-1})$
Desoutter [24]	0.92	48.2	401.9	0.097	242	17.2	28.9
present wall-refined	3.21	51.3	395.8	0.101	237	16.2	39.2

Table 5.1: Cases characteristics and results for local-gradient evaporation model validation. Δy_1^+: Dimensionless wall cell size in the wall normal direction; $\overline{u}_c$: Mean streamwise velocity in the center of the channel; $\overline{T}_c$: Mean temperature in the center of the channel; $\overline{Y}_{F,c}$: Mean mass fraction of the evaporated species in the center of the channel; Re_τ: Reynolds number based on wall shear velocity; $\overline{q}_{g\to l}$: Mean heat flux at the gas/liquid interface; $\overline{\dot{m}}$: Mean evaporation rate.

mass diffusion flux modeling considered for the DNS of Desoutter [24] are different from the ones used for this work. In the work of Desoutter [24]:

- **Numerical methods:** The AVBP [88] code was used with a third-order time and space Taylor-Galerkin scheme [89].
- **Species mass diffusion flux modeling:** The Hirschfelder and Curtiss approximation was used to model the species mass diffusion flux, while the Fick's law is considered in the present work. The diffusion coefficients were modeled in the same way as the current work: $\rho D_k = \mu / Sc_k$ with a constant set of Schmidt numbers for all the species. The same values of the Schmidt numbers are also used for this work: $Sc_{O2} = 0.6$; $Sc_{N2} = 0.54$; $Sc_{C7H16} = 1.83$. The differential diffusion of non-evaporating species was also considered in the evaporation rate expression while it is neglected in the present work.

Results and discussion

Figure 5.2 shows the instantaneous filtered mass fraction field of the evaporated species on the side boundaries and the distribution of the evaporation rate in the bottom wall. Desoutter [24] and this work results are summarized in Table 5.1 and Figure 5.3. The normalized mean streamwise velocity, the normalized temperature and the fuel mass fraction and their fluctuation profiles agree relatively well with the reference results. The Re_τ of the two computations are close with imposing U_c, showing that the shear stress at the liquid/gas interface is well predicted. The heat flux transferred to the liquid phase is underestimated by about 6% which is acceptable given the differences in the mesh grid resolution at the wall. However, the evaporation rate is over-estimated by about 35%. This error on the mass transfer is likely due to the differences on the species mass diffusion flux modeling between the two computations. Eq. (2.20) shows mathematically the differences between the Hirschfelder and Curtiss approximation and Fick's law. In order to get an idea on the importance of the omitted molecular weight gradient in the wall normal direction, a fuel mass diffusion error is defined as:

$$\epsilon_{Y_F V_F} = \left| \frac{\frac{Y_F}{W}\frac{\partial W}{\partial y}}{\frac{\partial Y_F}{\partial y} + \frac{Y_F}{W}\frac{\partial W}{\partial y}} \right| \tag{5.2}$$

Figure 5.4 shows $\epsilon_{Y_F V_F}$ on an instantaneous filtered field of the present wall-refined computation. The error ranges from 6% in the center of the channel to about 22% at the liquid/gas interface. So the molecular weight gradient has a relatively a high importance on the species mass diffusion above an evaporating wall-film, and thus on the evaporation rate.

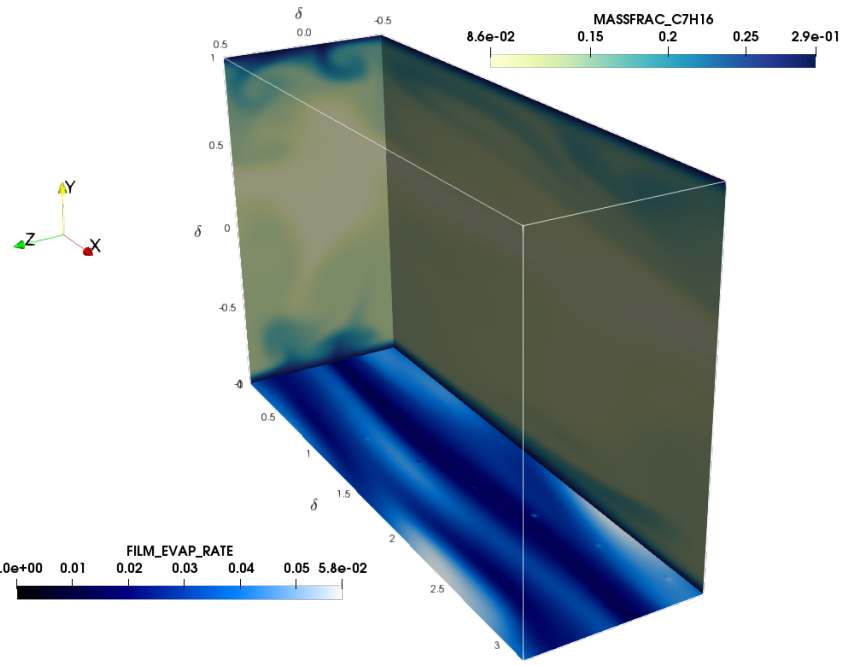

Figure 5.2: Snapshot of wall-film evaporation in stationary turbulent channel flow. Evaporated species mass fraction at side boundaries and evaporation rate at bottom wall.

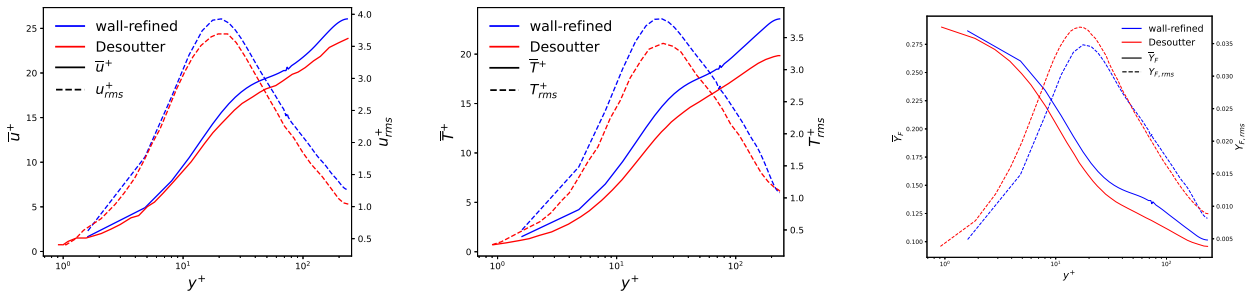

(a) $\overline{u}^+$ and u^+_{rms} **(b)** $\overline{T}^+$ and T^+_{rms} **(c)** $\overline{Y}_F$ and Y^+_{rms}

Figure 5.3: Validation case of the wall-refined evaporation model.

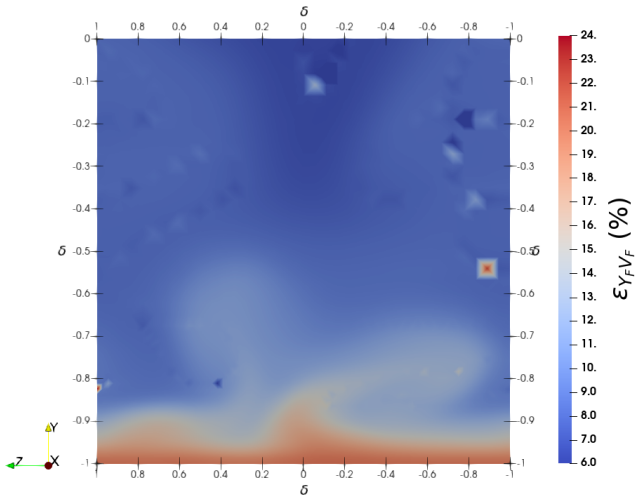

Figure 5.4: A postiriori evaluation of the error on the mass diffusion flux modeled by Fick's law instead of Hirschfelder and Curtiss approximation shown in half $y - z$ slice.

Conclusion

The wall-refined case succeeded in predicting the shear stress and the heat flux at the liquid/gas interface. However, this validation step highlights that considerable errors exist for the evaporation rate and for the species mass diffusion above the wall-film in general. These errors are mainly due to the use of Fick's law for mass diffusion in a highly stratified mixture. Although, the wall-refined results are not precise on the evaporation rate, they will be considered in the following as reference for the assessment of algebraic wall models. This assumption seem reasonable because wall-refined and wall-modeled cases both use Fick's law in this study.

5.1.3 Assessment of the algebraic evaporation model

The algebraic evaporation model based on the semi-analytical solution (Eq. (4.56)) is assessed against wall-refined results. As the film temperature and thickness are set constant and the evaporation is steady, the heat and mass transfer problems are decoupled at the liquid/gas interface. This decoupling means that the evaporation will not depend on the liquid phase energy variation. This allows to study the direct dependence of the evaporation rate modeling on the wall heat flux modeling. The assessment is performed with three wall heat models: *O'Rourke-Amsden*, *GruMo-UnoMORE* and *Angelberger*. The shear stress on the liquid/gas interface is computed using *Werner&Wengle* dynamic wall model in all the wall-modeled cases.

Conditions

The considered mixture for this assessment is air/iso-octane at atmospheric pressure. The imposed wall temperature is 370K which is below the saturation of iso-octane at atmospheric pressure ($T_{sat} = 372.3$K), ensuring to stay in the wetting regime. The energy and mass source terms are set to keep a mean temperature $T_{target} = 600K$ and a mean evaporated species mass fraction $Y_{F,target} = 0.2$ at the center of the channel. The used Schmidt numbers for the species diffusion are the following: $Sc_{O2} = 0.6$; $Sc_{N2} = 0.54$; $Sc_{C8H18} = 2.0$. The momentum source is set here to target a mean mass flow rate $\langle \rho u \rangle$, in the channel defined as:

$$\langle \rho u \rangle = \left\langle \frac{\int_y \int_z \overline{\rho u} dy dz}{\int_y \int_z dy dz} \right\rangle_x$$

In these simulations, mean mass flow rates were targeted instead of Re_τ. Two mean mass flow rates were targeted: a low turbulence condition with $\langle \rho u \rangle = 7.35\, kg.m^{-2}.s^{-1}$ corresponding in the wall-refined case to

		Mesh	Target conditions			Results						
		Δy_1^+	$\langle \rho u \rangle$ $(kg.m^{-2}.s^{-1})$	$\overline{T}_c$ (K)	$\overline{Y}_{F,c}$	Re_τ	$\overline{\tau}_s$ $(kg.m^{-1}.s^{-2})$	ϵ_τ (%)	$\overline{q}_{g\to l}$ $(kW.m^{-2})$	ϵ_q (%)	$\overline{\dot{m}}$ $(g.m^{-2}.s^{-1})$	$\epsilon_{\dot{m}}$ (%)
low	wall-refined	3.5	7.35	591	0.21	572	0.100		3.29		66.2	
	O'Rourke-Amsden	18.1	7.31	590	0.19	651	0.127	+27	5.32	+62	39.7	-40
	GruMo-UnoMORE	18.2	7.27	591	0.19	655	0.129	+29	5.32	+62	39.6	-40
	Angelberger	17.7	7.28	591	0.20	638	0.122	+22	5.41	+64	39.9	-40
high	wall-refined	3.6	17.08	598	0.20	1187	0.423		7.12		115.3	
	O'Rourke-Amsden	39.4	16.88	586	0.21	1417	0.594	+40	10.91	+53	67.3	-42
	GruMo-UnoMORE	42.6	17.32	593	0.20	1534	0.697	+65	9.61	+35	49.4	-57
	Angelberger	42.4	17.20	591	0.21	1525	0.689	+63	9.98	+40	52.5	-54

Table 5.2: Cases characteristics and results for the assessment of stationary film evaporation modeling. Δy_1^+: Dimensionless wall cell size in the wall normal direction; $\langle \rho u \rangle$: Mean mass flow rate; $\overline{T}_c$: Mean temperature in the center of the channel; $\overline{Y}_{F,c}$: Mean mass fraction of the evaporated species in the center of the channel; Re_τ: Reynolds number based on wall shear velocity; $\overline{\tau}_s$: Mean shear stress at the liquid/gas interface; $\overline{q}_{g\to l}$: Mean heat flux at the gas/liquid interface; $\overline{\dot{m}}$: Mean evaporation rate; ϵ: Relative error with respect to wall-refined case.

$Re_\tau = 572$ and $Re \approx 5400$; and a high turbulence condition with $\langle \rho u \rangle = 17.08\, kg.m^{-2}.s^{-1}$ corresponding in the wall-refined case to $Re_\tau = 1187$ and $Re \approx 12600$.

Results and discussion

Table 5.2 summarizes the dimensionless near wall mesh cell height, the mean mass flow rates, mean temperatures $\overline{T}_c$ and evaporated species mass fractions $\overline{Y}_{F,c}$ at the center of the channel for each case. The wall-modeled $\langle \rho u \rangle$ agrees with the wall-refined one within 2% for both turbulence conditions. $\overline{T}_c$ is within 0.2% in the low turbulence condition and within 2% in the high turbulence condition. $\overline{Y}_{F,c}$ is within 5% for both conditions. Table 5.2 also summarizes the mean shear stresses on the film surface $\overline{\tau}_s$, the mean heat fluxes $\overline{q}_{g\to l}$, the mean evaporation rates $\overline{\dot{m}}$ and their deviations from the wall-refined reference.

Errors on the shear stress

The wall-modeled simulations over-estimate the mean shear stress on the film surface with errors ranging from 22% to 29% for the low turbulence condition, and ranging from 40% to 65% for the high turbulence condition. Figure 5.5 shows the mean streamwise velocity and fluctuation without normalization. As the mean mass flow rate was targeted, the mean velocity profiles of the different cases are always in agreement. All the wall-modeled cases give also similar streamwise velocity fluctuations. The effect of the errors on the shear stress can be seen on the mean streamwise velocity profiles when they are plotted with the wall units (u^+, y^+) in Figure 5.6. So, the *Werner&Wengle* wall model fails in predicting accurately the shear stress and the near wall physics above an evaporating wall-film.

Errors on the heat flux and the evaporation rate

It is interesting to compare first the wall-refined results at the two turbulence conditions: the Re_τ is almost doubled from the low to the high turbulent condition, and the evaporation rate increases by 74%. All the wall-modeled simulations at low turbulence condition predict similar evaporation rate and heat flux transferred to the wall-film. The evaporation rate is about 40% smaller that the wall-refined result and the heat flux is about 62% higher than the wall-refined result. At high turbulence condition, there are slight differences between the wall-modeled cases, around 50% smaller than the wall-refined result on the evaporation rate, and around 40% higher on the heat flux. Figures 5.7 and 5.8 show the mean temperature and evaporation species mass fraction profiles and their fluctuations plotted without normalization. For the temperature profiles, the

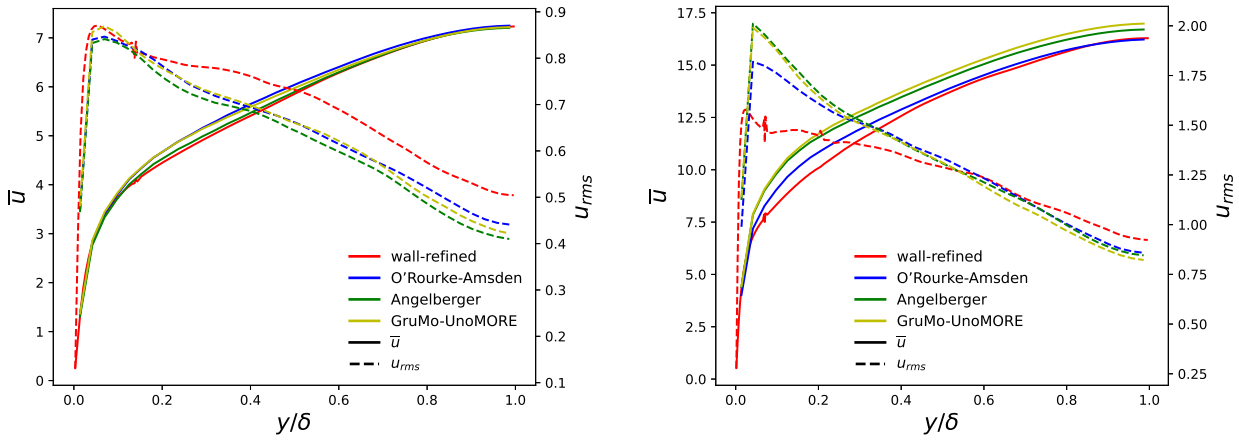

(a) At $Re_\tau = 550$ **(b)** At $Re_\tau = 1100$

Figure 5.5: Mean streamwise velocity and fluctuations in the case of an evaporating wall-film in stationary channel flow.

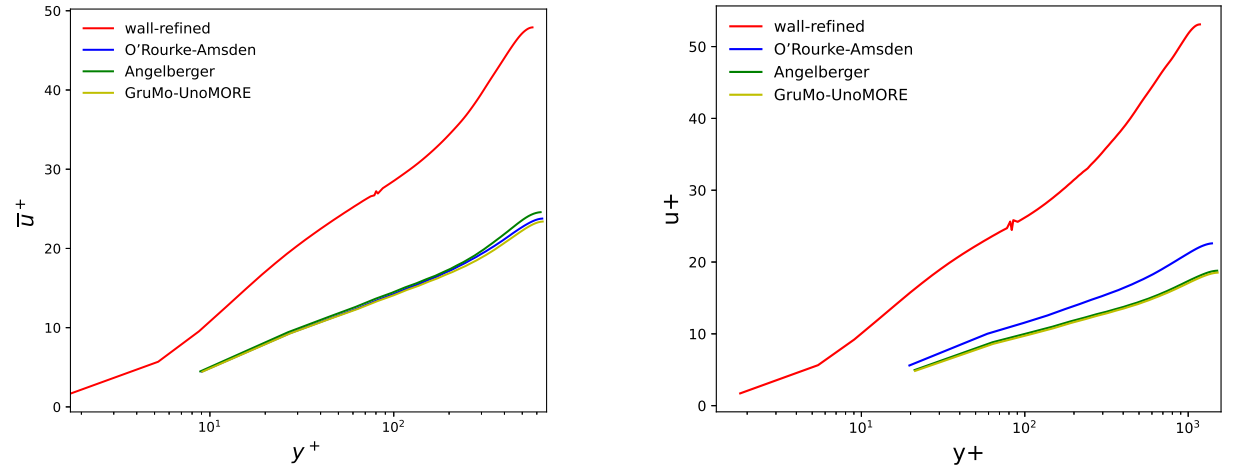

(a) At $Re_\tau = 550$ **(b)** At $Re_\tau = 1100$

Figure 5.6: Normalized mean streamwise velocity in the case of an evaporating wall-film in stationary channel flow.

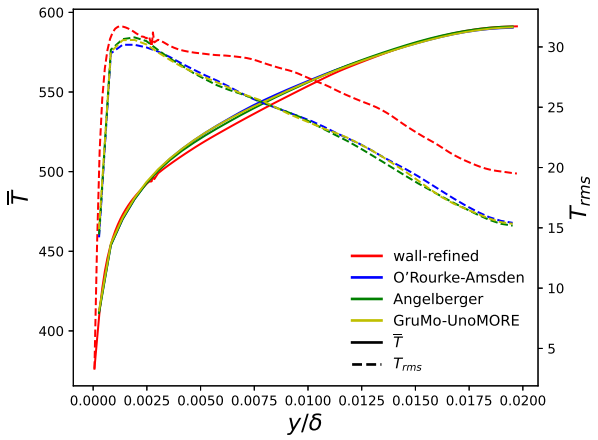

(a) At $Re_\tau = 550$

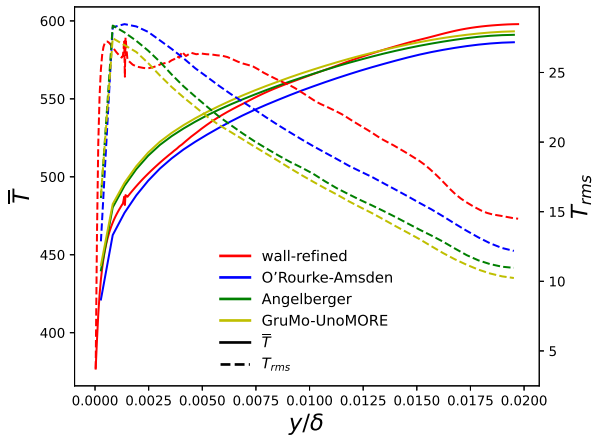

(b) At $Re_\tau = 1100$

Figure 5.7: Mean temperature and fluctuations in the case of an evaporating wall-film in stationary channel flow.

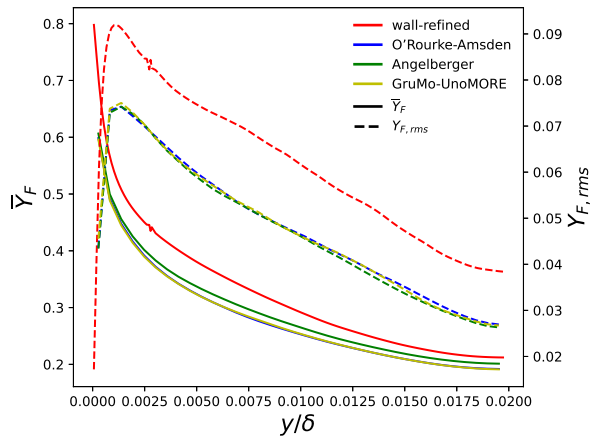

(a) At $Re_\tau = 550$

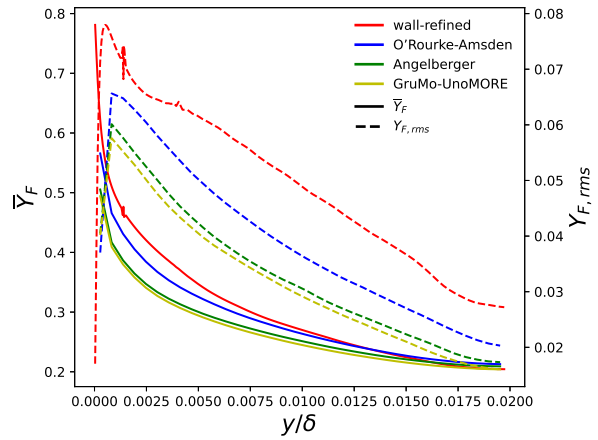

(b) At $Re_\tau = 1100$

Figure 5.8: Mean mass fraction of evaporated species and fluctuations in the case of an evaporating wall-film in stationary channel flow.

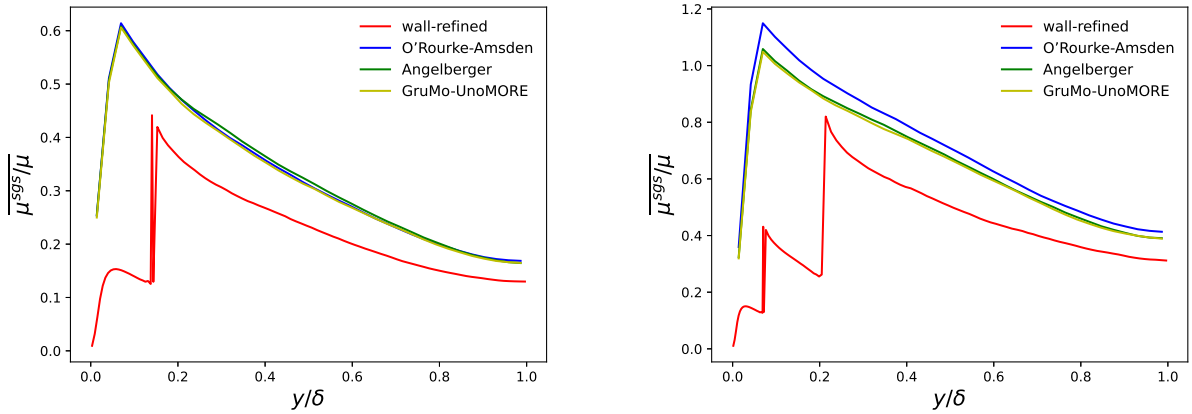

(a) At $Re_\tau = 550$ **(b)** At $Re_\tau = 1100$

Figure 5.9: Mean sub-grid scale to the molecular viscosity ratio in the case of an evaporating wall-film in stationary channel flow.

differences between the wall-modeled and wall-refined simulations can be noticed mainly on the fluctuations. For the evaporated species mass fraction, differences between the wall-modeled and wall-refined simulations can be noticed on both mean and fluctuation profiles.
It can be seen also that a higher error on the heat flux leads to a smaller error on the evaporation rate and vice versa. This result can be explained by the linear dependence of $\dot{m}$ on $q_{g\to l}$ in the formulation of the evaporation rate itself (Eq. (4.56)). This linear dependency between the evaporation rate and the heat flux is easy to notice as heat and mass transfer problems are decoupled in the stationary evaporation.
This assessment shows that the wall-modeled case under-predict the evaporation rate with an error of 40-50% with respect to the wall-refined results, while it was concluded previously that the wall-refined case over-predict the evaporation rate with an error of about 40% with respect to the DNS of Desoutter [24]. It is important to point out that this observation does not mean that the algebraic wall models behave better than the wall-refined formulations and the two errors are not related.

Analysis of the wall-refined instantaneous flow field

The wall-refined simulations also provide a detailed description of the turbulent boundary layer. The mean sub-grid scale to the molecular viscosity ratios of the different cases are shown in Figure 5.9 for both turbulence conditions. The jumps of the viscosity ratio in the wall-refined cases corresponds to the transition to a different mesh refinement level. The viscosity ratio in the wall-refined simulations peaks at 0.4 in the low turbulence condition and at 0.8 in the high turbulence condition. Giving this relatively low viscosity ratios, most of the turbulent structures might be considered as solved, and thus, wall-refined LES solutions might be interpreted as reference DNS solutions, at least under the numerical framework used. The analysis of the mean and correlation quantities give insights about the validity of the simplified Reynolds averaged balance equations used for model development. It should be pointed out that sampling convergence of the results was not checked and only qualitative conclusions should be drawn from this analysis.

Total mass balance: Using the assumptions considered in Chapter 4 (stationary two-dimentinal turbulent boundary layer over an evaporating wall-film), the Reynolds-averaged total mass balance in the turbulent boundary layer reads: $\overline{\rho v} = \overline{\dot{m}}$. This balance allowed to substitute $\overline{\rho v}$ with $\overline{\dot{m}}$ during the derivation of the wall-film evaporation model. Figure 5.10 shows the variation of the ratio $\overline{\rho v}/\overline{\dot{m}}$ along the channel half height for the two turbulence conditions. According to the average total mass balance, this ratio should be equal

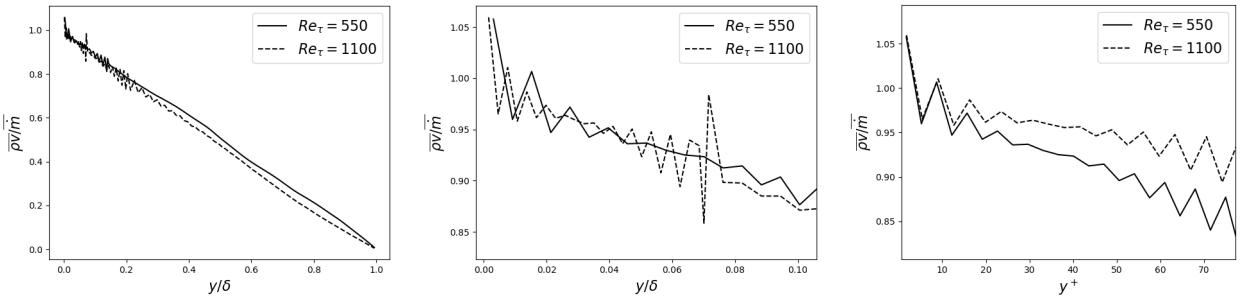

(a) **(b)** **(c)**

Figure 5.10: Variation of $\overline{\rho v}/\overline{\dot{m}}$ in the wall normal direction in the wall-refined cases.

to unity all along the boundary layer. At the liquid/gas surface the balance is verified, then $\overline{\rho v}$ decreases linearly until it vanishes in the center of the channel. This result is expected for a channel flow configuration as the two wall-films evaporates facing each other and the wall normal momentum is balanced in the center of the channel. In the wall-modeled cases, the modeled evaporation rate is computed at the center of the first wall mesh cell, thus, the validity of the balance equations should be mainly verified close to the liquid/gas interface. Figure 5.10 shows also the the variation of the ratio $\overline{\rho v}/\overline{\dot{m}}$ for $y < 0.1\delta$ and $y^+ < 70$. $\overline{\rho v}/\overline{\dot{m}}$ stays larger than 0.9 up to $y = 0.08\delta$ or up to $y^+ = 50$ for the two turbulence conditions.

Evaporated species mass balance: Again using the assumptions considered in Chapter 4, the Reynolds-averaged evaporated species mass balance reads:

$$\overline{\rho v}\,\overline{Y_F} + \overline{(\rho v)' Y_F'} - \overline{\frac{\mu}{Sc_F}\frac{\partial Y_F}{\partial y}} = \overline{\dot{m}} \tag{5.3}$$

The molecular viscosity fluctuations can be neglected. Using $\overline{\rho v} = \overline{\dot{m}}$ and normalizing by the mean evaporation rate, the later equality becomes:

$$\underbrace{\overline{Y_F}}_{\text{I}} + \underbrace{\frac{\overline{(\rho v)' Y_F'}}{\overline{\dot{m}}}}_{\text{II}} \underbrace{- \frac{\overline{\frac{\mu}{Sc_F}\frac{\partial \overline{Y_F}}{\partial y}}}{\overline{\dot{m}}}}_{\text{III}} \underbrace{-1}_{\text{IV}} = 0 \tag{5.4}$$

In the following, the analysis of the budgets will be focused only near the wall-film for $y^+ < 70$. Figure 5.11 shows the variation of each term, as well as the sum of all the terms, along the normalized distance from the wall. The mean evaporated mass fraction, term (I), shows a strong variation at the liquid/gas interface, then a linear decrease toward the targeted mass fraction at the center of the channel ($\overline{Y}_{F,c} \approx 0.2$). The variation of terms (II) and (III) is almost identical for the two turbulence conditions when they are plotted with respect to y^+. The turbulent species transport, term (II), is zero at the liquid/gas interface and it increases to reach a plateau starting from $y^+ \approx 50$, representing about 40% of the species mass balance gain. It is interesting also to mention that the molecular diffusion, term (III), represents at most 8% of the species mass balance loss at about $y^+ = 6$, then it decreases and became negligible starting from $y^+ \approx 50$. The sum of all the terms shows that the considered species mass balance lacks about 20% of its budget at the liquid/gas interface, then about 10% of its budget starting from $y^+ \approx 20$. It is interesting to mention that the solved species mass fraction transport equation (Eq. (2.37)) includes the effect of differential diffusion through the collection velocity. However, the evaporated species mass balance considered the modeling (Eq. (5.3)) does not include the effect of differential diffusion, which might explain the obtained error close to the liquid/gas interface.

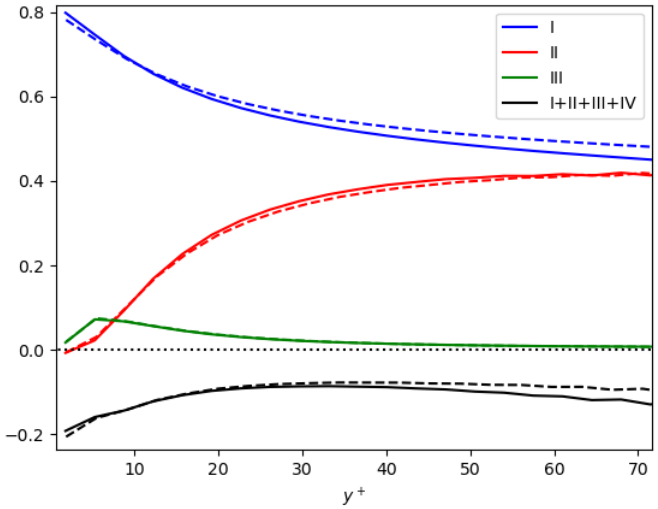

Figure 5.11: Variation of the evaporated species mass balance in the wall normal direction in the wall-refined cases. Notations are defined in Eq. (5.4). $Re_\tau = 550$ in solid line, $Re_\tau = 1100$ in dashed line.

Condition name	Initial Re_τ	$T_w(K)$	Initial $\delta_{film}(\mu m)$
`Base`	550	370	20
`ThickFilm`	550	370	**40**
`ColdWall`	550	**350**	20
`HighTurb`	**1100**	370	20

Table 5.3: Parameters variation for transient evaporation simulations.

5.2 Transient wall-film evaporation in turbulent channel flow

The wall-film thickness and surface temperature were set constant in the previous assessment, allowing to assess the direct dependence between the evaporation rate modeling and wall heat flux modeling. The transient response of wall-film thickness and temperature is considered in the wall-film evaporation in turbulent channel flow. This configuration is more representative of real practical wall-film evaporation as the heat and mass transfer problems are coupled. The sensitivity of the results to the initial wall-film thickness and to the wall temperature can also be studied in this configuration in addition to the sensitivity to the flow turbulence. In the following, the case setup and the simulated conditions will be presented. The wall-refined results will be first discussed and the sensitivity to parameters variation will be highlighted. Four conditions were considered to study the sensitivity to parameters variation, as illustrated in Table 5.3. The `Base` condition is initialized with a turbulent anisothermal flow with $Re_\tau \approx 550$ ($Re \approx 6000$), the wall temperature is fixed at 370K and the initial wall-film thickness at $20\mu m$. The initial wall-film thickness is doubled in the `ThickFilm` condition. The wall temperature, and thus the initial wall-film temperature as well, is decreased by 20K in the `ColdWall` condition. The initial turbulence was also varied using an initial map for the gas phase with $Re_\tau \approx 1100$ ($Re \approx 13500$) in the `HighTurb` condition. Then, the evaporation model based on the semi-analytical solution is assessed in the same conditions and with different wall heat models.

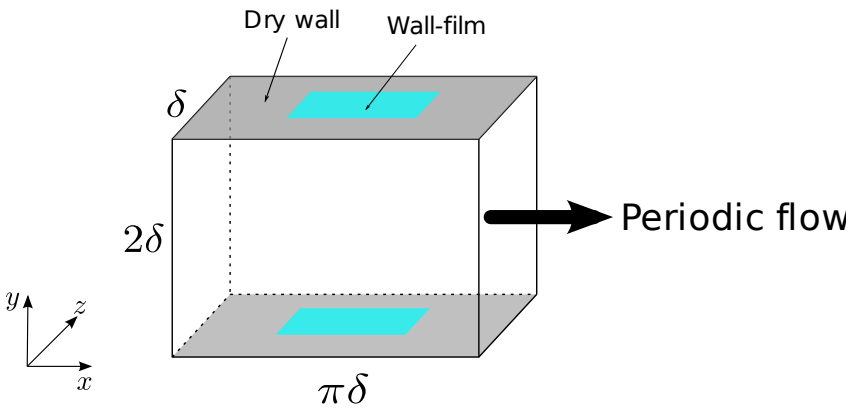

Figure 5.12: Minimal channel flow configuration with transient wall-film evaporation.

5.2.1 Cases setup

Configuration

Figure 5.12 shows the minimal channel flow configuration considered for the transient wall-film evaporation. No source term is applied in this case and the liquid mass will be completely added to the gas phase. The wall-film is initialized only on a portion of the upper and bottom walls surface, while the remaining surface stays in dry wall condition with a fixed temperature.

Initialization of the gas phase

The gas phase is initialized from a preliminary stationary turbulent channel flow simulation with thermal stratification and uniform composition, similar to the cases previously presented in section 3.2.3. The composition is a mixture of air/iso-octane at equivalence ratio 0.8 and pressure equal to 1.5 bars. The target mean temperature in the center of the channel is always set at 600K. The wall temperature and the targeted Re_τ are given for each case in Table 5.3. It should be noted that these preliminary simulations are always wall-refined and the same instantaneous filtered solution is later used for the initialization of both wall-refined and wall-modeled cases.

Initialization of the liquid phase

Wall-film thickness is initially uniform with all parcels distributed equally over the wetted surface and sharing the same mass, composition and temperature. The wall-film is initialized over about 9% of the walls surface and has approximately the same rectangular shape and aspect ratio as the channel walls. The wall-film thicknesses of each case are given in Table 5.3. The liquid temperature along the wall-film thickness is initialized at the wall temperature, which is not representative of practical cases.

5.2.2 Wall-refined results

Wall-refined formulations were used for momentum and heat transfer with the dry wall (Expressions (3.19) and (3.55)), and also for momentum, heat and mass transfer with the liquid/gas interface (expressions (4.1), (4.4) and (4.15)). Mesh embedding was adopted near the wall to ensure $y_1^+ < 1.6$ during the wall-film evaporation time as shown in Figure 5.13. The wall-film needs 47ms to completely evaporate in the `HighTurb` condition. Figure 5.14 shows the instantaneous filtered fields of the evaporated species mass fraction in the

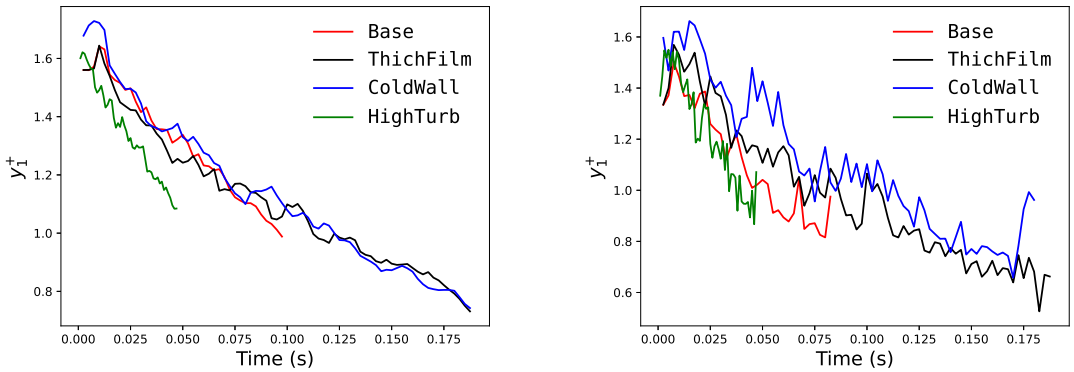

(a) Over the dry wall **(b)** Over the wall-film

Figure 5.13: Mean y_1^+ variation during the transient wall-film evaporation in the wall-refined cases.

same condition at two different time instants: at 5ms and at 39ms corresponding respectively to 10% and 90% loss of the liquid mass. Figure 5.15 shows the evolution over time of the volume average of the streamwise velocity, temperature and pressure for all conditions. The pressure decreases over time due to energy loss through the wall-film and dry wall. Figure 5.16 shows the evolution of the shear stresses magnitude and the heat heat fluxes averaged over the dry wall and at the liquid/gas interface. Although the variation of the shear stress and the heat flux is similar for all the conditions initialized with the flow at $Re_\tau \approx 550$, theses quantities vary differently at the liquid/gas interface, highlighting the influence of mass transfer on the near wall physics. Figures 5.17 and 5.18 show the evolution of the wetted surface area during the evaporation and the evolution of the wall-film thickness, evaporation rate and the liquid/gas interface temperature averaged over the wetted area. In all conditions, the surface-averaged evaporation rate undergoes an exponential increase at the end of the evaporation. This phenomena was also observed in the experiments of Shway [90]. Hypothesis can be made to explain this increase in the evaporation:

- Figure 5.19 shows the wall-film thickness, the evaporation rate, and the evaporated species mass fraction in the wall cell center at two different instants. The evaporation rate is much higher at the leading edge (the wall-film edge facing the streamwise flow direction) compared with the remaining wetted area. This high evaporation rate at the leading edge are due to the low values of the evaporated species mass fraction: the evaporation rate is linearly dependent on the evaporated species gradient at the liquid/gas interface, and thus, on the mass fraction in the first mesh cell (cf Eq. (4.15)). As the total wall-film surface decreases, there is more and more portion of the wall-film experiencing high evaporation rate, which increases the surface-averaged evaporation rate.
- As the wall-film thickness decrease, the liquid/gas temperature gets closer to the wall temperature as can be noticed in Figure 5.18c. The evaporation rate may be also enhanced due to this temperature increase. This hypothesis is similar to the conceptual model proposed by Maligne and Bruneaux [83], and shown in Figure 5.20, to explain the higher evaporation rate of discrete pocket structure compared to wall-films with continuous structure.

The detailed description of the wall-film evaporation was not further investigated. In order to characterize macroscopically the evaporation in each condition, the Global Evaporation Rate (GER) indicator is proposed and defined as the following:

$$GER = \frac{\text{initial liquid mass}}{\text{total evaporation time} \times \text{initial wetted surface area}}$$

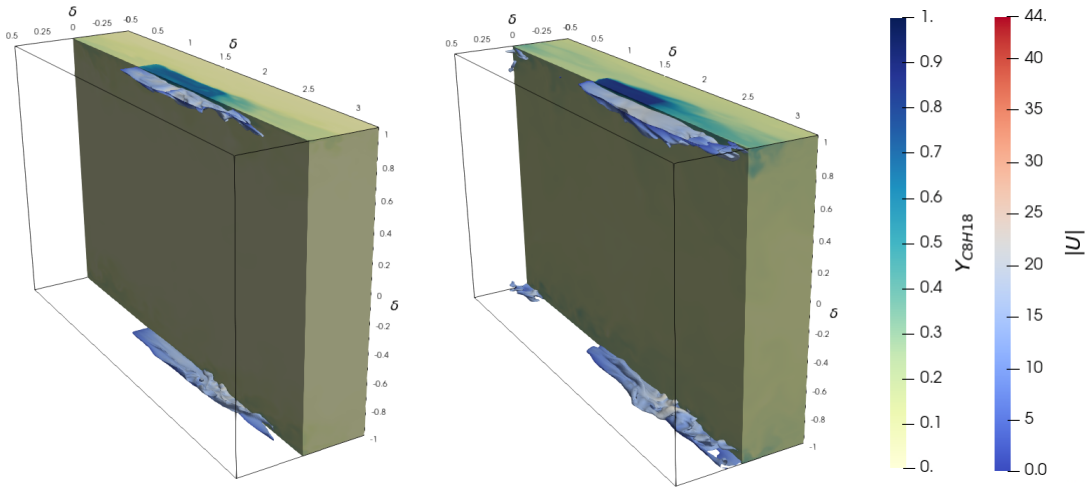

(a) At 5 ms **(b)** At 39 ms

Figure 5.14: Snapshots of the transient evaporation of wall-film in turbulent channel flow in `HighTurb` condition. Left side: evaporated species mass fraction; Right side: Iso-surfaces of $Y_F = 0.3$ colored with magnitude of the velocity field.

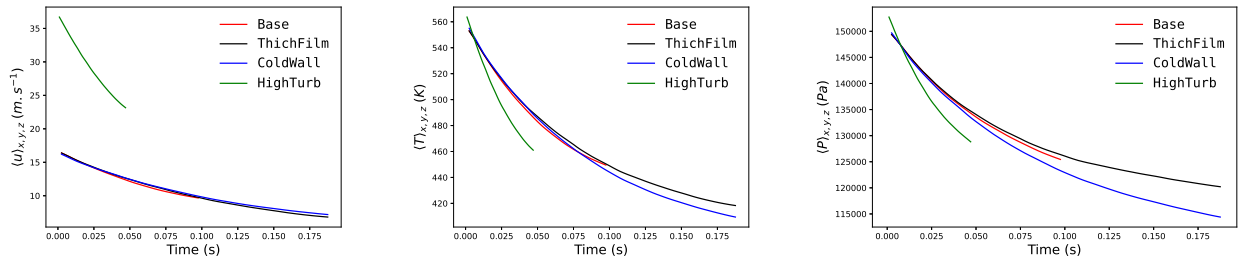

(a) Volumetric average of streamwise velocity **(b)** Volumetric average of temperature **(c)** Volumetric average of pressure

Figure 5.15: Evolution of the volumetric average of streamwise velocity, temperature and pressure over the domain of the wall-refined cases.

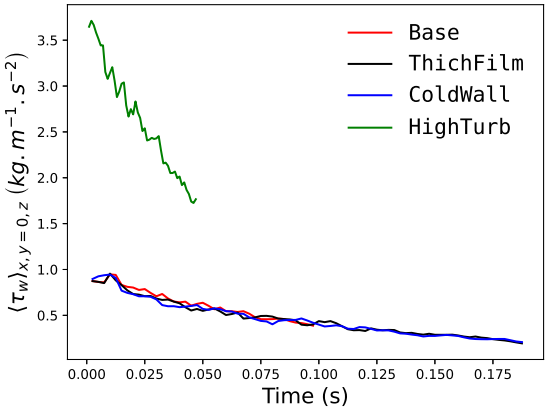

(a) Shear stress over the dry wall

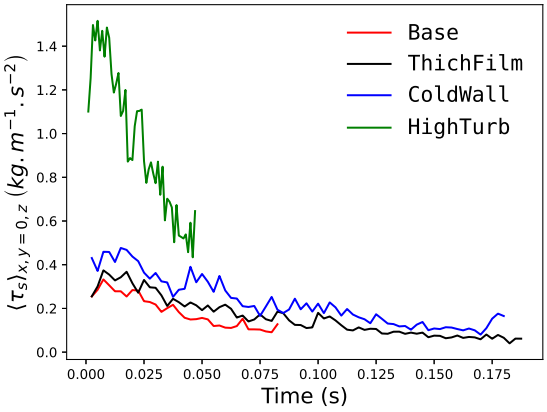

(b) Shear stress at the liquid/gas interface

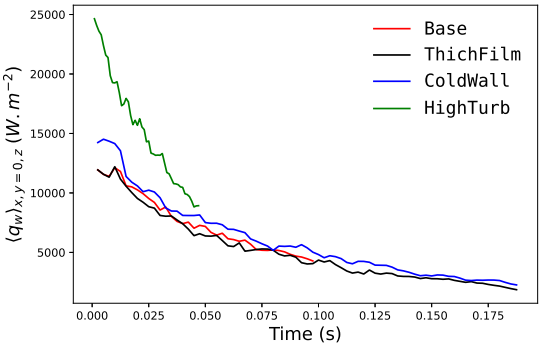

(c) Heat flux over the dry wall

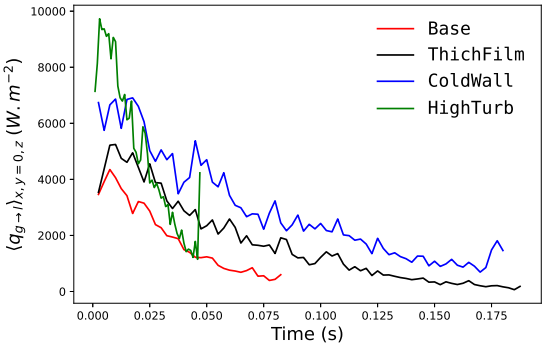

(d) Heat flux at the liquid/gas interface

Figure 5.16: Evolution the wall shear stress and heat flux of the wall-refined cases.

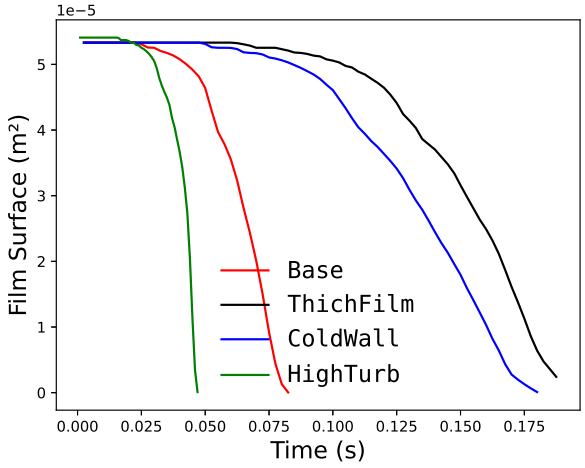

Figure 5.17: Evolution the wall-film surface of the wall-refined cases.

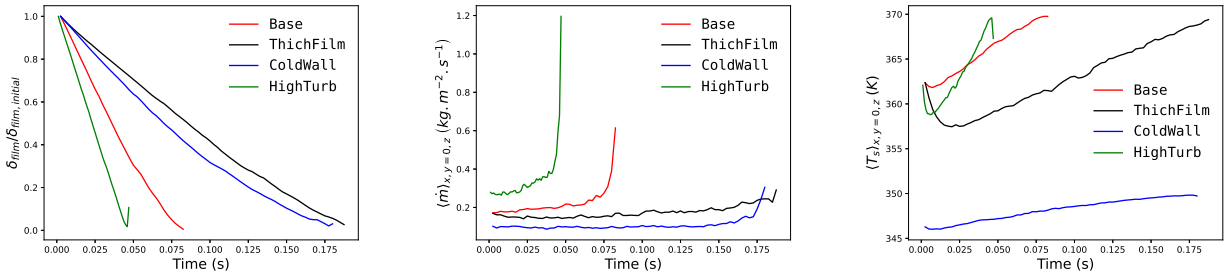

(a) Wall-film thickness **(b)** Evaporation rate **(c)** Wall-film surface temperature.

Figure 5.18: Evolution of wall-film quantities of the wall-refined cases.

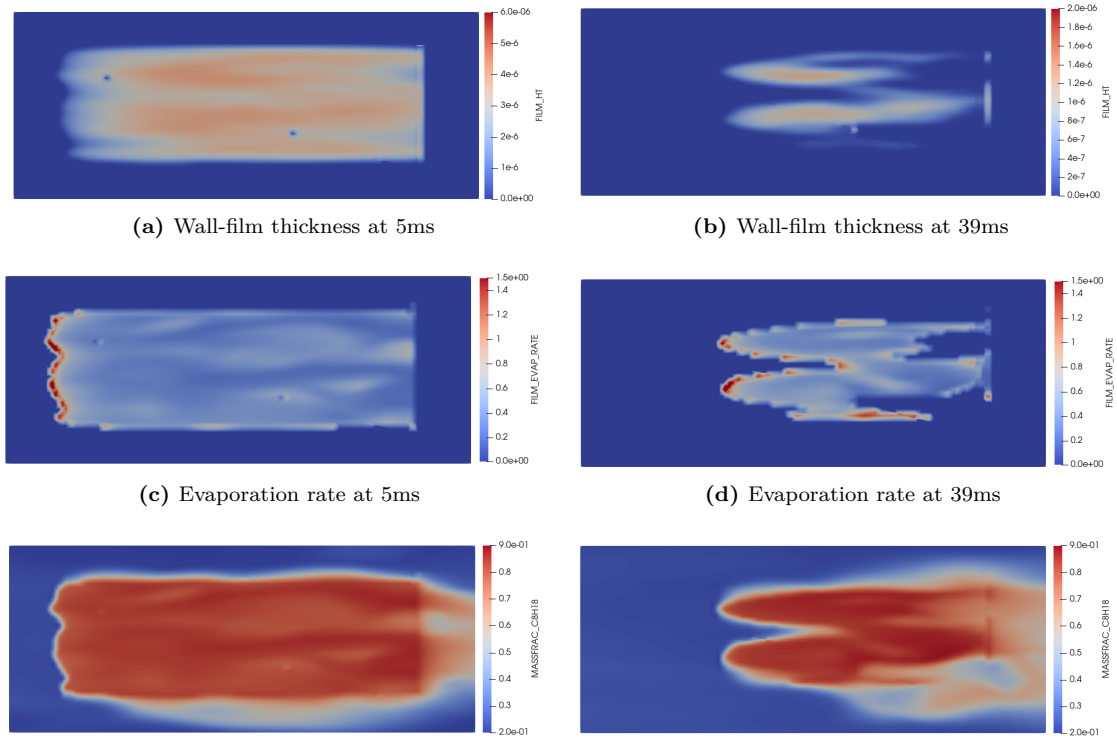

(a) Wall-film thickness at 5ms **(b)** Wall-film thickness at 39ms

(c) Evaporation rate at 5ms **(d)** Evaporation rate at 39ms

(e) $Y_{F,1}$ at 5ms **(f)** $Y_{F,1}$ at 39ms

Figure 5.19: Instantaneous shape of the wall-film in the `HighTurb` condition.

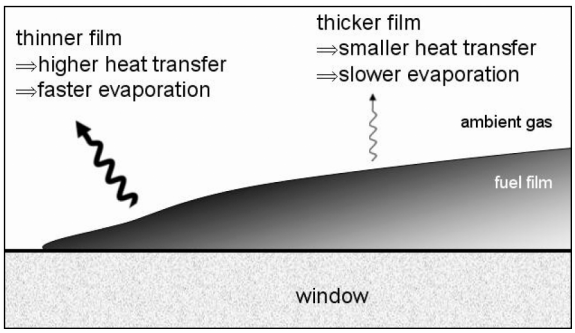

Figure 5.20: Schematic conceptual model for fuel evaporation dynamic at the film edge [83].

Condition name	Initial Re_τ	$T_w(K)$	Initial $\delta_{wf}(\mu m)$	GER $(g.m^{-2}.s^{-1})$
`Base`	550	370	20	180.9
`ThickFilm`	550	370	**40**	149.5
`ColdWall`	550	**350**	20	84.2
`HighTurb`	**1100**	370	20	313.5

Table 5.4: Wall-refined GER for each condition.

This indicator will be also used later to compare between the wall-modeled and wall-refined results. Table 5.4 gives the GER of the different conditions. Using twice the initial wall-film thickness leads to a decrease of the GER of 17% compared to the `Base` condition. Decreasing the wall temperature and the initial liquid temperature by 20K has a bigger effect on the evaporation as it decreases the GER by 53% compared to the `Base` condition. Similarly to the stationary wall-film evaporation, doubling the initial Re_τ increases the GER by 73%.

5.2.3 Wall-modeled results

In this section, the results of the four cases simulations performed using a coarser mesh and algebraic wall models are presented and discussed. The shear stress wall model is always *Werner&Wengle*, and the three wall heat models considered are the same as in Section 5.1.3 for the stationary assessment. For `Base`, `ThickFilm`, and `ColdWall` conditions, the mesh grid is uniform in all the domain with a cell size $\Delta x = \Delta y = \Delta z = \delta/36$, as in the previous wall-modeled cases. For the `HighTurb` condition however, two wall-modeled simulations are performed using two different mesh grids:

- A coarse mesh with same characteristics as the other conditions: $\Delta x = \Delta y = \Delta z = \delta/36$.
- Medium mesh: A base mesh grid with the same characteristics as the other conditions with an additional one level of embedding near the walls, leading to cell size of $\Delta x_1 = \Delta y_1 = \Delta z_1 = \delta/72$.

Table 5.5 summarizes the GER of the wall-modeled cases and the relative errors compared with their respective wall-refined results. When the initial $Re_\tau \approx 550$, i.e. for the conditions: `Base`, `ThickFilm` and `ColdWall`, the evaporation of wall-film is similar in overall between the wall-modeled cases using different wall heat models. All the wall-modeled cases for the `Base` and `ThickFilm` conditions underestimate the GER with close errors, ranging from 19% to 26%. The sensitivity to the choice of the wall heat model is even less noticeable in the `ColdWall` condition as all the wall-modeled cases underestimate the GER by about 12% compared to the wall-refined result at the same condition.

		wall-refined	Algebraic wall-model		
			O'Rourke-Amsden	*Angelberger*	*GruMo-UnoMORE*
`Base`		180.9	134.1 (-26%)	146.1 (-19%)	135.5 (-25%)
`ThickFilm`		149.5	117.2 (-22%)	120.4 (-19%)	117.6 (-21%)
`ColdWall`		84.2	73.9 (-12%)	73.6 (-13%)	73.9 (-12%)
`HighTurb`	coarse mesh	313.5	209.4 (-33%)	179.2 (-43%)	176.3 (-44%)
	medium mesh		233.9 (-25%)	238.6 (-24%)	233.5 (-26%)

Table 5.5: Wall-refined and wall-modeled GER for each condition, with errors with respect to wall-refined results.

For the `HighTurb` condition, the errors depends in the first place on the used mesh cell size. For the coarse mesh, for which the typical Δy_1^+ value at the beginning of the simulation is about 28 at the beginning of the simulation, the errors on the GER range from 33% to 44%, with the smaller error being obtained using *O'Rourke-Amsden* wall heat model, similarly to the stationary assessment. For the medium mesh on the other hand, the wall mesh cell size is two times smaller, and thus the Δy_1^+ values are similar to the ones found in wall-modeled cases in the `Base` condition, about 14 at the beginning of the simulation. The errors on the GER in these cases do not vary using different wall heat models and also they are similar to the obtained errors in the `Base` condition. This result confirms the fact that the wall-modeled results using the algebraic wall-models depend mainly on the wall mesh cell size expressed in wall units.

In the following, plots showing the comparison between the wall-refined and wall-modeled results will be presented only for the `Base` condition and `HighTurb` condition with the coarse mesh grid, as these conditions are relevant to show the dependence on the mesh cell size and the used wall heat model. Figure 5.21 shows the variation over time of the volume average of the streamwise velocity, temperature and pressure. The wall-modeled results agree very well with the wall-refined results, especially for the conditions with initial $Re_\tau \approx 550$, indicating that the wall-film in the wall-modeled simulations evaporates in the same conditions as in the wall-refined simulations. Figures 5.22 and 5.23 shows the variation of wall shear stress and the heat flux averaged over the dry wall and over the liquid/gas interface. The wall shear stress and heat flux results are well predicted with the wall-modeled simulations, while relatively high differences are obtained over the wall-film. Figure 5.24 shows the variation of the wall-film surface area and thickness and the variation of the evaporation rate.

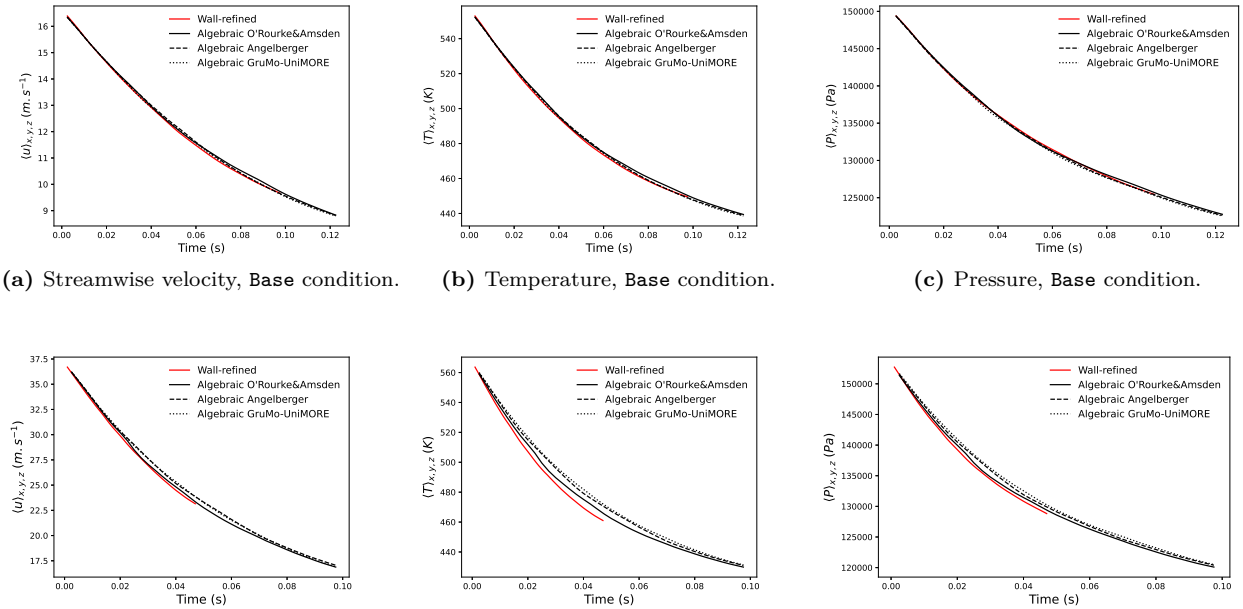

(a) Streamwise velocity, `Base` condition. **(b)** Temperature, `Base` condition. **(c)** Pressure, `Base` condition.

(d) Streamwise velocity, `HighTurb` condition. **(e)** Temperature, `HighTurb` condition. **(f)** Pressure, `HighTurb` condition.

Figure 5.21: Evolution of the volumetric average of streamwise velocity, temperature and pressure over the domain for the `Base` and `HighTurb` conditions.

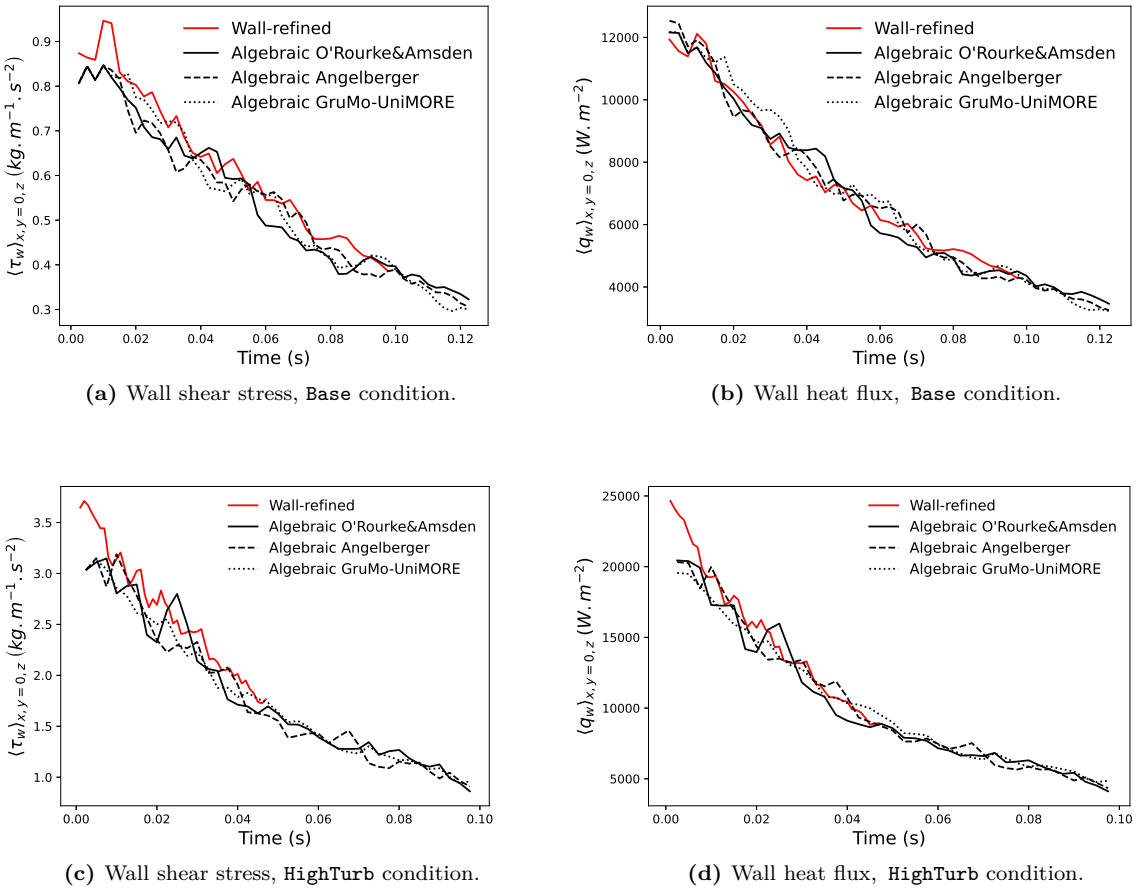

(a) Wall shear stress, `Base` condition. **(b)** Wall heat flux, `Base` condition.

(c) Wall shear stress, `HighTurb` condition. **(d)** Wall heat flux, `HighTurb` condition.

Figure 5.22: Evolution of the dry wall shear stress and heat flux for the `Base` and `HighTurb` conditions.

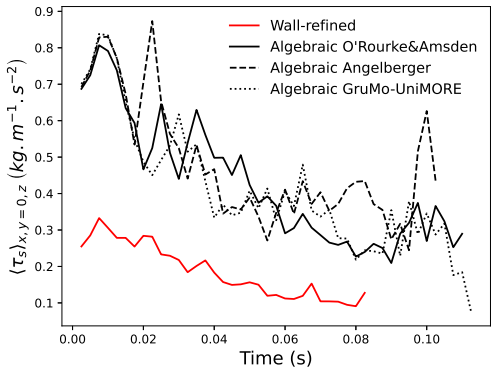

(a) Shear stress, `Base` condition.

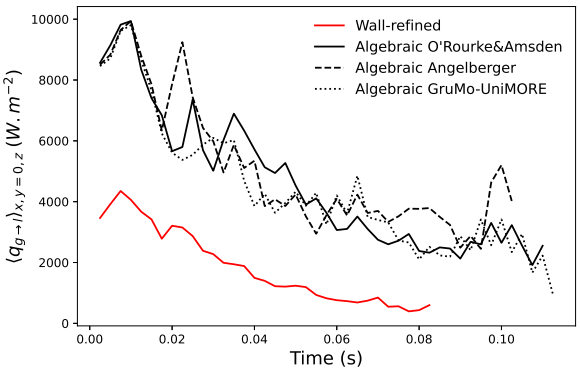

(b) Heat flux, `Base` condition.

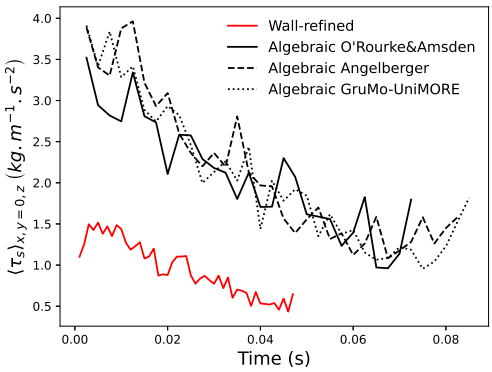

(c) Shear stress, `HighTurb` condition.

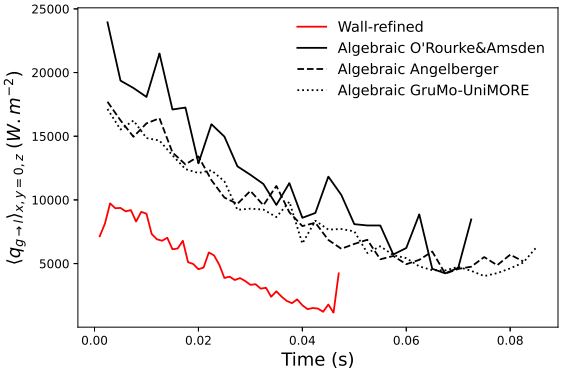

(d) Heat flux, `HighTurb` condition.

Figure 5.23: Evolution of the shear stress and heat flux at the liquid/gas interface for the `Base` and `HighTurb` (coarse mesh) conditions.

5.3 Conclusion

The wall-film evaporation has a significant influence on the near wall physics and the use of the evaporation model based on the semi-analytical solution along with the classical algebraic heat and dynamic wall models is not suited for wall-modeled LES. According to the present results and for these particular conditions, the main highlighted issue are the following:

- The stationary evaporation shows that classic algebraic dynamic wall models, which do not account for the effect of transpiration, fails to predict the correct shear stress at the liquid/gas interface.
- The algebraic wall heat models also fails to predict an accurate heat flux transferred from the gas to the liquid phase.
- The results depends in the first place on the dimensionless wall cell size. Dependency on the used wall heat model is also noticed when the wall cell center is located in the buffer layer.

It is important to point out that the results of this assessment were obtained for fixed values of n and m (Eq. (4.55)), and using different values may lead to different results.

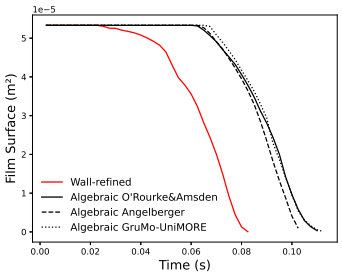

(a) Film surface, `Base` condition.

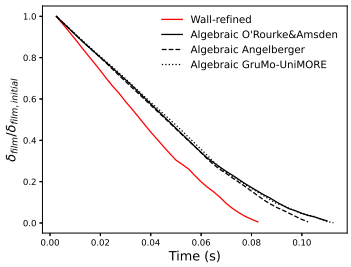

(b) Film thickness, `Base` condition.

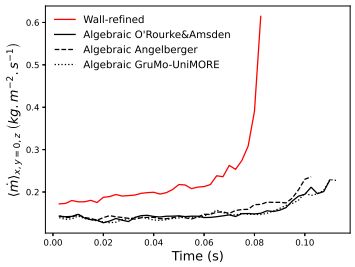

(c) Evaporation rate, `Base` condition.

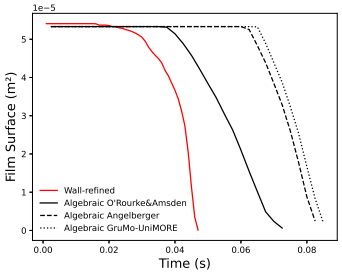

(d) Film surface, `HighTurb` condition.

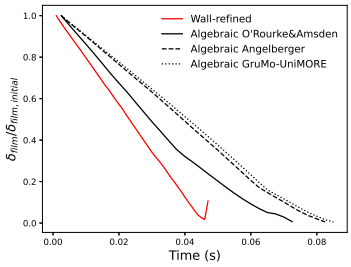

(e) Film thickness, `HighTurb` condition.

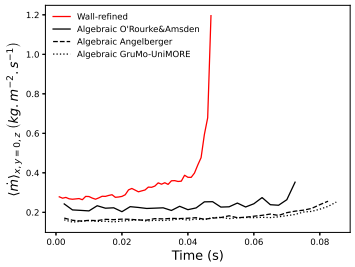

(f) Evaporation rate, `HighTurb` condition.

Figure 5.24: Evolution of wall-film quantities for the `Base` and `HighTurb` (coarse mesh) conditions.

Chapter 6

ODEs based WMLES of wall-film evaporation

Contents

In order to improve the wall-film evaporation physics, the previously pointed out algebraic models weaknesses need to be overcome. Instead of improving an existing algebraic wall-model or develop a new one, we propose in this work to extend the ODEs WMLES approach to cases with mass transfer. In the following, a brief review of the ODEs based WMLES will be presented. Then, the considered equations for the wall-film evaporation and their numerical implementation will be detailed. Finally, the proposed wall-model will be assessed on the stationary and transient wall-film evaporation cases introduced in Chapter 5.

6.1 Improved physical modeling with ODEs based WMLES

According to the classification of WMLES approaches proposed by Larsson et al. [40] and illustrated in Figure 3.4, ODEs based WMLES is a physics based modeling without wall-parallel grid connectivity. As shown in Figure 6.1, the ODEs are numerically solved in the wall normal direction using the LES filtered quantities at a distance δ_{wm} and the wall boundary conditions. The resulting wall shear stress and wall heat flux are used as boundary conditions for the LES. Solving the boundary layer governing equations allows to better account for relevant physical phenomena which are difficult to take into account with algebraic wall models. For near wall flows with wall heat transfer, the simplest momentum and energy equations that can be solved

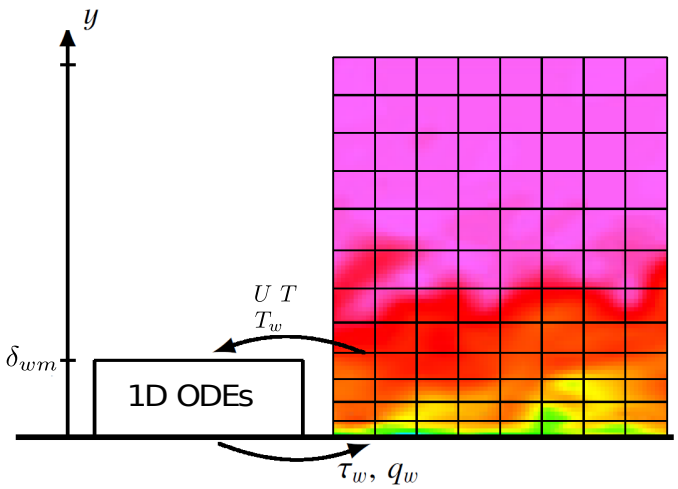

Figure 6.1: Schematic of ODEs based WMLES applied to anisothermal flow [40].

are similar to the ones generally considered by classical algebraic wall models:

$$\frac{d}{dy}\left(\left(\overline{\mu}+\mu_t\right)\frac{d\overline{U}_{//}}{dy}\right)=0 \tag{6.1}$$

$$\frac{d}{dy}\left(\left(\overline{\lambda}+\overline{c}_p\frac{\mu_t}{Pr_t}\right)\frac{d\overline{T}}{dy}\right)=0 \tag{6.2}$$

Solving numerically these equations along a 1D grid in the wall normal direction, instead of integrating them into a simple algebraic expression, still presents several advantages:

- Continuous turbulence modeling: The eddy viscosity μ_t can be modeled with a unique expression inside the inner layer using the Prandtl mixing length theory and a damping function (as it will be detailed in Section 6.2.1). So, unlike algebraic wall models, there is no need for considering two distinct expressions and an assumed transition distance.
- Better handling of variable properties: Variable flow properties (density, viscosity, heat capacity) are better taken into account as they can be evaluated all along the 1D grid.

The ODEs based WMLES is widely used in literature for the modeling of high speed turbulent boundary layer, as the heating due to shear stress can be easily added to the energy equation:

$$\frac{d}{dy}\left(\left(\overline{\lambda}+\lambda_t\right)\frac{d\overline{T}}{dy}\right)+\frac{d}{dy}\left(\left(\overline{\mu}+\mu_t\right)\overline{U}_{//}\frac{d\overline{U}_{//}}{dy}\right)=0 \tag{6.3}$$

Gelain [91] improved the modeling of a turbulent thermal boundary layer with non-equilibrium behavior by adding the effect of temperature gradient in the wall parallel direction:

$$\overline{\rho}\overline{c}_p\overline{U}_{//}\frac{\partial\overline{T}}{\partial x}-\frac{\partial}{\partial y}\left(\left(\overline{\lambda}+\lambda_t\right)\frac{\partial\overline{T}}{\partial y}\right)=0 \tag{6.4}$$

Gelain [91] numerically solved the later equation with a quasi-unidimentional procedure where $\partial\overline{T}/\partial x$ is updated in the 1D grid (the 1D grid is always along the wall normal direction) only once each flow solver iteration. Muto and his co-workers [92, 93] extended the ODEs based modeling approach for near wall reacting flows. They assumed chemical reactions in equilibrium state to derive additional terms in the energy equation and employed a table look-up procedure to estimate the contributions of chemical effect and mixture properties.

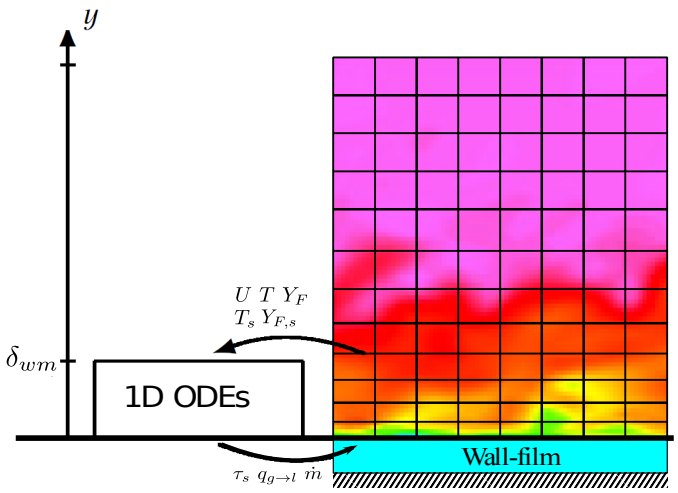

Figure 6.2: Schematic of ODEs based WMLES for wall-film evaporation (adapted from [40]).

6.2 Model formulation for wall-film evaporation

We consider here the same assumptions made in the introduction of Chapter 4 for the derivation of algebraic wall models. According to the Reynolds-averaged total mass conservation, the wall normal momentum $\overline{\rho v}$ will be always considered constant and equal to $\overline{\rho v} = \overline{\dot{m}}$. Figure 6.2 shows the updated schematic of ODEs based WMLES for wall-film evaporation. The solved ODEs are the following: wall-parallel momentum equation, the energy equation and the evaporated species mass equation. In order to keep a reasonable computational cost, the mass conservation equation of the other gas species are not solved and the differential diffusion and the correction velocity are neglected, as assumed in Chapter 4 for algebraic wall-film evaporation modeling.

6.2.1 1D momentum equation

The flow above an evaporating wall-film is characterized by the blowing evaporation rate. Thus, an advection term in the wall normal direction should be considered in the momentum equation which reads:

$$\overline{\dot{m}}\frac{d\overline{U}_{//}}{dy} - \frac{d}{dy}\left((\mu + \mu_t)\frac{d\overline{U}_{//}}{dy}\right) = 0 \tag{6.5}$$

The Cebeci-Smith wall-model [37, 49, 94] was chosen to model the turbulent viscosity as it has also the advantageous feature of including the effect of wall transpiration in a variable-property boundary layer. This wall-model was developed in the early 1970s and since then it has been widely used for various applications. In this context, it was used as algebraic wall-model by Levine [95] in a boundary layer computer program for wall transpiration and film cooling simulations. Chedevergne and Marchenay [71] used the Cebeci-Smith wall model as reference for comparison with RANS turbulence models in transpired turbulent boundary layer configuration. According to this wall-model, the turbulent viscosity has two expressions: a continuous expression based on the Prandtl mixing-length theory for the inner region, and another expression for the outer region. In this work, we will assume that the range of the 1D grid falls completely in the inner region of the boundary layer and only consider a unique expression. In the inner layer of fully turbulent boundary layer, the turbulent viscosity is given by:

$$\mu_t = \overline{\rho} l_m^2 \frac{d\overline{U}_{//}}{dy} \tag{6.6}$$

The mixing-length l_m is scaled on the wall distance and also damped in order to be valid for all the inner region of the boundary layer: $l_m = \kappa y D$ with D a damping function. Most of the ODEs based models

available in the literature ([40] for instance) substitutes the velocity gradient in Eq. (6.6) using Eq. (3.16), leading to $\mu_t = \overline{\rho}\sqrt{\tau_s/\rho_s}\kappa y D^2$. This widely used simplified expression avoids to include explicitly the velocity gradient in the momentum equation, and thus, allows an easier numerical implementation. However, two assumptions are hidden behind this simplification: (i) the contribution of molecular shear stress is negligible in the total shear stress, (ii) flow without pressure gradient neither wall transpiration, i.e. without mass transfer as well. The second assumption cannot be accepted in the context of the current work and we made the choice to keep Eq. (6.6) to express μ_t. So the 1D momentum equation considered for the present model reads:

$$\overline{\dot{m}}\frac{d\overline{U}_{//}}{dy} - \frac{d}{dy}\left(\left(\mu + \overline{\rho} l_m^2 \frac{d\overline{U}_{//}}{dy}\right)\frac{d\overline{U}_{//}}{dy}\right) = 0 \tag{6.7}$$

Cebeci-Smith model uses the van Driest damping function:

$$l_m = \kappa y\left[1 - exp\left(-\frac{y^*}{A_{VD}}\right)\right] \tag{6.8}$$

where A_{VD} is the Van Driest damping-length. This distance indicates the height above the wall where the molecular and turbulent viscosities become of the same order of magnitude [38]. It is interesting to mention that in the 1980s, i.e. after the development of the Cebeci-Smith wall-model, Chapman and Kuhn [96] proved physically and mathematically the cubic limiting behavior of the Reynolds stress $\overline{u'v'}$ at the wall. They showed also that the van Driest damping function lead to an incorrect limiting behavior of turbulence and that it is better to use other damping functions for eddy viscosity models. Chapman and Kuhn [96] pointed out that although different damping functions might yield similar results for $\overline{U}$, the near wall behavior of turbulence might have a significant importance in flows involving heat or mass transfer with high Prandtl or Schmidt numbers respectively. As the Cebeci-Smith model was not updated in the literature with other physical damping function, we continue here to consider its original formulation with the van Driest damping function, where the damping-length constant is given by:

$$A_{VD} = \frac{A_{VD}^+}{N_{CS}} \tag{6.9}$$

where the dimentionless van Driest damping-length constant $A_{VD}^+ = 26$ and N_{CS} is a model factor to account for pressure gradient and wall transpiration:

$$N_{CS}^2 = -\frac{dP}{dx}\frac{\mu}{\tau_s\overline{\dot{m}}}\left[1 - exp\left(\frac{2C_{CS}\overline{\dot{m}}\mu_s}{\sqrt{\tau_s\rho_s}\mu}\right)\right] + exp\left(\frac{2C_{CS}\overline{\dot{m}}\mu_s}{\sqrt{\tau_s\rho_s}\mu}\right) \tag{6.10}$$

with C_{CS} a model constant equal to $C_{CS} = 5.9$. One can notice that semi-local scaling (Eq. (3.52)) is used in Eq. (6.8) in order to account for variable properties boundary layer. Another expression of A_{VD} which account also for pressure gradient and wall transpiration can be found in the book of Kays and Crawford [38] but given only for constant property boundary layer. Cebeci and Cousteix [37] pointed out that the above N_{CS} expression is empirical and based on limited ranges of experimental data; the range of data is, however, extensive so that the full algebraic formulation is the most general available at the time of its development. The pressure gradient was neglected for the development of the present ODEs based model, an assumption also considered for the derivation of classical algebraic wall models. So the first term in Eq. (6.10) is simply neglected, leading to:

$$N_{CS} = exp\left(\frac{C_{CS}\overline{\dot{m}}\mu_s}{\sqrt{\tau_s\rho_s}\mu}\right) \tag{6.11}$$

Once the wall parallel velocity is solved on the 1D grid, the shear stress at the liquid/gas interface is computed using the local gradient similarly to the wall-refined formulation in Eq. (4.1).

6.2.2 1D evaporated species mass equation

The considered conservation equation of the mean evaporated species mass fraction reads:

$$\overline{\dot{m}}\frac{d\overline{Y}_F}{dy} - \frac{d}{dy}\left(\left(\frac{\mu}{Sc_F} + \frac{\mu_t}{Sc_t}\right)\frac{d\overline{Y}_F}{dy}\right) = 0 \tag{6.12}$$

Levine [95] assumed $Sc_t = Pr_t$ for transpiration and film-cooling simulations. Recently, van Reeuwijk and Hadžiabdić [97] studied the behavior of Sc_t through DNS of half turbulent channel flow configuration with mass transfer. The study was performed with different molecular Schmidt number flows ranging for 1 to 50. They proposed an expression for Sc_t which depend on Sc, the distance from the wall, the half channel height and the mass boundary layer thickness, which are here also unknown parameters of the problem. As a first step for the development of the present ODEs based model, we simply assume that $Sc_t = Sc_{t,\infty} = 0.7$. The evaporation rate is then computed using the local gradient of $\overline{Y}_F$ at the liquid/gas interface similarly to the wall-refined formulation in Eq. (4.15).

6.2.3 1D energy equation

The considered conservation equation of the mean temperature reads:

$$c_p\overline{\dot{m}}\frac{d\overline{T}}{dy} - \frac{d}{dy}\left(\left(\lambda + c_p\frac{\mu_t}{Pr_t}\right)\frac{d\overline{T}}{dy}\right) = 0 \tag{6.13}$$

Recently, Chen et al. [98] used a model for Pr_t for ODEs based WMLES with heat transfer and provided a discussion about the near wall scaling of eddy conductivity in variable property boundary layer. Several other expressions exist in the literature for the near wall turbulent Prandtl number [99–101], but generally they don't consider wall transpiration. In accordance with Cebeci-Smith eddy viscosity model, the turbulent Prandtl number model proposed by Cebeci [102] is the following:

$$Pr_t = \frac{\kappa}{\kappa_T}\frac{[1 - exp\,(-y^*/A_{VD})]}{[1 - exp\,(-y^*\,Pr^{0.5}/A_T)]} \tag{6.14}$$

with $\kappa_T = 0.44$, and

$$A_T = \frac{A_T^+}{N_{CS}} \tag{6.15}$$

with $A_T^+ = 34$. Levine [95] used this model for Pr_t for boundary layer simulations with transpiration and film-cooling. Kays [103] proposed a different expression for Pr_t which takes also takes into account wall transpiration but given only for air with constant properties. As a first step for the development and the assessment of the present ODEs based model, we consider the most simple way to express Pr_t, i.e. a constant value equal to the one used for the LES flow field ($Pr_t = Pr_{t,\infty} = 0.7$). The heat flux at the liquid/gas interface $q_{g\to l}$ is finally computed using the local temperature gradient similarly to the wall-refined formulation in Eq. (4.4).

Summary

In this work, the ODEs base WMLES was adapted for the simulation of an evaporating wall-film. Table 6.1 summarizes the main changes made compared to classical ODEs based WMLES for low speed flow with wall heat transfer:

- The evaporated species mass balance is solved along with the momentum and energy equations.
- All the governing equations includes the wall-normal advection term due to evaporation.
- The Cebeci-Smith model was used to model the turbulent viscosity as it allows to consider the effect of transpired boundary layer. The velocity gradient was not simplified in the expression of μ_t, and thus, explicitly included in the momentum equation.

Classical ODEs based WMLES for low speed flow with wall heat transfer	ODEs based WMLES for wall-film evaporation
$\frac{d}{dy}\left(\left(\mu+\mu_t\right)\frac{d\overline{U}_{//}}{dy}\right)=0$	$\overline{\dot{m}}\frac{d\overline{U}_{//}}{dy}-\frac{d}{dy}\left(\left(\mu+\mu_t\right)\frac{d\overline{U}_{//}}{dy}\right)=0$
$\frac{d}{dy}\left(\left(\lambda+c_p\frac{\mu_t}{Pr_t}\right)\frac{d\overline{T}}{dy}\right)=0$	$c_p\overline{\dot{m}}\frac{d\overline{T}}{dy}-\frac{d}{dy}\left(\left(\lambda+c_p\frac{\mu_t}{Pr_t}\right)\frac{d\overline{T}}{dy}\right)=0$
	$\overline{\dot{m}}\frac{d\overline{Y}_F}{dy}-\frac{d}{dy}\left(\left(\frac{\mu}{Sc_F}+\frac{\mu_t}{Sc_t}\right)\frac{d\overline{Y}_F}{dy}\right)=0$
$\mu_t=\overline{\rho}\sqrt{\tau_w/\rho_w}\kappa y D^2$	$\mu_t=\overline{\rho}\left(\kappa y D\right)^2\frac{d\overline{U}_{//}}{dy}$
$D=\left[1-exp\left(-\frac{y^*}{A^+_{VD}}\right)\right]$	$D=\left[1-exp\left(-\frac{y^*N_{CS}}{A^+_{VD}}\right)\right]$
	$N_{CS}=exp\left(\frac{C_{CS}\overline{\dot{m}}\mu_s}{\sqrt{\tau_s\rho_s\mu}}\right)$

Table 6.1: Differences between ODEs based WMLES for low speed flow with wall heat transfer Vs wall-film evaporation.

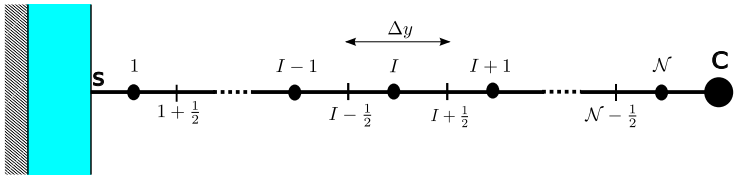

Figure 6.3: 1D grid used to solve the 1D ODEs above the wall-film.

6.3 Numerical implementation

Larsson et al. [40] provided guidelines for the numerical implementation of ODEs based models. A cell centered finite volume method is used to numerically solve the previous ODEs on 1D grid ranging from the liquid/gas interface to a certain distance normal to the wall δ_{wm}. As mentioned in Section 3.1.1.2, using the wall-adjacent LES data is known to cause the log-layer mismatch (LLM) and various remedies were proposed in the literature for this problem [40, 43]. We considered for this work a 1D grid up to the center of the wall mesh cell as a first step to assess the performance of the proposed model. Some notations used all along the manuscript are modified only in this section: Δy denotes here the cell size of the 1D grid and C refers to the wall mesh cell center. The 1D grid divided uniformly into $\mathcal{N}$ control volumes associated to $\mathcal{N}$ nodes as showed in Figure 6.3. The number of nodes is determined for each wall cell and for each flow solver iteration according to dimensionless distance at the center of the cell:

$$\mathcal{N}=max\left(\left\lceil\frac{y_C\sqrt{\tau_s\rho_s}}{\mu_s y^+_{min}}\right\rceil,2\right) \tag{6.16}$$

with $y^+_{min}=3$ for the present work. The momentum, energy and evaporated species ODEs are coupled: the turbulent viscosity depends on the velocity gradient, evaporation rate and the shear stress, the molecular properties depend on the temperature and mixture composition. Thus, an iterative algorithm is used to solve the ODEs as shown in Figure 6.4. The convergence is measured by the relative change in τ_s, $q_{g\rightarrow l}$ and $\dot{m}$ between successive iterations and the algorithm stops when the relative change is smaller than 0.01 for each quantity. The solved velocity, temperature and evaporated species 1D profiles are saved for each wall cell so they can be used to initialize the model at the next flow solver iteration. An interpolation procedure is applied if the 1D grid discretisation is modified. Two main constraints characterize the numerical discretisation of the ODEs of the present model compared to classical ODEs based models: the presence of the advection

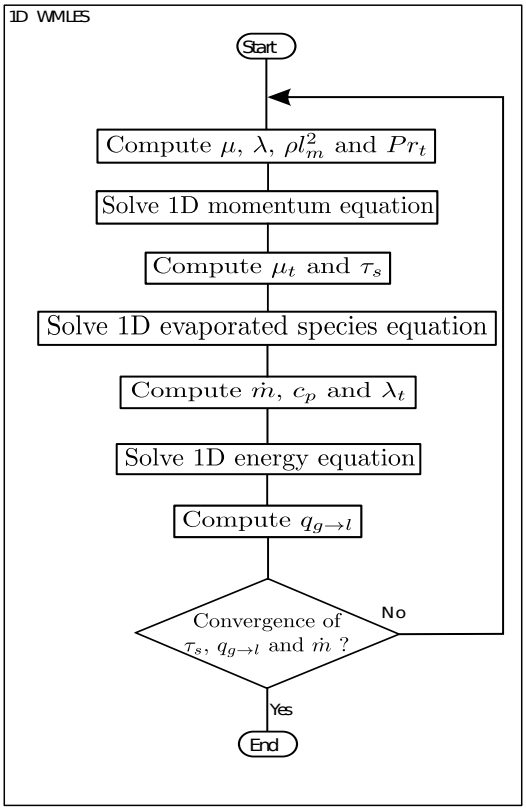

Figure 6.4: Flowchart of the numerical resolution of the ODEs base WMLES for wall-film evaporation.

term in all the equations, and the explicit dependence of the turbulent viscosity on the wall parallel velocity gradient. In the following a brief description of the applied numerical methods is proposed.

6.3.1 Advection-diffusion equation discretization

The 1D equations of the evaporated species mass (Eq. (6.12)) and energy (Eq. (6.13)) are advection-diffusion equations with variable properties. Let us consider the advection-diffusion equation of a variable ϕ:

$$a_\phi \frac{d\phi}{dy} + \frac{d}{dy}\left(b_\phi \frac{d\phi}{dy}\right) = 0 \tag{6.17}$$

with $a_\phi$and b_ϕ the advection and diffusion coefficients respectively and they are not necessarily constant along the 1D grid. We apply the integral conservation law to each control volume:

$$\int_{I-1/2}^{I+1/2} \left[a_\phi \frac{d\phi}{dy} + \frac{d}{dy}\left(b_\phi \frac{d\phi}{dy}\right)\right] dy = 0 \quad \text{for } I = 1..\mathcal{N} \tag{6.18}$$

$$\Rightarrow\ a_{\phi,I}\left(\phi_{I+1/2} - \phi_{I-1/2}\right) + b_{\phi,I+1/2}\left.\frac{d\phi}{dy}\right|_{I+1/2} - b_{\phi,I-1/2}\left.\frac{d\phi}{dy}\right|_{I-1/2} = 0 \quad \text{for } I = 1..\mathcal{N} \tag{6.19}$$

At all the faces between the control volumes, the values and the gradients are approximated as follows:

$$\phi_{I+1/2} = \frac{\phi_I + \phi_{I+1}}{2} \qquad \phi_{I-1/2} = \frac{\phi_I + \phi_{I-1}}{2} \tag{6.20}$$

$$\left.\frac{d\phi}{dy}\right|_{I+1/2} = \frac{\phi_{I+1} - \phi_I}{\Delta y} \qquad \left.\frac{d\phi}{dy}\right|_{I-1/2} = \frac{\phi_I - \phi_{I-1}}{\Delta y} \tag{6.21}$$

At the boundary conditions, we use the imposed values at the liquid/gas interface and at the mesh cell center C. The gradients at the boundary conditions are approximated by:

$$\left.\frac{d\phi}{dy}\right|_{1/2} = \frac{2\left(\phi_1 - \phi_s\right)}{\Delta y} \qquad \left.\frac{d\phi}{dy}\right|_{\mathcal{N}+1/2} = \frac{2\left(\phi_C - \phi_{\mathcal{N}}\right)}{\Delta y} \tag{6.22}$$

So, finally we need to solve a tri-diagonal square matrix of size $(\mathcal{N}, \mathcal{N})$. Thomas algorithm can be used to solve such system with a complexity of $\mathcal{O}(\mathcal{N})$ if and only if the matrix is diagonally dominant. This condition is always satisfied for a diffusion equation ($a_\phi = 0$) with constant diffusion coefficient but not necessarily for an advection-diffusion equation. If the matrix is not diagonally dominant, an iterative method is used to converge toward the stationary solution. This is equivalent to adding a fictitious transient term in Eq. (6.17) as the following:

$$\frac{\partial \phi}{\partial t} + a_\phi \frac{\partial \phi}{\partial y} + \frac{\partial}{\partial y}\left(b_\phi \frac{\partial \phi}{\partial y}\right) = 0 \tag{6.23}$$

A backward first order Euler scheme was used for time discretisation:

$$\frac{\partial \phi}{\partial t} \approx C_{dt}\left(\phi_I^n - \phi_I^{n-1}\right) \tag{6.24}$$

where ϕ^n is the solution at iteration n and C_{dt} is a stability coefficient set such that the system to solve is diagonally dominant. The iterative method is performed until the following convergence criteria is reached:

$$\left|\frac{\phi_I^n - \phi_I^{n-1}}{\phi_I^n}\right| < \epsilon_\phi \qquad \text{for } I = 1..\mathcal{N} \tag{6.25}$$

ϵ_ϕ is set here equal to 0.001.

6.3.2 1D momentum equation discretization

The 1D momentum equation (Eq. (6.7)) deserves a particular attention as turbulent viscosity depends on the velocity gradient itself. We start by applying the integral conservation law to each control volume:

$$\int_{I-1/2}^{I+1/2}\left[\overline{\dot{m}}\frac{d\overline{U}_{//}}{dy} - \frac{d}{dy}\left(\left(\mu + \bar{\rho} l_m^2 \frac{d\overline{U}_{//}}{dy}\right)\frac{d\overline{U}_{//}}{dy}\right)\right] dy = 0 \quad \text{for } I = 1..\mathcal{N} \tag{6.26}$$

$$\begin{aligned}\overline{\dot{m}}\left(\overline{U}_{//,I+1/2} - \overline{U}_{//,I-1/2}\right) &+ \left(\mu_{I+1/2} + \left(\bar{\rho} l_m^2\right)_{I+1/2}\left.\frac{d\overline{U}_{//}}{dy}\right|_{I+1/2}\right)\left.\frac{d\overline{U}_{//}}{dy}\right|_{I+1/2} \\ &- \left(\mu_{I-1/2} + \left(\bar{\rho} l_m^2\right)_{I-1/2}\left.\frac{d\overline{U}_{//}}{dy}\right|_{I-1/2}\right)\left.\frac{d\overline{U}_{//}}{dy}\right|_{I-1/2} = 0 \quad \text{for } I = 1..\mathcal{N}\end{aligned} \tag{6.27}$$

The values and gradients at the faces between the control volumes are expressed using Eq. (6.20) and Eq. (6.21). At the boundary conditions, we use the no-slip condition at the liquid/gas interface and $\overline{U}_{//,C}$ at the

mesh cell center C. The gradients at the boundary conditions are approximated as in Eq. (6.22). This yields a numerical scheme expressed as:

$$F\left(U_{//}\right) = 0 \tag{6.28}$$

where $F\left(U_{//}\right)$ is a non linear system. The under-relaxed Newton's method [104] is used to solve this non-linear system. It consists of an iterative method and the solution at each iteration n is given by:

$$\overline{U}^{n}_{//} = \overline{U}^{n-1}_{//} + \omega\, d\overline{U}_{//} \tag{6.29}$$

where ω is a relaxation parameter set equal to $\omega = 0.9$ and $d\overline{U}_{//}$ is the solution of:

$$J\, d\overline{U}_{//} = -F\left(\overline{U}^{n-1}_{//}\right) \tag{6.30}$$

with J the jacobian matrix defined by:

$$J_{I,J} = \frac{\partial F_I}{\partial \overline{U}_{//,J}} \tag{6.31}$$

J is a diagonally dominant tri-diagonal matrix and Thomas algorithm is used to solve the system (6.30). The iterative method is performed until the following convergence criteria is reached:

$$\left| \frac{\overline{U}^{n}_{//,I} - \overline{U}^{n-1}_{//,I}}{\overline{U}^{n}_{//,I}} \right| < \epsilon_U \qquad \text{for } I = 1..\mathcal{N} \tag{6.32}$$

ϵ_U is set here equal to 0.001.

6.4 Assessment of ODEs based wall-film evaporation modeling

6.4.1 Evaporating wall-film in a stationary turbulent channel flow

The ODEs based modeling of the wall-film evaporation is assessed in the same steady channel flow configuration and case setup presented in Section 5.1. Table 6.2 summarizes all the results: wall-refined LES, algebraic WMLES, and the new ODEs based WMLES. The mean shear stress at the liquid/gas interface is much better predicted using the ODEs based WMLES: only a relative error of 4% and 8% were obtained for the low and high turbulent conditions respectively, while they were at least 22% and 40% respectively using the algebraic wall models. This improvement of the shear stress prediction can be easily seen on the velocity profiles plotted with the wall units (u^+, y^+) in Figure 6.5. This net improvement suggests that the effect of evaporation on the near wall physics is better captured. This probably thanks to the consideration of the transpiration effect in the solved ODEs. The heat flux $\overline{q}_{g\to l}$ was slightly improved as the relative error dropped by about 10% for the two turbulent conditions. Finally, the modeled mean evaporation rate is also improved with relative error of 28% and 30% for the low and high turbulent conditions, while they were at least 40% and 42% respectively using the algebraic wall modeling.

6.4.2 Transient wall-film evaporation in turbulent channel flow

The ODEs based modeling of the wall-film evaporation is assessed in the same transient channel flow configuration and case setup presented in section 5.2. The assessment is performed for the four conditions: `Base`, `ThickFilm`, `ColdWall` and `HighTurb`. The `HighTurb` is again performed using the coarse and medium mesh grids. In this configuration, only a portion of the wall is wetted, while the other portion is an isothermal dry wall. Two modeling approaches can be used for the dry wall:

- ODEs based modeling all over the wall: The same proposed ODEs based model for the wall-film evaporation can be used for the dry wall (where $\dot{m} = 0$), and hence, a unique model is used all over the wall.

			Mesh	Target conditions			Results						
			Δy_1^+	$\langle \rho u \rangle$ $(kg.m^{-2}.s^{-1})$	$\overline{T}_c$ (K)	$\overline{Y}_{F,c}$	Re_τ	$\overline{\tau}_s$ $(kg.m^{-1}.s^{-2})$	ϵ_τ (%)	$\overline{q}_{g\to l}$ $(kW.m^{-2})$	ϵ_q (%)	$\overline{\dot{m}}$ $(g.m^{-2}.s^{-1})$	$\epsilon_{\dot{m}}$ (%)
low	wall-refined		3.5	7.35	591	0.21	572	0.100		3.29		66.2	
	Algebraic WMLES	O'Rourke-Amsden	18.1	7.31	590	0.19	651	0.127	+27	5.32	+62	39.7	-40
		Angelberger	17.7	7.28	591	0.20	638	0.122	+22	5.41	+64	39.9	-40
		GruMo-UnoMORE	18.2	7.27	591	0.19	655	0.129	+29	5.32	+62	39.6	-40
	ODEs based WMLES		16.5	7.27	594	0.21	595	0.104	+4	5.06	+53	47.4	-28
high	wall-refined		3.6	17.08	598	0.20	1187	0.423		7.12		115.3	
	Algebraic WMLES	O'Rourke-Amsden	39.4	16.88	586	0.21	1417	0.594	+40	10.91	+53	67.3	-42
		Angelberger	42.4	17.20	591	0.21	1525	0.689	+63	9.98	+40	52.5	-54
		GruMo-UnoMORE	42.6	17.32	593	0.20	1534	0.697	+65	9.61	+35	49.4	-57
	ODEs based WMLES		34.8	16.85	596	0.21	1252	0.455	+8	8.93	+25	81.1	-30

Table 6.2: Cases characteristics and results for the assessment of stationary wall-film evaporation modeling: Algebraic and ODEs based WLES. Δy_1^+: Dimensionless wall cell size in the wall normal direction; $\langle \rho u \rangle$: Mean mass flow rate; $\overline{T}_c$: Mean temperature in the center of the channel; $\overline{Y}_{F,c}$: Mean mass fraction of the evaporated species in the center of the channel; Re_τ: Reynolds number based on wall shear velocity; $\overline{\tau}_s$: Mean shear stress at the liquid/gas interface; $\overline{q}_{g\to l}$: Mean heat flux at the gas/liquid interface; $\overline{\dot{m}}$: Mean evaporation rate; ϵ: Relative error with respect to wall-refined case.

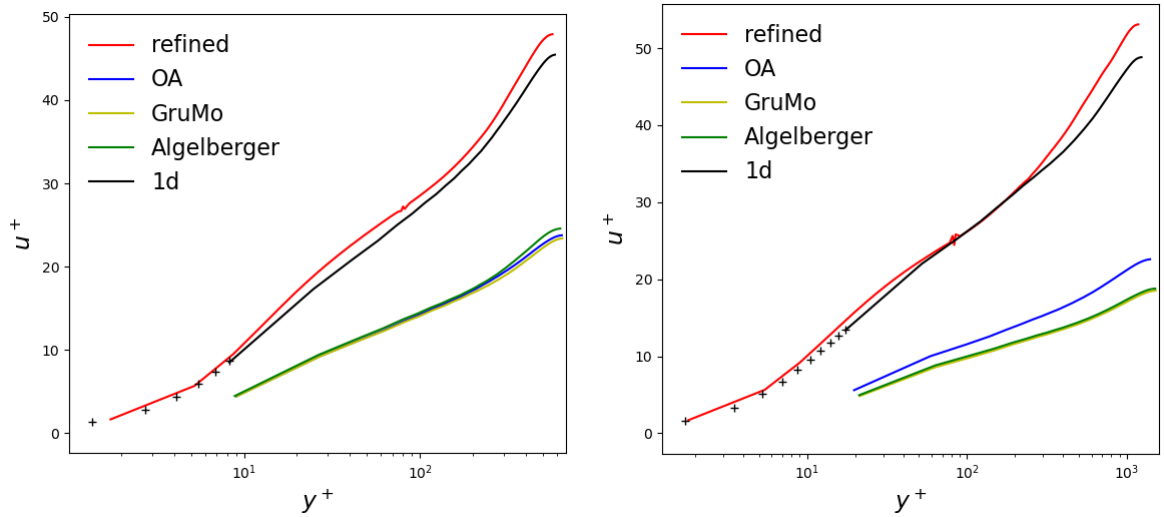

(a) At $Re_\tau = 550$ **(b)** At $Re_\tau = 1100$

Figure 6.5: Normalized mean streamwise velocity in the case of an evaporating wall-film in stationary channel flow: Algebraic and ODEs based WMLES.

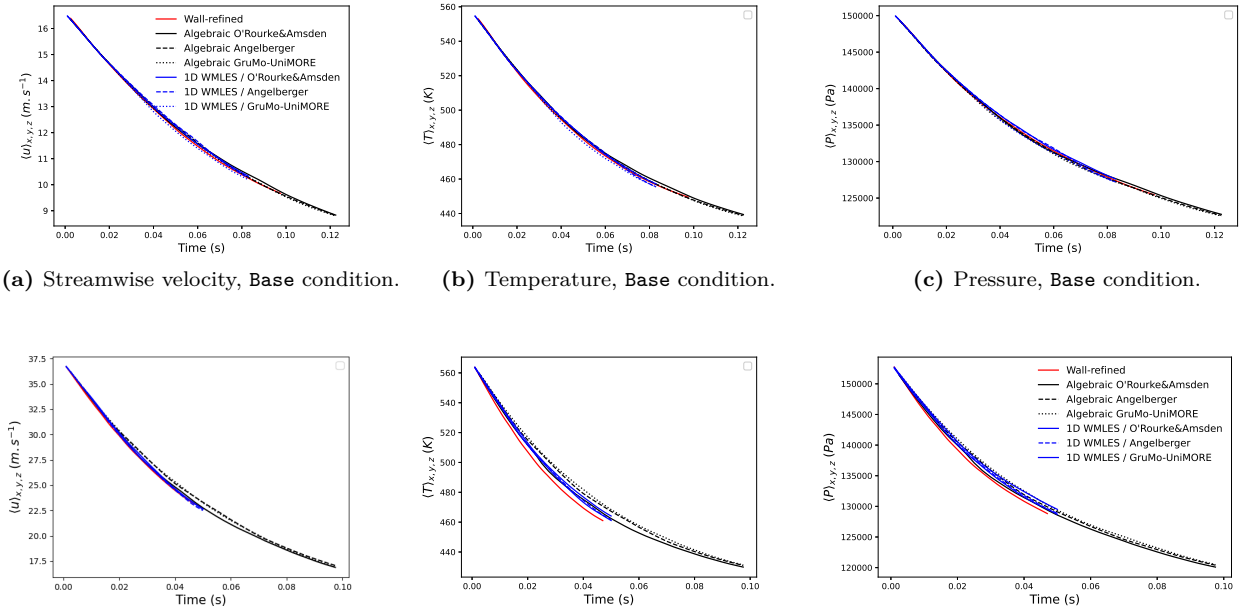

(a) Streamwise velocity, `Base` condition. **(b)** Temperature, `Base` condition. **(c)** Pressure, `Base` condition.

(d) Streamwise velocity, `HighTurb` condition. **(e)** Temperature, `HighTurb` condition. **(f)** Pressure, `HighTurb` condition.

Figure 6.6: Evolution of the volumetric average of streamwise velocity, temperature and pressure over the domain for the `Base` and `HighTurb` conditions: Algebraic and ODEs based WMLES.

- Algebraic wall modeling for the dry wall: The assessment of algebraic wall models in the transient wall-film evaporation in section 5.2 showed that the shear stress and the heat flux were relatively well predicted on the dry wall (see Figure 5.22), while modeling issues where pointed out over the wall-film. Thus, ODEs based modeling can be used over the wall-film, while classical algebraic wall models are used over the dry wall.

We opted here for the second choice as it will assess the impact the proposed ODEs based model only on the wall-film evaporation, without changing the remaining wall conditions. So, for the dry wall, the *Werner&Wengle* momentum wall model is used, and the dependence to the choice of the wall heat model is also assessed by considering the three models: *O'Rourke-Amsden*, *GruMo-UnoMORE* and *Angelberger.*

As in Section 5.2, only plots for the `Base` condition and `HighTurb` condition with the coarse mesh grid will be presented here. The new added results are plotted in blue. Figure 6.6 shows the variation over time of the volume average of the streamwise velocity, temperature and pressure. All the results agree very well, indicating that the wall-film in the wall-modeled simulations evaporates in the same conditions as in the wall-refined simulations. Figure 6.7 shows the evolution of the wall-film surface and thickness over time and Figure 6.8 shows the evolution over time of the shear stress, the heat flux, and the evaporation rate averaged on the liquid/gas interface. Before discussing the performance of the new ODEs based wall-film modeling, we point out first that, for all the conditions, the choice of the wall heat model used for the dry wall has almost no impact on the new results. This independence was expected as the different algebraic wall heat models already predicted similar results over the dry wall in section 5.2 (see Figure 5.22).

One can easily notice the net improvement brought by the ODEs based evaporation modeling compared with algebraic evaporation modeling. Figure 6.7 shows that the total evaporation time, as well as the evolution over time of the wall-film thickness and surface, predicted with the proposed ODEs based model are much closer to the wall-refined than the ones obtained by the algebraic models. Quantitative comparison is summarized

		wall-refined	Algebraic wall-model			ODEs based wall-model
			O'Rourke-Amsden	*Angelberger*	*GruMo-UnoMORE*	
`Base`		180.9	134.1 (-26%)	146.1 (-19%)	135.5 (-25%)	165.8 (-8%)
`ThickFilm`		149.5	117.2 (-22%)	120.4 (-19%)	117.6 (-21%)	132.8 (-11%)
`ColdWall`		84.2	73.9 (-12%)	73.6 (-13%)	73.9 (-12%)	81.0 (-4%)
`HighTurb`	coarse mesh	313.5	209.4 (-33%)	179.2 (-43%)	176.3 (-44%)	274.0 (-13%)
	medium mesh		233.9 (-25%)	238.6 (-24%)	233.5 (-26%)	268.1 (-14%)

Table 6.3: Wall-refined and wall-modeled GER for each condition, with errors with respect to wall-refined results: Algebraic and ODEs based WMLES.

in Table 6.3 which gives the Global Evaporation Rate (GER) (defined in section 5.2) obtained with the different modeling approaches and their relative errors with respect to wall-refined results. The relative error ranges with the ODEs based modeling approach between 4%, for the `ColdWall` condition, and about 13%, for `HighTurb` condition with the coarse mesh grid, while it ranges between about 12% and 33% at best using the algebraic wall-film modeling for the same conditions. This new wall-film modeling approach gives also very close results for the condition `HighTurb` with both coarse and medium mesh grids, suggesting that the results are less dependent less on the wall cell size unlike the algebraic wall-film modeling.

According to Figure 6.8, the shear stress at the liquid/gas interface predicted by the ODEs based model is closer to the wall-refined result. However, qualitatively, one can notice that the improvement of the error compared to the algebraic modeling is as relevant as the made improvement in the previous stationary assessment, highlighting the relevance of transient effects which are not considered in the present ODEs formulation. The heat flux and the evaporation are also always better predicted with the new proposed model. The evaporation rate agree now very well with the wall-refined results, especially for the `Base` condition (Figure 6.8c). The new model succeeds in the prediction of the exponential increase of the evaporation rate at the end of the wall-film evaporation, while it was not the case with algebraic models. It is also interesting to note that, using the algebraic semi-analytical model, a higher over-estimation of the heat flux lead to lower error on the evaporation rate (see "Algebraic *O'Rourke-Amsden*" result in Figures 6.8e and 6.8f), while the errors on the predicted heat flux and evaporation rate are no longer directly related with ODEs based model. In all the cases, the additional cpu time due to the use of the ODEs based modeling didn't exceeded 12% relatively to the cpu time when algebraic models are used, which is an acceptable additional computational cost given the improvements of the results.

6.5 Conclusion

In this chapter, the ODEs based WMLES was extended in order to improve wall-film evaporation modeling. The evaporated species balance equation is solved in the wall normal direction along with the momentum and energy equations. The proposed formulation takes into account the transpiration effect through the wall normal advection term in the wall normal direction and also in the near wall turbulent viscosity modeling. The assessment of the present ODEs based model shows clearly the improvement made compared to the algebraic wall models in both stationary and transient configurations and for all the considered conditions. The stationary assessment shows that the effect of evaporation on the turbulent boundary layer was well modeled as the shear stress at the liquid/gas interface was very well predicted. The heat flux between the liquid and gas phases and the evaporation rate were also improved compared to algebraic wall models and the remaining error are maybe related to the simplistic heat and mass turbulent transport considered in the present ODEs formulation (constant Pr_t and Sc_t). The transient assessment show that the wall-film evaporation dynamic is much better modeled, and this independently of the wall cell size. Hence, the proposed formulation can be considered as first step toward the development of a general strategy for ODEs based WMLES with heat and mass transfer.

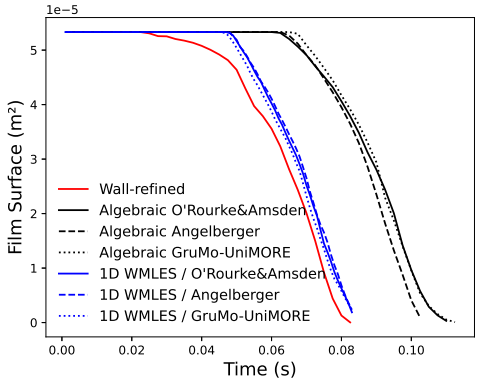

(a) Film surface, `Base` condition.

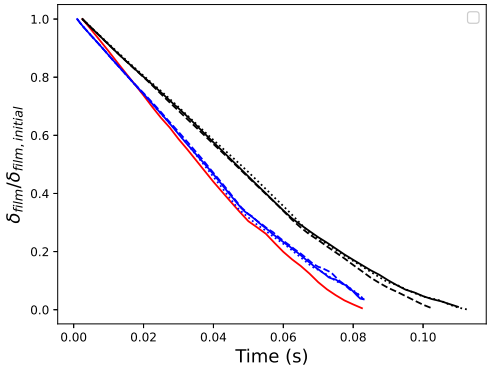

(b) Film thickness, `Base` condition.

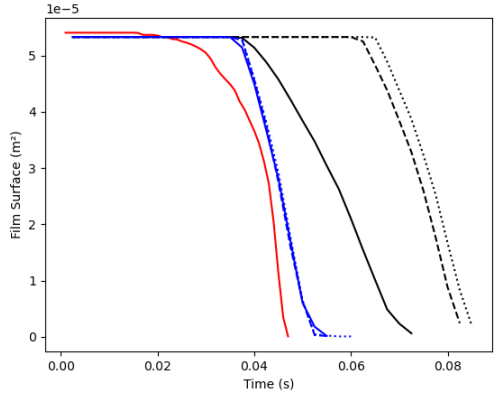

(c) Film surface, `HighTurb` condition.

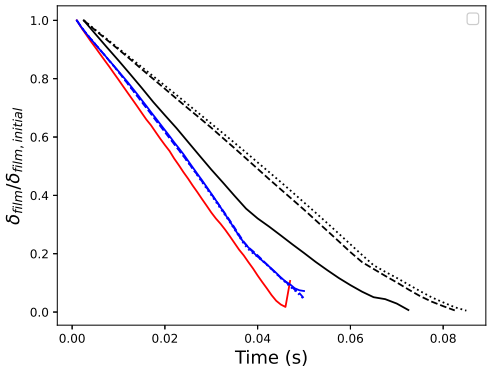

(d) Film thickness, `HighTurb` condition.gh

Figure 6.7: Evolution of wall-film surface and thickness for the `Base` and `HighTurb` (coarse mesh) conditions: Algebraic and ODEs based WMLES.

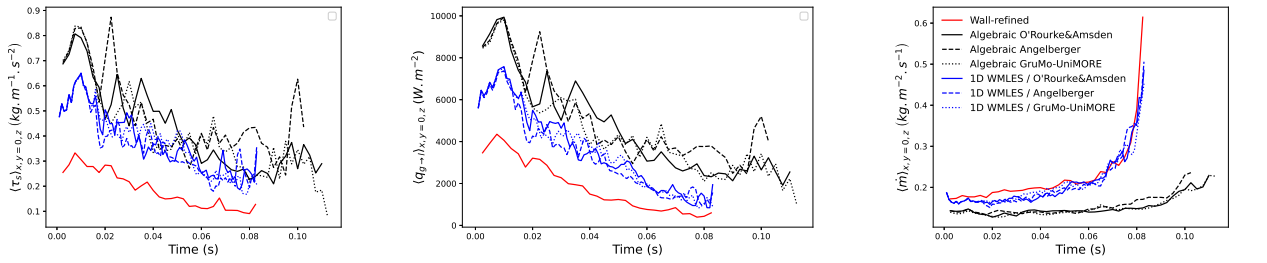

(a) Shear stress, `Base` condition. **(b)** Heat flux, `Base` condition. **(c)** Evaporation rate, `Base` condition.

(d) Shear stress, `HighTurb` condition. **(e)** Heat flux, `HighTurb` condition. **(f)** Evaporation rate, `HighTurb` condition.

Figure 6.8: Evolution of shear stress, heat flux and evaporation rate at the liquid/gas interface for the `Base` and `HighTurb` (coarse mesh) conditions: Algebraic and ODEs based WMLES.

Part III

LES of Flame-Film Interaction

Chapter 7

Flame-Wall Interaction

Contents

Combustion modeling is a key step in the simulation of Flame-Film Interaction (FFI) configuration. The Thickened Flame Model (TFM) is used during this work as it allows to model the detailed chemistry needed for the soot modeling. In this chapter, we will focus as a first step on the combustion modeling and the Flame-Wall Interaction (FWI) simulation. The use of TFM for the simulation of FWI will be investigated in two configurations: first in 1D flame HOQ case then in the turbulent channel flow case. The 1D flame HOQ configuration will give a first insight of the influence of TFM on the quenching phenomena. The FWI in turbulent channel flow will assess the use of TFM along with the wall modeling.

7.1 Combustion modeling

In GDI engines, the fuel chemical energy is mainly released through a propagating premixed flame. Laminar premixed flame is a fundamental canonical case to understand combustion process. This section provides some theoretical aspects about laminar and turbulent premixed flames. A general overview of turbulent combustion modeling is provided, then the Thickened Flame Model (TFM) is described.

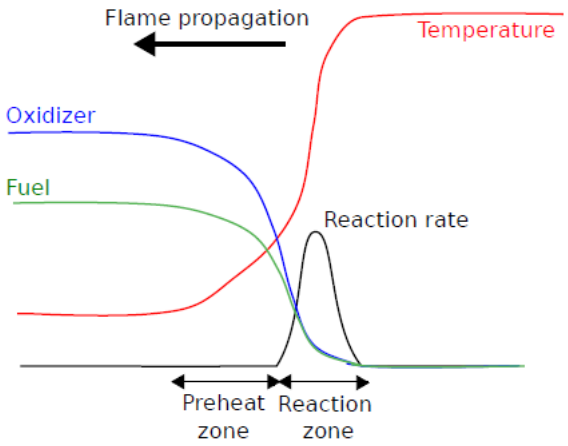

Figure 7.1: Scheme of a premixed flame structure

7.1.1 Laminar premixed flame

In premixed flame, fuel and oxidizer are considered to be perfectly mixed before combustion. As illustrated in figure 7.1, the flame front separates the fresh and the burnt gases. Because of the strong temperature gradient and the corresponding thermal fluxes, the fresh gases are preheated and then start to burn. The flame propagates towards the fresh gases with a thickness δ_L and a speed S_L, which depend on various parameters: fresh gases composition, temperature and pressure. The fresh gas composition is characterized by the equivalence ratio ϕ, defined as the ratio of the fuel-to-oxidizer ratio to the stoichiometric fuel-to-oxidizer ratio:

$$\phi = \frac{Y_F/Y_{Ox}}{(Y_F/Y_{Ox})_{st}} \tag{7.1}$$

where Y_F and Y_{Ox} are respectively the fuel and oxidizer mass fractions in the fresh gas. At stoichiometric conditions st ($\phi = 1$), the fuel and the oxidizer are completely transformed into products. When $\phi < 1$, the mixture is lean corresponding to an excess of oxidant, and when $\phi > 1$ the mixture is rich, the oxidizer becomes the limiting reactant. The flame can be described using a progress variable Θ, such as $\Theta = 0$ in the fresh gases and $\Theta = 1$ in the fully burnt gases. This progress variable may be defined as a reduced temperature as:

$$\Theta = \frac{T - T_u}{T_b - T_u} \tag{7.2}$$

where T, T_u, T_b are respectively the local, the unburnt gases and the burnt gases temperatures. Another typical choice to define the progress variable is based on the major products of combustion as:

$$c = \frac{Y_c}{Y_c^{eq}} \tag{7.3}$$

where typically $Y_c = Y_{CO} + Y_{CO_2} + Y_{H_2O}$ and the superscript ^{eq} denotes the equilibrium value. The characteristic flame thickness can be given by:

$$\delta_L = \frac{\lambda_u}{\rho_u C_p S_L} \tag{7.4}$$

The characteristic flame thickness can be also evaluated using the temperature gradient:

$$\delta_L = \frac{T_b - T_u}{max\,(\nabla T)} \tag{7.5}$$

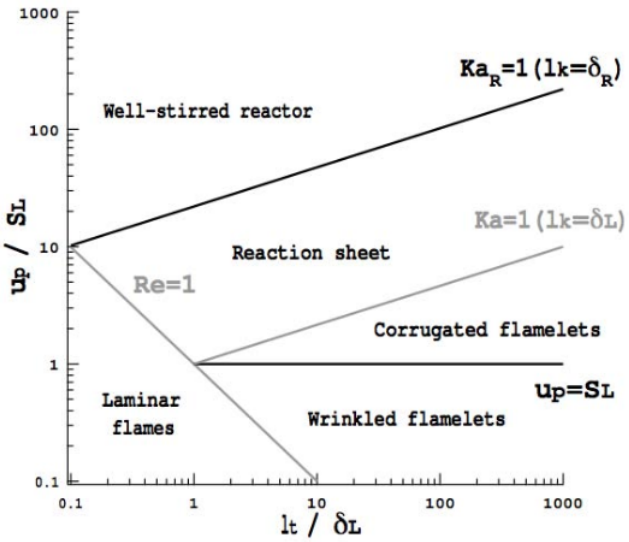

Figure 7.2: Turbulent premixed combustion diagram [105].

The flame speed is expressed by:

$$S_L = \frac{-1}{\rho_u Y_{F,u}} \int_{-\infty}^{+\infty} \dot{\omega}_F dx \tag{7.6}$$

7.1.2 Flame-turbulence interaction

The interaction between the turbulent flame and the flow can be assessed by comparing the turbulent flow and the flame characteristic time and length scales. From these scales, two essential dimensionless numbers calibrate the flame-turbulence interaction.

- The **Damköhler number** compares the turbulent (τ_t) and the chemical (τ_c) time scales:

$$Da = \frac{\tau_t}{\tau_c} = \frac{l_t}{\delta_L} \frac{S_L}{u'} \tag{7.7}$$

  where l_t is a characteristic turbulent scale and u' is the velocity fluctuation. When $Da \gg 1$, the chemical time is short compared to the turbulent one, corresponding to a thin reaction zone wrinkled and stretched by the flow. The internal structure of the flame is not directly impacted by turbulence and may be described as a laminar flame element called "flamelet". When $Da \ll 1$, reactants and products are strongly mixed by turbulence and react through slow reactions.

- The **Karlovitz number** characterizes the interaction between the reactive scales and the smallest (Kolmogorov) flow scales

$$Ka = \frac{\tau_c}{\tau_\kappa} = \frac{\delta_L}{\eta_\kappa} \frac{u_\kappa}{S_L} \tag{7.8}$$

  where τ_κ, η_κ and u_κ are the characteristic time, length and velocity of the Kolmogorov scales. For $Ka \gg 1$, small eddies penetrate the reaction zones and strongly impact on the overall flame structure.

The turbulent Reynolds number, defined as $Re_t = l_t u'/\nu$, is related to the Damköhler and Karlovitz numbers as follows:

$$Re_t = Da^2 Ka^2 \tag{7.9}$$

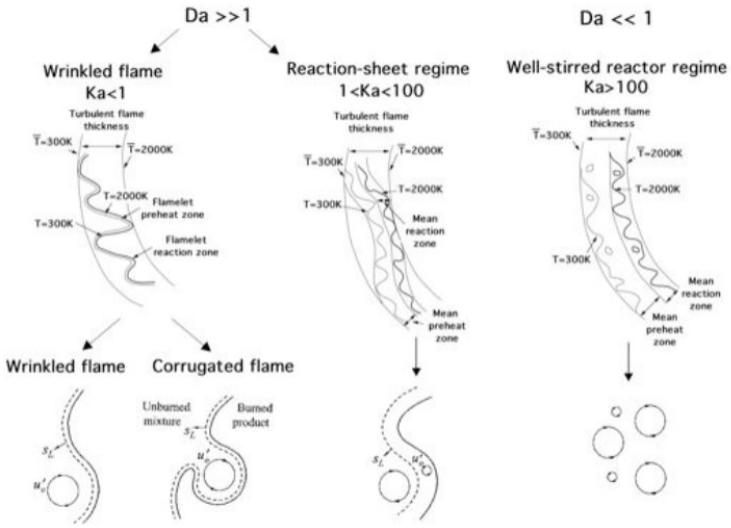

Figure 7.3: Illustration of turbulent combustion regimes [25].

The combustion regimes can be decomposed following the combustion diagram shown in figure 7.2. The following regimes are identified and illustrated in figure 7.3:

- **Laminar flame regime** ($Re_t < 1$): The flow is quasi-laminar and the flame is only slightly wrinkled.
- **Thin flame regime** ($Re_t < 1$, $Ka < 1$): Depending on the velocity ratio u'/S_L it may be decomposed into two regimes:
  - **Wrinkled flamelet regime** ($u'/S_L < 1$): The laminar propagation is predominant and flame-turbulence interaction remains limited.
  - **Corrugated flamelet regime** ($u'/S_L > 1$): Larger structures become able to induce flame front interactions leading to a wrinkled flame with pockets.
- **Thickened wrinkled flame** or **thin reaction zone** ($Re_t > 1$, $1 < Ka < 100$, $Da > 1$): Turbulent motions are able to affect and to thicken the flame preheat zone, but cannot modify the reaction zone which remains thin and close to laminar reaction zone.
- **Well-stired reactor** ($Re_t > 1$, $Ka > 100$, $Da < 1$): Preheat and reaction zones are strongly affected by turbulent motions. The flame has no distinct laminar structure.

7.1.3 The Thickened Flame Model

TFM is one of the main approaches that have been developed to manage the flame thickness issues. It was firstly proposed by O'Rourke and Bracco [106]. The basic idea is to consider a flame thicker than the actual one, as shown in figure 7.4a, but having the same laminar flame speed S_L. According to simple theories of laminar premixed flame, the S_L and the flame thickness δ_L may be expressed as:

$$S_L \propto \sqrt{a\bar{\dot{\omega}}} \qquad \delta_L \propto \frac{a}{S_L}$$

where a is the thermal diffusivity ($\lambda/(\rho c_p)$) and $\bar{\dot{\omega}}$ the mean reaction rate. An increase of the flame thickness δ_L by a factor F with a constant flame speed S_L is achieved by replacing the thermal diffusivity a by Fa and the reaction rate $\bar{\dot{\omega}}$ by $\bar{\dot{\omega}}/F$. If F is sufficiently large, the thickened flame front may then be resolved on

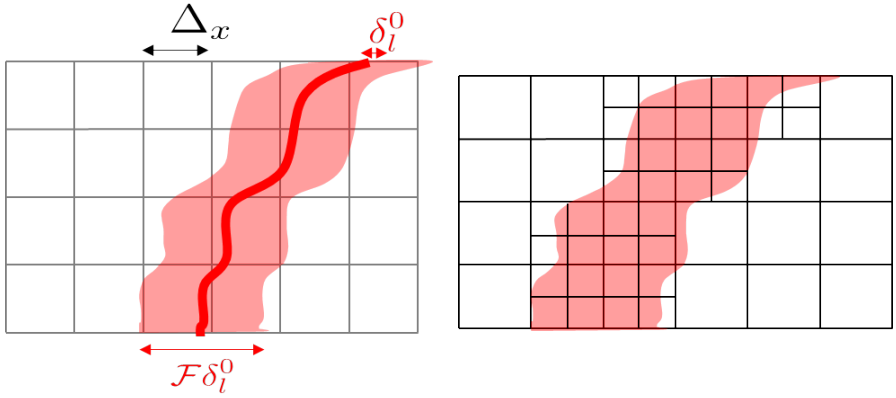

(a) Artificially thickened flame on a uniform mesh grid

(b) TFM coupled to AMR

Figure 7.4: Illustration of the Thickened Flame Model concept.

the LES computational mesh without sub-grid modeling. This has the advantage of describing the chemical reaction as in DNS on the LES computational grid, without an explicit sub-grid scale model. When the flame is thickened, the interaction between turbulence and chemistry may be modified. An efficiency factor E has been derived to counteract this effect [107]:

$$\begin{array}{rccccc} \text{Diffusivity:} a & \rightarrow & Fa & \rightarrow & EFa \\ \text{Reaction rate:} \bar{\dot{\omega}} & \rightarrow & \dfrac{\bar{\dot{\omega}}}{F} & \rightarrow & E\dfrac{\bar{\dot{\omega}}}{F} \\ & & \text{Thickening} & & \text{Wrinkling} \end{array}$$

The thickening factor is adjusted locally to act only in the reaction zone and preserve diffusion in non-reacting regions. The flame front is detected with a flame sensor S with $S = 1$ in the reactive part of the flame and shrinks to zero outside this region. The turbulent diffusion is not considered in the thickened region. The modified balance equation of the filtered species mass fractions Y_k is given by:

$$\frac{\partial \bar{\rho}\tilde{Y}_k}{\partial t} + \frac{\partial \bar{\rho}\tilde{U}_i\tilde{Y}_k}{\partial x_i} = \frac{\partial}{\partial x_i}\left(\left[FE\bar{\rho}D_k + (1-S)\frac{\mu_t}{Sc_t}\right]\frac{\partial \tilde{Y}_k}{\partial x_i}\right) + E\frac{\bar{\dot{\omega}}_k}{F} \tag{7.10}$$

The molecular diffusion coefficient was corrected as done by Quillatre [108]:

$$\bar{\rho}D_k = \frac{\mu F}{Pr\,(F-1) + Sc_k} \tag{7.11}$$

The thermal and species diffusive terms are also modified in the energy equation (2.22).

Flame sensor:

The reactive zone is detected with a chemical sensor defined as:

$$S_{chem} = max\left[min\left(\beta\frac{|\bar{\dot{\omega}}_T|}{\dot{\Omega}_T\,(\phi, T_u, P)} - 1, 1\right), 0\right] \tag{7.12}$$

where $\bar{\dot{\omega}}_T$ is the heat release rate as defined in Eq. (2.23) and $\dot{\Omega}_T$ is the maximal heat release rate tabulated from 1D laminar premixed flames for different equivalence ratios, unburnt temperatures and pressures. If too many species and reactions are considered, the flame structure is complex and the chemical sensor defined above fails at capturing the gradients at the flame trailing and leading edges because the sensor only detects

the narrow fuel oxidation layers. To overcome this problem, Jaravel [109] introduced a transported indicator function ψ using a relaxation procedure to broaden the sensor. It is transported in the flow according to:

$$\frac{\partial \bar{\rho}\tilde{\psi}}{\partial t} + \frac{\partial \bar{\rho}\tilde{U}_i\tilde{\psi}}{\partial x_i} = \frac{\partial}{\partial x_i}\left(\left[FE\frac{\mu}{Sc_\psi} + (1+S)\frac{\mu_t}{Sc_t}\right]\frac{\partial \tilde{\psi}}{\partial x_i}\right) + \bar{\dot{\omega}}_\psi \tag{7.13}$$

where $Sc_\psi = Sc_t$ and $\bar{\dot{\omega}}_\psi$ is a relaxation source term, computed as:

$$\begin{cases} \bar{\dot{\omega}}_\psi = \frac{0-\tilde{\psi}}{\tau_1} & \text{if } S < 0.05 \\ \bar{\dot{\omega}}_\psi = \frac{\psi_0-\tilde{\psi}}{\tau_0} & \text{if } S > 0.8 \end{cases} \tag{7.14}$$

with $\psi_0 = 20$, $\tau_0 = 20$ and $\tau_1 = \alpha_1\tau_c$ are relaxation times where $\tau_c = \delta_L/S_L$ is a characteristic combustion time scale and α_1 a dimensionless parameter, S is the flame sensor given by Eq. (7.16). Different α_1 values are chosen at the flame foot and tail:

$$\begin{cases} \alpha_1 = \alpha_1^{cold} = 0.05 & \text{if } T \leqslant T_s \\ \alpha_1 = \alpha_1^{hot} = 0.005 & \text{if } T > T_s \end{cases} \tag{7.15}$$

where $T_s = T_u + 1000K$ is a temperature selected to separate the fresh and burnt gas regions. The sensor S is finally filtered according to:

$$S = max\left(min\left(\tilde{\psi}, 1\right), S_{chem}\right) \tag{7.16}$$

In this work, the chemical sensor was also clipped according to the progress variable:

$$\begin{cases} S_{chem} = max\left[min\left(\beta\frac{|\bar{\dot{\omega}}_T|}{\bar{\Omega}_T(\phi,T_u,P)} - 1, 1\right), 0\right] & \text{if } 0.3 < c < 0.9 \\ S_{chem} = 0 & \text{otherwise} \end{cases} \tag{7.17}$$

Thickening factor:

The flame thickening factor is given by:

$$F = 1 + (F_{target} - 1)\,S \tag{7.18}$$

where the target thickening factor in the flame is given by:

$$F_{target} = \frac{n_{res}\Delta_x}{\delta_L} \tag{7.19}$$

where Δx is the LES grid size, n_{res} is a user specified model parameter representing the number of cells in the flame front and δ_L is the laminar flame thickness. δ_L is tabulated from 1D laminar premixed flames computed at several equivalence ratios, unburnt temperatures and pressures. Mehl et al. [110] coupled TFM with the AMR algorithm to reduce the computational cost by refining in the flame front and allowing coarser mesh otherwise, as shown in figure 7.4b. When TFM-AMR coupling is active, F_{target} becomes a user specified parameter and the mesh cell is divided by two in the three directions. Hence, the characteristic mesh size in regions where AMR is active is given by:

$$\Delta_x^{AMR} = \frac{\Delta_x^{Base}}{2^{n_{AMR}}} \tag{7.20}$$

where Δ_x^{Base} is the base mesh cell size, i.e. when the AMR is deactivated, and n_{AMR} is the AMR level. When the flame sensor $S > 0$, the AMR level is computed from the local flame conditions to reach the target flame thickening F_{target} as:

$$n_{AMR} = int\left[\frac{1}{log\,(2)}log\left(\frac{n_{res}\Delta_x^{Base}}{\delta_L F_{target}}\right)\right] \tag{7.21}$$

By setting $F_{target} = 1$, the TFM-AMR coupling is also an efficient way to detect the flame and activate the AMR for a resolved flame front simulation, i.e. chemistry computation without additional combustion modeling.

Efficiency factor:

The efficiency factor is estimated as the flame wrinkling factor Ξ_Δ [107, 111] clipped with the flame sensor:

$$E = 1 + (\Xi_\Delta - 1)\, S \tag{7.22}$$

where $\Delta = F\delta_L^0$ is the flame filter size. The flame wrinkling factor is computed using the non-dynamic Charlette et al. [111] model:

$$\Xi_\Delta \left(\frac{\Delta}{\delta_L}, \frac{u'_\Delta}{S_L} \right) = \left(1 + min \left[\frac{\Delta}{\delta_L} - 1, \Gamma \left(\frac{\Delta}{\delta_L}, \frac{u'_\Delta}{S_L}, Re_\Delta \right) \frac{u'_\Delta}{S_L} \right] \right)^{\beta_\Xi} \tag{7.23}$$

where Γ is an efficiency function proposed by Bougrine et al. [112] which accounts for the effect of turbulent eddies with sizes ranging from the Kolmogorov scale η to TFM filter size Δ. u'_Δ is the subgrid velocity at scale Δ modeled as done by Colin et al. [107], $Re_\Delta = u'_\Delta \Delta / \nu$ the subgrid Reynolds number and β_Ξ a model constant set here at $\beta_\Xi = 0.5$.

7.2 FWI simulation

7.2.1 Phenomenological description of FWI

Flame-Wall Interaction (FWI) is found in most practical industrial systems. The overall phenomenon of FWI is quite complex. In laminar flows, FWI can occurs in three different configurations: (i) Head-On Quenching (HOQ), (ii) Side Wall Quenching, and (iii) Tube Quenching, as illustrated in Figure 7.5. The canonical case of 1D HOQ configuration is generally considered as a base reference for the FWI study and widely investigated in the literature [31, 113, 114]. In the following, the main phenomenological description will be first presented for the flame HOQ configuration. Then the additional influence of turbulence will be briefly presented.

7.2.1.1 Premixed flame Head-On Quenching

Head On Quenching (HOQ) occurs when a premixed flame front propagates into fresh gas towards a wall as show in Figure 7.5. This case is characterized by two main parameters:

- The distance y_{flame} between the flame front position, defined with certain isotherm, and the wall. The wall distance can be scaled by the characteristic flame thickness, as defined in Eq. (7.4), to define the Peclet number:
$$P = \frac{\rho_u c_{p,u} S_L y_{flame}}{\lambda_u} \tag{7.24}$$
- The wall heat flux q_w, which can also be scaled by the reference flame power, to define a reduced wall heat flux:
$$\mathcal{F} = \frac{|q_w|}{\rho_u S_L c_{p,u} (T_b - T_u)} \tag{7.25}$$

The flame-wall distance and the wall heat flux change over time during the HOQ. Poinsot et al. [113] performed a DNS of 1D laminar premixed flame HOQ configuration using a single step chemistry. The normalized heat flux and Peclet number they computed are plotted as function of normalized flame time $t_F = \delta_L / S_L$ in Figure 7.6. The flame position is defined as the distance between the wall and the isotherm equal to $0.9\,(T_b - T_u) + T_u$. The minimal distance between the flame front and the wall defines the quenching

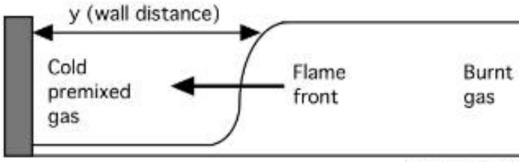

(a) Head-On Quenching

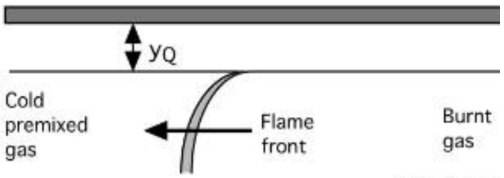

(b) Side Wall Quenching

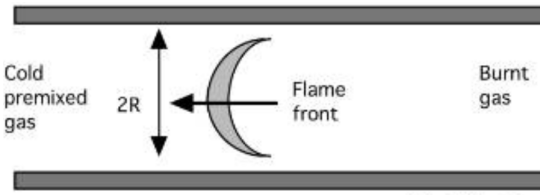

(c) Tube Quenching

Figure 7.5: Configurations for flame/wall interaction in laminar flows [25].

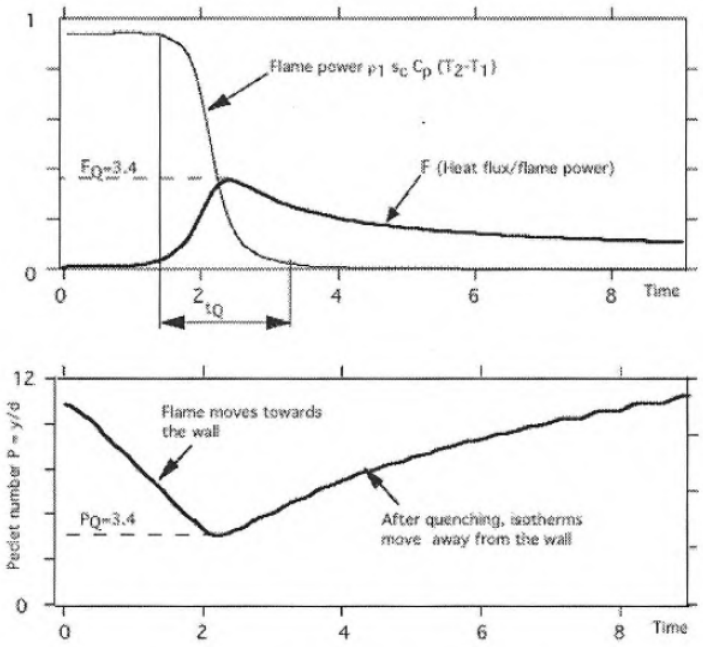

Figure 7.6: Simulation of Head on Quenching (HOQ) interaction [113].

distance. When the distance is minimal, the wall heat flux reaches its maximum. This is because the wall acts as heat sink. Quenching occurs when the rate of the heat loss through the wall is greater than the rate of internal heat generated by chemical reactions. In the simulation of Poinsot et al. [113], the reduced maximum wall heat flux was found equal to 0.34, which was in agreement with theoretical value given by Wichman and Bruneaux [114]. Hasse et al. [31] found that maximum reduced wall heat flux is about 0.41 during the HOQ of iso-octane/air at 10 bars simulated with complex chemistry. Although the quenching occurs when the maximum wall heat flux is reached, the flame power begins to decrease before that moment. Therefore, two zones can be recognized: the influence and the quenching zone. After the quenching, Wichman and Bruneaux [114] noted that there is no real extinction since the flame still consumes fuel. The reaction rate moves toward the burned gases, where conditions are more propitious to its existence. Even if the reaction rate becomes low, the fuel remaining near the wall diffuses into the reaction zone feeding the flame.
It is also interesting to mention that the near wall low temperature may have strong kinetic effects on the near wall combustion. The iso-octane flame HOQ simulation performed by Hasse et al. [31] with complex chemistry highlighted the significant impact of the Soret effect on the post oxidation process as it slows down the transport of UHCs into the hot gas region where they can be oxidized. Surface chemistry can have also an influence on the near-wall flame quenching as intermediate combustion radicals can be adsorbed by wall surface reactions [33].

7.2.1.2 Turbulent FWI

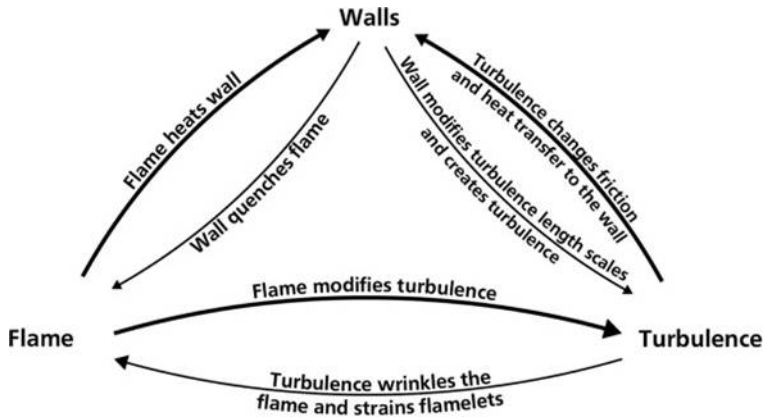

Figure 7.7: Interactions between walls, flame and turbulence [25].

Figure 7.7 summarizes the flame-wall-turbulence interaction. In addition to the local thermal effect between the flame and the wall, the wall modifies the flow turbulence, which modifies the flame turbulence interaction by decreasing the turbulent stretch and the flame wrinkling as illustrated in Figure 7.8. By the analysis of two-dimensional DNS of turbulent premixed FWI, Poinsot et al. [113] introduced a flame surface density balance that depends on the dimensionless distance from the wall. Bruneaux et al. [1] performed a DNS of FWI in turbulent channel flow where two flame fronts were initialized in the center of fully developed turbulent channel flow and propagate toward the walls as shown in Figure 7.9. The simulation was performed with a constant density and constant viscosity flow, allowing to investigate the effect of the wall on local and global flame structure, but not the effect of the flame on the near wall turbulence. They concluded that in turbulent flows the wall heat fluxes are much higher than in laminar FWI. Based on this DNS data, Bruneaux et al. [115] developed a flame surface density balance equation that accounts for the turbulent interaction with the wall through the enthalpy loss in isobaric conditions and using the approximation of the evolution of the flame speed during HOQ provided by the theoretical analysis of Wichman and Bruneaux [114]. This model was later extended by Angelberger et al. [116] to allow for non-isobaric engine combustion. More recently, Demesoukas et al. [117] proposed an algebraic model for the flame wrinkling factor for near wall flamelet based combustion modeling approach.

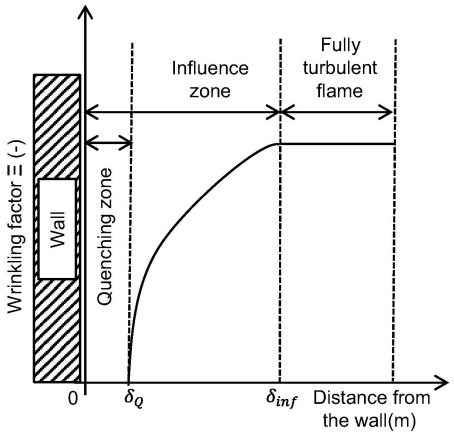

Figure 7.8: Effect of the wall on the flame wrinkling during turbulent FWI [117].

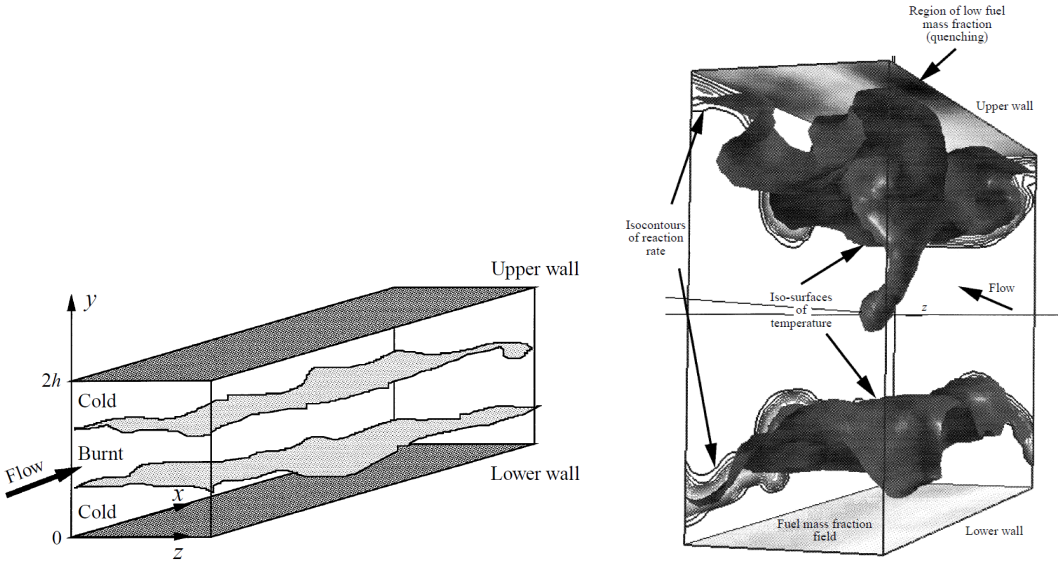

(a) Configuration of FWI in turbulent channel flow.

(b) Instantaneous snapshot of iso-surfaces of temperature.

Figure 7.9: DNS of FWI in turbulent channel flow performed by Bruneaux et al. [1].

FWI affects also the near wall turbulent heat transport and the wall heat modeling. Truffin et al. [118] proposed a model, named α-model, for the heat transferred to the wall during the quenching of two-dimensional turbulent flame. The α-model is based on the flame surface density concept and was used along with the Coherent Flame Model. Leveugle [119] further investigated this wall modeling approach for 3D RANS simulation of FWI. Recently, Bolla et al. [120] proposed an interesting novel algebraic WMLES approach for wall heat transfer for FWI in ICE based on intuitive arguments rather than physics based modeling.

7.2.2 On the use of TFM for FWI simulation

During this work, we use the TFM combustion model for FWI simulation. In the case of flame HOQ in 1D configuration, i.e. without considering the effect of turbulence, the use of TFM may arise few issues and questions:

- **Thermal issue:** As the flame front is thickened with a factor F, the temperature gradient in the flame front is also divided by a factor F. As described previously, the quenching phenomena occurs when the rate of heat loss through the wall is greater than the rate of internal heat generated by chemical reactions. So, what is the influence of this artificially modified temperature gradient on the wall heat flux when the flame front reaches the wall ? and consequently on the HOQ phenomena ?

- **Geometrical issue:** The artificially thickened flame front thickness is $F\delta_L$, with F in the order of 40 in practical ICE simulation. However, the quenching distance is in the order of few δ_L. So, how this geometrical limitation will affect the HOQ phenomena ?

It is also interesting to note that TFM is based on simple theories of laminar premixed flames to guarantee a correct adiabatic free flame speed. The reference heat release rate, the laminar flame thickness and speed used for the computation of the flame sensor and the thickening factor are then tabulated using adiabatic free flames. During HOQ phenomena, the behavior of a free flame is considerably altered until complete quenching and the combustion is no longer adiabatic. The consideration of the adiabatic effect on an artificially thickened flame with tabulated chemistry has already been the subject of some works in the literature [121, 122]. In this work, the chemistry is directly solved and the effect of heat loss on the chemical reactions will be automatically captured. Furthermore, the flame sensor and thickening factor should not necessary be exact. The tabulated laminar flame parameters should mainly allow to well detect the flame front and apply an appropriate thickening to solve the chemistry. For these reasons, the effect of wall heat loss on the tabulated flame parameters was not considered for this work.
When the turbulence influence is added to the FWI phenomena, additional modeling issues should be considered:

- **Near wall flame wrinkling:** The unresolved flame wrinkling is modeled by the efficiency factor E. As mentioned earlier, the flame/turbulence interaction is modified during FWI, and thus, a proper modeling of the efficiency factor is needed near the wall.

- **Wall modeling:** During FWI, the burnt gases expansion and high temperature modify the flow properties (viscosity greatly increased and density decreased in burnt gases), which affects the near wall turbulence.This modification is enhanced when the flame front is artificially thickened as the temperature profiles are stretched and the flow is laminarized. Thus, it is expected that TFM will have an influence on the wall shear stress and heat flux modeling.

In LES of a homogeneous-charge spark-ignition engine, Shekhawat [123] showed that using TFM for combustion modeling without any particular treatment leads to a lower engine pressure in the expansion stroke than the experimental envelope. He also noted that imposing $F = 1$ at the wall cell leads to an overall increase of the engine pressure and results were closer to the experimental envelope during expansion stroke. To our best knowledge, there are no works in the literature that investigated in details the problems raised above when TFM is used for FWI. In the following, we will try to better understand the influence of TFM on the simulation of FWI through two academic configurations.

- **1D HOQ of premixed flame in ICE relevant conditions:** This case will give a first insight on the influence of using TFM in the prediction of the wall heat flux, the fuel consumption rate and the quenching distance. A focus will be given to the influence of the used thermal conductivity in wall heat flux expression. The influence of the thickening factor F will be also investigated.

- **FWI in turbulent channel flow:** This case allows to include the influence of turbulence. The modeling of the flame wrinkling will not be investigated in this work. The focus will be given only to the influence of algebraic wall models.

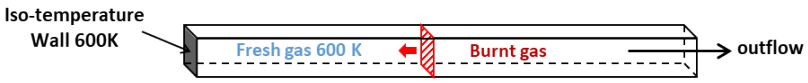

Figure 7.10: 1D case configuration of flame wall interaction.

7.3 Head-On Quenching configuration in engine relevant conditions

7.3.1 Case setup

Configuration

CONVERGE is a 3D CFD sotware and the governing equations are only written in a Cartesian 3D form. 1D configuration refer here to a 3D configuration with mesh cells disposed along one direction. As shown in Figure 7.10, the case is initialized with a premixed flame front propagating toward the wall in a static fresh gas mixture. The boundary condition in the fresh gas side is therefore a slip wall with an imposed temperature and a zero-gradient for pressure and species. The boundary condition in the burnt gas side is an outflow boundary condition. The remaining boundary conditions are slip walls with a zero-gradient for pressure, temperature and species. Cantera [26] is used to generate the initial free flame temperature and species profiles. In all the following cases, the mesh grid is uniform in the computation domain.

Selected conditions

The fresh gas is an iso-octane/air mixture with an equivalence ration equal to 1. Fresh gas temperature is set to 600K and pressure is set to 20 bars to be as close as possible to engine conditions at the beginning of the expansion stroke. The wall temperature is also set to 600K to avoid heat transfer before the flame-wall interaction. The chemical mechanism of An et al. [124] was considered for this case. It is a skeletal Toluene Reference Fuels oxidation mechanism consisted of 85 species and 232 reactions, and specifically developed for gasoline surrogates combustion at high pressures and for GDI engines simulations. In the selected temperature, pressure and mixture conditions, the premixed flame thickness based on the maximum temperature gradient δ_L (as defined in Eq. (7.5)) is equal to $34\mu m$ and the laminar flame speed S_L is equal to $0.439 m.s^{-1}$.

7.3.2 Reference results

In this reference case, the chemistry is directly computed without any additional combustion modeling. Thus, the mesh should be sufficiently refined to properly resolve the flame front. The wall heat flux is expressed using the gas thermal conductivity and the temperature gradient at the wall:

$$q_w = \lambda_w \left.\frac{\partial T}{\partial y}\right|_w \tag{7.26}$$

A first order approximation is always used to evaluate the temperature gradient: $\left(\partial T/\partial y\right)_w = \left(T_1 - T_w\right)/y_1$, where T_1 and y_1 are respectively the temperature and the wall distance at the center of the wall adjacent cell (see Figure 3.3). Thus, the mesh should be also sufficiently refined to well capture the wall temperature gradient during the HOQ phenomena. In order to insure both proper flame resolution and a correct estimation of the wall temperature gradient, the case will be performed with two different mesh cell sizes: $\Delta y = \delta_L/6$ and $\Delta y = \delta_L/20$. Figure 7.11 shows the evolution of the dimensionless wall heat flux, the integral wall heat flux over time, the flame speed computed using Eq. (7.6), and the evolution of the Peclet number. For all these quantities, the results obtained using the two mesh cell sizes are very close. In the following, the results obtained with $\Delta y = \delta_L/20$ will be considered as reference.

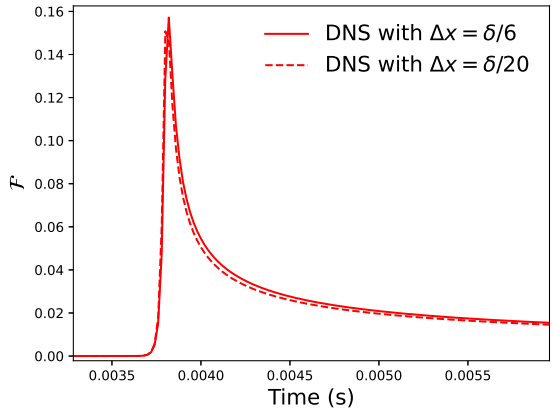

(a) Adimentional wall heat flux

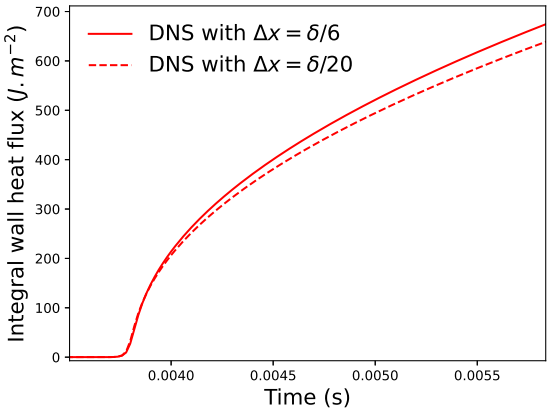

(b) Integral wall heat flux

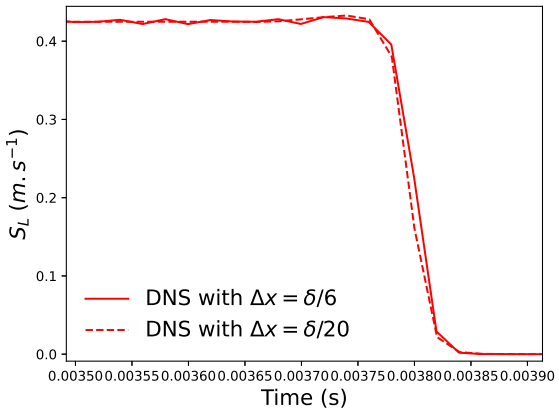

(c) Flame speed

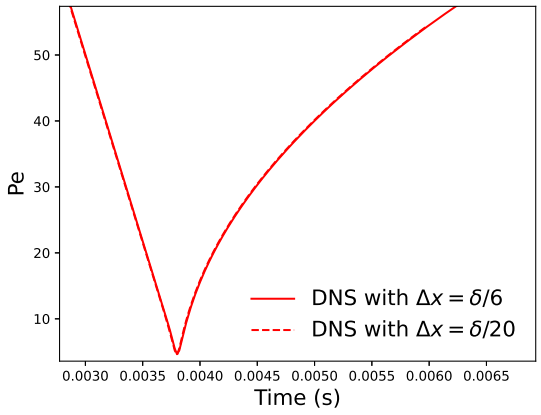

(d) Adimentional distance

Figure 7.11: Convergence of the reference result of the flame HOQ case.

		Thermal conductivity used for the wall heat flux		
		λ_w	$F\lambda_w$	λ_1
Thickening factor	$F = 44$	———	———	———
	$F = 22$	- - - -	- - - -	- - - -
	$F = 11$	.....	.....	.....

Table 7.1: Line stiles and colors used for the different cases of flame HOQ simulation using TFM

7.3.3 HOQ simulation using TFM

As pointed out in section 7.2.2, using TFM for the simulation of flame HOQ rises some modeling issues, the thermal and geometrical issues related to the artificial stretching of the flame front. Cantera [26] is used to set the adiabatic free flame characteristics needed to set TFM cases (laminar flame thickness, speed, and maximum heat release rate). The applied thickening factor is computed according to expression (7.19). n_{res} is set equal to 6 here. A typical mesh cell size used for the LES ICE simulation is in the order of $250\mu m$, which leads to thickening factor of 44. In order to study the effect of the thickening factor on the simulation of flame HOQ, three mesh grids with different cell sizes where considered: $\Delta y = 250\mu m$, $125\mu m$ and $62.5\mu m$, leading to thickening factors of 44, 22 and 11 respectively. The influence of TFM on the flame HOQ phenomena can be investigated in two main ways: (i) by investigating the influence of TFM formulation near the wall, (ii) by investigating the influence of the expression of the wall heat flux. Various approaches of disabling the thickening at a certain distance before the wall were tested during this thesis, but without leading to an interesting result. In the following, only the influence of the formulation of the wall heat flux is investigated, without any particular treatment of TFM near the wall.

Tested wall heat flux expressions

The simplest way to express the wall heat flux is by using the gas thermal conductivity and the temperature gradient at the wall as in the reference case (q_w as expressed in Eq. (7.26)). However for an artificially thickened flame front, the temperature gradient is divided with a factor F. Thus, one may intuitively suggest to enhance the wall thermal conductivity also by a factor F ($F\lambda_w$) in order to recover a correct heat loss during HOQ. A third way to express the wall heat flux is by considering the temperature gradient at the wall but with the thermal conductivity evaluated at the center of the wall adjacent cell:

$$q_w = \lambda_1 \left.\frac{\partial T}{\partial y}\right|_w \tag{7.27}$$

One can expect that this expression will lead to a wall heat flux higher than the one obtained with λ_w, as $\lambda_1 > \lambda_w$ when the flame front reaches the wall, but lower than $F\lambda_w$ for the F values applied in this case. The fact of using λ_1 instead of λ_w may seem unjustified and completely *ad-hoc* at first glance, but the relevance of testing such an expression in this case will be justified later when testing the wall heat models in the turbulent case. Table 7.1 summarizes the 9 tested TFM cases to investigate both the influence of the thickening factor and the expression of the wall heat flux, along with line style and color used for each case in the next plots.

Results and discussion

Figure 7.12 shows the evolution of the temperature profile of the different cases during the HOQ. At t=0.024, all the temperature profiles are not yet influenced by the wall, and cases with same thickening factor and different wall heat expressions are superposed. At t=0.0254, corresponding to the quenching instant of the reference case, the influence of the expression of the wall heat flux can be seen on the cases with $F = 44$ and $F = 22$, where lower temperature gradients at the wall are obtained using $F\lambda_w$, and still similar profiles are obtained with both λ_w and λ_1. At t=0.0259, all the cases with λ_w and λ_1 recover temperature profiles

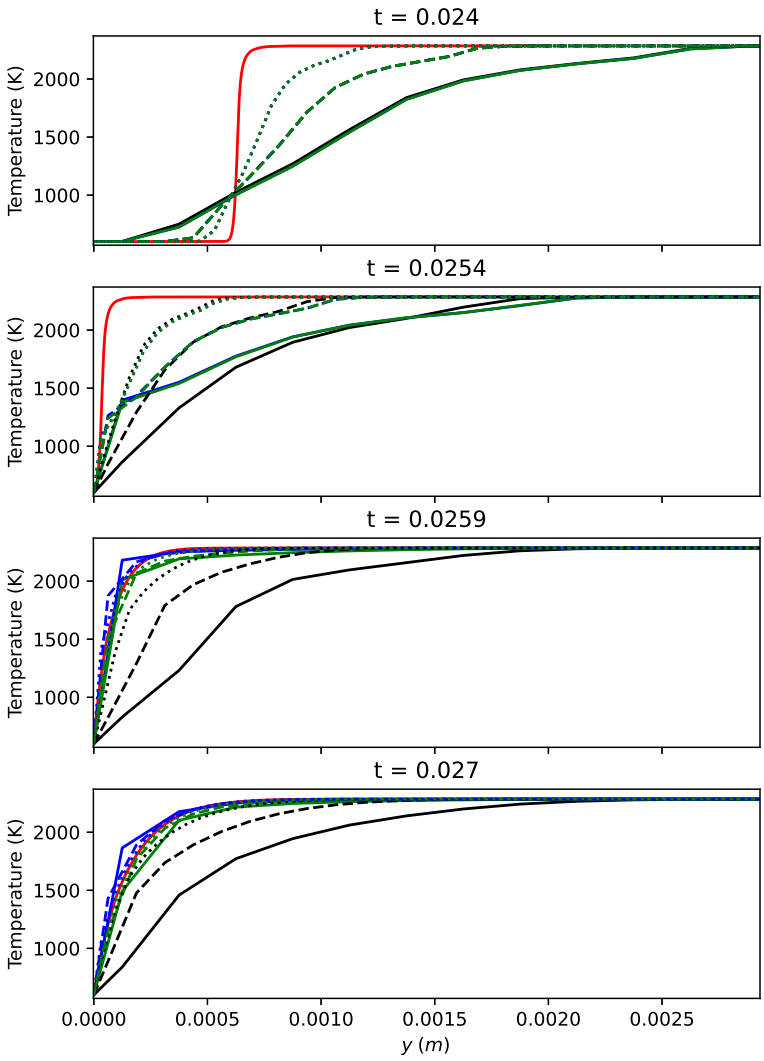

Figure 7.12: Evolution of temperature profile: DNS case in red line, line styles and colors used for the TFM cases in Table 7.1.

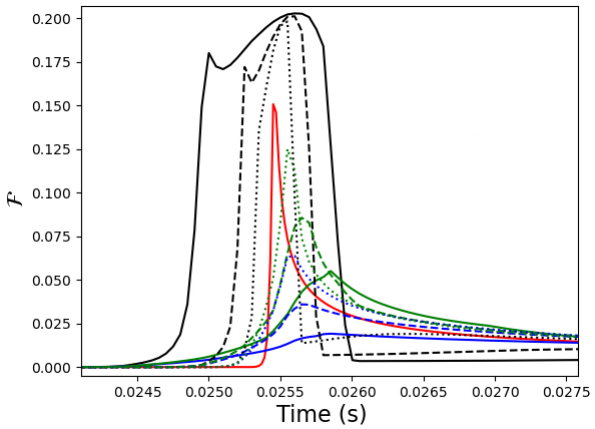

(a) Adimentional wall heat flux

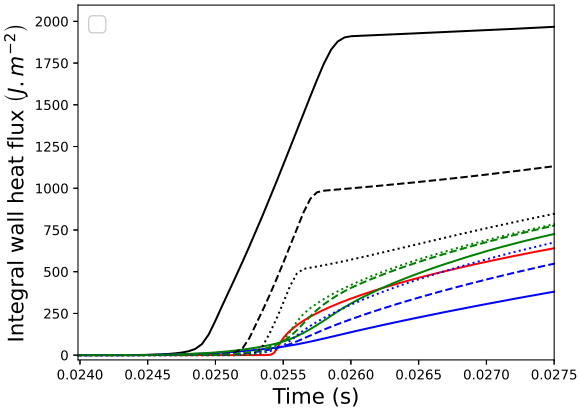

(b) Integral wall flux

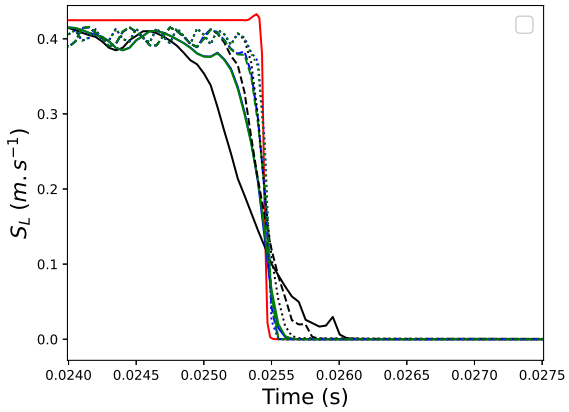

(c) Flame speed

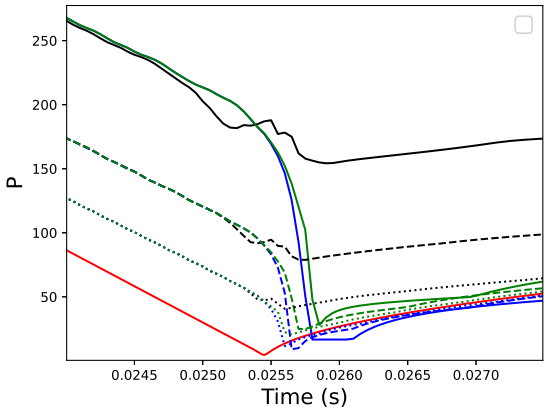

(d) Adimentional distance

Figure 7.13: Influence of TFM and the wall heat flux formulation on FWI: DNS case in red line, line styles and colors used for the TFM cases in Table 7.1.

very close to the one of the reference case, and this independently of the thickening factor. The temperature profiles obtained with λ_w need always longer distance to reach to burnt gas temperature, then they recover progressively the other profiles as can be seen at t=0.027.

Another way to compare the evolution of these temperature profiles is by looking at the evolution of the Peclet number shown in Figure 7.13d. Initially, the wall distance depends only on the thickening factor. During quenching, the Peclet number of the cases with λ_w and λ_1 drops to a value relatively close to the one of the reference case. The Peclet number stays however at high values when $F\lambda_w$ is used.
Figure 7.13c shows the evolution of the fuel consumption rate of the different cases computed using Eq. (7.6). Before HOQ, the laminar free flame speed predicted by TFM slightly fluctuates around $0.405\,m.s^{-1}$, i.e. about 5% lower than the value predicted in the DNS case. During quenching, and for a given thickening factor, the use of the λ_w and λ_1 leads to the same evolution of the fuel consumption rate. However the flame speed drops earlier when $F\lambda_w$ is used, which leads to a later complete consumption of the fuel. The more the thickening factor increases, the more the flame speed obtained with the latter expression deviates from the reference result.

Figures 7.13a and 7.13b show the evolution of the wall heat flux and the evolution of its integral over time. When λ_w is used, the wall heat flux is underestimated and become more and more flat by increasing the thickening factor, due to lower temperature gradient. The peak reaches only 13%, 23% and 42% of the reference value with the thickening factors 44, 22, and 11 respectively. The evolution of the integral of the heat flux is relatively well predicted when $F = 11$ and decreases with higher thickening factors. When $F\lambda_w$ is used, and for the three thickening factors, the dimensionless wall heat flux quickly rise to 0.175 and peaks at about 0.2, which is 33% higher than the reference peak, then quickly goes down to low values after the quenching. The heat flux stays longer at high value with increasing the thickening factor, which lead to higher integral of the flux. The behavior of the artificially thickened flame along with $F\lambda_w$ can be explained as follows: the heat flux quickly rises when the flame front reaches the wall as the wall heat flux is enhanced with the thickening factor. When the heat losses through the wall become important (of the same order of magnitude as the quenching heat flux of the reference case), the internal heat generated by chemical reactions can not support any longer the flame front propagation and the fuel consumption rate decreases. At this stage, the thickening is still applied and it still enhances the mass diffusion of fresh gas from the wall side and the heat diffusion from the burnt gas side, which maintains a nearly stationary reaction zone and prevent the flame quenching. When all the fuel is consumed, the flame completely extinguishes, the sensor is no longer able to detect any reaction zone and the thickening is removed, which leads to a sudden drop of the wall heat flux. So, enhancing the wall heat flux with a thickening factor modifies the flame HOQ quite considerably. These artifacts are more pronounced with larger thickening factor. Further analysis of the results are needed to detail all the aspects of this modified physics.
Finally, using λ_1 gives the closest evolution of the wall heat flux to the reference result. The peak reaches 36%, 57% and 83% of the reference value with the thickening factors 44, 22 and 11 respectively. Although the evolution of the wall heat flux depends of the thickening factor, the evolution of its integral only weakly varies with it, and it agrees relatively well with the reference result.

7.3.4 Conclusions

TFM was used for the simulation of flame HOQ in a 1D laminar case at temperature and pressure representative of ICE conditions and results were compared against reference results. The mesh cell size was also set to have a thickening factor of 44 as in practical engine LES. Two other mesh cell sizes, associated with F equal to 22 and 11, were also used to investigate the effect of the thickening factor. The flame parameters used for TFM were set based on the adiabatic premixed free flame without any consideration of heat losses. The wall heat flux was expressed with three different thermal conductivities: λ_w, $F\lambda_w$, and λ_1.

- Using λ_w does not alter much the evolution of the flame speed and recover well the shape and position of the temperature profiles after quenching. However, the wall heat flux diminishes increasing the thickening factor due to the decrease of the temperature gradient, which is not compensated by an increase of the thermal conductivity. Therefore, the difference with the DNS increases with the thickening factor.

- Using $F\lambda_w$ modifies considerably the HOQ phenomena. It causes high heat losses through the wall, which slows down the fuel consumption rate and stops the advancement of the flame front. The flame does not quench though, as it is maintained with the enhanced mass and heat fluxes until the complete consumption of the fuel. So, the wall heat flux stays at high values longer than it should be and the temperature profile and positions are quite altered during all the interaction.

- Using λ_1 better predicts the wall heat flux compared with the results when λ_w is used, but with almost the same evolution of the fuel consumption rate and temperature profiles. With this expression of the heat flux, the integral heat flux is also relatively well predicted and does not depend much on the thickening factor.

Although the model using λ_1 is not theoretically justified, it is shown to give the best results compared to the other two on this HOQ configuration, and to reproduce reasonably well the reference result in terms of fuel consumption rate and total heat flux. A more sophisticated model of thickening at the wall is still needed,

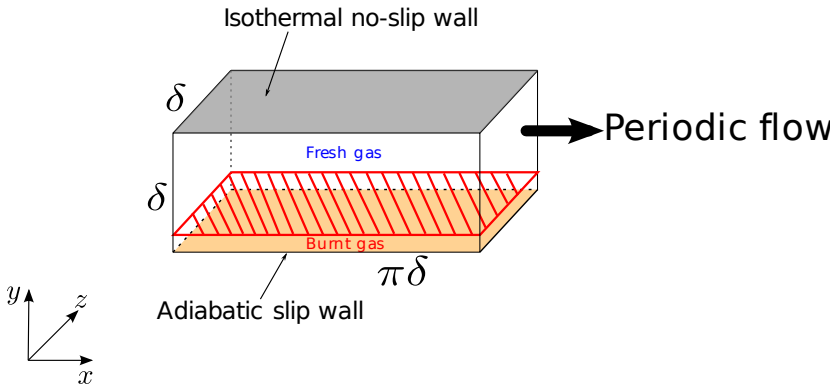

Figure 7.14: FWI in turbulent channel flow.

but in the context of this PhD where many other aspects had to be studied (wall law modeling, wall-film modeling, soot formation), such a model could not be developed.

7.4 Flame Wall Interaction in turbulent channel flow

In this section, FWI is simulated in turbulent channel flow. The flow conditions and the applied thickening factors in the wall-modeled cases are not representative of a practical ICE LES. The main purpose of this study is to assess the use of TFM for a turbulent FWI simulation and the focus will be given only to the influence of wall heat models. As noted in section 6.4.2, only algebraic wall models are used for the dry wall. Reference results are first obtained with wall-refined LES and resolved flame front. Then, three wall-modeled cases are performed, *Werner&Wengle* wall stress model but with different wall heat models: *O'Rourke-Amsden, Angelberger,* and *GruMo-UniMORE*. As in the 1D flame HOQ configuration, all these cases are performed with TFM combustion model without any particular treatment near the wall. As detailed in section 3.1.2.2, the algebraic wall heat models are expressed using properties evaluated at the center of the wall adjacent mesh cell. The algebraic wall heat models are used here with their original formulation without any modification related to TFM.

7.4.1 Case setup

Configuration

The configuration is inspired from the DNS of Bruneaux et al. [1] (see Figure 7.9). Only a half channel flow is considered in this work as shown in Figure 7.14. The flow is periodic in both streamwise and spanwise directions. The upper boundary condition is an isothermal no-slip wall at temperature $T_w = 370K$. The bottom boundary condition is an adiabatic slip wall. The gas phase is initialized from a prior computation of a complete stationary turbulent channel flow with air/iso-octane mixture at equivalence ratio 0.8, atmospheric pressure, and with target mean temperature at the center of the channel $\overline{T}_c = 600K$. The initial Re_τ is equal to 230. This configuration is performed without source terms. A planar flame front is added to the initial map close to the center of the channel using a premixed free flame temperature and species profiles computed by Cantera at the mean conditions at the center of the channel.

Meshing strategy and combustion modeling

- **Wall-refined case:** An isotropic base mesh grid is used with a cell size $\Delta x = \delta/95$ with a permanent one level embedding at the wall. The TFM-AMR coupling is used with $F_{target} = 1$ in order to track the flame front. Thus, the chemistry is directly solved in the flame front without applying any artificial thickening. Figure 7.15 shows a $y-z$ slice of the mesh grid during the flame propagation. During the whole simulation, the number of cells in the domain ranged between 5.3M and 7.4M cells.

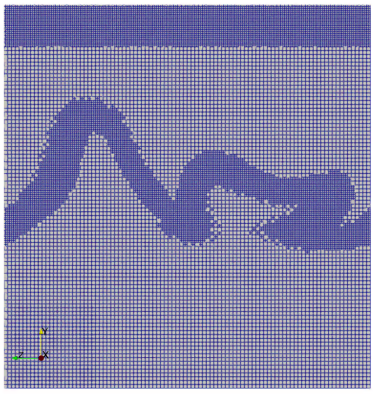

Figure 7.15: $y-z$ slice of the mesh grid during the flame propagation toward the wall.

- **Wall-modeled cases:** An isotropic mesh grid is used with a cell size $\Delta x = \delta/36$ without mesh embedding. TFM is used without AMR coupling. The total number of cells in the domain is about 150,000 cells.

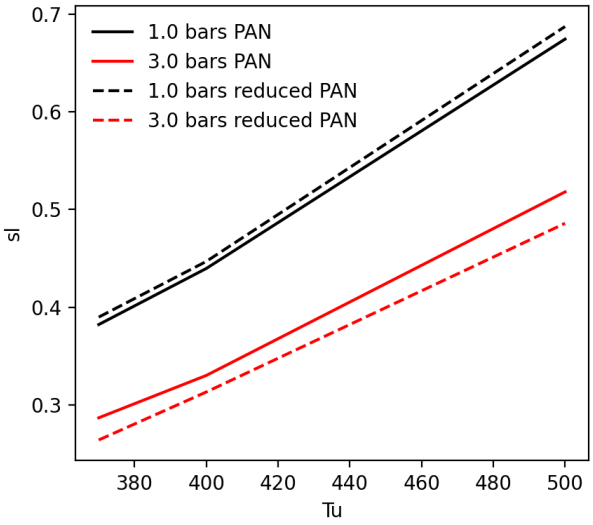

Figure 7.16: Validation mechanism reduction for FWI in turbulent channel flow.

Mechanism reduction

The chemical mechanism of An et al. [124] (85 species and 232 reactions) already used in the flame HOQ cases is also considered for this configuration. In order to accelerate the computation, the chemical mechanism is reduced using ORCh [125, 126] (Optimized Reduced Chemistry) tool. ORCh provides several automated methods to reduce detailed chemical schemes at a given operating conditions. It was originally developed at CORIA during the work of Jaouen [127], then used and improved during later works [128]. For this case, the reduction was based on free premixed canonical flames solved with Cantera. The reduction was performed with the target of minimizing the errors on the laminar flame speed, on the evolution of the temperature and major species (C8H18, O2, H2O, CO2, CO) profiles for each flame. Twelve flames are considered to cover the the following conditions: pressure ranging from 1 to 3 bar, fresh gas temperature

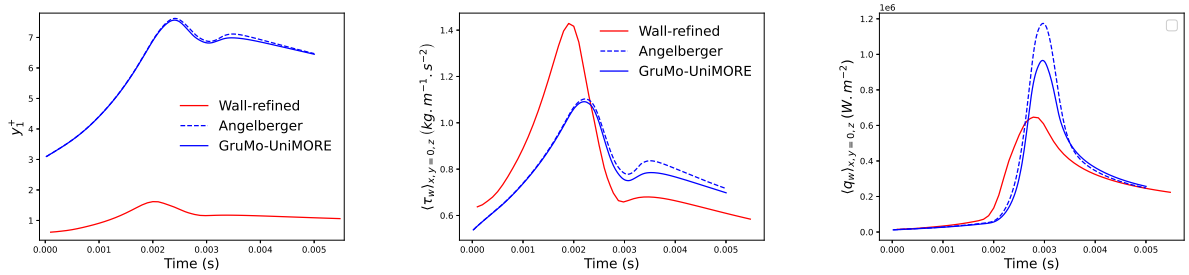

(a) Dimensionless distance at the wall adjacent cell center

(b) Wall shear stress

(c) Wall heat flux

Figure 7.17: Evolution of the dimensionless distance, wall shear stress and heat flux in FWI cases.

ranging from 300 to 600K, and equivalence ratio of 0.8. Directed Relation Graph with Error Propagation (DRGEP) [129] approach is first applied to remove the species which are poorly related to the targets. The reactions involving removed species are also eliminated. Then, DRGEP is also applied on the remaining reactions to retain only relevant ones. Next, the production of species respecting the Quasi-Steady State (QSS) assumption is analytically included in the chemical mechanism, then these species are not transported in the CFD simulation. Finally, the errors produced by the reduced mechanism are corrected using genetic algorithm to optimize the Arrhenius constants. The final reduced scheme contains 15 transported species, 4 QSS species, and 24 reactions. Figure 7.16 shows the laminar flame speed of air/iso-octane mixture at equivalence ratio 0.8, at different unburnt temperatures and pressures computed using the original An et al. [124] mechanism and the reduced one. The reduced mechanism predicts the laminar flame speed with an error less than 6% for all the conditions.

7.4.2 Results and discussion

In the following, the wall-refined results will be first presented. Next, the wall-modeled results will be discussed.

Wall-refined results

The y^+ value, evaluated at the center of wall cell, stays below 1.7 during all the wall-refined simulation as shown in Figure 7.17a, which is acceptable for a wall-refined LES. Figure 7.18 shows the evolution of the domain average streamwise velocity, temperature and pressure. The mean streamwise velocity slightly increases as the flame front gets close to the wall, then it decreases by about 10% during the quenching. As burnt gases occupy more and more volume during the flame propagation, the domain average temperature increases and reach a peak when all the fresh gases are burnt. Next, it starts to slowly decrease due to heat losses through the wall. The periodic half channel flow configuration is a closed domain, thus, the burnt gases expansion leads to the raise of the domain pressure. During the flame propagation and quenching, the pressure rises from 1 bar at about 3.6 bar, then it slowly decreases.
Figure 7.19 shows the iso-surface of temperature at 2000K of the wall-refined case colored by the wall distance and the temperature field at the side boundaries at different instants during the FWI. Figure 7.23 shows the evolution of the minimal and maximal distance of this iso-surafce from the wall. Figures 7.21 and 7.17c show respectively snapshots of the wall heat flux at different instants and its mean evolution over time. The initially planar flame front starts to wrinkle as it propagates towards the wall and the flame brush thickness (the difference between the maximal and minimal distance from the wall) increases. The mean wall heat flux stays at low value until about t=2ms. At this instant, the wrinkled flame front reach the wall and quenches (Figures 7.23 and 7.19c), which increases locally the wall heat flux (Figure 7.21a) and sharply increases the mean wall heat flux. At about t=3.5ms, all the flame surface has reached the wall, the flame brush thickness

becomes negligible, meaning that the iso-surface of temperature becomes almost planar and indicating the complete quenching of the turbulent flame front.
Figure 7.24 shows the evolution of the mass of species C_8H_{18}, H_2O, CO_2 and CO in the domain. The fuel mass progressively decreases until complete consumption after quenching. The masses of H_2O and CO_2 monotonically increase and they reach a plateau after quenching. The mass of CO increases and reach a peak approximately when the FWI starts, then it slowly decreases.

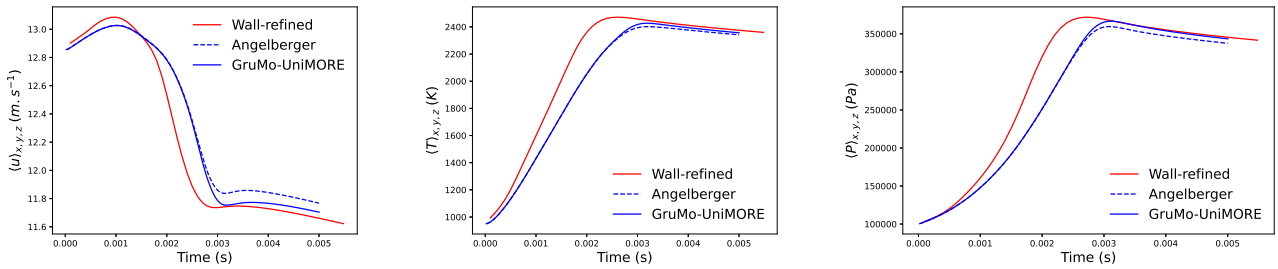

(a) Streamwise velocity **(b)** Temperature **(c)** Pressure

Figure 7.18: Evolution of the volumetric average of streamwise velocity, temperature and pressure over the domain in the FWI cases.

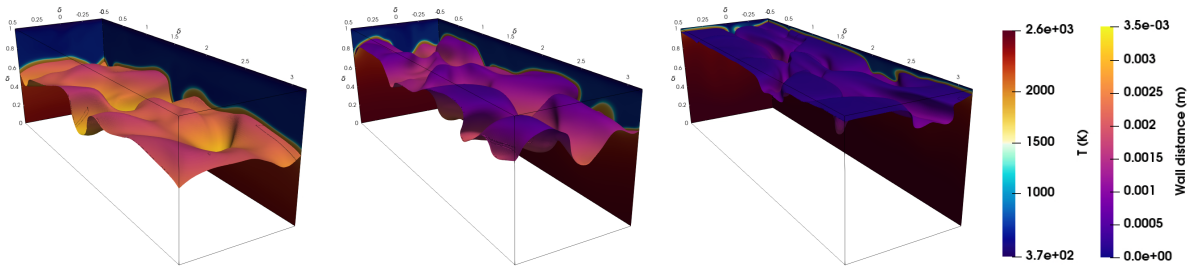

(a) At 1 ms **(b)** AT 1.5 ms **(c)** At 2 ms

Figure 7.19: Snapshots of FWI in the wall-refined case: Iso-surface of temperature (T=2000K) colored with the wall distance and the temperature field on the side boundaries.

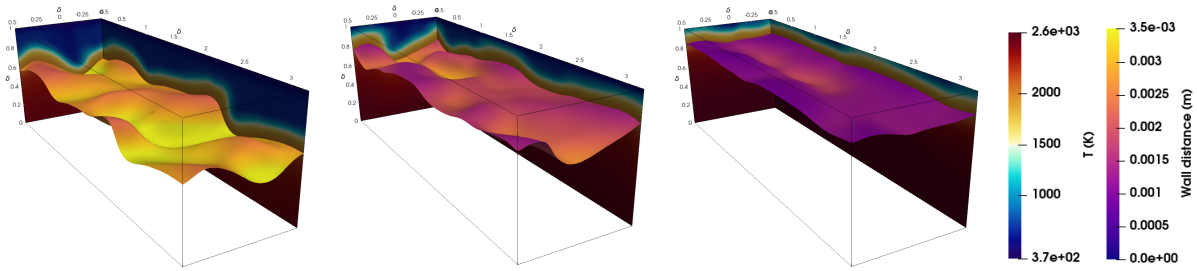

(a) At 1.5 ms **(b)** At 2 ms **(c)** At 2.5 ms

Figure 7.20: Snapshots of FWI in the wall-modeled case: Iso-surface of temperature (T=2000K) colored with the wall distance and the temperature field on the side boundaries.

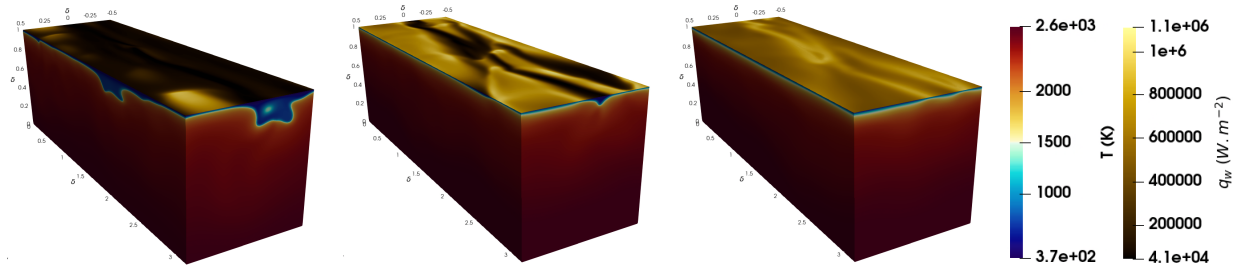

(a) 2ms **(b)** 2.5ms **(c)** 3ms

Figure 7.21: Snapshots of wall heat flux in the wall-refined case with the temperature field on the side boundaries.

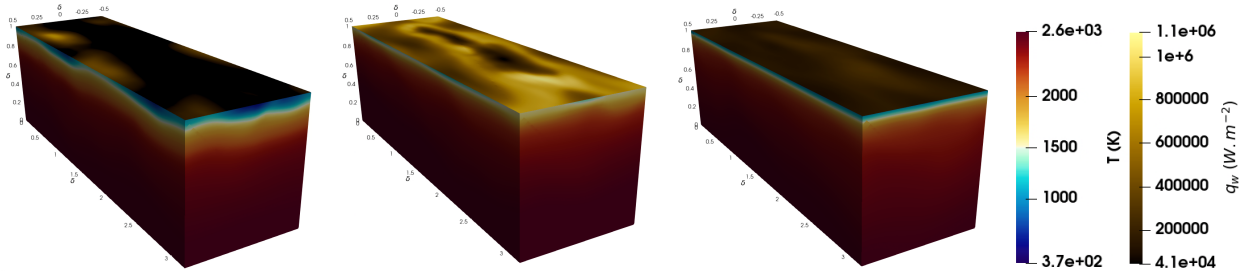

(a) 2.5ms **(b)** 3ms **(c)** 3.5ms

Figure 7.22: Snapshots of wall heat flux in the wall-modeled case with the temperature field on the side boundaries.

Assessment of wall-modeled cases

Three wall modeled cases are performed with respectively *O'Rourke&Amsden, Angelberger,* and *GruMo-UniMORE* heat models and always with the *Werner&Wengle* wall stress model. The y^+ value at the center of the wall cell stays below 7.7 during all the wall-modeled simulations as shown in Figure 7.17a. Hence, for the three considered algebraic wall heat models, the heat flux is mainly evaluated at low dimensionless distance from the wall using the linear expression (see Eqs (3.57), (3.64) and (3.68)). By substituting the Pr number by $\mu_1 c_{p,1}/\lambda_1$, the different heat flux expressions evaluated by the linear region can be written as the following:

- For the *O'Rourke&Amsden* model: $q_w = \lambda_1 \left(T_1 - T_w\right)/y_1$.
- For the *Angelberger* model: $q_w = \lambda_1 T_1 ln\left(T_1/T_w\right)/y_1$.
- For the *GruMo-UniMORE* model: $q_w = \lambda_1 \left(T_1 - T_w\right)/y_1$.

Thus, the *O'Rourke&Amsden* and *GruMo-UniMORE* models have the same expression, while the *Angelberger* has a different expression as it is derived using the LnKc transformations (see section 3.1.2). All the wall heat models are expressed using the thermal conductivity evaluated at the center of the wall cell λ_1, hence the relevance of considering λ_1 to express the wall heat flux in the investigation of using TFM in 1D flame HOQ configuration. The results of the wall-modeled cases performed with *O'Rourke&Amsden* and *GruMo-UniMORE* models are very close. For simplicity, only the results of the wall-modeled cases performed with *Angelberger* and *GruMo-UniMORE* models are presented and discussed in the following.

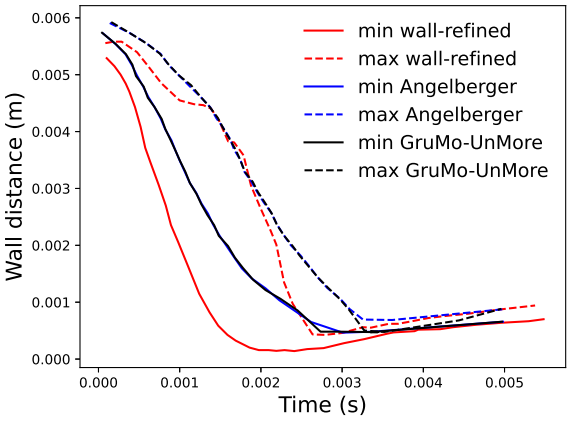

Figure 7.23: Evolution of the minimal and maximal distance of this iso-surface from the wall in the FWI cases.

Given the used mesh grid and flow conditions, the thickening factor is initially about $F = 3$ and reach a maximum of about $F = 6.5$ during the FWI as shown in Figure 7.25. These thickening factor values are relatively low and not representative of the thickening factors applied in an industrial case. Furthermore, according to the previous investigation on the use of TFM for the 1D HOQ configuration, this low thickening factor values may not alter much the FWI phenomena. Nevertheless, this evaluation with a thickening factor of about 6.5 is still interesting.

As long as the flame front is still far from the wall, all the wall modeled cases gives the same evolution of the domain average streamwise velocity, temperature and pressure as shown in Figure 7.18, and also the same evolution of the minimal and maximal flame front distance from the wall as shown in Figure 7.23. According to these plots, the propagation of the flame front toward the wall is slower when it is artificially thickened compared to the reference result and the FWI starts approximately with a delay of 0.5ms. The cause of this delay was not investigated in details in this work, but it is probably due to inaccurate flame turbulence interaction modeling. As detailed in section 7.1.3, Charlette model is used for the efficiency factor with the standard model constants. However, the wall has an influence on the flame turbulence interaction which normally should be included in the efficiency factor modeling.

Figures 7.20 and 7.22 show respectively the 2000K temperature iso-surface and wall heat flux snapshots of the case modeled with the *GruMo-UniMORE* wall heat model at instants that correspond approximately to the same flame front locations as for the wall-refined case shown in Figures 7.19 and 7.21. The artificially thickened flame is less wrinkled compared to the reference results when it approaches the wall and the quenching occurs with an almost planar flame front. The distribution of the heat flux on the wall is also smoother during the interaction. The evolution of the minimal and maximal wall distances of the flame front using the two wall heat models are very close. After the complete quenching of the flame front, the iso-surface of temperature of the wall-modeled cases retreats from the wall similarly as in the wall-refined case.

The wall-modeled cases results deviate from the wall-refined results mainly on the evolution of the wall shear stress and the wall heat flux as shown in Figure 7.17. The peak shear stress is underestimated by about 20%, then it is overestimated by about 25% after the quenching, with slightly smaller error when *GruMo-UniMORE* wall heat model is used. The error on the peak of the wall heat flux is different according to the used wall heat flux. The *Angelberger* model overestimate it by an error of almost 100%, while the error is only about 60% when *GruMo-UniMORE* model is used. After the quenching, the heat loss through the wall is well predicted by both wall heat models.

Concerning the evolution of the species mass in the domain, the evolution of CO in the wall-modeled cases is quite different from the wall-refined case. The peak of CO mass is much more accentuated with an over prediction of about 70%. After the quenching, the wall-modeled cases predicts very well the species mass.

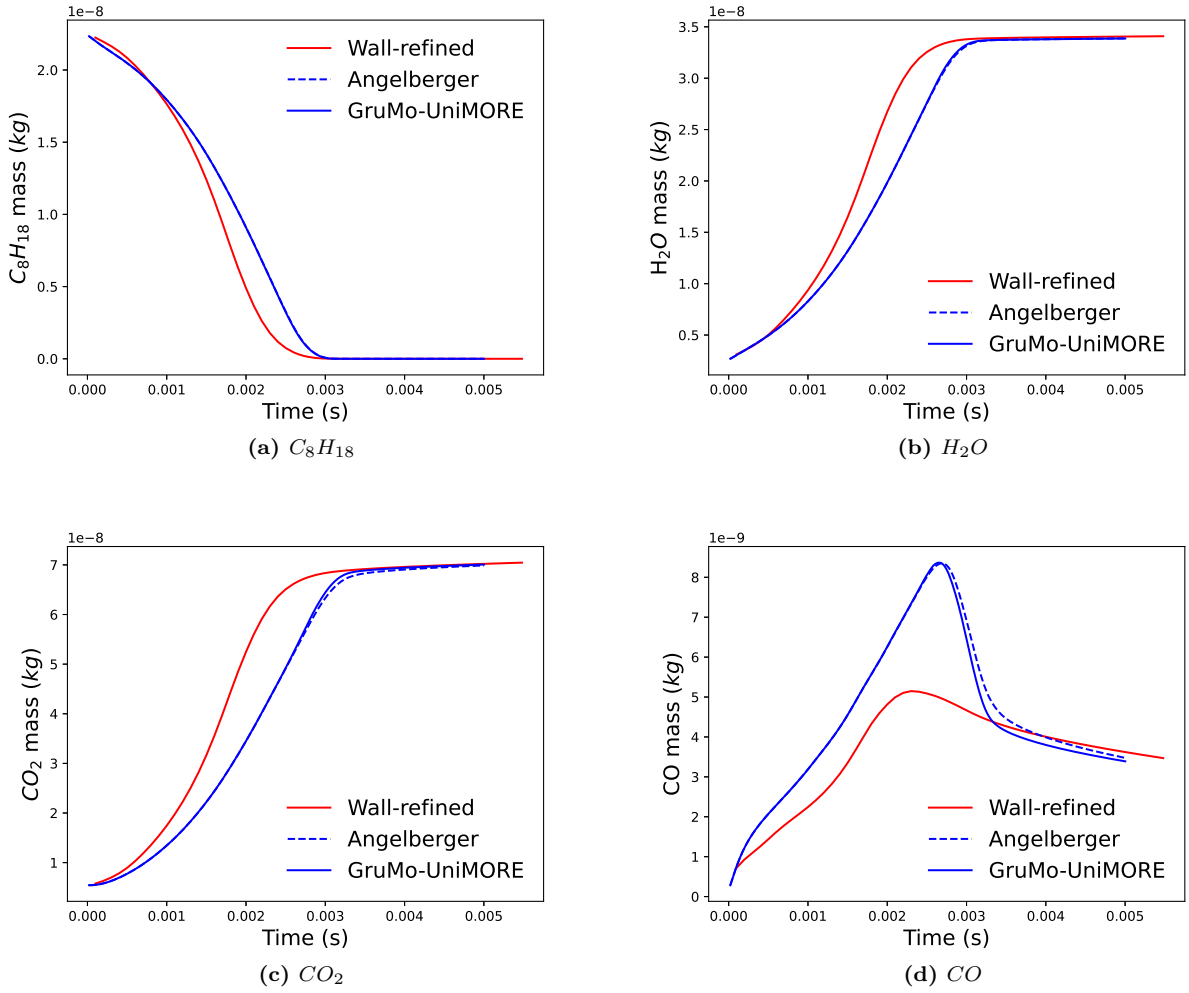

(a) C_8H_{18} **(b)** H_2O **(c)** CO_2 **(d)** CO

Figure 7.24: Evolution of species mass in the domain in FWI cases.

7.4.3 Conclusion

A turbulent FWI was studied in a turbulent channel flow. WMLES with an artificially thickened flame was compared to a reference wall-refined LES with a resolved flame front. This study showed that the use of low values of thickening factors (about $F = 6.5$) for an artificially thickened flame, along with algebraic wall stress and heat models evaluated with the linear sub-layer expression, allows in overall to reproduce the FWI phenomena. The variation of the wall shear stress is relatively well predicted with errors less than 25% compared to wall-refined results. *O'Rourke&Amsden* and *GruMo-UniMORE* better predict the peak wall heat flux during quenching (overestimation by about 60%) than *Angelberger* model (overestimation by about 100%). This better prediction is probably due to the different formulation of the wall heat flux in the linear sub-layer. It is interesting to point out that the heat flux was always overestimated in this case, i.e. with the turbulence influence, while it was underestimated in the case of 1D flame HOQ using the same heat flux formulation as *O'Rourke&Amsden* and *GruMo-UniMORE* models. Finally, it was noted that the predicted major species mass agree well with reference results after the quenching, and an overestimation of about 70% of CO mass was noted during the FWI.

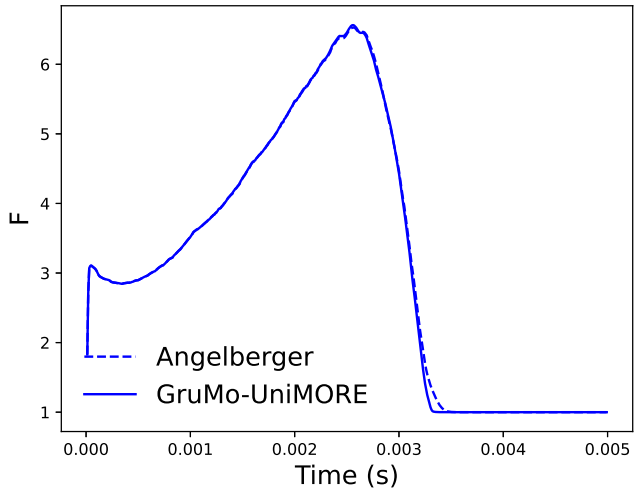

Figure 7.25: Evolution of mean flame thickening factor in wall-modeled LES of FWI.

Chapter 8

Flame-Film Interaction with soot formation

Contents

In this last chapter, all the models are used together to study the formation of soot in a pool-fire configuration. These simulations use the models described above coupled with a soot model which is described at the beginning of this chapter. Once again, we will not look for experimental validations. The main objective is to have a reference result in order to assess the different modeling approaches used in WMLES. Thus, the soot formation during Flame-Film Interaction (FFI) is first simulated in wall-refined LES with resolved flame front, then in WMLES with an artificially thickened flame. The wall-refined simulation describes also the complex physics leading to soot formation in this configuration. Only a brief description of the primary results are presented in the following and more detailed analysis is needed in future works.

8.1 Soot formation and modeling

8.1.1 Soot formation mechanisms

8.1.1.1 Soot particle inception

Soot particles inception process is still an uncertain step due to the very low concentration and life time of the involved species and the difficulty to identify experimentally the smallest particles. Desgroux and coworkers [130–132] investigated flames of methane, ethylene and butane at the critical equivalence ratio where soot can be first measured using the current state of art Laser Induced Incandescence method. Their work also include extended analyses of gas species, up to 4 rings PAH such as Pyrene and Fluoranthene, for the two alkane fuels. It is used in recent modeling effort, of Kholghy et al. [133] or Aubagnac-Karkar et al. [134] for instance, to evaluate various hypothesis and modeling strategies concerning PAH-soot interaction. These interactions fall into two main types usually called "nucleation" (inception due to PAH-PAH collisions) and

"condensation" (PAH adsorption on soot following PAH-soot collisions). These modeling works focus on the eventual reversibility of these processes. This possibility was originally studied by the molecular dynamic community [135–137] along with the identification of the species and processes leading to the formation of the first solid particles. For instance, Sabbah et al. [135] contested in 2010 that pyrene, whose dimerization was generally considered as the main source of nucleation previously, could lead to a stable dimer.

8.1.1.2 Soot particle growth and oxidation

There are two main types of phenomena leading to soot growth and oxidation: collisional phenomena and surface chemistry.

Collision phenomena

Collisional phenomena can be divided into two types:

- **Condensation:** PAH colliding with solid soot particle.
- **Coagulation:** collision between two solid soot particles, which in turn can be divided into:
  - **Coalescence:** the colliding particles completely merge and the resulted particle is spherical.
  - **Aggregation:** the colliding particles do not merge to form aggregates.

Condensation increases soot mass and size without impacting particles number, while coagulation increases particle size and decrease particles number without impacting the total soot mass. Condensation is currently as uncertain as particle inception for the reasons mentioned previously. There is no sharp line dividing coalescence and aggregation, part of the aggregated particles coalesce, depending on the particle age and structure. However, the difference between coalescence and aggregation is expected to have significant influence on the evolution of soot size distribution. Indeed, the surface to volume ratio of the particles as well as the measured diameters will be highly dependent of soot aggregate structure as shown by Yon et al. [138].

Surface chemistry

Soot surface reacts with the chemical species in the surrounding gas. Particle mass can increase or decrease by the addition or the abstraction of carbon atoms. Frenklach proposed a soot surface chemistry controlled by the HACA cycle, similar to PAH molecule growth. The reactions rates depend on soot surface and internal structure, which depend in turn on the particle age, history and thermochemical conditions.

8.1.2 The Sectional Soot Model

The Sectional Soot Model (SSM) was used for soot modeling. It is a detailed modeling approach which allows to predict the soot mass and size distribution. The used model in this work was developed by Aubagnac-Karkar [23, 134] based on previous works [139–142]. It describes the soot number density function as distinct dispersed phase interacting with the gaseous phase. The nucleation and condensation sub-models were also improved to include the effect of their reversibility [134]. The soot particles are separated with respect to their mass into discrete sections. The filtered soot mass fraction $Y_{soot,p}$ of each section p is transported in the flow according to the following governing equation:

$$\frac{\partial \overline{\rho}\tilde{Y}_{soot,p}}{\partial t} + \frac{\partial \overline{\rho}\tilde{U}_i\tilde{Y}_{soot,p}}{\partial x_i} = \frac{\partial}{\partial x_i}\left(\frac{\mu_t}{Sc_t}\frac{\partial \tilde{Y}_{soot,p}}{\partial x_i}\right) + \overline{\rho}\bar{\dot{\omega}}_{soot,p} \tag{8.1}$$

where $\bar{\dot{\omega}}_{soot,p}$ is the source term for the section p that includes sub-models of the different physical phenomena involved in the soot formation process. The soot modeling is coupled with the chemical species in the gaseous phase. Thus, if TFM is used for combustion modeling, the transport equation of the soot section are also thickened:

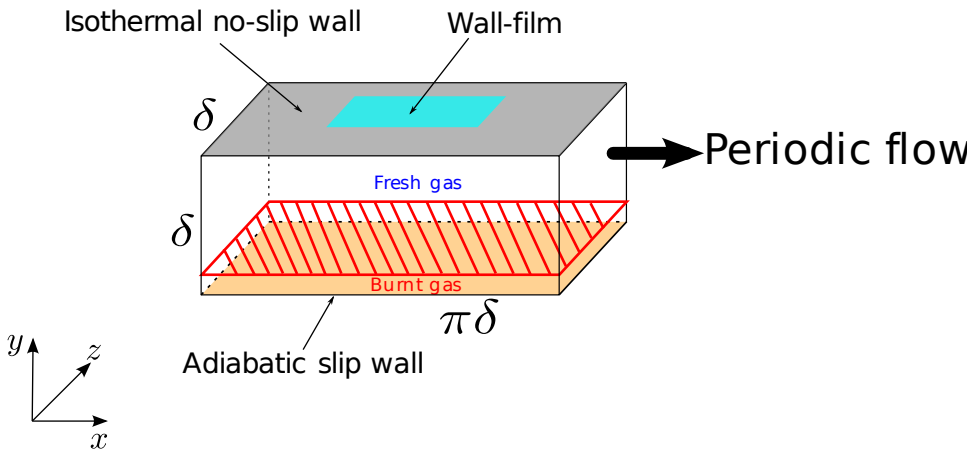

Figure 8.1: FFI in turbulent channel flow.

$$\frac{\partial \overline{\rho}\tilde{Y}_{soot,p}}{\partial t} + \frac{\partial \overline{\rho}\tilde{U}_i\tilde{Y}_{soot,p}}{\partial x_i} = \frac{\partial}{\partial x_i}\left(EF\frac{\mu_t}{Sc_t}\frac{\partial \tilde{Y}_{soot,p}}{\partial x_i}\right) + \frac{E}{F}\overline{\rho}\bar{\dot{\omega}}_{soot,p} \tag{8.2}$$

where F and E are the thickening and efficiency factors defined in section 7.1.3.

8.2 FFI and soot formation in turbulent channel flow

8.2.1 Case setup

Configuration

The configuration is the same as considered for the FWI in turbulent channel flow (see section 7.4.1) with adding an initial uniform wall-film as illustrated in Figure 8.1. The flow is periodic in both streamwise and spanwise directions. The upper boundary condition is an isothermal no-slip wall at temperature $T_w = 370K$. The bottom boundary condition is an adiabatic slip wall. The gas phase is initialized with the same map used to initialize the FWI case, i.e. a prior computation of a complete stationary turbulent channel flow at $Re_\tau = 230$ with air/iso-octane mixture at equivalence ratio 0.8, atmospheric pressure, and with target mean temperature at the center of the channel $\overline{T}_c = 600K$. A planar flame front is added to the initial map close to the center of the channel using a premixed free flame temperature and species profiles computed by Cantera at the mean conditions at the center of the channel. No source term is used for this simulation. The wall-film is initialized over about 9% of the wall surface with an initial thickness of $10\,\mu m$ and at wall temperature. The meshing strategies applied for the wall-refined and wall-modeled case are also the same as the FWI case. An isotropic mesh grid is used for the wall-refined case with a base cell size $\Delta x = \delta/95$ with a permanent one level embedding at the wall and an AMR to solve the flame front (see Figure 7.15). An isotropic mesh grid is used for the wall-modeled cases with a cell size $\Delta x = \delta/36$ without mesh embedding neither mesh refinement.

Mechanism selection and reduction

Soot formation requires detailed chemical mechanism able to well predict soot precursors, in this case the Pyrene (A4). The chemical mechanism of Raj et al. [143], composed of 231 species and 1350 reactions, was selected as it allows the prediction of PAH up to Coronene (7 benzene rings) for gasoline surrogate fuels combustion. In order to accelerate the computation, this mechanism is reduced using ORCh tool. For this case, the reduction was based on stochastic reactor that allow to cover a whole range of conditions [127]. The final reduced mechanism used in the simulation is composed of 86 species and 432 reactions.

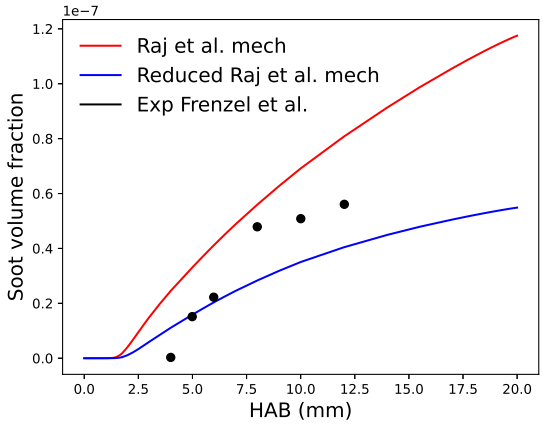

Figure 8.2: Experimental and simulated soot volume fraction in the burner flame of Frenzel et al. [144].

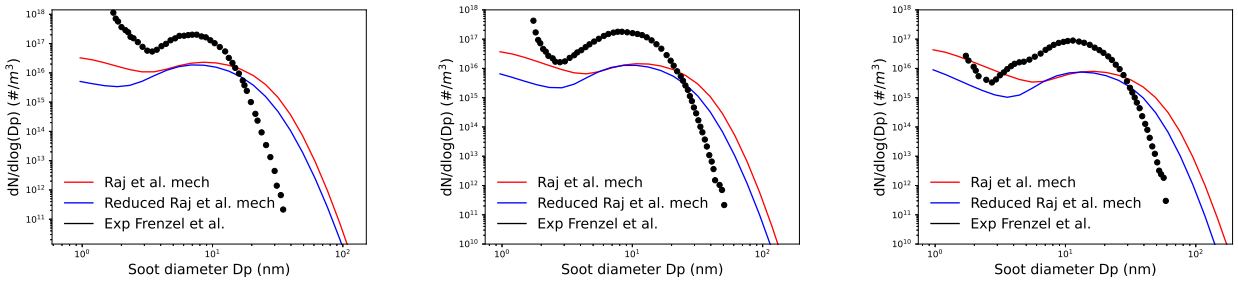

(a) At HAB = 6 mm **(b)** At HAB = 8 mm **(c)** At HAB = 12 mm

Figure 8.3: Experimental and simulated PSDFs in the burner flame of Frenzel et al. [144].

Soot model calibration

In this work, Pyrene (A4) is the only considered precursor for soot nucleation. The model parameters are the ones given in [134] except for the proportion of active reactive sites available for surface reaction α_{HACA} and the intermolecular vibrational wavenumbers $\lambda_{i,cond}$. α_{HACA} is used for decades to fit soot surface chemistry [134, 145–148] and several recent studies proposed to improve soot surface chemistry modeling such as including Arrhenius coefficients depending on particle size [149–151], following particles thermal history to adapt surface activity [148], or extending the surface chemistry mechanism [152, 153].This topic is still open and surface chemistry model remains very uncertain. Concerning $\lambda_{i,cond}$, this parameter is taken from molecular dynamic studies [154]. However, it cannot be evaluated accurately for soot modeling because it would require the knowledge of the soot surface structure at an atomic-scale so it is set with arbitrarily values in soot models taking into account the reversibility of PAH-soot interactions [134, 155–157]. Therefore, these two parameters have been set to arbitrary constants $\alpha_{HACA} = 0.3$ and $\lambda_{i,cond} = 4\,cm^{-1}$ since the present study focuses on flame-film interactions and the resulting soot formation instead of very detail soot physics and chemistry modeling. These values have been chosen to best fit the experimental results of sooting burner air/iso-octane flame at equivalence ratio 2.3 obtained by Frenzel et al. [144]. Figure 8.2 and 8.3 show the experimental and simulated soot volume fraction and the particle size distribution function (PSDF) at different heights above burner (HAB). The computation were performed using Cantera coupled with SSM. These plots shows the simulated results using both Raj et al. [143] chemical mechanism and the reduced one.

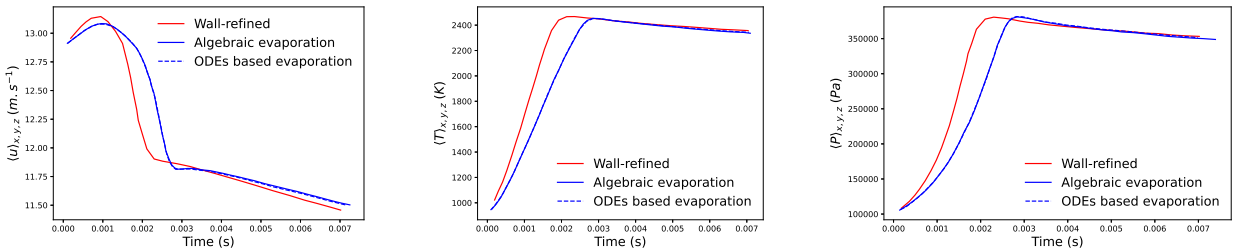

(a) Streamwise velocity **(b)** Temperature **(c)** Pressure

Figure 8.4: Evolution of the volumetric average of streamwise velocity, temperature and pressure over the domain in the FFI cases.

8.2.2 Wall-refined results

In the following plots, the wall-refined results are presented in red line, while wall-modeled results are plotted blue lines. Figure 8.4 shows the evolution of the domain average streamwise velocity, temperature and pressure. The evolution of these quantities is similar to the FWI case described in section 7.4.2. As in the FWI case, the initially planar flame front starts to wrinkle as it propagates toward the wall. In the meanwhile, the wall-film starts to evaporate. Due to this evaporation, the premixed flame encounters local mixture variation when it gets close to the wall. This mixture variation can be seen in Figure 8.5 which shows the iso-surface of temperature at 2000K colored by the wall distance and the local equivalence ratio at different instants during the FFI. Figure 8.6 shows the evolution of the minimal and maximal distance of this iso-surface from the wall. At about t=1.7ms, the wrinkled flame front reaches the wall and starts to quench. The locally rich zones in the evaporated fuel plume prevents the flame to get close to the dry or wetted wall as shown in Figure 8.5a. The temperature iso-surface can not penetrate regions with local equivalence ratio higher than 2. According to Figure 8.6, the maximal distance of this iso-surface does not get closer than 1mm to the wall, while this value was about 0.5mm in the FWI case (see Figure 7.23).
At t=3ms, the flame front becomes smooth, but not planar as it was the case in the FWI case. The minimal and maximal wall distance of the iso-surface of temperature do not join after quenching and the flame brush stays almost at a constant thickness of about 0.5mm as the iso-surface of temperature surrounds the fuel plume. At this instant, the premixed flame is almost totally quenched all over the wall, but combustion is maintained. This point is illustrated in Figure 8.7 showing $y-z$ slices of O_2 mass fraction, and the soot volume fraction at different instants after the premixed flame quenching. The red line line indicates the position of iso-temperature at 2000K. The initially premixed flame turns into diffusion like flame powered by the fuel from the wall side and the remaining O_2 in the premixed flame burnt gases. Figure 8.8 shows the evolution of the soot mass in the domain and its rate of production. Soot formation begins after the quenching of the main premixed flame, mainly in the diffusion like reaction zone. Further analysis of the results are needed for detailed description of the characteristics of the reactive zone after premixed flame quenching, the formation of PAH species, and soot formation.
Figure 8.9 shows the evolution of the mean heat flux through the dry wall and at the liquid/gas interface. The mean heat flux through the dry wall peaks at about $700\,kW.m^{-2}$ at t=2.3ms. However, the mean heat flux through the liquid/gas interface peaks at only $140\,kW.m^{-2}$ at about t=2.5ms. These results suggest that the flame quenching phenomenon is quite modified over the wall-film. According to Figure 8.10b, the wall-film evaporation rate continuously decreases before the interaction with the flame from its initial value as the region above the wall is more and more saturated with the evaporated fuel. Then, the evaporation rate increases again when the flame starts to interact with the wall-film.

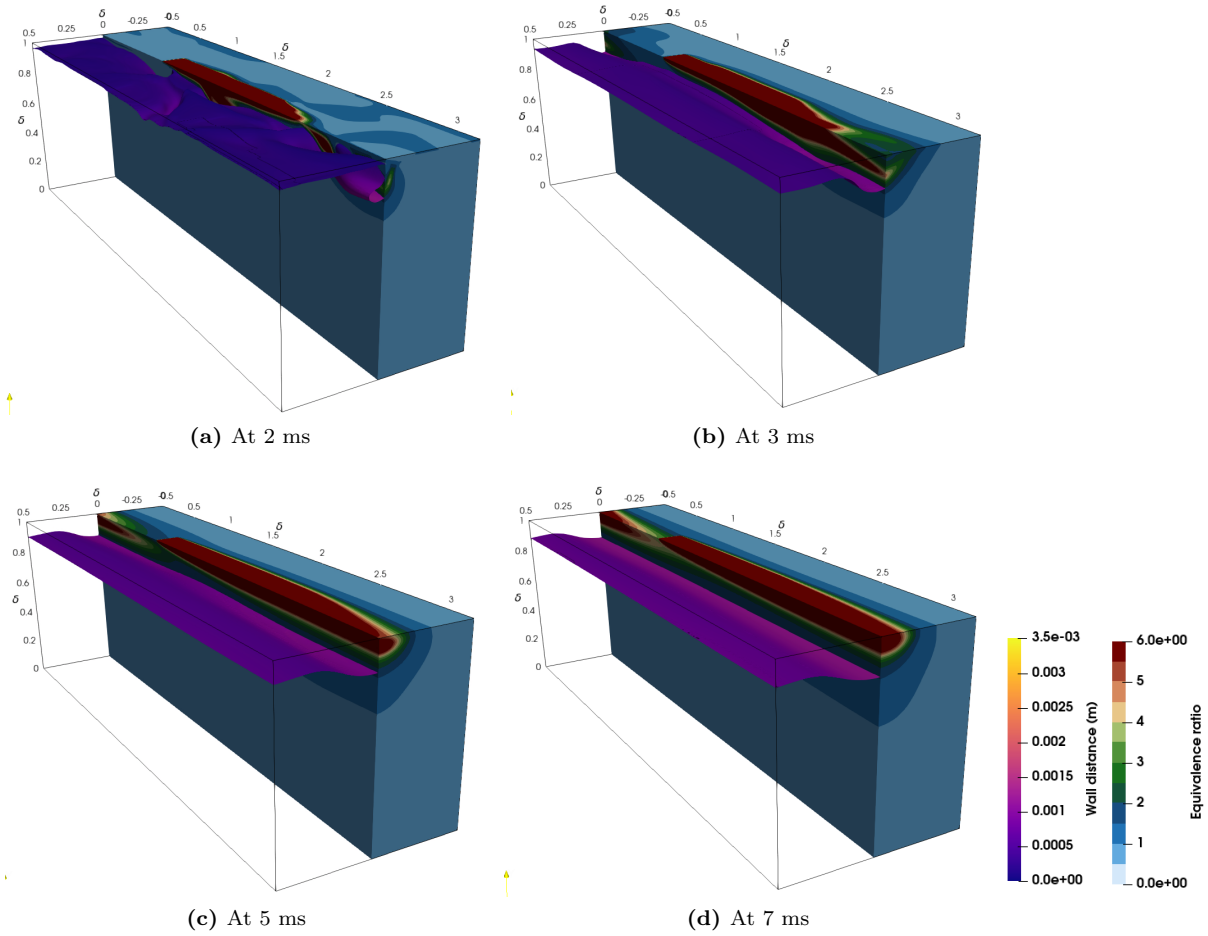

(a) At 2 ms **(b)** At 3 ms

(c) At 5 ms **(d)** At 7 ms

Figure 8.5: Snapshots of FFI in the wall-refined case: left half show iso-surface of temperature at 2000K colored with the wall distance, right half shows the local equivalence ratio.

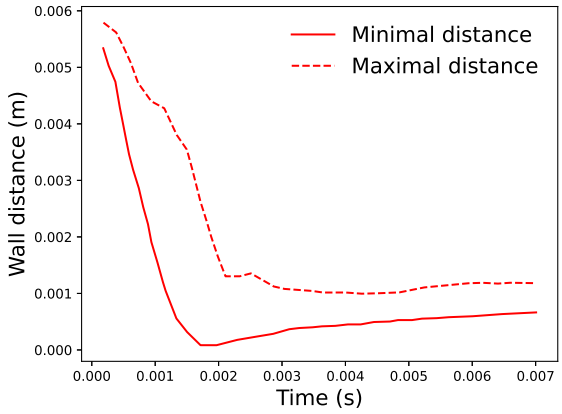

Figure 8.6: Evolution of the minimal and maximal wall distance of temperature iso-surface at 2000K in the wall-refined FFI case.

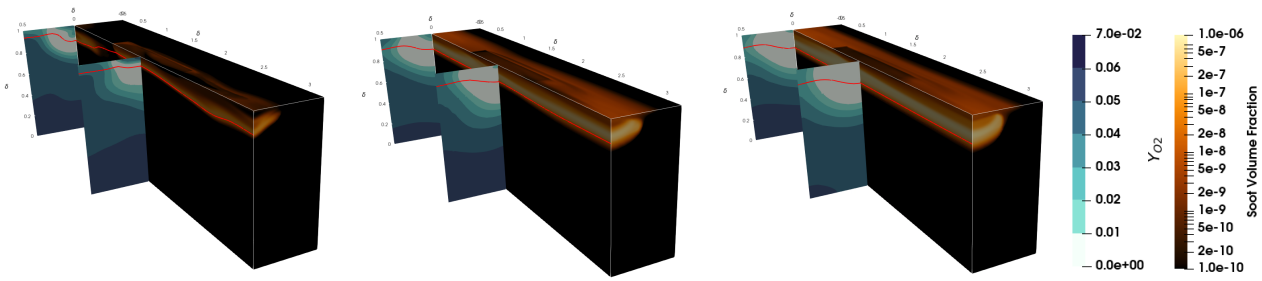

(a) At 3 ms **(b)** At 5 ms **(c)** At 7 ms

Figure 8.7: Snapshots of soot formation during FFI in the wall-refined case: left half show $y-z$ slices of O_2 mass fraction, right half shows the soot volume fraction, red line indicates the position of iso-temperature 2000K.

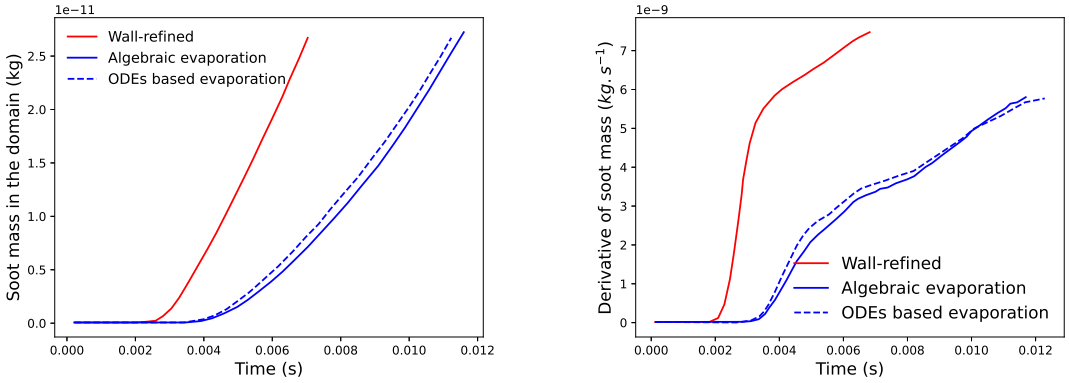

(a) Total soot mass **(b)** Rate of soot production

Figure 8.8: Evolution of soot mass and its rate of production in the FFI cases.

8.2.3 Wall-modeled results

The modeling of the different involved physical phenomena in the FFI configuration are assessed all together in a WMLES cases. The use of ODEs based WMLES for wall-film evaporation will be compared to the use of classical algebraic wall modeling. As mentioned in section 6.4.2, algebraic wall modeling is always applied over the dry wall, with the *Werner&Wengle* wall stress model and the *GruMo-UniMORE* wall heat model. Over the wall-film, two cases are considered:

- Algebraic modeling using *Werner&Wengle* model for stress modeling, *GruMo-UniMORE* model for heat modeling, and the evaporation model based on the semi-analytical solution. Results in Figures 8.4, 8.8, 8.9 and 8.10 are plotted in solid blue line.
- ODEs based wall-film evaporation modeling as proposed in Chapter 6. Results in Figures 8.4, 8.8, 8.9 and 8.10 are plotted in dashed blue line.

First, it is interesting to point out that the WMLES cases need about 1000 times less cpu time than the wall-refined simulation. The minimum cell size is 5.3 times smaller in the wall-refined compared to the wall-

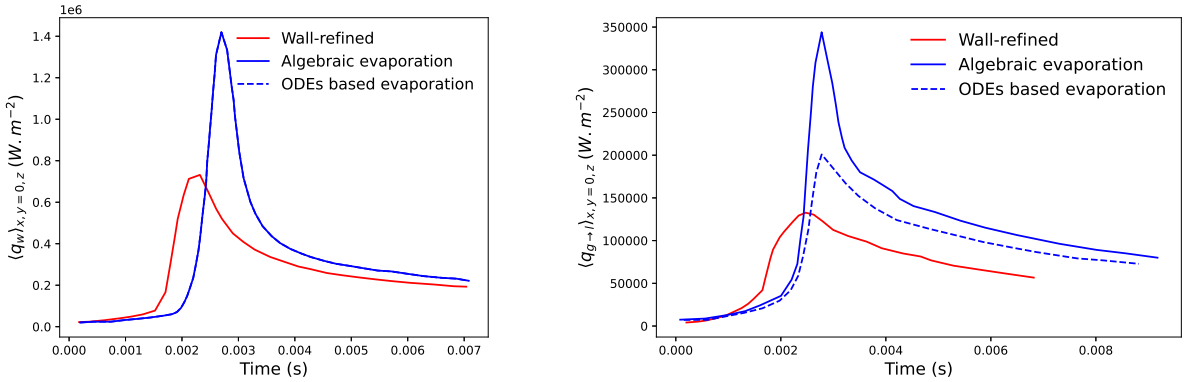

(a) Heat flux over the dry wall

(b) Heat flux at the liquid/gas interface

Figure 8.9: Evolution of the wall heat flux of the FFI cases.

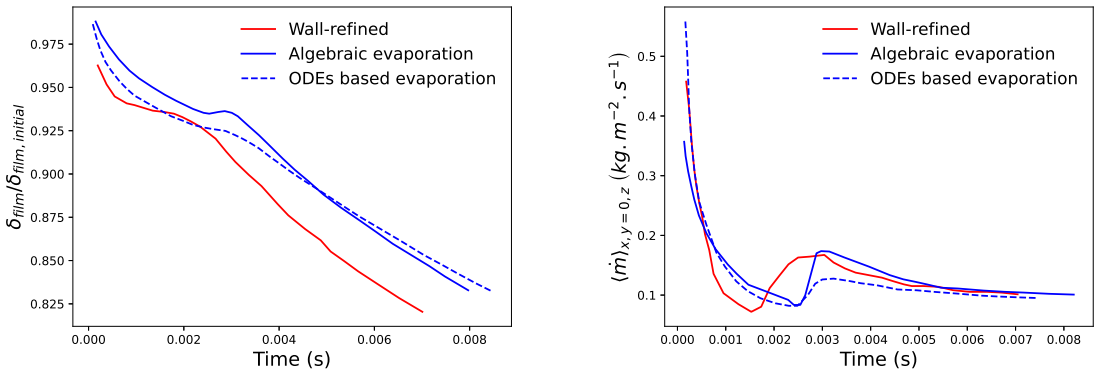

(a) Wall-film thickness

(b) Evaporation rate

Figure 8.10: Evolution of the mean wall-film thickness and evaporation rate of the FFI cases.

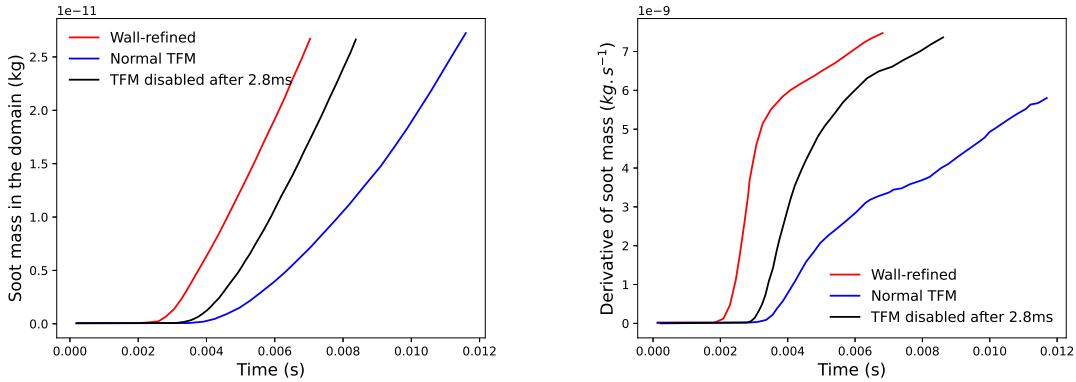

(a) Total soot mass

(b) Rate of soot production

Figure 8.11: Effect of TFM of soot formation in WMLES

modeled cases and the total number of cells ranges between 5.3M and 7.4M in the wall-refined case while it is only 150,000 cells in the wall-modeled cases.
The difference between wall-refined and wall-modeled results on the evolution of the domain average of streamwise velocity, temperature and pressure, shown in Figure 8.4, are similar to the differences already noted in the FWI configuration. The premixed flame propagation toward the wall is slower when TFM is used, which induces a delay of about 0.5ms in all the results.
The wall-modeled cases overestimate the peak heat flux over the dry wall with an error of about 100% compared to the wall-refined result (Figure 8.9a), while this error is about 60% in the FWI without wall-film (see Figure 7.17c) using the same wall heat model (*GruMo-UniMORE*). The choice of the wall-film evaporation model has no effect on the dry wall heat flux as the ODEs based model is used only above the wall-film. The effect of the modeling over the wall-film can be noticed on the prediction of the heat flux at the liquid/gas interface, shown in Figure 8.9b, and on the evolution of the evaporation rate, shown in Figure 8.10b. Before the interaction of the premixed flame with the wall-film, the evolution of evaporation rate predicted with the ODEs based model agrees very well with the wall-refined results. This leads to a better prediction of the wall-film thickness before t=2ms. During the premixed flame quenching, the heat flux at the liquid/gas interface is overestimated by about 40% using the ODEs based modeling, while it is overestimated by about 150% by algebraic modeling. Both models predict the increase of the evaporation rate during the flame quenching, but with better results obtained with the algebraic modeling. So, the high temperature of the flame front has a considerable effect on the wall-film evaporation modeling, and thus on the results of the WMLES of the FFI in overall.

Concerning the soot formation, the two WMLES cases underpredict the soot production rate, leading to slower increase of the soot mass in the domain. The choice of the wall-film evaporation modeling does not affect much the results as both models already predict close evolution of the wall-film thickness after the flame quenching. The error on soot prediction may be related to the use of TFM for combustion modeling. Indeed, the source term in the soot sections transport equation (Eq. (8.2)) are multiplied by E/F and may be the cause of the under prediction of soot production rate. In the process of understanding the source of errors, a WMLES case was performed with algebraic wall-film modeling and with disabling TFM after the 2.8ms, i.e. after the premixed flame quenching. The results are shown in black line in Figure 8.11. The soot production rate and the evolution of the soot mass became very similar to the wall-refined result, which confirms the role of the thickening of the soot section transport equation. The next step would consist in proposing an adaptation of TFM that allows to suppress the thickening after the flame/wall interaction. Due to a lack of time at the end of this study, such a modeling could not be proposed and is left to future work.

8.2.4 Conclusions

The soot formation during Flame-Film Interaction is simulated in turbulent channel flow in both wall-refined LES with resolved flame front, and WMLES with an artificially thickened flame. Only preliminary results and analysis were presented. The wall-refined case showed that the locally rich regions over the wall-film modifies the premixed flame quenching phenomena compared to its quenching over the dry wall. After the premixed flame quenching, a diffusion like reactive region is noticed around the evaporated fuel plume, powered by the evaporated fuel and by the remaining O_2 in the burnt gas of the main lean premixed flame. Soot are mainly formed in this post-quenching reactive zone. Further analysis of the results are also needed to better understand the post-quenching reactive zone and describe in details the soot formation. The WMLES results show that:

- The improved ODEs based wall model proposed in this work allows as expected to better predict the wall-film thickness prior to the flame/film interaction.
- During the flame-film interaction, the algebraic and new wall models behave in the same way, probably because of the very large increase of temperature dictated by the burned gases behind the flame.
- The soot formation process is greatly slowed down by the thickening factor used in TFM. A model that would allow to turn off this thickening after the flame/film interaction would lead to a correct agreement with the wall-refined LES. This result is encouraging as proposing such an adaptation does not seem too challenging.

Chapter 9

Conclusions and perspectives

Contents

Due to adverse environmental and health effects, particulate matters emissions are regulated with more and more strict standards. The interaction of a turbulent premixed flame with a liquid-fuel film is considered as the primary source of soot formation in GDI engines. To meet recent and future standards, high fidelity numerical tools should be able to well simulate the different physical phenomena involved in this configuration. The following modeling approaches were selected: (i) wall-modeled LES is used to solve the wall-bounded flow, (ii) the liquid phase is represented with the Lagrangian approach, (iii) The Thickened Flame Model (TFM) with reduced chemical mechanisms is used for combustion modeling, (iv) soot formation is modeled using the Sectional Soot Model (SSM). The work carried out during this thesis aimed to investigate in details the accuracy of the different involved models. The investigations were performed in the turbulent channel flow configuration, an academic setup that can be adapted to include near wall phenomena of interest of this work while being simple enough to allow the simulation of reference cases where wall boundary layers and flame front are resolved.

9.1 Conclusions

Wall-film evaporation

First, a literature review was conducted about wall-film evaporation models. An algebraic model based on a semi-analytical solution was selected. The use of this model along with classical algebraic wall stress and heat models was assessed on two different turbulent channel flow cases, one with stationary and the second with transient evaporation. These assessments showed that the wall-film evaporation has a significant influence on near wall physics and algebraic wall models are not suited for this configuration. Results were dependent in the first place on the dimensionless wall cell size. Dependency on the used wall heat model is also noticed when the wall cell center is located in the buffer layer.
In order to improve the results, a more detailed model had to be proposed. This model is an extension for wall-film evaporation of the ODEs based WMLES. The evaporated species balance equation is solved in the wall normal direction along with the momentum and energy equations. The proposed formulation takes into account the transpiration effect through the wall normal advection term in the wall normal direction and also in the near wall turbulent viscosity modeling. The assessment of the proposed model shows clearly the improvement made compared to the algebraic wall models in both stationary and transient configurations. The errors on the shear stress and heat flux at the liquid/gas interface and on the evaporation rate were much improved and became acceptable for the next step.

FWI simulation using TFM

Thermal and geometrical issues related to use of TFM for FWI simulations were pointed out during this work. These issues were first investigated in 1D flame Head-On Quenching (HOQ) configuration in engine relevant conditions. To do so, TFM was used with three wall heat flux formulations and results were compared against a well resolved case. The standard formulation of the wall heat flux using the thermal wall conductivity, without any other modification, does not alter much the evolution of the flame speed and recover well the shape and position of the temperature profiles after quenching. However, the wall heat flux diminishes with the increase of the thickening factor. Enhancing the wall thermal conductivity with the thickening factor modifies considerably the HOQ phenomena and yields large errors on the evolution of the flame speed, position and on the integral of the wall heat flux. The consideration of the thermal conductivity evaluated at the center of the wall mesh cell for the wall heat flux formulation gives the best results in this investigation, even though such a formulation is not theoretically justified.
Then, the turbulent channel flow case was adapted to complete the previous analysis to 3D flow. To that extend, a flame was initiated at the center of the channel and propagated towards the wall. This second part of the validation was focused on the assessment of using classical algebraic wall modeling with an artificially thickened flame. The main conclusion was that, for low thickening factors (about F = 6.5), using algebraic wall stress and heat models provide results in good agreement with the wall-refined simulations if the dimensionless distance of the center the wall adjacent cell is lower than the transition distance ($y_1^+ < 8$). The chosen test case did not allow to assess this modeling strategy for higher y_1^+ value. However, this conclusion was sufficient to progress to the next step of this work.

Soot formation in flame-film interaction configuration

An initial wall-film was added to the case of FWI in turbulent channel flow in order to study the Flame-Film Interaction (FFI). SSM was used to model the soot formation with prior calibration of the model constants. The wall-refined LES with resolved flame front showed that the locally rich region over the wall-film modifies the premixed flame quenching phenomena compared to its quenching over the dry wall. After the premixed flame quenching, a diffusion like reactive region is noticed around the evaporated fuel plume, powered by the evaporated fuel and by the remaining O_2 in the burnt gas of the main lean premixed flame. Soot are mainly formed in this post-quenching reactive zone.
The different modeling approaches of the involved phenomena were used all together in WMLES of the same configuration. The improved ODEs based wall model proposed in this work allows better predict the wall-film thickness prior to the flame/film interaction. The errors on soot formation does not depend on the first place on the wall-film evaporation, but rather on the using of TFM in the post-quenching reactive zone. The WMLES with disabled TFM after the premixed flame quenching lead to good prediction of the soot formation in this considered conditions.

9.2 Perspectives

Wall-film evaporation

The accuracy of the different investigations on wall-film evaporation carried out in this thesis can be improved in future works by considering the Hirschfelder and Curtiss approximation for the mass diffusion flux as the contribution of the molecular weight gradient can not be neglected for this configuration. The wall-film evaporation modeling should also be evaluated in a more realistic case which includes spray/wall interaction, film formation, variable wall surface temperature (using Conjugate Heat Transfer), and a multi-component fuel. The spray G impingement case with the wall-film evaporation in an inert constant volume chamber is a good case for such investigation as detailed wall-film measurements are provided thanks to the work of Shway [90].
The proposed ODEs based WMLES for film evaporation can be considered as a first step toward a general modeling strategy for WMLES with heat and mass transfer. Physical and numerical improvements can be considered for future works:

- Include more relevant physical phenomena in the governing equations: effect of pressure gradient, better representation of non-equilibrium behavior as done by Gelain [91], include near wall models for Pr_t and Sc_t, and check the sensitivity of the the model constants in the Cebeci-Smith model.
- Improvements can also be made on the numerical implementation of the model: better handling of the Log Layer Mismatch (by using the LES data it higher distance from the wall [40] or by applying a time filter [43]). A stretched 1D grid can also be used for lower computational cost.

FWI simulation using TFM

The 1D flame HOQ configuration showed that the artificially thickened flame modifies the wall heat loss and the FWI. So, a specific treatment of the thickening at wall need to be developed in future works. The investigations should be also extended to side-wall quenching. It is also interesting to investigate the effect of heat loss on the tabulation of flame parameters used for the computation of the thickening factor and flame sensor.
Concerning the flame-wall-turbulence interaction, several issues need to be improved. An efficiency factor adapted for near wall flame/turbulence interaction need to be developed. The effect of the artificially thickening need to be included in stress and heat wall models. The investigation of FWI in turbulent channel flow can be supported by cases with higher thickening factors and wall models evaluated at higher dimensionless wall distance. The importance of considering the Soret effect need also to be investigated, while giving a particular attention to the prediction of major and intermediate species near the wall.

Soot formation in Flame-Film Interaction configuration

The established academic case of FFI in turbulent channel flow is a good tool to study and investigate soot formation in this complex configuration. Further analysis of the wall-resolved results are needed to better understand the post-quenching reactive zone and describe in details the soot formation. In order to improve soot prediction in the WMLES cases, a specific TFM strategy need to be developed in order to automatically disable the thickening after the premixed flame quenching. The behavior of the wall-film evaporation modeling during the interaction with the flame front should be also further investigated and potentially improved. It is possible to consider the effect of the chemical reactions in the ODEs based modeling with similar approach considered by Muto and his co-workers [92, 93]. Furthermore, WMLES cases of this configuration can be used to perform fast investigations on the sensitivity of the results on various parameters: initial equivalence ratio of the premixed flame, wall-film thickness, wall temperature, etc.
The WMLES with the different modeling strategies need also to be validated against experimental results. The spray G impingement with the premixed flame ignition in constant volume chamber is a good case for such investigation as detailed wall-film and soot measurements are provided by Shway [90].

Bibliography

[1] G. Bruneaux, K. Akselvoll, T. Poinsot, and J.H. Ferziger. "Flame-wall interaction simulation in a turbulent channel flow". In: *Combustion and Flame* 107.1 (1996), pp. 27–44.

[2] BP. *BP Energy Outlook*. Tech. rep. 2019.

[3] IEA. *World Energy Outlook 2018*. Tech. rep. IEA, Paris, 2018.

[4] *Healthy environnment, healthy lives*. Tech. rep. EEA, 2019.

[5] Rajan K Chakrabarty, Payton Beeler, Pai Liu, Spondita Goswami, Richard D Harvey, Shamsh Pervez, Aaron van Donkelaar, and Randall V Martin. "Ambient PM2. 5 exposure and rapid spread of COVID-19 in the United States". In: *Science of The Total Environment* (2020), p. 143391.

[6] Silvia Comunian, Dario Dongo, Chiara Milani, and Paola Palestini. "Air pollution and Covid-19: The role of particulate matter in the spread and increase of covid-19's morbidity and mortality". In: *International journal of environmental research and public health* 17.12 (2020), p. 4487.

[7] Philip Price, Richard Stone, Tony Collier, and Marcus Davies. "Particulate Matter and Hydrocarbon Emissions Measurements: Comparing First and Second Generation DISI with PFI in Single Cylinder Optical Engines". In: *SAE Technical Paper*. SAE International, Apr. 2006.

[8] Paul Whitaker, Paul Kapus, Martin Ogris, and Peter Hollerer. "Measures to Reduce Particulate Emissions from Gasoline DI engines". In: *SAE International Journal of Engines* 4.1 (2011), pp. 1498–1512.

[9] Longfei Chen, Zhirong Liang, Xin Zhang, and Shijin Shuai. "Characterizing particulate matter emissions from GDI and PFI vehicles under transient and cold start conditions". In: *Fuel* 189 (2017), pp. 131 –140.

[10] Carolyn Farron, Nicholas Matthias, David E. Foster, Michael Andrie, Roger Krieger, Paul Najt, Kushal Narayanaswamy, Arun Solomon, and Alla Zelenyuk. "Particulate Characteristics for Varying Engine Operation in a Gasoline Spark Ignited, Direct Injection Engine". In: *SAE Technical Paper*. SAE International, Apr. 2011.

[11] M. Matti Maricq, Diane H. Podsiadlik, Diana D. Brehob, and Mohammad Haghgooie. "Particulate Emissions from a Direct-Injection Spark-Ignition (DISI) Engine". In: *SAE Technical Paper*. SAE International, May 1999.

[12] Chongming Wang, Hongming Xu, Jose Martin Herreros, Jianxin Wang, and Roger Cracknell. "Impact of fuel and injection system on particle emissions from a GDI engine". In: *Applied Energy* 132 (2014), pp. 178 –191.

[13] Zhiyu Han, Jianwen Yi, and Nizar Trigui. "Stratified Mixture Formation and Piston Surface Wetting in a DISI Engine". In: *SAE Technical Paper*. SAE International, Oct. 2002.

[14] Michele Bardi, Guillaume Pilla, and Xavier Gautrot. "Experimental assessment of the sources of regulated and unregulated nanoparticles in gasoline direct-injection engines". In: *International Journal of Engine Research* 20.1 (2019), pp. 128–140.

[15] Eric Stevens and Richard Steeper. "Piston Wetting in an Optical DISI Engine: Fuel Films, Pool Fires, and Soot Generation". In: *SAE Transactions* 110 (2001), pp. 1287–1294.

[16] Koichiro Aikawa, Takayuki Sakurai, and Jeff J. Jetter. "Development of a Predictive Model for Gasoline Vehicle Particulate Matter Emissions". In: *SAE International Journal of Fuels and Lubricants* 3.2 (2010), pp. 610–622.

[17] M. C. Drake, T. D. Fansler, A. S. Solomon, and G. A. Szekely. "Piston Fuel Films as a Source of Smoke and Hydrocarbon Emissions from a Wall-Controlled Spark-Ignited Direct-Injection Engine". In: *SAE Transactions* 112 (2003), pp. 762–783.

[18] Juhyeong Seo, Jae Seong Lee, Kwan Hee Choi, Ho Young Kim, and Sam S. Yoon. "Numerical investigation of the combustion characteristics and wall impingement with dependence on split-injection strategies from a gasoline direct-injection spark ignition engine". In: *Proceedings of the Institution of Mechanical Engineers, Part D: Journal of Automobile Engineering* 227.11 (2013), pp. 1518–1535.

[19] Juhyeong Seo, Ho Young Kim, Simsoo Park, Scott C. James, and Sam S. Yoon. "Experimental and Numerical Simulations of Spray Impingement and Combustion Characteristics in Gasoline Direct Injection Engines under Variable Driving Conditions". In: *Flow, Turbulence and Combustion* 96.2 (Mar. 2016), pp. 391–415.

[20] Stephen B. Pope. *Turbulent Flows*. Cambridge University Press, 2000.

[21] Henning Bockhorn. *Soot Formation in Combustion*. Jan. 1994.

[22] *https://orch.coria-cfd.fr*.

[23] Damien Aubagnac-Karkar. "Sectional soot modeling for Diesel RANS simulations". Thèse de doctorat dirigée par Darabiha, Nasser Énergétique Châtenay-Malabry, Ecole centrale de Paris 2014. PhD thesis. 2014.

[24] Gaëtan Desoutter. "Étude numérique de la propagation d'une flamme sous influence d'un film liquide de carburant sur la paroi". Thèse de doctorat dirigée par Cuenot, Bénédicte Énergétique et transferts Toulouse, INPT 2007. PhD thesis. 2007, 1 vol. (239 p.)

[25] Thierry Poinsot and Denis Veynante. *Theoretical and numerical combustion*. RT Edwards, Inc., 2005.

[26] https://cantera.org/.

[27] Olivier Cabrit and Franck Nicoud. "Direct simulations for wall modeling of multicomponent reacting compressible turbulent flows". In: *Physics of Fluids* 21.5 (2009), p. 055108.

[28] Pedro Rodrigues. "Modélisation multiphysique de flammes turbulentes suitées avec la prise en compte des transferts radiatifs et des transferts de chaleur pariétaux." Theses. Université Paris-Saclay, June 2018.

[29] B.V. Derjaguin, A.I. Storozhilova, and Ya. I. Rabinovich. "Experimental verification of the theory of thermophoresis of aerosol particles". In: *Journal of Colloid and Interface Science* 21.1 (1966), pp. 35–58.

[30] Mahdi Faghih, Wang Han, and Zheng Chen. "Effects of Soret diffusion on premixed flame propagation under engine-relevant conditions". In: *Combustion and Flame* 194 (2018), pp. 175–179.

[31] C. Hasse, M. Bollig, N. Peters, and H.A. Dwyer. "Quenching of laminar iso-octane flames at cold walls". In: *Combustion and Flame* 122.1 (2000), pp. 117–129.

[32] Marc Chauvy, Bruno Delhom, Julien Reveillon, and Francois-Xavier Demoulin. "Flame/Wall Interactions: Laminar Study of Unburnt HC Formation". In: *Flow, Turbulence and Combustion* 84.3 (2010), pp. 369–396.

[33] Kosuke Narukawa, Yuki Minamoto, Masayasu Shimura, and Mamoru Tanahashi. "Near-wall flame propagation behaviour with and without surface reactions". In: *Fuel* 268 (2020), p. 117216.

[34] Franck Nicoud, Hubert Baya Toda, Olivier Cabrit, Sanjeeb Bose, and Jungil Lee. "Using singular values to build a subgrid-scale model for large eddy simulations". In: *Physics of Fluids* 23.8 (2011), p. 085106.

[35] R. Mercier, T.F. Guiberti, A. Chatelier, D. Durox, O. Gicquel, N. Darabiha, T. Schuller, and B. Fiorina. "Experimental and numerical investigation of the influence of thermal boundary conditions on premixed swirling flame stabilization". In: *Combustion and Flame* 171 (2016), pp. 42–58.

[36] Chaï Koren, Ronan Vicquelin, and Olivier Gicquel. "Multiphysics Simulation Combining Large-Eddy Simulation, Wall Heat Conduction and Radiative Energy Transfer to Predict Wall Temperature Induced by a Confined Premixed Swirling Flame". In: *Flow, Turbulence and Combustion* 101.1 (2018), pp. 77–102.

[37] T Cebeci and J Cousteix. "Modeling and Computation of Boundary-Layer Flows". In: *Modeling and Computation of Boundary-Layer Flows: Laminar, Turbulent and Transitional Boundary Layers in Incompressible and Compressible Flows*. Berlin, Heidelberg: Springer Berlin Heidelberg, 2005. Chap. Two-Dimensional Incompressible Turbulent Flows, pp. 163–208.

[38] W.M. Kays and M.E. Crawford. *Convective heat and mass transfer*. McGraw-Hill Series in Management. McGraw-Hill Ryerson, Limited, 1980.

[39] Thomas A. Zang, J. D. A. Walker, and F. T. Smith. "Numerical simulation of the dynamics of turbulent boundary layers: perspectives of a transition simulator". In: *Philosophical Transactions of the Royal Society of London. Series A: Physical and Engineering Sciences* 336.1641 (1991), pp. 95–102.

[40] Johan Larsson, Soshi Kawai, Julien Bodart, and Ivan Bermejo-Moreno. "Large eddy simulation with modeled wall-stress: recent progress and future directions". In: *Mechanical Engineering Reviews* 3.1 (2016), pp. 15–00418–15–00418.

[41] Sanjeeb T. Bose and George Ilhwan Park. "Wall-Modeled Large-Eddy Simulation for Complex Turbulent Flows". In: *Annual Review of Fluid Mechanics* 50.1 (2018), pp. 535–561.

[42] Francesco De Vanna, Michele Cogo, Matteo Bernardini, Francesco Picano, and Ernesto Benini. "Unified wall-resolved and wall-modeled method for large-eddy simulations of compressible wall-bounded flows". In: *Phys. Rev. Fluids* 6 (3 2021), p. 034614.

[43] Xiang I. A. Yang, George Ilhwan Park, and Parviz Moin. "Log-layer mismatch and modeling of the fluctuating wall stress in wall-modeled large-eddy simulations". In: *Phys. Rev. Fluids* 2 (10 2017), p. 104601.

[44] Chalearmpol Plengsaard and Christopher Rutland. "Improved Engine Wall Models for Large Eddy Simulation (LES)". In: *SAE 2013 World Congress & Exhibition*. SAE International, 2013.

[45] H. Werner and H. Wengle. "Large-Eddy Simulation of Turbulent Flow Over and Around a Cube in a Plate Channel". In: *Turbulent Shear Flows 8*. Ed. by Franz Durst, Rainer Friedrich, Brian E. Launder, Frank W. Schmidt, Ulrich Schumann, and James H. Whitelaw. Berlin, Heidelberg: Springer Berlin Heidelberg, 1993, pp. 155–168.

[46] C.D. Rakopoulos, G.M. Kosmadakis, and E.G. Pariotis. "Critical evaluation of current heat transfer models used in CFD in-cylinder engine simulations and establishment of a comprehensive wall-function formulation". In: *Applied Energy* 87.5 (2010), pp. 1612–1630.

[47] Jingjie Cao, Ming Jia, Bo Niu, Yachao Chang, Zhen Xu, and Hong Liu. "Establishment of an improved heat transfer model based on an enhanced thermal wall function for internal combustion engines operated under different combustion modes". In: *Energy Conversion and Management* 195 (2019), pp. 748–759.

[48] Christian Angelberger. "Contributions à la modélisation de l'interaction flamme-paroi et des flux pariétaux dans les moteurs à allumage commandé". Thèse de doctorat dirigée par Poinsot, Thierry Mécanique des fluides Toulouse, INPT 1997. PhD thesis. 1997, 206 p.

[49] T Cebeci and J Cousteix. "Modeling and Computation of Boundary-Layer Flows". In: *Modeling and Computation of Boundary-Layer Flows: Laminar, Turbulent and Transitional Boundary Layers in Incompressible and Compressible Flows*. Berlin, Heidelberg: Springer Berlin Heidelberg, 2005. Chap. Two-Dimensional Compressible Turbulent Flows, pp. 387–415.

[50] E. R. VAN DRIEST. "Turbulent Boundary Layer in Compressible Fluids". In: *Journal of the Aeronautical Sciences* 18.3 (1951), pp. 145–160.

[51] A. Trettel. "Velocity transformation for compressible wall turbulence with heat transfer". In: 2015.

[52] Andrew Trettel and Johan Larsson. "Mean velocity scaling for compressible wall turbulence with heat transfer". In: *Physics of Fluids* 28.2 (2016), p. 026102.

[53] Ashish Patel, Jurriaan W. R. Peeters, Bendiks J. Boersma, and Rene Pecnik. "Semi-local scaling and turbulence modulation in variable property turbulent channel flows". In: *Physics of Fluids* 27.9 (2015), p. 095101.

[54] Ashish Patel, Bendiks J. Boersma, and Rene Pecnik. "The influence of near-wall density and viscosity gradients on turbulence in channel flows". In: *Journal of Fluid Mechanics* 809 (2016), 793–820.

[55] Ashish Patel, Bendiks J. Boersma, and Rene Pecnik. "Scalar statistics in variable property turbulent channel flows". In: *Phys. Rev. Fluids* 2 (8 2017), p. 084604.

[56] Kevin Patrick Griffin, Lin Fu, and Parviz Moin. "Velocity transformation for compressible wall-bounded turbulent flows with and without heat transfer". In: *Proceedings of the National Academy of Sciences* 118.34 (2021).

[57] F. Nicoud and P. Bradshaw. "A velocity transformation for heat and mass transfer". In: *Physics of Fluids* 12.1 (2000), pp. 237–238.

[58] Zhiyu Han and Rolf D. Reitz. "A temperature wall function formulation for variable-density turbulent flows with application to engine convective heat transfer modeling". In: *International Journal of Heat and Mass Transfer* 40.3 (1997), pp. 613 –625.

[59] P. G. Huang, G. N. Coleman, and P. Bradshaw. "Compressible turbulent channel flows: DNS results and modelling". In: *Journal of Fluid Mechanics* 305 (1995), 185–218.

[60] FC Nicoud. "flow with variable properties". In: *Annual Research Briefs-1998* (1998), p. 289.

[61] Myoungkyu Lee and Robert D. Moser. "Direct numerical simulation of turbulent channel flow up to $Re_\tau \approx 5200$". In: *Journal of Fluid Mechanics* 774 (2015), 395–415.

[62] Juan A. Sillero, Javier Jiménez, and Robert D. Moser. "One-point statistics for turbulent wall-bounded flows at Reynolds numbers up to $\delta+ \approx 2000$". In: *Physics of Fluids* 25.10 (2013), p. 105102.

[63] A A Amsden. "KIVA-3V: A block-structured KIVA program for engines with vertical or canted valves". In: (July 1997).

[64] Fabio Berni, Giuseppe Cicalese, and Stefano Fontanesi. "A modified thermal wall function for the estimation of gas-to-wall heat fluxes in CFD in-cylinder simulations of high performance spark-ignition engines". In: *Applied Thermal Engineering* 115 (2017), pp. 1045 –1062.

[65] Sanjin Saric and Branislav Basara. "A Hybrid Wall Heat Transfer Model for IC Engine Simulations". In: *SAE International Journal of Engines* 8.2 (2015), pp. 411–418.

[66] Gaëtan Desoutter, Chawki Habchi, Bénédicte Cuenot, and Thierry Poinsot. "DNS and modeling of the turbulent boundary layer over an evaporating liquid film". In: *International Journal of Heat and Mass Transfer* 52.25 (2009), pp. 6028–6041.

[67] Vladislav Efros. "Large eddy simulation of channel flow using wall functions". In: *Goteborg, Sweden: Chalmers Reproservice* (2006).

[68] Seyed Vahid Ebrahimian Shiadeh. "Développement de modeles d'évaporation multi-composants et modélisation 3D des systèmes de réduction de NOx (SCR)". Thèse de doctorat dirigée par Cuenot, Bénédicte et Habchi, Chawki Energétique et transferts Toulouse, INPT 2011. PhD thesis. 2011.

[69] Chia fon F. Lee, Way Lee Cheng, and Dongyao Wang. "Finite diffusion wall film evaporation model for engine simulations using continuous thermodynamics". In: *Proceedings of the Combustion Institute* 32.2 (2009), pp. 2801 –2808.

[70] Sandeep Mouvanal, Quentin Lamiel, Nicolas Lamarque, Jerome Helie, Axel Burkhardt, Shamit Bakshi, and Dhiman Chatterjee. "Evaporation of thin liquid film of single and multi-component hydrocarbon fuel from a hot plate". In: *International Journal of Heat and Mass Transfer* 141 (2019), pp. 379 –389.

[71] François Chedevergne and Yann Marchenay. “Transpired turbulent boundary layers: a general strategy for RANS turbulence models”. In: *Journal of Turbulence* 20.11-12 (2019), pp. 681–696.

[72] Hong Liu, Yan’an Yan, Ming Jia, Yanzhi Zhang, Maozhao Xie, and Hongchao Yin. “An analytical solution for wall film heating and evaporation”. In: *International Communications in Heat and Mass Transfer* 87 (2017), pp. 125 –131.

[73] Yanzhi Zhang, Ming Jia, Ping Yi, Hong Liu, and Maozhao Xie. “An efficient liquid film vaporization model for multi-component fuels considering thermal and mass diffusions”. In: *Applied Thermal Engineering* 112 (2017), pp. 534–548.

[74] P.J. O’Rourke and A. A. Amsden. “A Particle Numerical Model for Wall Film Dynamics in Port-Injected Engines”. In: *SAE Technical Paper*. SAE International, Oct. 1996.

[75] D J Torres, P J O’rourke, and A A Amsden. “Efficient multicomponent fuel algorithm”. In: *Combustion Theory and Modelling* 7.1 (2003), pp. 66–86.

[76] *Modeling of Wall Film Formed by Impinging Spray Using a Fully Explicit Integration Method*. Vol. ASME 2005 Internal Combustion Engine Division Spring Technical Conference. Internal Combustion Engine Division Spring Technical Conference. Apr. 2005, pp. 271–280.

[77] Qi Jiao and Rolf D Reitz. “Modeling soot emissions from wall films in a direct-injection spark-ignition engine”. In: *International Journal of Engine Research* 16.8 (2015), pp. 994–1013.

[78] Yanzhi Zhang, Ming Jia, Hong Liu, and Maozhao Xie. “Development of an improved liquid film model for spray/wall interaction under engine-relevant conditions”. In: *International Journal of Multiphase Flow* 79 (2016), pp. 74–87.

[79] Yoshimitsu Kobashi, Yoshio Zama, and Tatsuya Kuboyama. “Modeling wall film formation and vaporization of a gasoline surrogate fuel”. In: *International Journal of Heat and Mass Transfer* 147 (2020), p. 119035.

[80] Hong Liu, Yan’an Yan, Ming Jia, Chang Cai, and Yanzhi Zhang. “An analytical model of the heating and evaporation of bi-component wall film”. In: *International Communications in Heat and Mass Transfer* 105 (2019), pp. 28 –36.

[81] H. Foucart, C. Habchi, J. F. Le Coz, and T. Baritaud. “Development of a Three Dimensional Model of Wall Fuel Liquid Film for Internal Combustion Engines”. In: *International Congress & Exposition*. SAE International, 1998.

[82] D.B. Spalding. *Convective mass transfer*. McGraw-hill, 1963.

[83] David Maligne and Gilles Bruneaux. “Time-Resolved Fuel Film Thickness Measurement for Direct Injection SI Engines Using Refractive Index Matching”. In: *SAE 2011 World Congress & Exhibition*. SAE International, 2011.

[84] Yangbing Zeng and Chia-Fon Lee. “Multicomponent-Fuel Film-Vaporization Model for Multidimensional Computations”. In: *Journal of Propulsion and Power* 16.6 (2000), pp. 964–973.

[85] Song Liye, Zhang Weizheng, Zhang Ti’en, and Qin Zhaoju. “A new approach to transient evaporating film heating modeling based on analytical temperature profiles for internal combustion engines”. In: *International Journal of Heat and Mass Transfer* 81 (2015), pp. 465 –469.

[86] S.S. Sazhin, O. Rybdylova, and C. Crua. “A mathematical model for heating and evaporation of a multi-component liquid film”. In: *International Journal of Heat and Mass Transfer* 117 (2018), pp. 252 –260.

[87] S.S. Sazhin, P.A. Krutitskii, I.G. Gusev, and M.R. Heikal. “Transient heating of an evaporating droplet with presumed time evolution of its radius”. In: *International Journal of Heat and Mass Transfer* 54.5 (2011), pp. 1278–1288.

[88] Thilo Schonfeld and Michael Rudgyard. “Steady and Unsteady Flow Simulations Using the Hybrid Flow Solver AVBP”. In: *AIAA Journal* 37.11 (1999), pp. 1378–1385.

[89] Olivier Colin and Michael Rudgyard. “Development of High-Order Taylor–Galerkin Schemes for LES”. In: *Journal of Computational Physics* 162.2 (2000), pp. 338–371.

[90] K. Shway. *A current PhD candidate at IFPEN performing precise optical wall-film thickness and soot measurements during inert wall-film evaporation and falame-film interaction, results will be published soon.*

[91] Matteo Gelain. "Aerothermal characterisation of a surface heat exchanger implemented in a turbofan by-pass duct". Theses. Université Paris-Saclay, Nov. 2021.

[92] Daiki Muto, Yu Daimon, Taro Shimizu, and Hideyo Negishi. "An equilibrium wall model for reacting turbulent flows with heat transfer". In: *International Journal of Heat and Mass Transfer* 141 (2019), pp. 1187–1195.

[93] Daiki Muto, Yu Daimon, Hideyo Negishi, and Taro Shimizu. "Wall modeling of turbulent methane/oxygen reacting flows for predicting heat transfer". In: *International Journal of Heat and Fluid Flow* 87 (2021), p. 108755.

[94] T. Cebeci and A. M. O. Smith. "Analysis of turbulent boundary layers". In: *NASA STI/Recon Technical Report A* 75 (Jan. 1974), p. 46513.

[95] J.N. Levine. *Transpiration and film cooling boundary layer computer program. Volume 1: Numerical solutions of the turbulent boundary layer equations with equilibrium chemistry*. Research rep. NASA-CR-125683. NASA, 1971.

[96] Dean R. Chapman and Gary D. Kuhn. "The limiting behaviour of turbulence near a wall". In: *Journal of Fluid Mechanics* 170 (1986), 265–292.

[97] Maarten van Reeuwijk and Muhamed Hadžiabdić. "Modelling high Schmidt number turbulent mass transfer". In: *International Journal of Heat and Fluid Flow* 51 (2015). Theme special issue celebrating the 75th birthdays of Brian Launder and Kemo Hanjalic, pp. 42–49.

[98] Peng E. S. Chen, Yu Lv, Haosen H. A. Xu, Yipeng Shi, and Xiang I. A. Yang. *LES wall modeling for heat transfer at high speeds*. 2021.

[99] R. A. Antonia. "Behaviour of the turbulent Prandtl number near the wall". In: *International Journal of Heat and Mass Transfer* 23 (June 1980), pp. 906–908.

[100] M. C. Silva, L. C. De Lima, and R. F. Miranda. "Comparative Analysis of Different Models for the Turbulent Prandtl Number". In: *Journal of Heat Transfer* 121.2 (May 1999), pp. 473–477.

[101] A.J. Reynolds. "The prediction of turbulent Prandtl and Schmidt numbers". In: *International Journal of Heat and Mass Transfer* 18.9 (1975), pp. 1055–1069.

[102] T. Cebeci. "Calculation of compressible turbulent boundary layers with heat and mass transfer". In: *3rd Fluid and Plasma Dynamics Conference*.

[103] W.M Kays. "Heat transfer to the transpired turbulent boundary layer". In: *International Journal of Heat and Mass Transfer* 15.5 (1972), pp. 1023–1044.

[104] Hans Petter Langtangen and Svein Linge. *Finite difference computing with PDEs: a modern software approach*. Springer Nature, 2017.

[105] Norbert Peters. *Turbulent Combustion*. Cambridge Monographs on Mechanics. Cambridge University Press, 2000.

[106] P.J O'Rourke and F.V Bracco. "Two scaling transformations for the numerical computation of multidimensional unsteady laminar flames". In: *Journal of Computational Physics* 33.2 (1979), pp. 185–203.

[107] O. Colin, F. Ducros, D. Veynante, and T. Poinsot. "A thickened flame model for large eddy simulations of turbulent premixed combustion". In: *Physics of Fluids* 12.7 (2000), pp. 1843–1863.

[108] Pierre Quillatre. "Simulation aux grandes échelles d'explosions en domaine semi-confiné". Thèse de doctorat dirigée par Poinsot, Thierry et Vermorel, Olivier Energétique et transferts Toulouse, INPT 2014. PhD thesis. 2014.

[109] Thomas Jaravel. "Prediction of pollutants in gas turbines using large eddy simulation". PhD thesis. 2016.

[110] Cédric Mehl, Shuaishuai Liu, Yee Chee See, and Olivier Colin. "LES of a stratified turbulent burner with a Thickened Flame Model coupled to Adaptive Mesh Refinement and detailed chemistry". In: *2018 Joint Propulsion Conference*. 2018.

[111] Fabrice Charlette, Charles Meneveau, and Denis Veynante. "A power-law flame wrinkling model for LES of premixed turbulent combustion Part I: non-dynamic formulation and initial tests". In: *Combustion and Flame* 131.1 (2002), pp. 159 –180.

[112] S. Bougrine, S. Richard, O. Colin, and D. Veynante. "Fuel Composition Effects on Flame Stretch in Turbulent Premixed Combustion: Numerical Analysis of Flame-Vortex Interaction and Formulation of a New Efficiency Function". In: *Flow, Turbulence and Combustion* 93.2 (2014), pp. 259–281.

[113] T.J. Poinsot, D.C. Haworth, and G. Bruneaux. "Direct simulation and modeling of flame-wall interaction for premixed turbulent combustion". In: *Combustion and Flame* 95.1 (1993), pp. 118 –132.

[114] Indrek S. Wichman and Gilles Bruneaux. "Head-on quenching of a premixed flame by a cold wall". In: *Combustion and Flame* 103.4 (1995), pp. 296–310.

[115] G. Bruneaux, T. Poinsot, and J. H. Ferziger. "Premixed flame–wall interaction in a turbulent channel flow: budget for the flame surface density evolution equation and modelling". In: *Journal of Fluid Mechanics* 349 (1997), 191–219.

[116] C. Angelberger, T. Poinsot, and B. Delhay. "Improving Near-Wall Combustion and Wall Heat Transfer Modeling in SI Engine Computations". In: *SAE Technical Paper*. SAE International, Oct. 1997.

[117] Sokratis Demesoukas, Christian Caillol, Pascal Higelin, Andrei Boiarciuc, and Alain Floch. "Near wall combustion modeling in spark ignition engines. Part A: Flame–wall interaction". In: *Energy Conversion and Management* 106 (2015), pp. 1426–1438.

[118] Karine Truffin, B Leveugle, Gilles Bruneaux, Y D'Angelo, and Julien Reveillon. "Modeling the effect of flame-wall interaction on the wall heat flux". In: *THMT-12. Proceedings of the Seventh International Symposium On Turbulence Heat and Mass Transfer*. Begel House Inc. 2012.

[119] Benoît Leveugle. "Simulation DNS de l'interaction flamme-paroi dans les moteurs à allumage commandé". Theses. INSA de Rouen, Dec. 2012.

[120] Michele Bolla, Matteo Impagnatiello, Karri Keskinen, George Giannakopoulos, Christos E. Frouzakis, Yuri M. Wright, and Konstantinos Boulouchos. "Development of an algebraic wall heat transfer model for LES in IC engines using DNS data". In: *Proceedings of the Combustion Institute* 38.4 (2021), pp. 5811–5819.

[121] Anja Ketelheun, Guido Kuenne, and Johannes Janicka. "Heat Transfer Modeling in the Context of Large Eddy Simulation of Premixed Combustion with Tabulated Chemistry". In: *Flow, Turbulence and Combustion* 91.4 (2013), pp. 867–893.

[122] Renaud Mercier. "Turbulent combustion modeling for Large Eddy Simulation of non-adiabatic stratified flames". Theses. Ecole Centrale Paris, Sept. 2015.

[123] Yajuvendra Singh Shekhawat. "Large-eddy simulations of motored flow and combustion in a homogeneous-charge spark-ignition engine". PhD thesis. 2016.

[124] Yan zhao An, Yi qiang Pei, Jing Qin, Hua Zhao, Sheng ping Teng, Bing Li, and Xiang Li. "Development of a PAH (polycyclic aromatic hydrocarbon) formation model for gasoline surrogates and its application for GDI (gasoline direct injection) engine CFD (computational fluid dynamics) simulation". In: *Energy* 94 (2016), pp. 367 –379.

[125] Nicolas Jaouen, Luc Vervisch, Pascale Domingo, and Guillaume Ribert. "Automatic reduction and optimisation of chemistry for turbulent combustion modelling: Impact of the canonical problem". In: *Combustion and Flame* 175 (2017). Special Issue in Honor of Norbert Peters, pp. 60–79.

[126] Nicolas Jaouen, Luc Vervisch, and Pascale Domingo. "Auto-thermal reforming (ATR) of natural gas: An automated derivation of optimised reduced chemical schemes". In: *Proceedings of the Combustion Institute* 36.3 (2017), pp. 3321–3330.

[127] Nicolas Jaouen. “An automated approach to derive and optimise reduced chemical mechanisms for turbulent combustion”. Thèse de doctorat dirigée par Domingo, Pascale et Vervisch, Luc Energétique Normandie 2017. PhD thesis. 2017.

[128] Andrea Seltz. “Application of deep learning to turbulent combustion modeling of real jet fuel for the numerical prediction of particulate emissions”. Theses. Normandie Université, Sept. 2020.

[129] Perrine Pepiot and Heinz Pitsch. “Systematic reduction of large chemical mechanisms”. In: *4th joint meeting of the US Sections of the Combustion Institute, Philadelphia, PA*. 2005, pp. 324–330.

[130] Alessandro Faccinetto, Xavier Mercier, T. Mouton, Abderrahman El Bakali, Damien Aubagnac-Karkar, Christopher Betrancourt, and Pascale Desgroux. *Experimental and modeling study of the soot formation process in very low sooting low pressure methane flames.*

[131] Mamady Keita, Damien Aubagnac-Karkar, Christopher Betrancourt, A. Nicolle, Xavier Mercier, Pascale Desgroux, and Abderrahman El Bakali. “Modeling of soot particles nucleation in premixed laminar ethylene and n-butane flames.” In.

[132] D. Boufflers, Abderrahman El Bakali, Pascale Desgroux, Laurent Gasnot, and L. Rigolet. “Experimental Study of Atmospheric Laminar Sooting Premixed n-Butane Flames”. In.

[133] M. R. Kholghy, G. A. Kelesidis, and S. E. Pratsinis. “Reactive polycyclic aromatic hydrocarbon dimerization drives soot nucleation”. In: *Phys. Chem. Chem. Phys.* 20 (16 2018), pp. 10926–10938.

[134] Damien Aubagnac-Karkar, Abderrahman Bakali, and Pascale Desgroux. “Soot Particles Inception and PAH Condensation Modelling Applied in a Soot Model Utilizing a Sectional Method”. In: (Jan. 2018).

[135] Hassan Sabbah, Ludovic Biennier, Stephen J. Klippenstein, Ian R. Sims, and Bertrand R. Rowe. “Exploring the Role of PAHs in the Formation of Soot: Pyrene Dimerization”. In: *J. Phys. Chem. Lett.* 1.19 (Oct. 2010), pp. 2962–2967.

[136] Hong-Bo Zhang, Xiaoqing You, Hongmiao Wang, and Chung K. Law. “Dimerization of Polycyclic Aromatic Hydrocarbons in Soot Nucleation”. In: *J. Phys. Chem. A* 118.8 (Feb. 2014), pp. 1287–1292.

[137] Paolo Elvati, Kirk Turrentine, and Angela Violi. “The role of molecular properties on the dimerization of aromatic compounds”. In: *Proceedings of the Combustion Institute* 37.1 (2019), pp. 1099 –1105.

[138] J. Yon, F. Liu, J. Morán, and A. Fuentes. “Impact of the primary particle polydispersity on the radiative properties of soot aggregates”. In: *Proceedings of the Combustion Institute* 37.1 (2019), pp. 1151 –1159.

[139] Fabian Mauss, Thomas Schäfer, and Henning Bockhorn. “Inception and growth of soot particles in dependence on the surrounding gas phase”. In: *Combustion and Flame* 99.3 (1994). 25th Symposium (International) on Combustion Papers, pp. 697 –705.

[140] Karl Netzell. “Development and Applications of Detailed Kinetic Models for the Soot Particle Size Distribution Function”. English. Defence details Date: 2006-11-23 Time: 10:15 Place: Room F, Department of Physics, "Fysicum", Professorsgatan 1, Lund Institute of Technology External reviewer(s) Name: Pratsinis, Sotiris Title: Professor Affiliation: Swiss Federal Institute of Technology —. PhD thesis. Combustion Physics, 2006.

[141] Caroline Marchal. “Modélisation de la formation et de l’oxydation des suies dans un moteur automobile”. Theses. Université d’Orléans, Dec. 2008.

[142] Pauline Vervisch. “Modélisation des oxydes d’azote et des suies dans les moteurs Diesel,” Thèse de doctorat dirigée par Darabiha, Nasser Energétique Châtenay-Malabry, Ecole centrale de Paris 2012. PhD thesis. 2012.

[143] Abhijeet Raj, Iran David Charry Prada, Amer Ahmad Amer, and Suk Ho Chung. “A reaction mechanism for gasoline surrogate fuels for large polycyclic aromatic hydrocarbons”. In: *Combustion and Flame* 159.2 (2012), pp. 500–515.

[144] I. Frenzel, H. Krause, and D. Trimis. “Study on the influence of ethanol and butanol addition on soot formation in iso-octane flames”. In: *Energy Procedia* 120 (2017). INFUB - 11th European Conference on Industrial Furnaces and Boilers, INFUB-11, pp. 721–728.

[145] Michael Frenklach and Hai Wang. “Detailed modeling of soot particle nucleation and growth”. In: *Symposium (International) on Combustion* 23.1 (1991). Twenty-Third Symposium (International) on Combustion, pp. 1559–1566.

[146] Jasdeep Singh, Michael Balthasar, Markus Kraft, and Wolfgang Wagner. “Stochastic modeling of soot particle size and age distributions in laminar premixed flames”. In: *Proceedings of the Combustion Institute* 30.1 (2005), pp. 1457–1465.

[147] R.P. Lindstedt and B.B.O. Waldheim. “Modeling of soot particle size distributions in premixed stagnation flow flames”. In: *Proceedings of the Combustion Institute* 34.1 (2013), pp. 1861–1868.

[148] Armin Veshkini, Seth B. Dworkin, and Murray J. Thomson. “A soot particle surface reactivity model applied to a wide range of laminar ethylene/air flames”. In: *Combustion and Flame* 161.12 (2014), pp. 3191–3200.

[149] A. D’Anna and J.H. Kent. “Modeling of particulate carbon and species formation in coflowing diffusion flames of ethylene”. In: *Combustion and Flame* 144.1 (2006), pp. 249–260.

[150] A. D’Anna and J.H. Kent. “A model of particulate and species formation applied to laminar, nonpremixed flames for three aliphatic-hydrocarbon fuels”. In: *Combustion and Flame* 152.4 (2008), pp. 573–587.

[151] Andrea D’Anna. “Detailed Kinetic Modeling of Particulate Formation in Rich Premixed Flames of Ethylene”. In: *Energy & Fuels* 22.3 (2008), pp. 1610–1619.

[152] Chiara Saggese, Sara Ferrario, Joaquin Camacho, Alberto Cuoci, Alessio Frassoldati, Eliseo Ranzi, Hai Wang, and Tiziano Faravelli. “Kinetic modeling of particle size distribution of soot in a premixed burner-stabilized stagnation ethylene flame”. In: *Combustion and Flame* 162.9 (2015), pp. 3356–3369.

[153] Michael Frenklach. “New form for reduced modeling of soot oxidation: Accounting for multi-site kinetics and surface reactivity”. In: *Combustion and Flame* 201 (2019), pp. 148–159.

[154] Tim S. Totton, Alston J. Misquitta, and Markus Kraft. “A quantitative study of the clustering of polycyclic aromatic hydrocarbons at high temperatures”. In: *Phys. Chem. Chem. Phys.* 14 (12 2012), pp. 4081–4094.

[155] Hai Wang. “Formation of nascent soot and other condensed-phase materials in flames”. In: *Proceedings of the Combustion Institute* 33.1 (2011), pp. 41–67.

[156] N.A. Eaves, S.B. Dworkin, and M.J. Thomson. “The importance of reversibility in modeling soot nucleation and condensation processes”. In: *Proceedings of the Combustion Institute* 35.2 (2015), pp. 1787–1794.

[157] C. Betrancourt, D. Aubagnac-Karkar, X. Mercier, A. El-Bakali, and P. Desgroux. “Experimental and numerical investigation of the transition from non sooting to sooting premixed n-butane flames, encompassing the nucleation flame conditions”. In: *Combustion and Flame* (In press).

[158] P. K. Senecal, E. Pomraning, K. J. Richards, T. E. Briggs, C. Y. Choi, R. M. McDavid, and M. A. Patterson. “Multi-Dimensional Modeling of Direct-Injection Diesel Spray Liquid Length and Flame Lift-off Length using CFD and Parallel Detailed Chemistry”. In: *SAE 2003 World Congress & Exhibition*. SAE International, 2003.

[159] A Babajimopoulos, D N Assanis, D L Flowers, S M Aceves, and R P Hessel. “A fully coupled computational fluid dynamics and multi-zone model with detailed chemical kinetics for the simulation of premixed charge compression ignition engines”. In: *International Journal of Engine Research* 6.5 (2005), pp. 497–512.

[160] R.I Issa. “Solution of the implicitly discretised fluid flow equations by operator-splitting”. In: *Journal of Computational Physics* 62.1 (1986), pp. 40–65.

[161] C. M. Rhie and W. L. Chow. “Numerical study of the turbulent flow past an airfoil with trailing edge separation”. In: *AIAA Journal* 21.11 (1983), pp. 1525–1532.

Appendix A

CONVERGE Numerics

The flowchart of the solution procedure for each time step is shown in Figure A.1. At the start of each time-step, explicit source terms are calculated for each sub-model (combustion, evaporation, ...). The conservation equations are solved next with a compressible pressure-velocity coupling procedure and an iterative numerical method. The passive transport equations are solved at the end of the time step. In the following, each step of the solution procedure is briefly described.

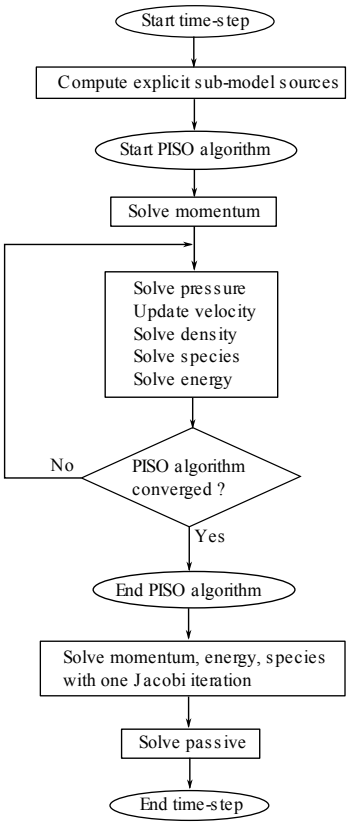

Figure A.1: Flowchart of the solution procedure

Chemical kinetics solver

The mass reaction rate and heat release rate are computed at the beginning of the time step. CONVERGE uses the SAGE solver [158] which models detailed chemical kinetics via a set of CHEMKIN-formatted input files. The system of ordinary differential equations are solved using CVODE solver. The Adaptive Zoning [159] accelerates the chemistry calculations by grouping together similar computational cells and then invoking the chemistry solver once per group rather than once per cell. The cells are grouped together into zones based on their temperature and composition. The common thermodynamic state of each zone is based on the average temperature and composition of all the cells in that zone. The result is mapped again to the cells using a mapping technique [159].

Time advancement

Crank-Nicolson time advancement is used for the momentum equation and first order implicit Euler method is used for the other governing equations. The time step is limited by constant Courant-Friedrichs-Lewy (CFL) numbers. Three different CFL numbers are considered: a velocity based CFL ($CFL_U = U\Delta t/\Delta x$), a diffusion based CFL ($CFL_\nu = \nu\Delta t/\Delta x$) and a CFL based on the speed of sound ($CFL_{mach} = c\Delta t/\Delta x$). For the present work, the following values where used: $CFL_U = 0.2$, $CFL_\nu = 0.2$ and $CFL_{mach} = 50$.

Spatial discretization

CONVERGE uses a colocated finite volume method to numerically solve the conservation equations. The integral form of these equation is discretized for each cell by summing fluxes on the cell faces. The cell face value is obtained by averaging the adjacent cell values, which results in a centered second-order accurate spatial scheme. Flux limiters are also applied to ensure numerical stability.

Pressure-velocity coupling

CONVERGE is a pressure based solver which accounts for compressibility. A modified Pressure Implicit with Splitting of Operator (PISO) method [160] is used for the pressure-velocity coupling. The PISO algorithm starts with a predictor step where the momentum equation is solved. After the predictor, a pressure equation is solved, which leads to a correction, which is applied to the momentum equation. The ideal gas law (Eq. (2.26)) is used to relate density with pressure in the derived pressure equation, and so account for compressibility. The total mass equation is transported in this algorithm together with all the species mass equations in order to ensure the total mass conservation. This process of correcting the momentum equation and re-solving is repeated until the desired accuracy is achieved. All the flow quantities (velocity, pressure, density, temperature, species, ...) are calculated and stored at cell centers. The use of colocated quantities can result in a decoupling of pressure and velocity and produce fluctuations in the pressure and velocity solution that appears in a checkerboard pattern. The Rhie-Choe interpolation scheme [161] is used to maintain colocated variables and eliminate the undesirable checkerboarding.

Numerical solution

After the spatial and the implicit temporal discretization, the solution of the conservation equations are obtained by solving a linear system. The Successive Over-Relaxation (SOR) iterative algorithm is performed to solve the conservation equations. The iterative algorithm will search for a solution within a specified tolerance or if the maximum number of iterations is reached. An additional Jacobi iteration is performed to enforce strict conservation of mass, energy, species and passives. The Jacobi iteration guarantees that the quantity is conserved to zero machine rather than to the tolerance set for the iterative algorithm.

Simulation aux Grandes Echelles de l'interaction entre un film liquide de combustible et une flamme turbulente en région de proche paroi, application à la formation de suie

Chapitre 1: Introduction

Contexte

Avec environ 20% de la consommation mondiale d'énergie, le secteur des transports est considéré comme l'un des principaux émetteurs de gaz à effet de serre [1]. L'amélioration de l'efficacité énergétique des moteurs thermiques des voitures est essentielle pour limiter ces émissions [2]. Outre les émissions de gaz à effet de serre, les moteurs de voitures sont également l'un des principaux responsables de la pollution locale à cause des émissions de NOx et de particules (PM). Ces émissions ont des effets dangereux sur la santé et provoquent de nombreuses maladies. Les particules d'un diamètre moyen de 2.5μm ou moins ($PM_{2.5}$) sont l'un des principaux polluants liés aux problèmes de santé et à la mortalité prématurée [3-5]. En raison de leurs effets négatifs sur l'environnement et la santé, les particules émises par les moteurs à essence sont réglementées par des normes de plus en plus strictes.

Afin de réduire la consommation de carburant des moteurs à essence, et donc les émissions de CO2, le carburant est injecté directement dans le cylindre dans les moteurs à Injection Directe Essence (IDE). L'interaction de la flamme avec le film liquide sur les parois est considérée comme un des sources principales de formation de suie dans ce type moteur. Grâce à l'injection directe, le carburant pulvérisé atteint le piston et les parois du cylindre pour former un film liquide. Les observations expérimentales ont montré une corrélation claire entre la quantité du liquide sur les parois restante lors de l'allumage et les émissions de particules [6, 12, 13]. Des expériences sur des moteurs optiques ont montré que l'interaction de la flamme avec le film liquide peut conduire à un feu de nappe au-dessus du piston [13,14]. Lorsque ces feux de nappes sont détectés, le nombre global de particules augmente considérablement.

La modélisation de la suie dans les moteurs à combustion interne a fait l'objet de recherches récentes en raison de la réglementation croissante sur les émissions de suie. Pour répondre aux normes récentes et futures, les outils numériques doivent être capables de bien prédire non seulement la masse de suie, mais aussi leur distribution de taille. La modélisation de la formation de suie dans la configuration interaction flamme-film nécessite la simulation de tous les phénomènes chimiques et physiques impliqués, qui comportent: l'écoulement turbulent près de la paroi, la combustion turbulente, l'interaction flamme-paroi, la formation et l'évaporation du film liquide, la formation des précurseurs des suies, la formation, la croissance et l'oxydation des suies. La simulation de tous ces phénomènes avec un compromis entre la précision des résultats et un coût de calcul raisonnable reste encore une tâche difficile. Certaines simulations CFD de moteur IDE incluant la modélisation de la suie peuvent être trouvées dans la littérature. Les simulations de Seo et de ses collègues [17, 18] ont réussi à mettre en évidence une corrélation entre la quantité de liquide déposer sur les parois et les émissions de suie, mais sans description détaillée de la dynamique de formation des suies ni de l'influence des paramètres de combustion sur la distribution des tailles des particules.

Outils et modèles numériques sélectionnés

Le logiciel CFD CONVERGE est utilisé au cours de cette thèse. Il est actuellement le logiciel CFD de référence dans l'industrie automobile française, américaine et japonaise. IFPEN est l'un des laboratoires de recherche qui soutient le développement de modèles dans ce logiciel. Différentes approches de modélisation ont été choisies pour étudier les phénomènes considérés:

- La simulation aux grandes échelles (LES pour Large Eddy Simulation) est utilisée pour résoudre l'écoulement fluide afin d'obtenir des résultats instantanés et précis des phénomènes transitoires. Les

LES avec couche limite résolue seront considérés comme des résultats de référence pour évaluer les modèles de paroi utilisés pour les LES plus grossiers.

- La phase liquide sera représentée par l'approche lagrangienne. L'interaction spray-paroi et la formation du film n'est pas considéré dans ce travail. L'accent sera mis uniquement sur l'étude de l'évaporation stationnaire et transitoire d'un film liquide. Le film sera toujours initialisé sur les parois au début de la simulation.
- Une prédiction précise des espèces chimiques est essentielle pour la modélisation de la suie. Le modèle de flamme épaissie (TFM pour Thickened Flame Model) est choisi pour la modélisation de la combustion puisqu'il permet la résolution des espèces chimiques dans le front de flamme.
- Afin d'obtenir des précurseurs de suie, des mécanismes chimiques détaillés doivent être utilisés. Une méthodologie de réduction efficace est nécessaire pour avoir un coût de calcul raisonnable tout en maintenant une prédiction précise des précurseurs de suie. L'outil Optimized Reduced Chemistry (ORCh) est utilisé pour réaliser cette tâche.
- Le modèle de suie sectionnel (SSM pour Sectional Soot Model) développé par Aubagnac-Karkar [21] est utilisé pour la modélisation de la suie. Ce modèle décrit les particules comme une phase dispersée distincte interagissant avec la phase gazeuse. Il repose sur la discrétisation de l'intervalle de masse des particules, et permet ainsi d'avoir la distribution de leurs tailles. Des sous-modèles sont utilisés pour la description détaillée de la formation, de la croissance et de l'oxydation des suies.

Objectifs

L'objectif principal de cette thèse est d'améliorer la modélisation de la suie pour les simulations de moteurs GDI. Les mécanismes de formation des suies pendant l'interaction d'une flamme turbulente prémélangée avec un film de combustible liquide ne sont pas encore bien compris. La description détaillée de la dynamique de formation de la suie nécessite un outil numérique de haute-fidélité. Chacun des phénomènes physiques impliqués dans cette configuration doit être étudié afin d'évaluer la précision de l'approche de modélisation choisie, et éventuellement de l'améliorer.

Réaliser de telles investigations détaillées dans un cas de moteur n'est pas simple et un cas académique spécifique doit être mis en place à cette fin. Le cas de l'écoulement de canal turbulent a été choisi comme configuration de base pendant tout ce travail. Cette configuration permettra de se concentrer sur les phénomènes de proche paroi avec une turbulence et des conditions thermodynamiques bien définies. Cette configuration a déjà été prise en compte dans des études multi-physiques similaires dans la littérature. Bruneaux et al. [22] ont réalisé un calcul DNS (Direct Numerical Simulation) d'interaction flamme-paroi dans un écoulement de canal turbulent. Desoutter [23] a aussi considéré cette configuration pour réaliser un calcul DNS de la couche limite turbulente au-dessus d'un film liquide stationnaire en évaporation.

Le travail réalisé au cours de cette thèse s'articule autour des points suivants :

- L'évaluation des modèles de paroi algébriques dynamiques et thermiques dans les écoulements turbulents isothermes et non-isothermes.
- L'évaluation et l'amélioration de la modélisation de l'évaporation du film liquide à travers l'évaporation stationnaire et instationnaire dans des écoulements en canal turbulent.
- L'étude de l'utilisation du modèle de flamme épaissie pour la simulation de l'interaction de flamme-paroi:
  - Dans la configuration 1D d'interaction d'une flamme normale à la paroi (dite aussi HOQ pour Head-On Quenching) dans des conditions moteur.
  - Interaction flamme-paroi dans un semi canal turbulent.
- Simulation de l'interaction flamme-film avec la formation des suies dans un semi canal turbulent.

Le manuscrit se décompose en chapitres comme se suit :

- **Chapitre 2 : Equations régissant l'écoulement fluide**

  Ce chapitre introduit les équations résolues et la modélisation physique considérée pour la phase gazeuse. La modélisation des flux de diffusion de masse et de chaleur ont été détaillées. Les équations filtrées LES sont aussi présentées. Un bref résumé des méthodes numériques utilisées pour la résolution de ces équations est présenté dans l'Annexe A.

- **Chapitre 3 : Modélisation de couche limite turbulente**

  Ce chapitre présente les caractéristiques fondamentales des couches limites turbulentes isothermes et non-isothermes. Une revue de la littérature est également effectuée sur la modélisation des contraintes pariétales et du transfert thermique sur les parois afin de comprendre les développements des modèles et de mettre en évidence les principales hypothèses. La configuration du cas de canal turbulent est également présentée dans ce chapitre. Les cas avec maillage raffiné aux parois et paroi modélisée sont réalisés afin de fournir une première évaluation avant de passer aux cas avec film liquide.

- **Chapitre 4 : Equations régissant le film liquide et revue de littérature**

  Ce chapitre est consacré aux équations régissant le film liquide et aux différentes approches de modélisation de l'évaporation existantes dans la littérature. La description numérique du film utilisée dans ce travail est également présentée.

- **Chapitre 5 : Évaluation des modèles algébriques d'évaporation de film liquide**

  Le modèle d'évaporation sélectionné grâce à la revue de littérature du chapitre 4 est évalué dans deux configurations :

  - L'évaporation stationnaire du film liquide dans un écoulement de canal turbulent. Il s'agit d'une première étape pour évaluer la modélisation du film liquide dans un problème simplifié où les transferts de chaleur et de masse sont découplés à l'interface liquide/gaz.
  - L'évaporation transitoire du film liquide dans un écoulement de canal turbulent, qui permet l'évaluation dans une configuration plus proche du cas réel.

- **Chapitre 6 : Modèle de paroi pour l'évaporation de film liquide basé sur les Equations Différentiels Ordinaires**

  Dans ce chapitre, l'approche de modélisation de paroi basée sur la résolution numérique des Equations Différentiels Ordinaires (EDO) est étendue pour l'évaporation de film liquide. Les équations considérées ainsi que leur implémentation numérique sont détaillées. Le modèle proposé est évalué dans les cas d'évaporation stationnaire et instationnaire introduit dans le chapitre 5.

- **Chapitre 7 : Simulation d'interaction flamme-paroi**

  Le chapitre 7 présente la formulation du modèle de flamme épaissie TFM. Une revue de la phénoménologie de l'interaction flamme-paroi est également présentée. Les problématiques liées à l'utilisation de la TFM pour la simulation flamme-paroi sont mises en évidence. Ces problématiques sont étudiées, tout d'abord à travers une configuration 1D d'interaction laminaire de flamme normale à une paroi dans des conditions moteur, puis par l'interaction flamme-paroi dans un écoulement turbulent en canal. Le mécanisme chimique utilisé est spécifiquement réduit pour ce cas.

- **Chapitre 8 : Interaction flamme-film avec formation de suie**

  Dans ce chapitre, tous les différents phénomènes physiques sont assemblés dans un même cas pour simuler l'interaction flamme-film avec formation de suie. La physique complexe menant au mécanisme de formation des suies dans cette configuration est décrite grâce à la simulation avec couche limite résolue. Les différents modèles impliqués sont évalués dans les cas LES avec modèle de paroi.

Dans ce qui suit, un résumé étendu est fourni pour les chapitres 3-8.

Chapitre 3 : Modélisation de couche limite turbulente

A cause de la condition d'adhérence à la paroi (vitesse nulle), une couche limite se développe dans les écoulements en proche paroi. La couche limite turbulente isotherme dans un canal plan développé peut se décomposer en deux principales régions : la couche interne (inner layer) et la couche externe (outer layer). La couche interne se décompose elle-même en différentes sous-couches: la sous-couche visqueuse, la sous-couche tampon (buffer layer), et la zone logarithmique. Le profil de vitesse dans la couche interne a une forme universelle et ne dépend que de la distance adimensionnelle à la paroi. En se basant sur cette universalité, des modèles de paroi sont développés pour prédire les contraintes pariétales lorsque le maillage ne permet pas de bien calculer le gradient de vitesse à la paroi. Deux modèles algébriques ont été considérés dans ce travail : Standard law-of-the-wall et Werner&Wengle [44].

Pour les écoulements non-isothermes, la variation de température le long de couche limite provoque aussi la variation de la viscosité et de la densité. L'unique dépendance du profil de vitesse à la distance adimensionnelle à la paroi n'est plus vérifiée non plus. Plusieurs approches ont été proposées dans la littérature pour développer des modèles de paroi pour prédire les contraintes pariétales et les flux de chaleur pariétales dans des couches limites turbulentes non-isothermes. Quatre modèles thermique algébriques ont été considérés dans ce travail : O'Rourke&Amsden [62], Han&Reitz [57], Angelberger [47] et GruMo-UniMORE [63]. Ces modèles partagent des hypothèses de modélisation communes. Ils supposent tous un gaz idéal avec un mélange sans variation de composition. Les choix de modélisation se différencient principalement sur l'effet de la variation de la densité ou l'effet du nombre de Prandtl de l'écoulement.

Cas d'écoulement minimum dans un canal

La configuration de cas canal minimal est utilisée comme configuration de base le long de cette thèse. Le domaine est périodique dans les directions principale et transversale de l'écoulement. Des conditions de paroi adhérente isotherme sont appliquées sur les faces inférieure et supérieure du domaine. Tout au long de ce travail, deux stratégies de maillage ont été appliquées en fonction du cas:

- **Le cas avec paroi raffiné:** Dans une couche limite turbulente, les structures turbulentes deviennent de plus en plus petites à mesure que la distance à la paroi diminue. La stratégie de maillage de ce cas vise principalement à satisfaire la bonne résolution des différentes structures turbulentes et bien prédire le gradient de vitesse à la paroi.
- **Cas avec modèles de parois:** Dans ce cas, des modèles de parois sont utilisés, une bonne résolution de la couche limite en proche paroi n'est plus nécessaire. La grille est alors dimensionnée pour résoudre correctement les grandes échelles intégrales dans le domaine.

Des simulations de canal turbulent avec des écoulements isothermes ou non-isothermes sont réalisées afin de fournir une première évaluation de la configuration et des différents modèles avant de passer aux cas avec film liquide. Les simulations avec les écoulements isotherme à canal minimal est réalisée afin de : (i) valider le cas LES avec maillage raffiné à la paroi par rapport au DNS de référence de Lee et Moser [60], (ii) évaluer les modèles dynamiques de paroi (lin-log et Werner&Wengle) dans les cas LES avec modèle de paroi.

Deux conditions turbulentes ont été ciblées ($Re_\tau = 550$ et $Re_\tau = 1000$) afin d'évaluer l'effet de la taille de cellule adjacente à la paroi (ou simplement appelé cellule de paroi). Les profil de vitesse moyen dans la direction de l'écoulement avec maillage raffiné à la paroi sont en bon accord avec les résultats de Lee et Moser [60] dans les deux conditions de turbulence. La forme des fluctuations normalisées est bien reproduite bien qu'elle soit sous-estimée par rapport aux résultats de référence à $Re_\tau = 1000$. Cette sous-estimation peut être acceptée compte tenu de la différence de précision entre les méthodes numériques (code DNS Lee&Moser basé sur la méthode spectrale [60]). En utilisant les modèles de paroi, les profils de vitesse moyenne dans le sens du courant sont relativement bien prédits à $Re_\tau = 550$. Cependant, pour $Re_\tau = 1000$, Werner-Wengle donne un résultat beaucoup plus proche du DNS.

Le cas de l'écoulement canal turbulent non-isotherme est réalisé afin d'évaluer les quatre modèles thermique par la paroi par rapport au cas raffiné à la paroi. Le modèle dynamique de paroi pour tous les cas modélisés par paroi est Werner-Wengle. L'écoulement dans ce cas présente une stratification thermique. La température de paroi imposée est de 373K et les termes sources sont fixés pour maintenir une température moyenne de 600K

au centre du canal. Comme pour les cas isothermes, deux conditions turbulentes ont été ciblées : $Re_\tau = 550$ et $Re_\tau = 1100$. Pour ces conditions, les profils de vitesse moyenne dans la direction de l'écoulement et leurs fluctuations ne dépendent que du modèle de paroi dynamique utilisé et ne dépendent pas du choix du modèle thermique à la paroi. Pour $Re_\tau = 550$, les profils de température moyenne des LES avec modèle de paroi sont très similaires et correspondent très bien aux profils LES raffinés. Pour $Re_\tau = 1100$, les profils de température moyenne des LES modélisées diffèrent légèrement avec globalement la même pente et la même magnitude que le cas raffiné. A $Re_\tau = 550$, tous les modèles thermiques prédisent bien le flux thermique de la paroi. A $Re_\tau = 1100$, les erreurs sont plus importantes. O'Rourke&Amsden, Han&Reitz et Angelberger sous-estiment le flux thermique de la paroi avec des erreurs allant de 6 à 14%, tandis que GruMo-UnoMORE surestime le flux thermique de la paroi d'environ 11%. L'évaluation de ces modèles dans des configurations académiques de couches limites turbulentes non-isotherme est très limitée dans la littérature. A notre connaissance, il n'existe pas d'évaluation de l'utilisation de ces modèles dans le contexte de LES avec loi de paroi.

Chapitre 4 : Equations régissant le film liquide et revue de littérature

Au cours de ce travail, certaines hypothèses simplificatrices ont été considérées afin d'établir les équations bilans du film liquide et les différents modèles d'évaporation. Comme les conditions de démarrage à froid du moteur sont visées dans ce travail, il est supposé que la température de paroi est inférieure à la température de saturation du carburant. Ainsi, le film s'évapore dans le régime mouillant sans ébullition. Dans le cas des moteurs, il est important de considérer la nature multi-composante des carburants pratiques, comme le soulignent de nombreux auteurs [67-69]. Dans ce travail, seul un film liquide mono-composant est considéré pour comprendre la physique de l'évaporation et les différentes approches de modélisation. L'extension des modèles discrets multi-composants est possible par la suite.

Contraintes à l'interface liquide/gaz

À l'interface liquide/gaz, la composante de vitesse tangentielle de la paroi est nulle et les espèces évaporées sont soufflées avec une quantité de mouvement égale au taux d'évaporation dans la direction normale à la paroi. Par conséquent, l'effet de l'évaporation du film de paroi sur la couche limite est similaire à l'effet d'une paroi transpirante [23]. Il est connu dans la littérature que la transpiration modifie assez considérablement la structure de la couche limite turbulente, affectant la distribution de la contrainte de cisaillement, et affectant également l'épaisseur de la sous-couche visqueuse [23, 37]. Dans le cadre de simulation nécessitant l'utilisation de modèles de paroi, la prise en compte de l'effet de transpiration dans les modèles dynamiques reste à ce jour un challenge. Chedevergne et Marchenay [70] ont formulé une stratégie générale pour la modélisation des couches limites turbulentes transpirant dans le contexte des simulations RANS (pour Reynolds-Avereged Navier-Stockes). Dans le contexte LES, les modèles algébriques classiques comme lin-log et werner-wengle, qui ne tiennent pas compte de l'effet de transpiration, sont encore généralement utilisés pour les simulations d'évaporation de film liquide.

Bilan d'énergie dans la phase liquide

La température de la phase liquide varie de manière continue entre la température de la paroi et la température de l'interface liquide/gaz. L'épaisseur du film de la paroi est généralement négligeable par rapport à la surface mouillée, par conséquent l'hypothèse de modélisation 1D de la température du liquide dans la direction normale à la paroi peut être appliquée. L'advection à l'intérieur la phase liquide est plus faible que la diffusion et peut aussi être négligée. Le bilan de température liquide à deux conditions aux limites : d'un côté le flux thermique échangé avec la paroi, et de l'autre côté le flux thermique échangé à l'interface liquide/gaz. Le flux thermique échangé avec la paroi dépend de la température de la paroi, qui est un des paramètres les plus influant sur l'évaporation du film [23,69,71]. Le flux thermique échangé à l'interface liquide/gaz prend en compte deux contributions : la chaleur latente en raison du changement de phase et le transfert de chaleur vers la partie liquide par conduction. Le flux thermique échangé à l'interface liquide/gaz est souvent modélisé par les modèles thermiques algébriques comme ceux considérés dans le chapitre 3. Du plus le fait que ces modèles ne prennent pas en compte l'effet de transpiration, tous ces modèle repose sur l'hypothèse de mélange sans variation de composition, ce qui n'est pas le cas dans au-dessus un film liquide en évaporation.

Modélisation du taux d'évaporation

Deux principales approches de modélisation algébrique sont disponibles dans la littérature pour modéliser le taux d'évaporation du film liquide dans les simulations CFD. La première approche est une modélisation basée sur les lois des parois [23, 67, 73-78]. Cette approche de modélisation est similaire aux modèles de paroi algébriques dynamique et thermique. O'Rourke et Amsden [73] ont proposé ce modèle pour les simulations RANS. Ce modèle a ensuite été utilisé dans la littérature pour des simulations RANS [74-77] et récemment pour LES [78], toujours pour des cas de moteurs à combustion interne. Cependant, ce modèle montre une grande dépendance à la taille du maillage près de la paroi. Dans le but d'établir une loi de paroi plus universelle, Desoutter [23] a effectué des DNS de film liquide stationnaire s'évaporant dans un écoulement de canal turbulent. Sur la base de ces résultats, il a développé un ensemble de lois de paroi dynamiques,

thermiques et de masse d'espèces évaporées qui prennent en compte l'effet de transpiration sur la couche limite turbulente. Cependant, la transition de la sous couche laminaire à la partie turbulente de la couche limite varie considérablement d'un cas à l'autre. Comme les modèles d'évaporation basés sur les lois des parois manquent d'universalité, ils ne sont pas considérés pour ce travail.

La deuxième approche de modélisation est une solution semi-analytique basée sur une analogie de transfert chaleur-masse. Elle est basée sur les premiers travaux de Spalding [81]. Elle a été d'abord développée pour approximer le taux d'évaporation de gouttelette ou de film liquide en utilisant des quantités de champ lointain, et elles ont été introduites plus tard dans le contexte de la CFD. Les modèles dynamiques et les modèles thermiques classiques qui ne prennent pas en compte le transfert de masse sont classiquement utilisés avec ce modèle d'évaporation. Le taux d'évaporation dépend directement du flux de chaleur à l'interface liquide/gaz. L'effet du transport turbulent est donc inclus implicitement à travers le flux de chaleur modélisé. C'est l'approche retenue pour l'évaluation de la précision de l'évaporation dans les cas avec modèle de paroi.

Description numérique du film liquide

Dans les cas moteur, la modélisation de la phase liquide du film de paroi est étroitement liée à la modélisation du spray. L'approche lagrangienne est généralement choisie pour les cas de moteurs compte tenu de son efficacité en termes de calcul. Cette approche est également utilisée dans le cadre de ce travail pour la description du film liquide. La phase liquide est divisée en parcelles où chaque parcelle est suivie comme un point matériel dans le référentiel lagrangien et interagit avec les autres parcelles et l'écoulement environnant. Lorsqu'une parcelle est située dans une cellule de paroi, elle est comptabilisée comme faisant partie du film liquide. La formation du film liquide et ses caractéristiques initiales (surface mouillée, forme, épaisseur, température, ...) dépendent de l'étape de modélisation de l'interaction spray/paroi. La formation et l'étalement du film ont une grande influence sur la dynamique d'évaporation. La modélisation du spray et son interaction avec la paroi n'entre pas dans le cadre de cette thèse et le film liquide sera toujours initialisé avec une distribution uniforme des particules sur les parois. Cette procédure d'initialisation a été spécifiquement développée pour les besoins de ce travail. La température du liquide est résolue que dans la direction de la normale à la paroi. La méthode sélectionnée est une méthode de discrétisation par volumes finis fournie par CONVERGE. Cette méthode est adaptée de la résolution du profil de température pour les gouttelettes lagrangiennes telle que décrite par Sazhin et al [86].

Chapitre 5 : Évaluation des modèles algébriques d'évaporation par film de paroi

Bien que le modèle d'évaporation basé sur la solution semi-analytique est largement utilisé pour les simulations de cas moteur, sa validation et sa dépendance à la modélisation du flux thermique et la taille de la cellule paroi est très limité, surtout pour les simulations LES. Dans ce chapitre, on évalue cette approche pour l'évaporation stationnaire et transitoire de film liquide dans un écoulement de canal turbulent. L'évaporation stationnaire permet dans un premier temps d'évaluer le modèle dans un problème simplifié où les transferts de chaleur et de masse sont découplés à l'interface liquide/gaz. La configuration transitoire permet l'évaluation de l'évaporation réelle du film de paroi.

Configuration de l'évaporation stationnaire

La configuration est similaire à celle considérée par Desoutter [23] pour conduire le calcul DNS de la couche limite turbulente au-dessus d'un film liquide en évaporation. Le film liquide couvre toutes les surfaces des parois dans une configuration d'écoulement de canal turbulent. Le film liquide est considéré comme suffisamment épais pour que son épaisseur et la température de surface puissent être fixées comme constantes pendant la simulation, permettant une configuration d'évaporation stationnaire. En plus des termes sources ajoutés aux équations de quantité de mouvement et d'énergie, un terme source est ajouté à l'équation de transport de l'espèce évaporée afin de compenser de l'effet de la masse ajouté par évaporation et garder ainsi un écoulement stationnaire.

Le modèle algébrique d'évaporation basé sur la solution semi-analytique est évalué par rapport aux résultats paroi raffinée. L'évaluation est réalisée avec trois modèles de chaleur de paroi : O'Rourke-Amsden, GruMo-UnoMORE et Angelberger. Ceci permet d'étudier la dépendance directe de la modélisation du taux d'évaporation sur la modélisation du flux thermique de paroi. La contrainte de cisaillement sur l'interface liquide/gaz est calculée à l'aide du modèle de paroi dynamique de Werner&Wengle dans tous les cas de modélisation de la paroi.

Configuration de l'évaporation transitoire

La réponse transitoire de l'épaisseur du film et de la température est considérée dans l'évaporation du film dans un canal turbulent. Cette configuration est plus représentative de la pratique réelle de l'évaporation de film de paroi car les problèmes de transfert de chaleur et de masse sont couplés. La sensibilité des résultats à l'épaisseur initiale du film et à la température de la paroi peut également être étudiée dans cette configuration, en plus de la sensibilité à la turbulence de l'écoulement.

Conclusions

L'évaporation du film liquide a une influence significative sur la physique en proche paroi. L'utilisation du modèle d'évaporation basé sur la solution semi-analytique avec les modèles algébriques dynamique et thermique classiques de chaleur et de paroi dynamique n'est pas adaptée à la LES avec modèle de paroi. D'après les résultats actuels et pour ces conditions particulières, les principaux problèmes mis en évidence sont les suivants:

- L'évaporation stationnaire montre que les modèles algébriques classiques de paroi dynamique, qui ne tiennent pas compte de l'effet de la transpiration, ne parviennent pas à prédire la contrainte de cisaillement correcte à l'interface liquide/gaz.
- Les modèles algébriques de chaleur de paroi ne parviennent pas non plus à prédire un flux de chaleur précis transféré de la phase gazeuse à la phase liquide.
- Les résultats dépendent en premier lieu de la taille sans dimension adjacente à la paroi. La dépendance vis-à-vis du modèle de chaleur de paroi utilisé est également constatée lorsque le centre de la cellule de paroi est situé dans la couche tampon.

Chapitre 6 : Modèle de paroi pour l'évaporation de film liquide basé sur les Equations Différentiels Ordinaires

Afin d'améliorer la physique de l'évaporation du film liquide, les faiblesses des modèles algébriques soulignées dans le chapitre précédent doivent être améliorées. Nous avons proposé dans ce travail d'étendre le modèle basé sur la résolution d'équations différentielles ordinaires aux cas avec transfert de masse. Ces équations 1D sont résolues numériquement dans la direction normale à la paroi en utilisant les quantités filtrées LES à une certaine distance et les conditions limites à la paroi. La contrainte de cisaillement et le flux de chaleur qui en résulte sont utilisés comme conditions limites pour le LES. La résolution numérique des équations de la couche limite permet de mieux prendre en compte les phénomènes physiques pertinents qui sont difficiles à prendre en compte avec les modèles de paroi algébriques.

Formulation et implémentation du modèle pour l'évaporation sur film de paroi

Les équations résolues sont les suivantes : l'équation de quantité de mouvement dans la direction parallèle à la paroi, l'équation d'énergie et l'équation de masse de l'espèce évaporée. Afin de maintenir un coût de calcul raisonnable, les équations de conservation de la masse des autres espèces de gaz ne sont pas résolues et la diffusion différentielle et la vitesse de correction sont négligées. Le terme d'advection dans la direction normale à la paroi due au taux d'évaporation a été pris en compte dans les équations. Le modèle de paroi de Cebeci-Smith [36, 48, 93] a été choisi pour modéliser la viscosité turbulente car il a aussi l'avantage d'inclure l'effet de la transpiration de la paroi dans une couche limite à propriétés variables.

Une méthode de volumes finis est utilisée pour résoudre numériquement les équations précédentes sur une grille 1D allant de l'interface liquide/gaz à une certaine distance normale à la paroi. Les équations de quantité de mouvement, d'énergie et de l'espèce évaporée sont couplées. Ainsi, un algorithme itératif est utilisé pour les résoudre.

Évaluation du modèle proposé

Le modèle proposé a été évalué les mêmes configurations de canal turbulent présentées dans le chapitre précédent. Dans la configuration d'écoulement stationnaire, la contrainte de cisaillement moyenne à l'interface liquide/gaz est beaucoup mieux prédite : seulement une erreur relative de 4% et 8% a été obtenue pour les conditions de turbulence faible et forte respectivement, alors qu'elles étaient d'au moins 22% et 40% respectivement en utilisant les modèles algébriques. Le flux de chaleur du gaz vers le liquide s'est légèrement amélioré puisque l'erreur relative a chuté d'environ 10% pour les deux conditions de turbulence. Enfin, le taux d'évaporation moyen s'est également amélioré avec une erreur relative de 28% et 30% pour les conditions de faible et forte turbulence, alors qu'ils étaient au moins 40% et 42% respectivement en utilisant les modèles algébriques.

Dans la configuration d'écoulement transitoire, Le nouveau modèle réussit à prédire l'augmentation exponentielle de la vitesse d'évaporation à la fin de l'évaporation du film de paroi, alors que ce n'était pas le cas avec les modèles algébriques. De plus, les résultats dépendent moins de la taille de la cellule à la paroi.

Dans tous les cas, le temps de calcul supplémentaire dû à l'utilisation de la modélisation basée sur les ODEs n'a pas dépassé 12% par rapport au temps de calcul lorsque des modèles algébriques sont utilisés, ce qui est un coût de calcul supplémentaire acceptable étant donné les améliorations des résultats.

Chapitre 7 : Simulation d'interaction flamme-paroi

La modélisation de la combustion est une étape clé dans la simulation de la configuration de l'interaction flamme-film. Dans ce chapitre on s'intéresse d'abord à la phénoménologie et à la modélisation de l'interaction d'un front de flamme de prémélange avec une paroi sèche.

Le cas canonique de la configuration 1D d'interaction de flamme normale à la paroi (dite Head-On Quenching) est généralement considéré comme une référence de base pour l'étude de la FWI et largement étudié dans la littérature [30, 112, 113]. Dans cette configuration, la distance entre la flamme et la paroi et le flux thermique de la paroi évoluent dans le temps. Le phénomène d'extinction se produit lorsque le taux de perte de chaleur à travers la paroi est supérieur au taux de chaleur interne généré par les réactions chimiques. A l'extinction, la distance entre le front de flamme et la paroi est minimale, et le flux thermique de la paroi atteint son maximum.

Le modèle de flamme épaissie TFM est utilisé dans ce travail car il permet de modéliser la chimie détaillée nécessaire à la modélisation de la formation des suies. L'utilisation du modèle de flamme épaissie pour la simulation de cette configuration pose certaines problématiques:

- **Un problème thermique :** Comme le front de flamme est épaissi d'un facteur F , le gradient de température dans le front de flamme est également divisé par un facteur F. Ainsi, quelle est l'influence de ce gradient de température artificiellement modifié sur le flux de chaleur de la paroi lorsque le front de flamme atteint la paroi ? et par conséquent sur les phénomènes d'extinction ?
- **Un problème géométrique :** L'épaisseur du front de flamme artificiellement épaissie est multiplié avec un facteur F par rapport à l'épaisseur d'une flamme laminaire, avec F de l'ordre de 40 dans une simulation moteur. Cependant, la distance d'extinction est de l'ordre de quelques épaisseur de flamme laminaire. Ainsi, comment cette limitation géométrique affecte-t-elle le phénomène d'interaction flamme-paroi ?

Lorsque l'influence de la turbulence est ajoutée au phénomène d'interaction flamme-paroi, des problèmes de modélisation supplémentaires doivent être pris en compte :

- **Le plissement de la flamme près de la paroi :** Le plissement non résolu de la flamme est modélisé par le facteur d'efficacité. L'interaction flamme-turbulence est modifiée pendant l'interaction avec la paroi, et donc, une modélisation appropriée du facteur d'efficacité est nécessaire près de la paroi.
- **Modèle de paroi :** Pendant l'interaction flamme-paroi, l'expansion des gaz brûlés et la température élevée modifient les propriétés de l'écoulement (la viscosité augmente considérablement et la densité diminue dans les gaz brûlés), ce qui affecte la turbulence à proximité de la paroi. Ainsi, on s'attend à ce que le modèle de flamme épaissie ait une influence sur la modélisation de la contrainte et du flux de chaleur à la paroi.

A notre connaissance, il n'existe pas de travaux dans la littérature qui étudient en détail les problèmes soulevés ci-dessus lorsque le modèle de flamme épaissie est utilisé pour l'interaction flamme-paroi. Dans ce qui suit, nous allons essayer de mieux comprendre l'influence de ce modèle de combustion sur la simulation de l'interaction flamme-paroi à travers deux configurations académiques.

Interaction 1D d'une flamme de prémélange normale à la paroi dans des conditions moteur IDE

Ce cas donnera un premier aperçu de l'influence de l'utilisation du modèle de flamme épaissie dans la prédiction du flux thermique de la paroi, du taux de consommation de carburant et de la distance d'extinction. L'accent sera mis sur l'influence de la conductivité thermique utilisée dans l'expression du flux thermique à la paroi. L'influence du facteur d'épaississement F sera également étudiée. Le cas est initialisé avec un front de flamme de prémélange se propageant vers la paroi dans un mélange statique de gaz frais. Les gaz frais est un mélange isooctane/air avec un rapport à la stoechiométrie. La température des gaz frais est fixée à 600K et la pression est fixée à 20 bars pour être aussi proche que possible des conditions moteur IDE au début du

temps de détente. La température de la paroi est également fixée à 600K pour éviter le transfert de chaleur avant l'interaction flamme-paroi. Le mécanisme chimique de An et al. [123] a été considéré pour ce cas. Il s'agit d'un mécanisme squelettique composé de 85 espèces et de 232 réactions, et spécialement développé pour la combustion de substituts de l'essence à haute pression et pour les simulations de moteurs GDI.

Dans le cas de référence, la chimie est directement calculée sans aucune modélisation supplémentaire de la combustion. Ainsi, le maillage doit être suffisamment raffiné pour résoudre correctement le front de flamme et pour bien capturer le gradient de température à la paroi pendant les phénomènes l'interaction flamme-paroi.

Concernant les cas avec modèle de flamme épaissie, le senseur de Jaravel [108] est utilisé pour appliquer localement le facteur d'épaississement dans la zone de réaction et préserver une diffusion normale ailleurs. Trois maillages avec des tailles de cellules différentes ont été utilisés, associés à des facteurs d'épaississement de 44, 22 et 11 afin d'étudier la sensibilité à ce facteur. Trois formulations du flux de thermique à la paroi ont été testées lorsque le modèle de flamme épaissie est utilisé. Les résultats ont été comparés au cas de référence.

La façon la plus simple d'exprimer le flux thermique de paroi est d'utiliser la conductivité thermique du gaz et le gradient de température à la paroi comme dans le cas de référence. L'utilisation de cette formulation ne modifie pas beaucoup l'évolution de la vitesse de la flamme et récupère bien la forme et la position des profils de température après l'extinction. Cependant, le flux de chaleur de la paroi diminue avec l'augmentation du facteur d'épaississement en raison de la diminution du gradient de température qui n'est pas compensée par une augmentation de la conductivité thermique.

On peut intuitivement suggérer de multiplier la conductivité thermique à la paroi par le facteur d'épaississement. L'utilisation d'une telle formulation modifie considérablement le phénomène l'interaction flamme-paroi. Elle provoque des pertes thermiques importantes à travers la paroi, ce qui ralentit le taux de consommation de combustible et freine l'avancée du front de flamme. La flamme ne s'éteint pas pour autant, car elle est maintenue avec les flux de masse et de chaleur épaissis jusqu'à la consommation complète du combustible. Ainsi, le flux de chaleur de la paroi reste à des valeurs élevées plus longtemps qu'il ne devrait l'être, ce qui résulte à une altération importante du profil de température la position du front de flamme pendant toute l'interaction.

Une troisième méthode pour exprimer le flux thermique à travers la paroi est d'utiliser le la conductivité thermique évaluée au centre de la cellule adjacente à la paroi. L'utilisation d'une telle formulation améliore la prédiction du flux de chaleur à la paroi tout en ayant une bonne prédiction de l'évolution du taux de consommation du combustible et des profils de température. Avec cette expression du flux thermique, l'intégrale du flux thermique est aussi relativement bien prédit et elle est moins dépendante du facteur d'épaississement. Bien que cette formulation ne soit pas justifiée théoriquement, il est montré qu'il donne les meilleurs résultats par rapport aux deux autres sur cette configuration, et qu'il reproduit raisonnablement bien le résultat de référence en termes de vitesse de consommation de carburant et de flux thermique total. Un modèle plus sophistiqué de l'épaississement à la paroi est encore nécessaire, mais dans le contexte de cette thèse où de nombreux autres aspects ont dû être traités (modélisation de la loi de la paroi, modélisation du film de paroi, formation de la suie), un tel modèle n'a pas pu être développé.

Interaction flamme-paroi dans un canal turbulent

Ce cas permet d'inclure l'influence de la turbulence. L'objectif principal de cette étude est d'évaluer l'utilisation du modèle de flamme épaissi pour une simulation d'interaction flamme turbulente paroi turbulent et l'accent sera mis uniquement sur l'influence des modèles de paroi. La configuration est inspirée du calcul DNS de Bruneaux et al [22]. Seul un écoulement en demi-canal est considéré dans ce travail. L'écoulement est périodique dans le sens de l'écoulement et dans la direction transverse. La condition limite supérieure est une paroi avec condition d'adhérence isotherme à température de 370K. La condition limite inférieure est une paroi adiabatique sans condition d'adhérence. La phase gazeuse est initialisée à partir d'un calcul préalable d'un écoulement de canal turbulent stationnaire avec un mélange air/iso-octane au rapport d'équivalence de 0,8, à la pression atmosphérique, et avec une température moyenne au centre du canal de 600K. Le Re_τ initial est égal à 230. Aucun terme source n'a été utilisé puisque la simulation est transitoire. Un front de flamme de prémélange plan a été ajouté à l'écoulement initial près du centre du canal. Le mécanisme chimique de An et al. [123] (85 espèces et 232 réactions) a été considéré pour cette configuration. Afin d'accélérer le calcul,

ce mécanisme a été réduit en utilisant l'outil ORCh [124, 125] (Optimized Reduced Chemistry). Le schéma réduit final contient 15 espèces transportées, 4 espèces d'état quasi-stationnaire (QSS), et 24 réactions.

Les résultats de référence sont d'abord obtenus avec une LES raffinée à la paroi et un front de flamme résolu sans appliquer aucun épaississement artificiel. Ensuite, trois cas LES avec paroi modélisée sont réalisés. Seuls des modèles de paroi algébriques sont utilisés pour la paroi sèche. Le modèle de contrainte pariétale de Werner&Wengle a été utilisé avec différents modèles thermiques : O'Rourke-Amsden, Angelberger, et GruMo-UniMORE. La valeur y+ au centre de la cellule de la paroi reste inférieure à 7,7 pendant toutes les simulations de modélisation de la paroi. Comme détaillé dans la section 3.1.2.2, les modèles algébriques de chaleur de paroi sont exprimés en utilisant des propriétés évaluées au centre de la cellule de maillage adjacente à la paroi. Les modèles algébriques de chaleur de paroi sont utilisés ici avec leur formulation originale sans aucune modification liée au modèle de flamme épaissie. Le facteur d'efficacité appliqué par le modèle de flamme épaissie est calculé à l'aide du modèle de Charlette et al [110].

Cette étude a montré que l'utilisation de faibles valeurs de facteurs d'épaississement (environ F = 6.5) pour une flamme artificiellement épaissie, ainsi que des modèles algébriques de contrainte de paroi et de chaleur évalués avec l'expression linéaire de sous-couche, permet globalement de reproduire les phénomènes d'intéraction flamme-paroi. La variation de la contrainte de cisaillement de paroi est relativement bien prédite avec des erreurs inférieures à 25% par rapport aux résultats de référence. O'Rourke&Amsden et GruMo-UniMORE prédisent mieux le pic du flux thermique de paroi pendant l'extinction (surestimation d'environ 60%) que le modèle d'Angelberger (surestimation d'environ 100%). Cette meilleure prédiction est probablement due à la formulation différente du flux thermique de la paroi dans la sous-couche linéaire. Il est intéressant de souligner que le flux thermique a toujours été surestimé dans ce cas, c'est-à-dire avec l'influence de la turbulence, alors qu'il a été sous-estimé dans le cas de la flamme 1D HOQ en utilisant la même formulation du flux thermique que les modèles O'Rourke&Amsden et GruMo-UniMORE. Enfin, il a été noté que la masse prédite des espèces majeures est en bon accord avec les résultats de référence après la trempe, et une surestimation d'environ 70% de la masse de CO a été notée pendant l'interaction flamme-paroi.

Chapitre 8 : Interaction flamme-film avec formation de suie

Dans ce dernier chapitre, tous les modèles sont utilisés ensemble pour étudier la formation des suies dans une configuration interaction flamme-film. Une fois encore, nous ne chercherons pas à obtenir des validations expérimentales. L'objectif principal est d'avoir un résultat de référence afin d'évaluer les différentes approches de modélisation des différents phénomènes physiques impliquées.

Modèle de suie

Le modèle sectionnel SSM a été utilisé pour la modélisation de la suie. Il s'agit d'une approche de modélisation détaillée qui permet de prédire la masse des suies et la distribution de leurs tailles. Le modèle utilisé dans ce travail a été développé par Aubagnac-Karkar [21, 133] sur la base de travaux antérieurs [138-141]. Il décrit la fonction de densité numérique de la suie comme une phase dispersée distincte interagissant avec la phase gazeuse. Les sous-modèles de nucléation et de condensation ont également été améliorés pour inclure l'effet de réversibilité [133]. Les particules de suie sont séparées en fonction de leur masse en sections distinctes. La fraction de masse de suie filtrée de chaque section est transportée dans l'écoulement. La modélisation de la suie est couplée avec les espèces chimiques de la phase gazeuse. Ainsi, si le modèle de flamme épaissie est utilisé pour la modélisation de la combustion, les équations de transport des sections de suie sont également épaissies.

Réduction de mécanisme chimique

La formation de la suie nécessite un mécanisme chimique détaillé capable de bien prédire les précurseurs, dans ce cas le Pyrène (A4). Le mécanisme chimique de Raj et al. [142], composé de 231 espèces et 1350 réactions, a été sélectionné car il permet la prédiction des aromatiques jusqu'au Coronène (7 cycles benzéniques) pour la combustion de carburants de substitution à l'essence. Afin d'accélérer le calcul, ce mécanisme est réduit en utilisant l'outil ORCh. Dans ce cas, la réduction a été basée sur un réacteur stochastique qui permet de couvrir toute une gamme de conditions de température et de mélange [126]. Le mécanisme réduit final utilisé dans la simulation est composé de 86 espèces et de 432 réactions.

Interaction flamme-film et formation de suie dans un écoulement de canal turbulent

La formation des suies a été étudiée dans la même configuration que celle considérée pour l'interaction flamme-paroi sèche, présentée dans le chapitre précédent, avec l'ajout d'un film liquide sur la paroi. Le film de paroi est initialisé sur environ 9% de la surface de la paroi avec une épaisseur initiale de 10μm et à la température de la paroi.

Les résultats de référence sont d'abord obtenus grâce au calcul LES avec une couche limite et un front de flamme résolus. Cette simulation raffinée décrit également la physique complexe menant à la formation de suie dans cette configuration. Seule une brève description des résultats primaires est présentée dans ce manuscrit. Le calcul de référence a montré que les régions localement riches sur le film de la paroi modifient les phénomènes d'extinction de la flamme de prémélange par rapport à son extinction sur la paroi sèche. Après l'extinction de la flamme prémélangée, une région réactive de type diffusion est observée autour du panache de combustible évaporé, alimentée par le combustible évaporé et par l'O2 restant dans les gaz brûlés de la flamme de prémélange pauvre. Les suies sont principalement formées dans cette zone réactive post-extinction. Une analyse plus approfondie des résultats est nécessaire pour mieux comprendre la zone réactive post-extinction et décrire en détail le mécanisme de la formation des suies.

Ensuite des calculs LES avec modèle de paroi et une flamme artificiellement épaissie ont été réalisés pour évaluer les modèles. Ces calculs montrent que :

- Le modèle de paroi basé sur la résolution des équations 1D proposé dans ce travail permet comme prévu de mieux prédire l'épaisseur du film de paroi avant l'interaction flamme-film.

- Pendant l'interaction flamme-film, les modèles algébriques et le nouveau modèle de paroi se comportent de la même manière, probablement à cause de la très forte augmentation de température due aux gaz brûlés derrière la flamme.
- Le processus de formation de la suie est fortement ralenti par le facteur d'épaississement appliqué par le modèle de flamme épaissie. Un modèle qui permettrait de couper cet épaississement après l'interaction flamme-film conduirait à un accord correct avec le calcul de référence. Ce résultat est encourageant car proposer une telle adaptation ne semble pas une tâche trop difficile.

Chapitre 9: Conclusions et perspectives

L'interaction d'une flamme turbulente de prémélange avec un film de combustible liquide est considérée comme la principale source de formation des suies dans les moteurs IDE. La simulation de cette configuration nécessite la modélisation de différents phénomènes physiques. Le travail effectué au cours de cette thèse visait à étudier en détail la précision des différents modèles impliqués. Les approches de modélisation suivantes ont été choisies : (i) La simulation des grandes échelles LES avec modèles de paroi pour résoudre l'écoulement turbulent en proche paroi. (ii) La phase liquide est représentée par l'approche lagrangienne, (iii) Le modèle de flamme épaissie (TFM) avec des mécanismes chimiques réduits sont utilisés pour la modélisation de la combustion. (iv) La formation des suies est modélisée par le modèle sectionnel SSM. Les investigations ont été réalisées dans un écoulement de canal turbulent. Cette configuration académique permet d'inclure les phénomènes de proches paroi qui sont d'intérêt pour ce travail, tout en étant suffisamment simple pour permettre le calcul de cas de référence où la couche limite et le front de flamme sont résolus.

Evaporation de film liquide

Tout d'abord, une revue de la littérature a été réalisée sur les modèles d'évaporation par film de paroi. Un modèle algébrique basé sur une solution semi-analytique a été sélectionné. L'utilisation de ce modèle avec des modèles algébriques dynamiques et thermiques a été évaluée sur deux cas différents d'écoulement de canal turbulent, l'un avec évaporation stationnaire et l'autre avec évaporation transitoire. Ces évaluations ont montré que l'évaporation du film liquide a une influence significative sur la physique en proche paroi et que les modèles algébriques ne sont pas adaptés à cette configuration. Les résultats dépendent en en premier lieu de la taille adimensionné des cellules à la paroi. La dépendance au choix du modèle thermique utilisé est également remarquée lorsque le centre de la cellule à la paroi est situé dans la sous-couche tampon de la couche limite.

Afin d'améliorer les résultats, un modèle de paroi plus détaillé a dû être proposé. Ce modèle est basé sur la résolution d'équations différentielles ordinaires 1D et qui tiennent compte l'évaporation du film liquide. L'équation d'équilibre des espèces évaporées est résolue dans la direction normale à la paroi avec l'équation de la quantité de mouvement et de l'énergie. La formulation proposée prend en compte l'effet de transpiration grâce au terme d'advection dans la direction normale à la paroi, et à travers la formulation du modèle de la viscosité turbulente. L'évaluation du modèle proposé montre clairement une amélioration des résultats par rapport aux modèles algébriques dans les configurations stationnaires et transitoires. Les erreurs sur la contrainte de cisaillement et le flux de chaleur à l'interface liquide/gaz et sur le taux d'évaporation ont été considérablement améliorées et sont devenues acceptables pour les configurations suivantes.

La simulation de l'interaction flamme-paroi en utilisant le modèle de flamme épaissie

Les problèmes thermiques et géométriques liés à l'utilisation du modèle de flamme épaissie pour la simulations de l'interaction flamme-paroi ont été soulignés au cours de ce travail. Ces questions ont d'abord été étudiées dans une configuration 1D d'interaction de flamme normale à la paroi (ou Head-On Quenching) dans des conditions pertinentes pour un moteur IDE. Pour ce faire, le modèle de flamme épaissie a été utilisé avec trois formulations de flux de chaleur à la paroi et les résultats ont été comparés à un calcul résolu de référence. La formulation standard du flux de chaleur utilisant la conductivité thermique évaluée à la paroi, sans aucune autre modification, n'altère pas beaucoup l'évolution de la vitesse de flamme et prédit relativement bien la forme et la position des profils de température après l'extinction. Cependant, le flux de chaleur pariétal diminue en augmentant le facteur d'épaississement. La formulation du flux de chaleur pariétal avec une conductivité thermique évaluée à la paroi et multipliée par le facteur d'épaississement modifie considérablement le phénomène d'extinction et donne des grandes erreurs sur l'évolution de la vitesse de la flamme, et sur l'intégrale du flux thermique pariétal. Enfin, la formulation utilisant la conductivité thermique évaluée au centre de la cellule donne les meilleurs résultats dans cette étude, même si une telle formulation n'est pas justifiée théoriquement.

Ensuite, le cas de canal turbulent a été adapté pour compléter l'analyse précédente à un écoulement 3D. Pour cela une flamme a été initiée au centre du canal pour se propager vers la paroi. Cette deuxième partie des validations était axée sur l'évaluation de l'utilisation des modèles de paroi algébriques avec une flamme

artificiellement épaissie. La principale conclusion est que, pour de faibles facteurs d'épaississement (environ 6.5), l'utilisation des modèles dynamiques et thermiques algébriques fournissent des résultats en bon accord avec le calcul raffiné de référence si la distance adimensionnée du centre de la cellule à la paroi est inférieure au seuil de la transition laminaire/turbulent de la couche limite. Le cas établi n'a pas permis d'évaluer cette stratégie de modélisation pour des tailles adimensionnées de cellules à la paroi plus grandes. Cependant, cette conclusion était suffisante pour passer à l'étape suivante de ce travail.

Formation des suies dans une configuration d'intéraction flamme-film

Un film liquide a été ajouté à la configuration d'interaction flamme-paroi dans un écoulement de canal turbulent afin d'étudier l'interaction flamme-film. Le modèle sectionnel SSM a été utilisé pour modéliser la formation des suies. Le calcul avec couche limite et front de flamme résolus a montré que la région localement riche au-dessus du film liquide modifie les phénomènes d'extinction de la flamme de prémélange par rapport à son extinction sur une paroi sèche. Après l'extinction de la flamme de prémélange, une région réactive est observée autour du panache de combustible évaporé, alimentée par le combustible évaporé et par l'oxygène restant dans les gaz brûlés de la flamme de prémélange pauvre. Les suies sont principalement formées dans cette zone réactive post-extinction.

Les différentes approches de modélisation des phénomènes impliqués ont été utilisées ensemble pour simuler cette configuration avec paroi modélisée. Le modèle de paroi pour l'évaporation de film liquide proposé dans ce travail permet de mieux prédire l'épaisseur du film avant le début de l'interaction avec le front de flamme. Les erreurs sur la formation des suies ne dépendent pas en premier lieu de la modélisation de l'évaporation du film liquide, mais plutôt de l'utilisation du modèle de flamme épaissie dans la zone réactive post-extinction. Le calcul avec épaississement désactivé après l'extinction de la flamme de prémélange conduit à une bonne prédiction de la formation des suies dans les conditions considérées.

Perspectives

Evaporation de film liquide

La précision des différentes études sur la modélisation de l'évaporation de film liquide réalisées dans cette thèse peut être améliorée dans des travaux futurs en considérant l'approximation de "Hirschfelder and Curtiss" pour le flux de diffusion des espèces puisque la contribution du gradient de masse moléculaire est non négligeable dans cette configuration. La modélisation de l'évaporation du film liquide devrait également être évaluée dans un cas plus réaliste qui inclut l'interaction spray-paroi, la formation du film, une température variable de la surface de la paroi, et un combustible composé de plusieurs espèces. Le cas de l'impact du spray G avec évaporation du film liquide dans une chambre non réactive à volume constant est un bon cas pour une telle investigation [89].

Le modèle de paroi basée sur la résolution des équations 1D pour l'évaporation de film liquide peut être considérée comme une première étape vers une stratégie de modélisation générale pour la simulation LES en proche paroi avec transfert de masse et de chaleur. Des améliorations physiques et numériques peuvent être envisagées pour des travaux futurs.

Simulation de l'interaction flamme-paroi en utilisant le modèle de flamme épaissie

La configuration 1D d'interaction de flamme normale à la paroi (HOQ) a montré que la flamme artificiellement épaissie modifie la perte de chaleur à la paroi. Ainsi, un traitement spécifique de l'épaississement à la paroi doit être développé dans des travaux futurs. Les recherches devraient également être étendues à l'interaction entre un front de flamme laminaire avec une paroi transversale (Side Wall-Quenching). Il est également intéressant d'étudier l'effet de la perte de chaleur sur la tabulation des paramètres utilisés pour le calcul du facteur d'épaississement et du capteur de flamme.

Concernant l'interaction flamme-paroi-turbulence, plusieurs points doivent être améliorés. Un facteur d'efficacité adapté à l'interaction flamme-paroi-turbulence proche doit être développé. L'effet de l'épaississement artificiel doit être inclus dans les modèles de paroi dynamique et thermique. L'étude de l'interaction flamme paroi dans un écoulement de canal turbulent peut être complétée par des cas avec des facteurs d'épaississement

plus élevés et des tailles de cellule à la paroi plus importantes. L'importance de la prise en compte de l'effet Soret doit également être étudiée, en accordant une attention particulière à la prédiction des espèces principales et intermédiaires près de la paroi.

Formation de suie dans une configuration d'interaction flamme-film

Le cas académique l'interaction de flamme-film dans un canal turbulent établi dans cette thèse est un bon outil pour étudier et investiguer la formation des suies dans cette configuration complexe. Une analyse plus approfondie des résultats obtenus sur la paroi est nécessaire pour mieux comprendre la zone réactive post-extinction et décrire en détail la formation des suies. Afin d'améliorer la prédiction de la formation des suies, un modèle de flamme épaissie spécifique doit être développé afin de désactiver automatiquement l'épaississement après l'extinction de la flamme de prémélange. Le comportement de la modélisation de l'évaporation du film de paroi pendant l'interaction avec le front de flamme doit également être étudié plus en détail et potentiellement amélioré. Il est possible de considérer l'effet des réactions chimiques dans la modélisation basée sur la résolution des équations 1D avec une approche similaire à celle de Muto et ses co-auteurs [91, 92].

Les différentes stratégies de modélisation doivent également être validées par rapport à des résultats expérimentaux. La configuration d'impact du spray G avec allumage de la flamme de prémélange dans une chambre à volume constant est adéquate pour une telle investigation [89].